UNIVERSITÉ CATHOLIQUE DE LOUVAIN
FACULTY OF SCIENCE
EARTH AND LIFE INSTITUTE
GEORGES LEMAÎTRE CENTRE FOR EARTH AND CLIMATE RESEARCH

Influence of small-scale processes on ocean-cryosphere-atmosphere interactions off Adélie Land, East Antarctica

DOCTORAL DISSERTATION PRESENTED BY

PIERRE-VINCENT HUOT

IN FULFILLMENT OF THE REQUIREMENTS
FOR THE DEGREE OF DOCTOR IN SCIENCE

THESIS COMMITTEE:

Prof. Thierry Fichefet (Supervisor)	Université catholique de Louvain
Prof. Marie-Laurence De Keersmaecker (Chair)	Université catholique de Louvain
Prof. François Massonnet	Université catholique de Louvain
Prof. Hugues Goosse	Université catholique de Louvain
Dr. Camille Lique	IFREMER
Dr. Nicolas Jourdain	Université Grenoble Alpes
Prof. Xavier Fettweis	Universtié de Liège

August 2021

Remerciements

Pour commencer, je souhaiterais remercier les membres du jury d'avoir accepté de lire et d'évaluer mon travail. Je suis honoré que ma thèse soit passée entre vos mains et j'ai grandement apprécié nos échanges tant en dehors que lors de la défense.

Merci ensuite à Thierry de m'avoir offert la possibilité de réaliser cette thèse. Merci pour la confiance et la liberté que tu m'as accordée. Merci aussi pour ta compréhension et tes conseils qui m'ont souvent ramené sur le droit chemin, là où j'ai tendance à un peu trop divaguer. Merci à toi et à Hugues de m'avoir permis de bénéficier d'une cinquième année grâce à laquelle j'ai pu mener à bien ce projet.

Si cette thèse est à mon nom, cela ne doit pas éclipser la contribution de tous ceux qui ont, à leur manière, rendu ce travail possible. Ainsi, je souhaiterais commencer par remercier Nicolas pour toutes les discussions et interactions que nous avons eues depuis ma première année de master. Merci aussi à Xavier, co-directeur du projet, et Christoph, mon homologue liégeois: ce fut un plaisir de collaborer avec vous deux. Merci à PY pour les coups de pouce quand ni internet, ni ma patience ne parvenaient à résoudre mes soucis. Merci à Pierre et Clément pour leur soutien technique dans l'enfer des BDYs, ice shelfs et autres, et merci à la NEMO-team louvaniste, grâce à qui je me suis senti beaucoup moins seul. Merci enfin à Monique, Dominique et Livia qui ont tout fait pour me faciliter la vie en dehors du travail de recherche.

D'ici quelques années, j'aurais sans doute oublié toutes les galères qui parsèment le chemin d'un doctorant. Je suis sûr que je n'aurais par contre pas oublié les souvenirs forgés pendant ma thèse. Quand je suis arrivé à LLN, je me demandais comment j'allais bien pouvoir m'occuper pendant ces quatre (spoil: cinq) années. Mais force est de constater qu'à force de rencontres, on se retrouve vite à écumer les terrains de badminton ou les sentiers boueux des Ardennes (ça fait à peu près 10 km, promis), partager des boulets liégeois ou des gaufres très sucrées, faire les barakis sur une piste de karting, pédaler sur les pavés entre deux points nœuds ou s'initier au paddle (et ne surtout pas tomber) à l'écluse d'Ittre. Finalement, l'essentiel c'est la compagnie. Alors, merci à Koffi, Sylvain, Sam, Max, John, Quentin, Lilian, Jeanne, Madeleine, Jean, Charles, François, François, Guillian, Steve, Raph et à tous les autres, d'avoir partagé ces quelques années avec moi et de les avoir rendus mémorables. Mentions spéciales à la "Bande des deux litres", à ceux qui n'ont pas eu peur des grizzlys et à ceux qui ont pris ou raté le train avec moi. Ce n'est pas tout, mais je vais m'arrêter là, car au final, on raconte toujours les mêmes histoires. Merci enfin à tous les copains hors Belgique, qu'ils soient "Grenoblois", Franciliens ou Sarthois, nos

amitiés comptent beaucoup pour moi et j'ai bien l'intention de rattraper mes absences !

Un immense merci à ma famille. Cette thèse est aussi la vôtre, en consolation du temps passé loin de vous. Merci maman et papa de m'avoir transmis l'amour de la nature, le goût de l'effort et un certain talent pour la rêverie. Merci surtout de m'avoir offert la chance de suivre ces (longues) études et la liberté d'en faire ce que je voulais. Merci également à mon très cher frère et ma très chère sœur qui contribuent pour beaucoup à mon bonheur.

Mes derniers remerciements vont à toi qui as partagé ma vie ces deux dernières années. Il fallait être un peu folle pour tout quitter et venir s'installer en Belgique avec un thésard en dernière année (deux ans d'affilée), mais je n'en attendais pas moins de toi ;) Merci d'être là, de continuer à me faire rire tous les jours, de m'écouter quand j'en ai besoin. Merci pour le soutien quotidien et merci de m'avoir donné confiance. J'y suis arrivé grâce à toi.

Contents

1 Introduction **3**

1.1 Foreword . . . 3
1.2 The Antarctic Climate . . . 5
1.2.1 Overview . . . 5
1.2.2 The coastal atmosphere-cryosphere-ocean system . . . 10
1.2.3 The Southern Ocean Meridional Overturning Circulation . . . 14
1.2.4 Existing and needed observations . . . 16
1.2.5 Antarctic Climate in GCMs . . . 17
1.3 Small-scale climate processes . . . 19
1.3.1 The notion of scale in the climate system . . . 19
1.3.2 The issue of small-scale processes . . . 20
1.3.3 Need for higher resolution? . . . 22
1.4 Contributions of the present thesis . . . 25
1.4.1 Overview . . . 25
1.4.2 Development of a regional ocean–sea ice–atmosphere model . . . 28
1.4.3 Influence of ocean tides and ice shelves on ocean-ice interactions and DSW formation off Adélie Land . . . 30
1.4.4 Effects of the atmospheric forcing resolution on simulated sea ice and polynyas off Adélie Land . . . 32
1.4.5 Effects of ocean mesoscale eddies on atmosphere–sea ice–ocean interactions off Adélie Land . . . 35

2 Influence of ocean tides and ice shelves on ocean-ice interactions and dense shelf water formation in the D'Urville Sea, Antarctica **38**

2.1 Summary . . . 38
2.2 Introduction . . . 40
2.3 The model, boundary conditions and experimental design . . . 43
2.4 Model evaluation . . . 47
2.4.1 Sea ice . . . 47
2.4.2 Water masses . . . 50
2.4.3 Ice shelves . . . 53

2.5 Sensitivity of ice, ocean and DSW to tides and ice shelves 54
2.5.1 Ice shelf melting induced by tides 54
2.5.2 Effect of tides and ocean–ice shelf interactions on the modeled ocean mean state 55
2.5.3 Water mass transport and production of dense water 59
2.6 Discussion 64
2.7 Conclusion 68

3 Effects of the atmospheric forcing resolution on simulated sea ice and polynyas off Adélie Land, East Antarctica 70
3.1 Foreword 70
3.2 Summary 71
3.3 Introduction 72
3.4 The model and forcing 75
3.4.1 MAR atmospheric model 75
3.4.2 Ocean–sea ice model 76
3.4.3 Experimental design 78
3.5 Atmospheric forcing and effects of resolution 79
3.6 Sensitivity of the sea ice to the atmospheric forcing resolution 86
3.6.1 Effects of the atmospheric forcing resolution on sea ice 86
3.6.2 Polynya dynamics and sensitivity to atmospheric forcing resolution 92
3.7 Effects of atmospheric forcing resolution on salt flux and water mass transformations 100
3.8 Discussion 102
3.9 Conclusion 104

4 Effects of ocean mesoscale eddies on atmosphere–sea ice–ocean interactions off Adélie Land, East Antarctica 106
4.1 Foreword 106
4.2 Summary 107
4.3 Introduction 108
4.4 The model, experimental design, and analysis strategy 111
4.4.1 The NEMO ocean–sea ice model 111
4.4.2 The atmospheric model MAR 111
4.4.3 NEMO-MAR coupling 112
4.4.4 Experimental design: REF and SMOOTH experiments 113
4.4.5 Eddy tracking and compositing 117
4.5 Atmosphere–sea ice–ocean interactions at the mesoscale 117
4.5.1 Small-scale atmosphere–sea ice–ocean coupling 118

4.5.2 Imprint of eddies on the sea ice and atmosphere 121
4.5.3 Eddies imprint on the ocean 125
4.6 Effects of eddies on momentum and buoyancy fluxes at the ocean surface 128
4.6.1 Momentum transfer and kinetic energy budget 128
4.6.2 Freshwater and buoyancy fluxes 130
4.7 Discussion 133
4.8 Conclusion 136

5 Conclusions and perspectives **138**
5.1 Main achievements 138
5.2 Perspectives 143

6 Appendix **147**
6.1 Supplementary material for Chapter 2 147
6.2 Supplementary material for Chapter 3 153
6.2.1 Comparison between ERA5 and MAR simulations when used as forcing 153
6.3 Comparison of the coupled model with atmospheric reanalysis and ocean climatology 156
6.3.1 Atmosphere 156
6.3.2 Ocean 157

Acronyms

AABW: Antarctic Bottom Water
AASW: Antarctic Surface Water
ACC: Antarctic Circumpolar Current
AIS: Antarctic Ice Sheet
ASC: Antarctic Slope Current
AWS: Automatic Weather Station
B9BP: B9B iceberg polynya
CDW: Circumpolar Deep Water
CMIP: Climate Model Intercomparison Project
CTD: Conductivity Temperature Depth
DBP: Dibble Bank Polynya
DDU: Dumont d'Urville
DSW: Dense Shelf Water
EIP: Eddy-ice pumping
GCM: Global Climate Model
ISW: Ice Shelf Water
LIM: Louvain la Neuve sea Ice Model
MAR: Modèle Atmosphérique Régional
MBP: Mertz Bank Polynya
MGP: Mertz Glacier Polynya
MIZ: Marginal Ice Zone
MLD: Mixed Layer Depth
MOC: Meridional Overturning Circulation
MSW: Modified Shelf Water
NADW: North Atlantic Deep Water
NBP: Ninnis Bank Polynya
NEMO: Nucleus For European Modelling of the Ocean
NGP: Ninnis Glacier Polynya
PBL: Planetary Boundary Layer
SIC: Sea Ice Concentration
SLA: Sea Level Anomaly
SSS: Sea Surface Salinity
SST: Sea Surface Temperature
SW: Shelf Water
WOA: World Ocean Atlas
WW: Winter Water

List of publications

First author:

Influence of ocean tides and ice shelves on ocean-ice interactions and dense shelf water formation in the D'Urville Sea, Antarctica. **Huot, P.V.**, Fichefet, T., Jourdain, N.C., Mathiot, P., Rousset, C., Kittel, C., Fettweis,X.; Ocean Modelling (2021).

Effects of the atmospheric forcing resolution on simulated sea ice and polynyas off Adélie Land, East Antarctica. **Huot, P.V.**, Kittel, C., Fichefet, T., Jourdain, N.C., Sterlin, J., Fettweis, X.; submitted to Ocean Modelling (2021), revised.

Effects of ocean mesoscale eddies on atmosphere–sea ice–ocean interactions off Adelie Land, East Antarctica. **Huot, P.V.**, Kittel, C., Fichefet, T., Jourdain, N.C., Fettweis, X.; submitted to Climate Dynamics (September 2021).

Co-author:

Sensitivity of the current Antarctic surface mass balance to sea surface conditions using MAR. Kittel, C., Amory, C., Agosta, C., Delhasse, A., Doutreloup, S., **Huot, P.V.**, Wyard,C., Fichefet, T., Fettweis, X., The Cryosphere (2018).

Diverging future surface mass balance between the Antarctic ice shelves and grounded ice sheet. Kittel, C., Amory, C., Agosta, C., Jourdain, N.C., Hofer, S., Delhasse, A., Doutreloup,S., **Huot, P.V.**, Lang, C., Fichefet, T., The Cryosphere (2021).

Modelling landfast sea ice and its influence on ocean-ice interactions in the area of the Totten Glacier, East Antarctica. Van Achter, G., Fichefet, T., Goosse, H., Pelletier, C., **Huot, P.V.**, Sterlin, J., Fraser, A.D., Parter-Smith, R., Lemieux, J.F., Haubner, K., submitted to Ocean Modelling (January 2021).

PARASO, a circum-Antarctic fully-coupled ice-sheet - ocean - sea-ice - atmosphere - land model involving f.ETISh1.7, NEMO3.6, LIM3.6, COSMO5.0 and CLM4.5 Charles Pelletier, Thierry Fichefet, Hugues Goosse, Konstanze Haubner, Samuel Helsen, **Pierre-Vincent Huot**, Christoph Kittel, François Klein, Sebastien Le clec'h, Nicole P. M. van Lipzig, Sylvain Marchi, François Massonnet, Pierre Mathiot, Ehsan Moravveji, Eduardo Moreno, Pablo Ortega, Frank Pattyn, Niels Souverijns, Guillian Van Achter, Sam Vanden Broucke, Alexander Vanhulle, Deborah Verfaillie, and Lars Zipf, submitted to Geophysical Model Development (September 2021).

Chapter 1

Introduction

1.1 Foreword

In the mid-18th century, the first observations of ocean temperature at depths greater than 1000 m were going to revolutionize the understanding of ocean circulation (see Rahmstorf (2006)). Despite being performed in the tropical Atlantic, the measurements revealed that the ocean temperature quickly decreases with depth and stabilizes in a thick layer of nearly constant but very low value. These observations contradicted the idea that the heat received at the surface of tropical oceans was warming up the whole ocean layer. Benjamin Thompson hypothesized in 1797 that these low temperatures originated from the advection of cold waters formed in the polar regions. Observations performed during the 20th century were going to prove him right. In particular, two distinct water masses were identified: the North Atlantic Deep Water (NADW) and the Antarctic Bottom Water (AABW). With the warming of waters near the equator and their cooling at high latitudes, the first concept of a global oceanic thermohaline circulation was born. Yet, the knowledge of the location where these cold and dense waters are formed and the responsible mechanisms were missing. It appeared that the NADW was produced from dense overflows between Greenland, Iceland and Scotland (Swift, 1984) and deep convection in the Labrador Sea (Killworth, 1983). The formation of AABW was traced back to the continental shelf seas surrounding Antarctica and it was first observed in the Ross (Jacobs et al., 1970) and Weddell Seas (Foster et al., 1987). The proposed mechanism was the mixing of cold waters with Circumpolar Deep Water (CDW) along the continental shelf break. Circum-antarctic measurements of ocean properties (Condie, 1998) suggested that AABW production takes place in at least two other regions in East Antarctica. In 1998, Rintoul (1998) observed the formation of Dense Shelf Water (DSW) and AABW in the Adélie Land sector of East Antarctica. It was only in 2013 that the "last" location of AABW formation was identified in the Cape Darnley polynya (Ohshima et al., 2013).

The discovery of the existence of a global thermohaline circulation associated with the sinking of dense waters in polar regions changed our conception of the climate system. The global thermohaline circulation is one of the backbones of modern climate understanding. This finding revealed that polar regions are essential for the Earth's climate, as local processes turn out to be at the origin of the redistribution of heat affecting the planet globally.

The formation of dense waters is not the only way that polar regions affect the Earth's climate. The snow or ice surfaces have high albedos that reduce the amount of incoming solar radiation absorbed by the Earth (Hall, 2004). The storage of freshwater in polar ice caps affects the global sea level and the ocean salinity (Adkins et al., 2002). Through these different mechanisms, polar regions play an important role in regulating the Earth's climate.

Over the past decades, polar regions have undergone profound changes in response to human-induced global warming (Foster and Rahmstorf, 2011). The extents of sea ice (Comiso, 2012) and snow cover (Callaghan et al., 2011) are declining in the Northern Hemisphere, the Southern Ocean has been warming (Swart et al., 2018) and the Antarctic Ice Sheet (AIS) glaciers are accelerating (Rignot et al., 2019). Polar regions are responding faster to the anthropogenic forcing than the rest of the globe. The arctic surface air temperature has for instance been rising twice as fast as the global average over the past 20 years Ballinger et al. (2020). These higher sensitivities are due to the effects of positive feedbacks that locally amplify the global warming signal (Goosse et al., 2018).

As polar regions influence the Earth's climate, their current changes pose a significant threat and their future evolution would likely shape the global climate variability in the next centuries. Unfortunately, owing to limited observations, numeral aspects of polar regions are still poorly understood, such as cloud microphysics (Lenaerts et al., 2017; Taylor et al., 2019), processes leading to air mass transformations (Pithan et al., 2018) or the variability of the ocean mixed layer depth Heuzé et al. (2015). In parallel, Global Climate Models (GCMs) present important and persistent biases in their representation of polar clouds (Lenaerts et al., 2017), deep water properties (Heuzé, 2021), ocean circulation (Beadling et al., 2020) or sea ice (Roach et al., 2020; Mohrmann et al., 2021), hampering the quality of climate projections. To address these issues, it is essential today to understand what are the processes shaping the polar climate, what are GCMs missing, and how to incorporate missing processes. The overall objective of the present thesis is to contribute to answering these two questions. Most particularly, our aim is to understand the role of small-scale processes, which length scales limit direct observations and render

their explicit representation in models delicate, in the atmosphere-cryosphere-ocean interactions of the Adélie Land sector, in East Antarctica. The Adélie Land sector is unique, as it hosts the formation of dense water in the Mertz Glacier polynya (Rintoul, 1998) and is relatively well-observed thanks to the presence of the Dumont D'Urville French base and the proximity with Australia. It shares many common characteristics with the cold coastal seas of East Antarctica, often less studied than the western sectors or the Ross and Weddell Seas.

1.2 The Antarctic Climate

1.2.1 Overview

The climate of Antarctica is characterized by a tight coupling between the ocean, atmosphere, sea ice, and continental ice sheet evolving under the influence of a variety of forcings. Antarctica and the Southern Ocean are known for their extreme characteristics: surface temperatures in Antarctica are the coldest recorded on Earth, the Southern Ocean hosts the strongest currents and coastal Antarctica experiences the highest surface yearly wind speeds.

To understand the Antarctic climate particularities, it can be useful to describe the series of events that led to its installation. The AIS is estimated to be around 34 Million years old (Galeotti et al., 2016). The openings of Southern Ocean gateways (the Tasmanian and Drake Passages) are believed to be one of the causes leading to the installation of the extremely cold climate characterizing today's Antarctica. This series of events permitted the formation of a circumpolar ocean channel aligned with the mid-latitude westerly winds which enabled the emergence of the strongest ocean current on earth: the Antarctic Circumpolar Current or ACC (Scher et al., 2015), with an estimated present transport at the Drake Passage of 180 Sv (Sverdrup, 1 $Sv = 10^6$ m^3/s) (Donohue et al., 2016). The ACC onset likely acted to insulate the Antarctic continent from the meridional heat transfer and potentially contributed to a decrease of global CO_2 level via enhanced upwelling and primary production in the Southern Ocean (Lear and Lunt, 2016). The subsequent global and polar-amplified cooling established adequate conditions for the development of the AIS, which further cooled the Antarctic climate via the positive albedo feedback (Fyke et al., 2018). The current topography, bathymetry, and ice draft of Antarctica and the Southern Ocean are shown in Figure 1.1.

The mid-latitude westerlies and the ACC mark the limit of the southern polar regions and of the associated regional climate. The AIS covers the Antarctic continent

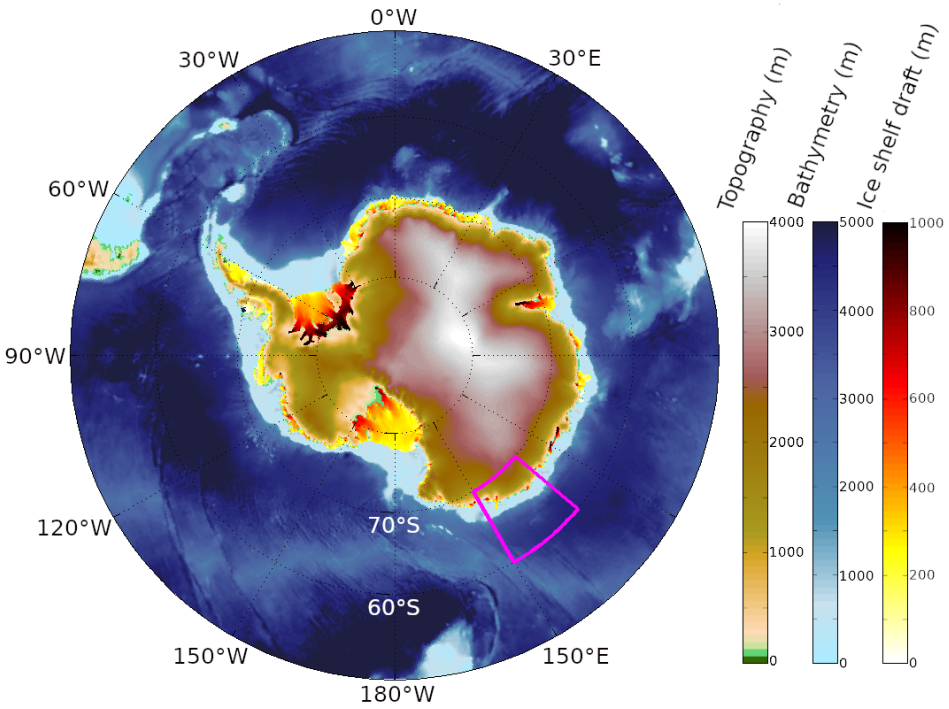

Figure 1.1: Topography, bathymetry and ice draft (thickness of the ungrounded ice) of Antarctica and the Southern Ocean (in meters). The pink box indicate the location of the Adélie Land sector studied in this thesis. The topography is the one of ERA5 (Hersbach et al., 2020) i.e., using the Radarsat Antarctic Mapping Project Digital Elevation Model, Version 2 (RAMP2) dataset (`https://nsidc.org/data/nsidc-0082`). The bathymetry is obtained from ETopo1 (Amante and Eakins, 2009) and from IBCSO (Arndt et al., 2013) for the coastal seas of Antarctica.

with a thick (up to 4 km) layer of ice formed from the accumulation of snow over millions of years. Under the effect of gravity, the ice slowly flows towards the coast where terminating glaciers start to float in the ocean and to form ice shelves (Rignot et al., 2011). The AIS loses most of its mass at its interface with the ocean, either through basal melting (Pritchard et al., 2012) or iceberg calving (Depoorter et al., 2013). Despite the very dry conditions found inland Antarctica, the positive surface mass balance (budget of precipitation minus sublimation, surface melt, and erosion) compensates for the ice mass loss (Shepherd et al., 2018).

The extremely dry conditions of Antarctica arise from the persistence of a high-pressure system over the ice sheet, which favors subsidence of cold and dry air from the high atmosphere and limits the advection of moister air from the coast. The blocking of inland advection of oceanic air masses is enhanced by the steep slopes of the AIS in coastal regions. The surface wind circulation over the AIS is divergent and oriented towards the ocean. The surface winds tend to blow down the slopes, indicating a strong control of the topography on the atmospheric circulation (Parish,

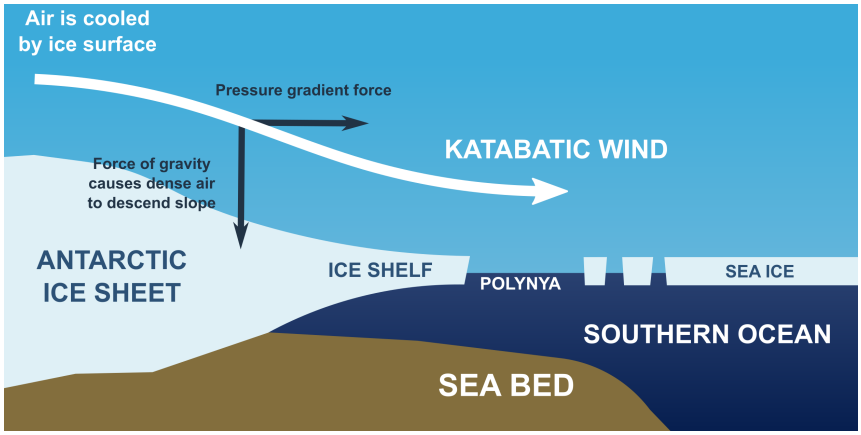

Figure 1.2: Schematic view of the generation and flow of katabatic winds along a cross-slope section of Antarctica. https://commons.wikimedia.org/wiki/File:Katabatic-winds-antarctica.png

1988; Parish and Bromwich, 2007). The alignment of the winds with the surface elevation gradient is partially originating from the nature of the surface winds of Antarctica: the main continental winds originate from the cooling of the near-surface air over the slopes of the AIS during the polar night (see Figure 1.2). These winds (called katabatic winds) flow down the slopes of the AIS under the effect of gravity before reaching the ocean. After the coastline, the katabatic winds deviate towards the west under the influence of the Coriolis force. There, they merge with the easterly winds formed by the meridional pressure gradient between the high pressures of the continent and the low pressure of the Antarctic Circumpolar Trough in coastal Antarctica.

A fundamental aspect of the Antarctic climate is the importance of coupling with the Southern Ocean. The Southern Ocean and atmosphere mutually influence each other: the zonal winds drive the main currents of the Southern Ocean, and the ocean feeds the atmosphere with heat and moisture. The ACC is thought to be driven by the mid-latitude westerlies (Allison et al., 2010), while the Antarctic Slope Current (ASC), a westward flowing current surrounding the continental shelf break, is partially forced by the easterlies (Thompson et al., 2018). Another important force driving ocean circulation is the horizontal density gradient generated by temperature and salinity contrasts, for instance across the ACC or the ASC. The circulation of the Southern Ocean is also shaped by bathymetry (Hughes, 2005). For instance, the flow of the ACC presents large zonal variability between quasi-laminar states and heavily eddying regimes after crossing submarine ridges (Rintoul, 2018). The paths of the main ocean currents and the prevailing winds are shown in Figure 1.3.

One of the characteristics of the Southern Ocean is its rich mesoscale activity arising from the strength of the ACC. Mesoscale eddies are generated by instabilities of the ACC, either due to the sloping of isopycnals (baroclinic instabilities), or to

the interactions of the flow with submarines seamounts (Rintoul, 2018). Eddies are circular circulation patterns in near-geostrophic balance (balance between horizontal pressure forces and the Coriolis force), with spatial scales of the order of a few to a few tens of kilometers close to the local Rossby radius of deformation. The Rossby radius, $Ro = \frac{c_i}{f}$ (with c_i the speed of internal gravity waves for mode i and $f = 2\Omega sin(\phi)$, the Coriolis parameter for latitude ϕ and the Earth's rotation rate Ω) is a characteristic length scale indicating the distance across which the Coriolis force starts to significantly affect the fluid's motion. The size of eddies strongly depends on the ocean stratification and the local influence of the Earth's rotation (determined by the latitude): eddies are on average smaller in strongly stratified fluids and at higher latitudes. Mesoscale eddies are often presented as the oceanic equivalent of the atmospheric synoptic-scale low and high pressure systems: eddies can rotate in cyclonic or anticyclonic ways and live from a few days to several weeks or months (Frenger et al., 2015). Eddies affect both the thermohaline structure of the ocean (by contributing to horizontal mixing and by transporting preserved water masses) and the ocean energy budget by providing a way for energy transfer from the large scale down to molecular diffusion and by affecting the air-sea momentum transfer (Renault et al., 2017b).

The Southern Ocean has a significant influence on the Earth's climate and on the global ocean circulation as it controls the exchanges between the different ocean sub-basins. In addition, the ACC governs the meridional transport of heat (Martinson, 2012) either by the mean flow (Volkov et al., 2010) or via the activity of eddies (Volkov et al., 2008; Dufour et al., 2015). The Southern Ocean also plays an important role in storing heat and CO_2: climate models suggest that the Southern Ocean could have stored up to 73% of the excessive heat and 43% of the anthropogenic CO_2 over the historical period (Frölicher et al., 2015).

The interactions between the Southern Ocean and the atmosphere are tempered by the seasonal formation of Antarctic sea ice. During the polar winter, a large portion of the Southern Ocean becomes covered by a thin layer of sea ice. The properties of the Antarctic sea ice and the processes leading to its formation or melting differ from the ones of the Arctic sea ice, illustrating the specificities of the Antarctic ocean–sea ice–atmosphere connections. Contrarily to the Arctic sea ice, the Antarctic sea ice is mostly seasonal as it is found at lower latitudes and as it is exported towards warmer waters by the westerly winds. Thus, the Antarctic sea ice is relatively thin (1 m) compared to its Arctic counterpart. The thickness of the Antarctic sea ice is however highly variable due to the formation of pressure ridges owing to the strength of the winds (Williams et al., 2015). The strength of winds and waves in the Southern

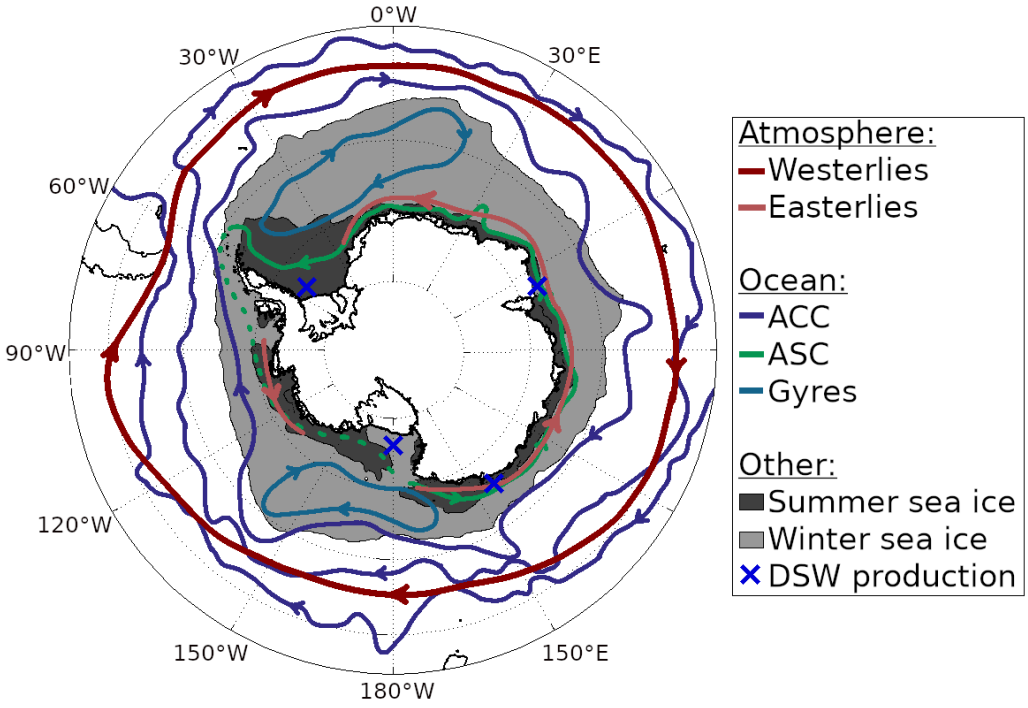

Figure 1.3: Schematic representation of the Southern Ocean depth-averaged circulation, prevailing winds, sea ice extents and DSW production location. The path of the ASC was reproduced from Thompson et al. (2018). Summer and winter sea ice extents are obtained from the 2000-2010 climatology of sea ice concentration from the OSI-450 dataset (Lavergne et al., 2019).

Ocean limit the thermodynamical vertical growth of sea ice, which would require quiescent conditions: most of the Antarctic sea ice is formed of a collection of small sea ice fragments called "frazil", aggregated into flat "pancakes" that can later pile up to produce larger, thicker and more compact floes (see the review of Maksym et al. (2012)). A second important mechanism for Antarctic sea ice growth is the "snow-ice" formation: the relative snow load on the Antarctic sea ice is higher than in the Arctic leading to more frequent flooding and refreezing (Massom et al., 2001). The fate of sea ice differs in the two polar regions: sea ice melts mostly through basal melting (i.e., from ocean-ice heat exchanges) in the Southern Ocean, helped by the weak ocean stratification, while it melts from below and from the surface in the Arctic. As it inhibits the exchange of heat, moisture, and momentum between ocean and atmosphere, sea ice plays a substantial role in the southern polar climate. It also controls the stratification of the Southern Ocean due to the ocean–sea ice salt and freshwater fluxes. Sea ice formation is associated with brine rejection that destratifies the water column, sometimes leading to convection, while sea ice melting stratifies the ocean by forming a surface layer of fresh and cool water. By governing air-sea heat, momentum and moisture fluxes, the Antarctic sea ice also influences the atmosphere. Smith et al. (2017) showed that the Antarctic sea ice affected the position of the mid-latitude westerly jet (Smith et al., 2017) and Raphael et al. (2011) suggested an

influence on the extension of the polar cell or the phase of the Southern Annular Mode.

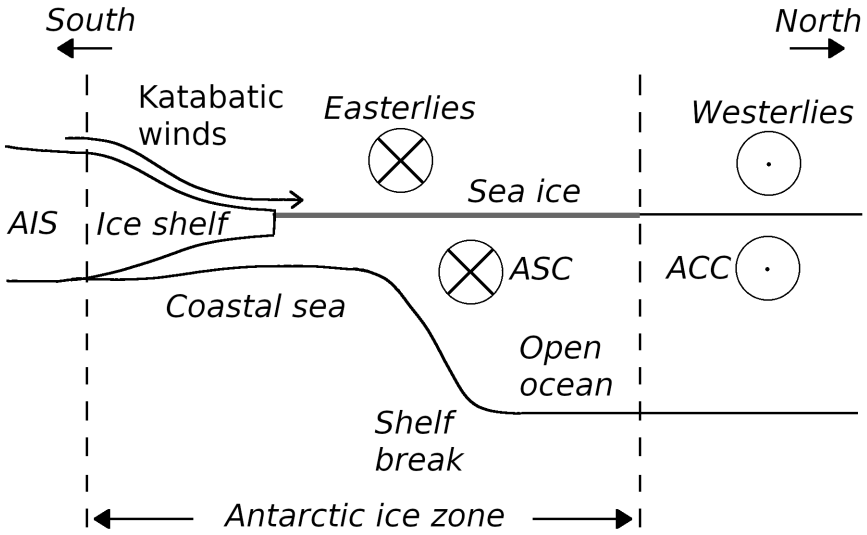

Figure 1.4: Schematic view of a meridional section of the Southern Ocean. AIS: Antarctic Ice Sheet, ASC: Antarctic Slope Current, ACC: Antarctic Circumpolar Current.

An overview of the Antarctic climate system is illustrated in the schematic section of Figure 1.4. In this thesis, we are particularly interested in the interactions between the ocean, sea ice, ice sheet, and atmosphere. Therefore, we will focus on the region of the "Antarctic Ice Zone", i.e. the region defined by the coastline or grounding line of ice shelves in the south and the maximum extent of the sea ice in winter in the north. In this region, the interactions between atmosphere and ocean are modulated by the presence of sea ice, and the AIS directly interacts with the ocean.

1.2.2 The coastal atmosphere-cryosphere-ocean system

Some of the principal interactions between the ocean, atmosphere, and ice in the Southern Hemisphere that affect the global climate take place within the coastal seas. Coastal seas are relatively shallow seas, with widths ranging from 100 to 600 km and typical depths of a few hundred meters (rarely exceeding 1000 m), separated from the open ocean by the continental shelf break.

The dominant interactions between the atmosphere, sea ice, ocean, and ice shelves in the coastal seas of Antarctica are illustrated in Figure 1.5. In East Antarctica, the prevailing winds in coastal regions are the polar easterlies and the katabatic winds blowing from the continent. The easterlies drive a southward Ekman drift that leads to the onset of the ASC at the shelf break and of a westward coastal current. Easterlies

also generate coastal downwelling that contributes to the isolation of the coastal seas from the open ocean. Katabatic winds often have an important offshore component and thus tend to export the sea ice away from the coast.

In addition to the role of winds, on-shelf ocean circulation is strongly governed by bathymetry and horizontal density gradients between the light and dense water masses produced in summer or winter (Martin et al., 2017). Ocean tides are another source of circulation: the interactions of the high-frequency tidal currents with the bathymetry or with the stratification leads to the emergence of mean tidal currents, contributing to the redistribution of water masses in the shelf seas. Tides also contribute to water masses modification by generating vertical mixing above bathymetric highs and by increasing the turbulent ocean-ice heat fluxes due to the friction of tidal currents on the overlying ice.

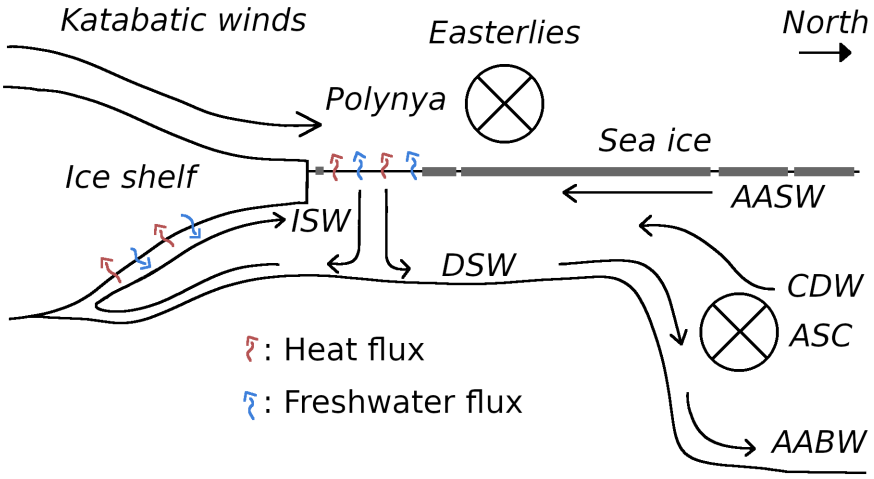

Figure 1.5: Schematic view of a meridional section of an Antarctic coastal sea illustrating the atmosphere-cryosphere-ocean interactions. ISW: Ice Shelf Water, AASW: Antarctic Surface Water, DSW: Dense Shelf Water, CDW: Circumpolar Deep Water, AABW: Antarctic Bottom Water, ASC: Antarctic Slope Current.

The Antarctic sea ice present near the coast differs quite substantially from the one found offshore. The action of winds and the presence of obstacles to sea ice advection leads to the formation of polynyas and landfast ice patches. Polynyas are areas of low sea ice concentration within the ice pack. They are often divided into two categories (Morales Maqueda et al., 2004): latent heat polynyas and sensible heat polynyas. In the first case, the low sea ice concentration is due to dynamical factors which locally favor sea ice divergence. In the second case, the low sea ice concentration is due to anomalous oceanic heat content, inhibiting sea ice growth. Latent heat polynyas are mostly encountered in coastal regions due to the export of sea ice by katabatic winds (such as the Mertz or Cape Darnley polynyas), and sensible heat polynyas

mainly occur in the deep ocean (such as the Weddell Sea polynya). Polynyas play a substantial role in the Antarctic climate. Due to the low sea ice concentrations, the ocean in coastal polynyas continuously loses heat to the atmosphere, supporting a high rate of sea ice production. Tamura et al. (2008) estimated that sea ice production within polynyas accounted for 10% of the total Antarctic sea ice production. These high sea ice production rates trigger a destratification of the water column and the formation of DSW (Rintoul, 1998; Williams et al., 2008; Ohshima et al., 2013), that can later spill into the open ocean and form AABW. Coastal polynyas are closely related to landfast ice: portions of the ice pack that remains immobile (Massom et al., 1998; Nihashi and Ohshima, 2015). Landfast ice forms in areas where sea ice converges against an obstacle and is thus often found upwind of grounded icebergs, ice shelf tongues, or against the coastline (Fraser et al., 2012). Contrarily to the Arctic and due to the important depths of Antarctic coastal seas, Antarctic sea ice is rarely attached to the seafloor. As landfast ice is not advected outside the coastal seas, it can persist throughout the summer melt season and live for several years. Therefore, landfast ice reaches a much higher thickness than the rest of the Antarctic sea ice, with values approaching 10 m (Arndt et al., 2020). The thickening of landfast ice occurs through snow accumulation, bottom freezing, and the accumulation of platelet ice originating from the freezing of ice shelf waters (Lei et al., 2010; Arndt et al., 2020). Landfast ice limits the air-sea heat fluxes and the summer warming and thus has important implications for the coastal seas.

A major aspect of the Antarctic coastal climate system is the interactions of the ocean (and atmosphere) with the floating ice shelves. Despite the low temperature of the ocean, the ocean can drive basal melting due to the lowering of the melting point with increased pressure. Jacobs et al. (1992) identified three modes of melting, depending on the water masses involved. Ice shelves can either melt from the interactions with cold and saline dense waters formed in polynyas, with warmer surface waters formed during summer or with warm CDW advected onto the shelf seas and into the ice shelf cavity. Intensified intrusions of CDW in the Amundsen and Bellingshausen Seas (West Antarctica) are expected to be the cause of the observed thinning and acceleration of glaciers in this region (Shepherd et al., 2004; Jenkins et al., 2018). Ocean and ice shelves form a tightly coupled system: the ocean properties and circulation drive the basal melt of the ice shelves, and the basal melt drives ocean circulation and water masses transformation in return. The positive buoyancy flux associated with melting drives the upwelling of the Ice Shelf Water (ISW) out of the cavity (Nicholls et al., 1991; Jenkins and Holland, 2002) and the onset of an overturning circulation. Ice shelf–driven overturning can either upwell cold waters and locally increase sea ice formation (Hellmer, 2004), or warmer waters and

contribute to warm the upper ocean (Jourdain et al., 2017). Besides, ice shelves have a buttressing effect on the AIS and slow down its flow. The thinning of ice shelves or the retreat of their grounding line due to increased basal melt could limit this buttressing effect and destabilize the glaciers. Another way by which the AIS affects the ocean is through the calving of icebergs. Icebergs have several implications for the ocean and sea ice: icebergs grounded to the seafloor act as anchors for the formation of landfast ice (Fraser et al., 2012) and the ones that leave the coastal seas redistribute the freshwater over the Southern Ocean (Tournadre et al., 2012; Merino et al., 2016).

Exchanges between the coastal seas and the open ocean are key for the dynamics of the coastal atmosphere-cryosphere-ocean system, though being limited by the shelf break, the cross–shelf break density contrast, the easterly wind–driven subsidence, and the ASC. One of the main heat sources for the coastal seas is the intrusion of CDW. These intrusions are permitted by the local indentations of the bathymetry (St-Laurent et al., 2013) and partially driven by mesoscale eddies (Stewart and Thompson, 2016), tides (Stewart et al., 2018) or Ekman drift. The DSW formed in coastal polynyas sinks down to the continental shelf, before spilling further down to the Southern Ocean's abysses, where the mixing with surrounding CDW produces the AABW essential for the global oceanic thermohaline circulation.

Coastal seas off Antarctica differ from one sector to the other, as illustrated by the limited number of AABW sources. The Adélie Land sector (pink box in Figure 1.1), in East Antarctica, is a key region for the formation of AABW (Rintoul, 1998; Williams et al., 2008; Lacarra et al., 2014; Snow et al., 2016) and thus for the global oceanic thermohaline circulation. Several factors explain the presence of AABW formation in this area. First, Adélie Land is known for the intensity of its katabatic winds and is sometimes referred to as the "windiest place on Earth" (mean annual wind speeds of 20 m/s were measured at Cape Denison by Wendler et al. (1997)). Due to these extraordinary winds and the presence of ice shelf tongues or grounded icebergs, polynyas open frequently and are responsible for intense sea ice production (Massom et al., 1998; Tamura et al., 2008, 2016). In particular, the Mertz Glacier Polynya is thought to be the birthplace of the DSW of Adélie Land. However, following the calving of the Mertz Glacier Tongue (Kusahara et al., 2011b; Mayet et al., 2013), the polynya became much smaller (Tamura et al., 2012), questioning the current and future production of DSW in the sector. Another specificity of the Adélie Land sector is the intensity of the easterly winds (Hazel and Stewart, 2019), which drive a marked ASC (Thompson et al., 2018) limiting cross-shelf exchanges and leading to a predominant role of surface fluxes in water masses transformations.

1.2.3 The Southern Ocean Meridional Overturning Circulation

In Section 1.2.1, we have presented the Southern Ocean circulation as being mostly zonal. This hides the importance of meridional currents which, though being weaker than zonal ones, are of paramount importance for the Antarctic climate. One of the main features of the Southern Ocean circulation is the Meridional Overturning Circulation (MOC). The Southern Ocean MOC arises from the interactions between the ocean, ice, and atmosphere, and is an essential constituent of the global oceanic thermohaline circulation.

The Southern Ocean MOC can be divided into an upper cell and a lower cell (see Figure 1.6), each of them being forced by distinct interactions with the atmosphere or sea ice. The starting point is the wind curl that arises from the meridional wind shear between the mid-latitude westerlies and the polar easterlies centered around the Antarctic Circumpolar Trough. This wind curl leads to the divergence of surface waters (advection towards the south by easterlies and towards the north by westerlies) that has to be compensated by the upwelling of deep waters (Marshall and Speer, 2012). The upwelled water masses can then take two different paths: they can join the lower cell of the overturning circulation if they are advected south, or the upper cell if they are advected north. Depending on their path, water masses will undergo different interactions with the sea ice and atmosphere that will dictate their fate.

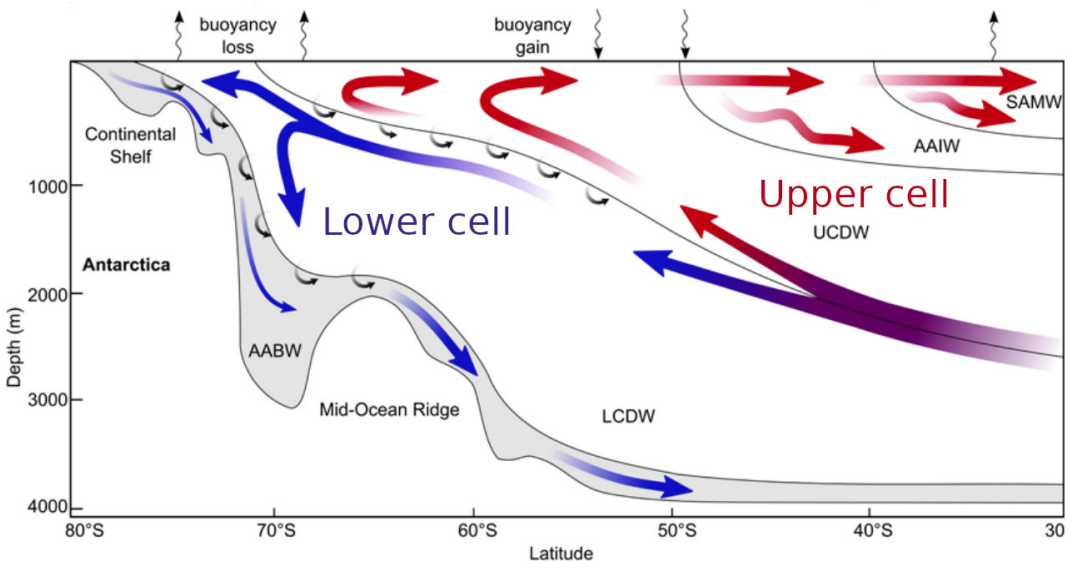

Figure 1.6: Schematic view of the Southern Ocean MOC, adapted from Speer et al. (2000). LCDW: Lower Circumpolar Deep Water, UCDW: Upper Circumpolar Deep Water, AAIW: Antarctic Intermediate Waters, SAMW: Sub-Antarctic Mode Water, AABW: Antarctic Bottom Water.

In the lower cell, the ocean loses heat to the cold and dry air of polar origin. This has for effect to cool the water masses, initiating seawater freezing, and overall increasing surface ocean density leading to ocean convection. For the most part, these transformations take place in coastal seas and in particular in coastal polynyas (Rintoul, 1998; Jacobs, 2004; Ohshima et al., 2013). The dense waters formed during winter can have several fates. Dense waters can be consumed (i.e. transformed into lighter water masses) via their mixing with other water masses or due to buoyancy fluxes. The dense waters that are not consumed spill into the deep ocean, where they mix and acquire AABW properties. AABW is then advected northward into all the ocean basins (Johnson, 2008; Purkey et al., 2018), where it can slowly be brought back to the surface via the Southern Ocean upwelling (Marshall and Speer, 2012) or through mixing and geothermal heating (De Lavergne et al., 2016), thus closing the lower cell of the MOC. Though the time scales associated with the upwelling are still debated, recent attempts based on numerical models and hydrographic observations give a characteristic timescale ranging from few decades up to one century (Drake et al., 2018; Tamsitt et al., 2018). The second option for the upwelled deep waters is to be advected northward and to enter the upper cell of the MOC. There, the ocean gains buoyancy due in part to increased solar radiation, but mostly to freshwater fluxes (Pellichero et al., 2018) dominated by sea ice melting (Abernathey et al., 2016). The resulting water masses occupy the upper layers of the Southern Ocean before sinking below lighter tropical water masses.

The Southern Ocean MOC and its associated water mass transformations are easily identifiable in meridional sections of ocean temperature and salinity, such as the one showed in Figure 1.7. This section was taken off the Adélie Land sector off East Antarctica but is representative of the whole Southern Ocean. The isothermal and isohaline contours are tilted towards the north and intersect the surface between 55°S and 65°S. It is along these iso-contours that the deep water masses are upwelled. The northward return flows of the upper cell can be identified by the relatively fresh water tongue subducting towards a depth of 1000 m north of 55°S, and by the cold water tongue coating the ocean floor, which illustrates the formation of cold deep water that spills northward.

The Southern Ocean MOC is thought to have a substantial effect on the Antarctic and global climate. Its strength is likely linked to the evolution of the AIS as the MOC heavily influences meridional heat fluxes (Volkov et al., 2010; Spence et al., 2012) and global CO_2 levels (Lear and Lunt, 2016). The sinking of waters in the south (Arrigo et al., 2008; Pardo et al., 2014; Murakami et al., 2020), the subduction of mode waters in the north (Sallée et al., 2012), or the seasonal growth of sea ice (Delille et al., 2014)

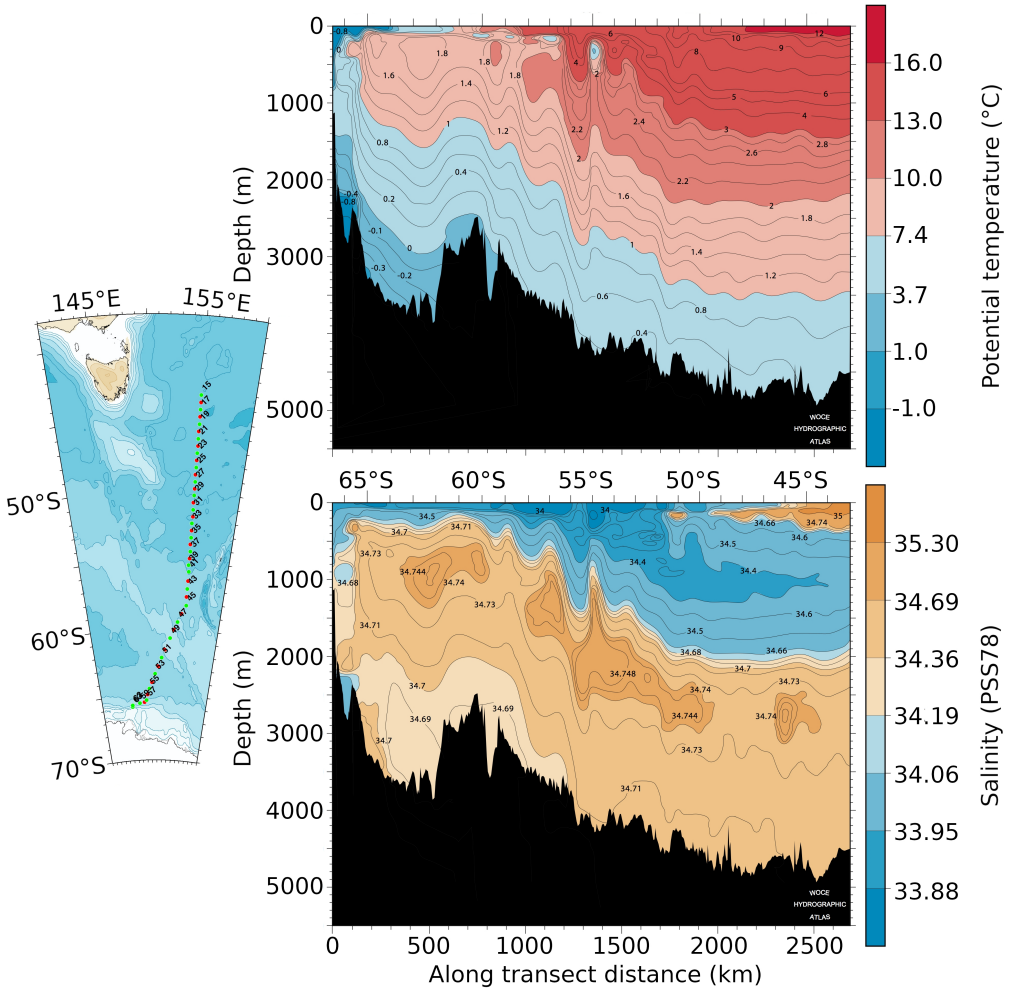

Figure 1.7: Section of ocean potential temperature and ocean salinity measured between Tasmania and Adélie Land. From the WOCE Southern Ocean Atlas (Orsi and Whitworth, 2005).

contribute to sequestrate CO_2 acquired through the interactions with the atmosphere. The upwelling of nutrient-rich deep waters through the MOC makes the Southern Ocean a hotspot of primary productivity (Arrigo et al., 1998). Changes in AABW properties would have major implications for heat storage and global sea level (Purkey and Johnson, 2013). The response of the MOC to global warming will likely shape the evolution of the climate in the next decades to centuries (Armour et al., 2016; Liu et al., 2018).

1.2.4 Existing and needed observations

Observations are essential to understand the Antarctic climate dynamics and to guide model development or calibration. Rather than providing a comprehensive list of existing observations, our goal here is to quickly present which aspects of the Antarctic climate are well observed and what are the major unknowns.

The most comprehensive measurements are obtained directly in the field, either on-board scientific ships, around manned land stations, or during raids inside the continent. The strength of manned in-situ measurements lies in the diversity of measurable quantities: snow and sea ice thicknesses can be retrieved via ice-coring, providing information on the variability of precipitation on various timescales or on conductive heat fluxes through the sea ice, weather balloon or conductive-temperature-depth (CTD) casts probe the vertical structure of the atmosphere or ocean, etc. But such measurements are very scarce and bounded to specific sectors centered around the main scientific bases. To extend the coverage of in-situ measurements, several autonomous networks have been deployed. Automatic Weather Stations (AWS) are distributed all around Antarctica and continuously measure near-surface atmospheric state and radiative fluxes. The ARGO float network and the equipped elephant seals of the MEOP network (Roquet et al., 2014) allowed to build a broad picture of the Southern Ocean state by providing measurements where manned cruises are absent (Zweng et al., 2018). Finally, satellite remote-sensing provides information at high frequency, high resolution, and with a large spatial coverage. Remote sensing allows estimating the mass balance of the AIS and the velocities of the continental ice (Rignot et al., 2019). It also provides the concentration of sea ice at a daily frequency and with resolution ranging from 1/4° down to 6 km, and some knowledge about sea ice thickness (Guerreiro et al., 2017) or drift. Remote sensing also enables to estimate geostrophic ocean currents, near-surface wind speed, or sea surface temperature in ice-free conditions. These observations can be used to construct atmospheric or oceanic reanalyses by using numerical models and data-assimilation methods. Such reanalyses provide a complete representation of the Antarctic climate in three dimensions and at high frequencies.

Despite the variety of existing observations, many aspects of the Antarctic geography and climate are poorly known. This includes the properties of the atmospheric boundary layer above the ocean or sea ice, the state of the ocean beneath the sea ice and below the surface, or the air-sea-ice fluxes and their dependencies on surface conditions. In addition, the bathymetry in coastal seas or the ice shelf draft are in some places highly uncertain, as for instance illustrated by Beaman et al. (2011).

1.2.5 Antarctic Climate in GCMs

Over the past decades, GCMs have been developed as tools to understand the Earth's climate and to predict its future evolution. They mimic the functioning of the Earth's climate, its different sub-components, and the main interactions between them. For this purpose, it is essential for GCMs to represent realistically the main aspects of the Earth's climate, such as the particularities of the Antarctic climate.

The representation of the Antarctic climate is one of the main limits of current GCMs, and GCMs have historically presented large biases over the high latitudes of the Southern Hemisphere (Beadling et al., 2020). The Southern Ocean was shown to be too warm and not dense enough compared to observations in the GCMs of the CMIP5 (Climate Model Intercomparison Project phase 5) exercise (Sallée et al., 2013b). In addition, GCMs simulate too fresh, too shallow, and poorly distributed winter maximum mixed layer owing to excessive freshwater fluxes (Sallée et al., 2013a). The MOC was also biased, with a stronger than observed upper cell and a weaker than observed lower cell (Sallée et al., 2013b). The weak lower cell can be traced back to the poor representation of bottom water properties (Heuzé et al., 2013): AABW is often too warm and too fresh in GCMs, and the mechanisms of AABW production are often unrealistic. Most models do not produce DSW in coastal seas, which might be due do their coarse resolution. A low resolution prevents models from representing small-scale polynyas and the associated heat loss and sea ice production, and the poor representation of bathymetry might limit the accumulation and transformations of dense waters in coastal seas.

The new generation of GCMs developed for CMIP6 shows improvement with respect to the previous generation, with a decreasing number of models simulating open-ocean deep convection, and some models being able to represent AABW formation with the right mechanisms (Heuzé, 2021). Still, the AABW simulated by CMIP6 models is on average not dense enough and too warm. The representation of Antarctic sea ice in GCMs is also problematic. Simulated sea ice declines too quickly during the melt season, leading to smaller than observed summer sea ice areas and many models still simulate a strong sea ice extent decrease over the past decades (Roach et al., 2020), while the observations show a slight increase. The representation of polynyas in GCMs also remains poor. GCMs simulate wider than observed coastal polynyas (Mohrmann et al., 2021), which contrasts with the low density of their AABW, and many models still produce polynyas in the open ocean every year. The representation of the wind fields over the Southern Ocean has improved compared to previous generations of GCMs (Bracegirdle et al., 2020), which lead to improvement of ocean circulation such as the ACC (Beadling et al., 2020). Yet, the strength of the ACC is too weak in several models, (Beadling et al., 2020) and models with correct ACC poorly represent polynyas (Mohrmann et al., 2021). With no or simplistic representations of the interactions between the ocean or atmosphere with the AIS, projections of global sea-level rise for the end of the century remains highly uncertain (Hermans et al., 2021).

Despite the significant improvements in the representation of the Antarctic climate in GCMs over the past decades, a number of biases persist. This suggests that GCMs might be missing or misrepresenting key processes acting in the Antarctic atmosphere-cryosphere-ocean system.

1.3 Small-scale climate processes

1.3.1 The notion of scale in the climate system

The components of the Earth's climate (ocean, atmosphere, sea ice ...) evolve on a wide spectrum of time and length scales. For instance, the main ocean circulation patterns range from the scale of the planet (global thermohaline circulation) down to sub-mesoscale flows at sub-kilometric scales, passing by basin-scale gyres and mesoscale eddies. The same observation can be done for the atmosphere (Williams et al., 2017) or the sea ice (Weiss and Dansereau, 2017), for instance. While the separation of scales is often more practical than phenomenological, it illustrates the different behaviors of the components of the climate system at various scales. Besides the range of spatial scales of variability, the climate and its sub-components also evolve on a range of time scales. Spatial and time scales are often related, such that the processes with the larger characteristic length scales will have the longer associated time scales. A convenient way to illustrate the distribution of specific processes of the climate system is to place them in a spatial scale / time scale diagram such as the one of Figure 1.8, that was adapted from Steele (1995).

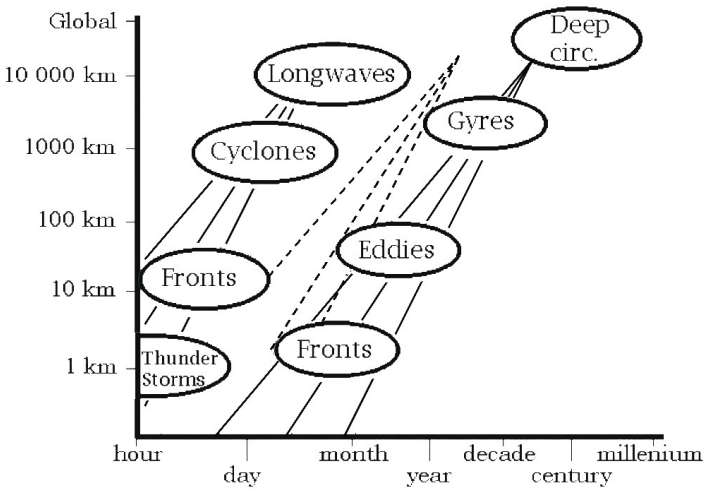

Figure 1.8: Representation of typical atmospheric and oceanic processes in a diagram of time and spatial scales adapted from Steele (1995)

The separation between scales suggested in Figure 1.8 is actually much vaguer in reality, and cross-scale interactions are everywhere. A fundamental aspect of geophysical fluid dynamics is the cascade of energy, i.e., the transfer of kinetic energy from one scale to a less energetic neighboring scale. For geophysical fluid dynamics, this cascade can either be directed towards the smaller scales (Nastrom et al., 1984) or the larger scales (Scott and Wang, 2005). Interactions between scales shape many aspects of climate variability. For the ocean side, it is now clear that mesoscale eddies have important implications for the evolution of large-scale flows such as the ACC (Hughes and Ash, 2001; Rintoul, 2018) or western boundary currents (Waterman and Jayne, 2011; Yan et al., 2019). In turn, eddies might be generated from the instability of the mean flow (Ferrari and Wunsch, 2009). At the same time, eddies are themselves influenced by sub-mesoscale processes (Klein et al., 2019).

The interactions between the components of the climate system depend on the considered scale. For instance, including small-scale atmospheric variability in the forcing of an ocean model leads to a spin-up of the mean circulation (Jung et al., 2014). Another striking example of the scale dependence of air-sea interactions is the relationship between ocean temperature gradients and near-surface winds. At scales larger than 1000 km, the correlation between ocean temperature gradients and near-surface winds is negative. This is interpreted as the ocean passively responding to wind-driven air-sea heat flux anomalies, and suggests a driving of the ocean by the atmosphere. However, at smaller scales, the relationship appears to be reversed (O'Neill et al., 2005; Small et al., 2008; Chelton and Xie, 2010a). Winds are found to be stronger over small-scale warm sea surface anomalies and weaker above the cold ones, which might be related to changes in atmospheric stability due to near-surface air warming or cooling (Small et al., 2008). The positive correlation between surface temperature gradients and wind speed at small scales suggests that the ocean can drive the wind variability at these scales.

1.3.2 The issue of small-scale processes

The idea that components of the climate system evolve on scales ranging from 1000s of kilometers down to meters and below has long been recognized. However, the understanding of the effect of the various processes taking place at these different scales is sometimes limited. In particular, the processes taking place at "small scales" are often poorly described. The understanding of so-called "small-scale processes" is indeed hampered by the limited spatial density of observations. Satellite remote sensing offers a high resolution, but a limited variety of measurable properties. In-situ measurements, either through campaigns or via autonomous sensors networks,

enable to obtain much more information, but their coverage and spatial density are very limited. The situation is even worse in polar regions, where the harsh conditions are strongly constraining the possibilities for observations. Campaigns such as the MODE (Gould et al., 1974) or POLYGON experiments (Brekhovskikh et al., 1971; Morozov, 2020) in the tropical Atlantic, which revealed the existence of mesoscale eddies, or the SEMAPHORE experiment (Eymard, 1998), which described the air-sea interactions at mesoscale near the Azores, would be almost impossible to set up in the stormy and ice-covered Southern Ocean.

Climate models are facing the same kind of limitation. The dynamical core of GCMs is founded on the resolution of a form of the Navier-Stokes equations which describe the conservation of energy and mass in a fluid (such as the ocean or the atmosphere). However, solving analytically these mathematical equations for the global ocean or atmosphere is practically impossible. Hence, they are solved numerically. The spatial and temporal domains are divided in "small" distance or time increments over which the differentials of the primitive equations are approximated by local finite differences. The spatial and temporal increments determine the spatial and temporal resolutions of a model (see Figure 1.9). Ideally, we would want to have the smaller increments as possible, but increasing the resolution of a model comes at a high computational cost. If it is possible to represent the main aspects of the climate with relatively coarse resolution, GCMs face the issue of the resolution of sub-grid–scale processes: a model cannot numerically represent a process with a characteristic length scale lower than a few grid points.

GCMs are particularly expensive to run: they need to simulate several components of the climate system at a global scale and on the scale of centuries. An additional constraint is the necessity to perform multiple runs or ensemble runs to reflect the natural or chaotic variability of the climate system. Designing a numerical climate simulation requires achieving a compromise between the time scales, the number of components, the number of ensemble members, and the resolution of the model so that it can be run on the available infrastructures. Though the computational power is quickly increasing, the resolution of current GCMs is often limited to 1° in the ocean and 100 km in the atmosphere (Figure 1.9). Thus, most GCMs are not explicitly representing the processes with length scales smaller than 100 km.

However, many processes take place at scales lower than 100 km, such as atmospheric or oceanic turbulence, sea ice leads, storms, clouds, etc. The effects of such processes might be significant for the dynamics of the climate system. To deal with the non-representation of sub-grid–scale processes, GCMs are complemented

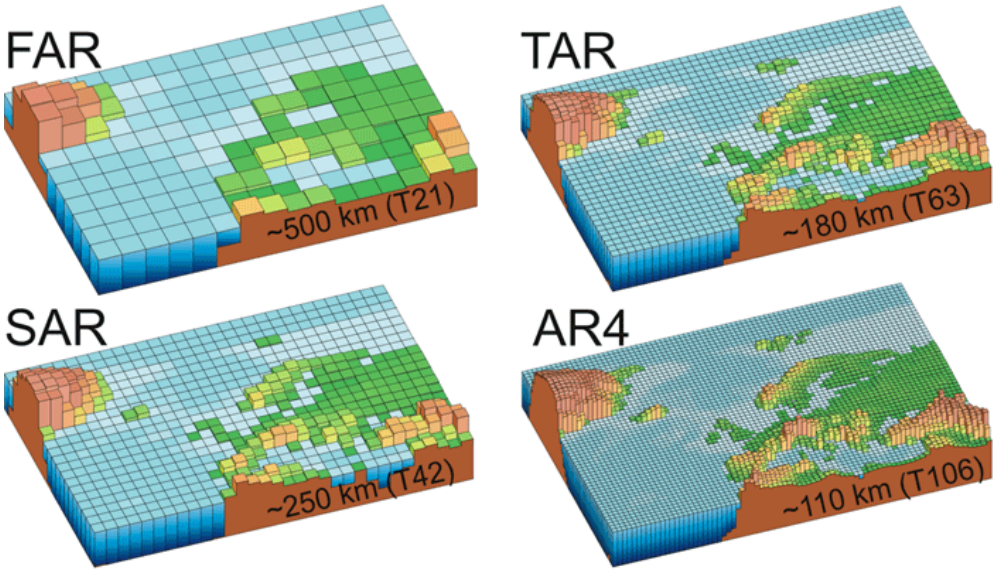

Figure 1.9: Illustration of the evolution of GCMs horizontal resolution between the First (FAR) and the 4th Assessment Report of the Intergovernmental Panel on Climate Change (IPCC). The figure was adapted from Figure 1.4 of the 4th Assessment Report of the IPCC (Solomon et al., 2007).

by a series of parameterizations. Parameterizations aim at representing the effects of sub-grid–scale processes on the larger scale. They are built upon observed or simulated relationships or derived from theory. These parameterizations are a fundamental aspect of climate models which yield major improvements in the capabilities of models to represent the climate of the Earth. The parameters and coefficients in these parameterizations do not necessarily have a physical meaning and sometimes cannot be "measured", they have to be tuned. However, the observations needed to support and tune parameterizations are often missing in polar regions, and the tuning of a model for the given present climate might not hold in a future, warmer climate. Besides, parameterizations cannot represent the complex cross-scales and cross-media interactions associated with certain processes.

1.3.3 Need for higher resolution?

While ocean climatologies built upon years of in-situ measurements offer a good ensemble view of the ocean state, the understanding of the underlying processes is lacking. This is for instance illustrated by the uncertainties of the driving mechanisms of the Global Overturning Circulation (Kuhlbrodt et al., 2007; Lavergne et al., 2016). High-resolution models can be used to bridge the gaps of observational products: by using models capable of explicitly representing small-scale processes, we can learn about their dynamics and influences on the climate system.

Most of current GCMs cannot resolve processes with scales below 100 km. Their effects are either parameterized or omitted. But, with the ever-going increase in computational power, a step up in model resolution is foreseeable in the next years to decades. An increase in resolution would enable models to represent the topography and bathymetry in a more detailed way and to represent processes taking place at smaller scales.

Increasing the resolution of GCMs could improve the overall realism of the simulated climate, as demonstrated by a series of recent findings. Roberts et al. (2018) reviewed the benefits of increasing the resolution of GCMs, focusing mainly on atmospheric processes and the global freshwater budget. For instance, the representation of extra-tropical storms structure and intensity was shown to be improved with horizontal resolution higher than 100 km, affecting the moisture transport by the atmosphere (Catto et al., 2010; Zappa et al., 2013). The storm track and cyclogenesis in the sub-tropical northern Atlantic is highly improved when the grid spacing is refined to 10 km (Manganello et al., 2012). Resolving ocean eddies in GCMs has been shown to improve the transport and pathways of major ocean currents such as the ACC (Hewitt et al., 2020) and leads to more realistic Atlantic meridional overturning circulation (Roberts et al., 2016) or oceanic heat transport in the Northern Atlantic (Docquier et al., 2019). Refining the resolution of sea ice models could also enable the representation of the sea ice cover heterogeneity, such as leads, that strongly govern air-sea heat fluxes.

Processes taking place at small scales might have implications for the whole climate. Coastal polynyas off the coast of Antarctica have spatial scales of a few tenths of km but are responsible for the production of AABW that flood the global ocean and participate in the global oceanic thermohaline circulation. Local current-topography interactions deeply affect the flow of the ACC (Rintoul, 2018). A high resolution might be needed to represent the grounding line retreat of West Antarctic glaciers, which could lead to the destabilization of the West Antarctic Ice Sheet (Favier et al., 2014).

High-resolution GCMs can also prove to be more useful for short-term predictions or for the design of local adaptation. For instance, the EC-Earth climate model was shown to have better regional forecast skills at higher resolution (Prodhomme et al., 2016) and the absence of small-scale sea ice heterogeneity was shown to be a source of uncertainty in short-term forecasts (Batrak and Müller, 2018). Coarse-resolution models struggle to represent several extreme events such as hurricanes (Walsh et al., 2013) or extreme precipitations (Norris et al., 2021). While southern polar regions are mostly uninhabited, measurements campaign or provisioning of scientific

bases would greatly benefit from improved climate modeling and forecast capabilities.

If it appears that small-scale processes have important influence for the interactions between the ocean and atmosphere, and that increasing the resolution of models improves their representation of the Earth's climate, the case of small-scale processes in the polar regions and in Antarctica is much less clear. **'What are the effects of small-scale processes on the atmosphere-cryosphere-ocean interactions in Antarctica?'** is an open question that need to be addressed to advance our understanding of the Antarctic climate and our capacity to forecast its evolution.

1.4 Contributions of the present thesis

1.4.1 Overview

Understanding how the Antarctic environment will evolve under the present climate change is crucial in regard to its importance for the global oceanic thermohaline circulation, global sea-level rise, and CO_2 or heat sequestration. Yet, several aspects of the atmosphere-cryosphere-ocean interactions taking place in the Southern Ocean area are poorly understood, especially the role of processes taking place at small spatial scales due to missing observations. Current GCMs exhibit large biases in the southern polar latitudes, suggesting that they might be missing key processes such as small-scale processes that GCMs are unable to explicitly resolve. High-resolution GCMs should be able to represent more small-scale processes, which could improve their simulation of climate (Roberts et al., 2018; Hewitt et al., 2020), but very little is known about the case of polar regions. Today, it is essential to better understand the role of small-scale processes in the Antarctic climate system and to improve the representation of this system in models.

In this context, the goal of the present thesis is to evaluate the role of small-scale processes in atmosphere-cryosphere-ocean interactions off Adélie Land. This first requires identifying small-scale processes that are poorly understood because rarely observed, likely to be misrepresented in coarse-resolution models, while potentially having significant effects on climate-relevant atmosphere-cryosphere-ocean interactions. Then, it is necessary to quantify the effects of the selected processes on the atmosphere-cryosphere-ocean interactions off Adélie Land. This thesis contributes to improving the understanding of rarely observed small-scale processes and their effects on the Antarctic climate. Our results can later be used to support the development of the next generation of GCMs, by substituting to currently missing observations and by identifying methods to simulate small-scale processes. From this knowledge, teams responsible for GCMs development can make better-informed choices about the processes to be included and the way to do so (either with parameterizations or by deciding to increase models resolution).

The Southern Ocean MOC is a central element of the Antarctic climate, and we will use it as a common thread throughout the thesis. As our goal is to investigate how small-scale processes influence the Antarctic climate, we will focus on processes that can be expected to affect the Southern Ocean MOC in some ways.

First, we focus on the lower cell of the MOC, i.e., on the formation and evolution of DSW. The formation of DSW is difficult to observe, as it mostly takes place during the core of winter. It is often studied with summer hydrographic measurements revealing the aftermaths of the winter convection, though some year-round moorings have been installed off Adélie Land. Thus, the knowledge of subsurface processes affecting the formation of DSW is limited. The effects of ocean tides in the coastal seas of Antarctica, and especially in the Adélie Land sector, are poorly known as observing tidal currents is particularly demanding. Tides might affect the transformation (as a source of vertical mixing) and the transport (by the high-frequency or mean tidal currents) of water masses such as DSW and also affect sea ice production due to the friction of tidal currents on the sea ice (driving both ocean-ice momentum and heat fluxes). Besides, the basal melt of ice shelves is a source of super-cooled freshwater that can either drive the production of dense waters by cooling dense CDW or on the contrary, freshen Winter Water inhibiting their conversion into dense waters. The interactions between the ocean and ice shelves are poorly known as direct observations are extremely rare. Apart from estimates of ice shelf basal melt (which remains highly uncertain), the ocean-ice fluxes and their effects on circulation and water masses beneath and outside the ice shelf cavities are largely unknown. Both tides and ocean–ice shelf interactions appear to be able to affect the lower cell of the MOC, and as such, will be the first focus of this thesis. In Chapter 3, we address the question: how are ocean tides and ocean–ice shelf interactions affecting the formation of DSW off Adélie Land?

The importance of wind-driven polynyas for the lower cell of the MOC via the production of DSW formation is well documented. However, it is unclear how important are local small-scale winds over large-scale winds in driving the different polynyas found in coastal Antarctica. Better understanding the relative role of local katabatic winds in driving polynyas and DSW production is however needed to estimate future dense water production rates that will result from the possible perturbation of the Antarctic wind fields. Besides, it is also crucial to understand how to adequately represent the drivers of coastal polynyas in models and, in particular, the resolution needed. Topography applies a strong control on the winds of Antarctica leading to high spatial variability of the wind intensity and direction in coastal regions. Due to the low density of AWS, knowledge about coastal winds

and their effects on dense water production is limited. Low-resolution models are likely misrepresenting local coastal winds, and global atmospheric reanalyses might not represent correctly the key mechanisms (boundary layer stability, air-snow interactions) leading to the formation of katabatic winds in Antarctica. In Chapter 4, we tackle this knowledge gap by investigating what is the sensitivity of sea ice and polynyas simulated by a numerical model to the resolution of the atmospheric forcing?

The processes influencing the upper cell of the MOC are equally poorly understood. Ocean mesoscale eddies in the Southern Ocean are too small to be adequately detected by most remote sensors, and they are too elusive to be observed by the network of autonomous sensors (MEOP or ARGO). Most of the knowledge regarding the role of mesoscale eddies in the Southern Ocean has been derived from models, but high-resolution coupled models are rare, and the way eddies interact with both the sea ice and atmosphere has never been studied. By driving the variability of the mixed layer depth and surface temperature, salinity, and currents, mesoscale eddies have the potential to modulate the interactions between the ocean and the sea ice or the atmosphere, and thus, to affect the upper cell of the MOC. This is what we aim to understand in Chapter 5, or more precisely: how do ocean mesoscale eddies modulate the atmosphere–sea ice–ocean interactions off Adélie Land?

To summarize, this thesis is articulated around the three aforementioned questions, namely:

- How are ocean tides and ocean–ice shelf interactions affecting the formation of DSW off Adélie Land?
- What is the sensitivity of sea ice and polynyas simulated by a numerical model to the resolution of the atmospheric forcing?
- How do ocean mesoscale eddies modulate the atmosphere–sea ice–ocean interactions off Adélie Land?

Tides and ice shelves influence on DSW production is addressed in Chapter 2, the sensitivity of sea ice to the atmospheric forcing resolution in Chapter 3, and the influence of mesoscale eddies on atmosphere–sea ice–ocean interactions in Chapter 4. The main achievements, our general conclusions and some envisioned perspectives are presented in Chapter 5. We summarize hereafter the main contributions of the present thesis to these scientific questions together with the associated technical work, i.e. the development of a regional ocean–sea ice–atmosphere model.

1.4.2 Development of a regional ocean–sea ice–atmosphere model

The main tools used throughout this thesis are numerical simulations performed with models specifically configured for the study of small-scale processes in the Adélie Land region. A general overview of the models used in this thesis is presented hereafter. For a more detailed description of the modeling and experimental choices, the readers are referred to the methodological sections of the following chapters.

During this thesis, I have used the ocean general circulation model NEMO (Nucleus for European Modeling of the Ocean, Madec (2016)). NEMO is a hydrostatic model simulating the three-dimensional circulation of the ocean generated by a variety of forces (pressure gradients, surface or bottom stress, Coriolis ...) and the water masses transformation due to mixing or heat and freshwater fluxes. Sea ice being an essential component of the Adélie Land regional climate, it is essential to account for it. The sea ice is here managed by the LIM (Louvain-la-Neuve sea Ice Model) model (Vancoppenolle et al., 2009; Rousset et al., 2015). LIM represents the whole life-cycle of sea ice, from its formation due to the freezing of seawater, its thickening due to the heat loss through sea ice and within leads or to the flooding and freezing of the snow load, its transport and deformation under the action of ocean currents and winds, to its melting due to solar radiation or basal melting. The representation of sea ice dynamics is delicate in global models: sea ice is a complex media that behaves like a fragmented solid blanket at small scales but resembles a fluid at larger scales. Since LIM has been developed to represent sea ice on a broad spectrum of spatial scales and in particular for the global scale, it uses the continuum assumption and represents sea ice as a continuous elastic-viscous-plastic material.

To explicitly represent the small-scale processes targeted in this thesis, the resolution of the NEMO-LIM model had to be greatly refined. The goal is to achieve a resolution close to 2 km, which is translated in terms of spherical coordinates to a resolution of 1/24° in longitude and latitude, hence a much higher resolution than the 1° used in previous configurations used at the UCLouvain (Barthélemy et al., 2017; Lecomte et al., 2017). With the increase of resolution, some parameterizations have to be turned off, such as the parameterization of the eddy diffusivity, since part of the mesoscale activity can be explicitly resolved by the high-resolution numerical model. As discussed previously, one of the main drawbacks of increasing the resolution of models is the accompanied increase in the computational cost. A bulk approximation is that dividing the resolution by two leads to an eight-fold increase of the computational cost (multiply the number of grid cells by 4 and divide the time step by 2). To reach the desired resolution despite the limits of computational power and as we are interested in the region of Adélie Land, we have developed here a

regional configuration of the NEMO-LIM model. It allows us to attain high resolution at a reasonable cost but has a major drawback: the model does not represent the large-scale circulation and the interactions between the region of interest and the rest of the World Ocean. Thus, it is needed to account for the influence of the large-scale circulation on the Adélie Land sector. In the model, this is done thanks to the application of open boundary conditions at the lateral limits of the domain. They impose the flow and the sea ice or water masses properties on the sides of the simulated domain and allow currents from within to exit the area. The choice of the dataset used to provide the information about the ocean or sea ice state at the boundaries of the domain is crucial, as it will partly dictate the state of the ocean and sea ice within the domain. As the domain is relatively small, it is important to have a high-resolution external dataset to avoid a too sharp transition at the boundaries. Here, we use the PSY4V3R1 dataset produced by Mercator Ocean. It is a 1/12° ocean and sea ice analysis, i.e. a model that takes benefits from several observational datasets through data assimilation. PSY4V3R1 for instance assimilates in-situ observations of ocean temperature and salinity or remote sensed sea ice concentrations.

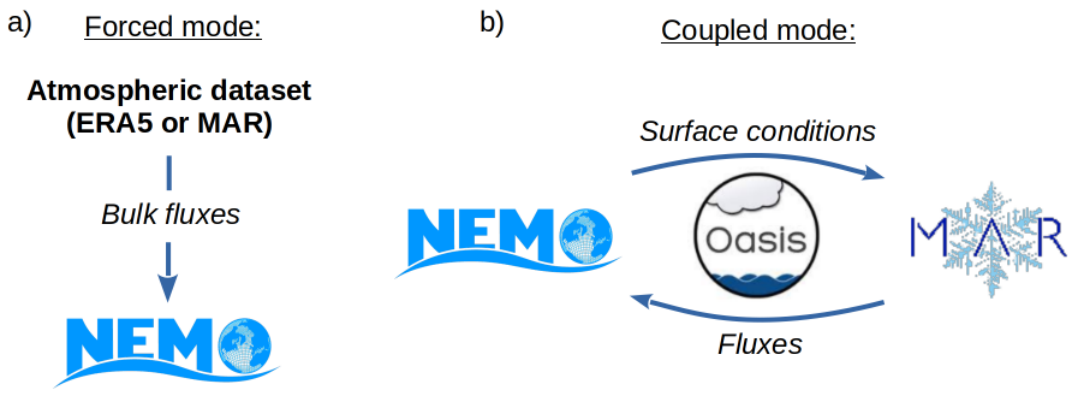

Figure 1.10: Simplified representation of the interactions of the ocean-sea ice model LIM with the atmosphere in a) the forced mode (by the global atmospheric reanalysis ERA5 or outputs from MAR) and b) the coupled mode with the MAR model.

The influence of the atmosphere is essential in the evolution of the sea ice and ocean and investigating how small-scale processes affect air-sea-(ice) interactions is also one of the goals of this thesis. In the present work, the interactions of the ocean–sea ice with the atmosphere are represented in two different manners. In Chapters 3 and 4, the ocean–sea ice model is run in "forced" mode (see Figure 1.10a for a simple schematic view). The state of the atmosphere is prescribed using either outputs from a global atmospheric reanalysis in Chapter 3 or outputs from the atmospheric model MAR (Modèle Atmospherique Régional, (Gallée and Schayes, 1994)) in Chapter 4. The fluxes are computed by the ocean–sea ice model, using so-called

bulk formulae, allowing to account for the state of the ocean surface in the forcing of the ocean–sea ice by the atmosphere. In the "forced" mode, the ocean-atmosphere interactions are "one-way": the atmosphere influences the ocean, but it does not respond to the evolution of the ocean or sea ice simulated by NEMO-LIM. To account for the two-ways interactions, it is needed to couple the ocean–sea ice model to an atmospheric model (here the MAR model). This is done in Chapter 5. The coupling, illustrated in Figure 1.10b, is handled by the OASIS-MCT3 libraries (Craig et al., 2017), which manages the timing and the interpolations of the fields exchanged between the two models. In this coupling, NEMO-LIM sends its surface conditions to MAR, which computes and sends the surface fluxes back to NEMO-LIM. This way, both models evolve in pairs, allowing to account for the effects of air-sea-ice feedbacks.

1.4.3 Influence of ocean tides and ice shelves on ocean-ice interactions and DSW formation off Adélie Land

The formation of DSW (and subsequently AABW) off Adélie Land is fundamental for the ventilation of the deep ocean and the global oceanic thermohaline circulation. Such a process has only been registered in four regions of coastal Antarctica, illustrating the importance of regional processes. Understanding what are the processes affecting DSW production off Adélie Land is crucial to forecast future AABW formation. The DSW production in the Adélie Land sector is thought to mostly take place in the Mertz glacier polynya which, as its name suggests, is adjacent to the Mertz glacier, the largest ice flow of the Adélie Land sector. The basic principle behind DSW production in the Mertz glacier polynya is the continuous extraction of heat and the addition of salt as surface waters freeze, leading to the destratification of the water column. The formed Winter Water can reach the state of DSW if its salinity is high enough. Processes affecting the heat or freshwater budget in the sector can thus affect the formation of DSW. Later, processes impacting the transport and mixing of DSW will ultimately determine the amount of AABW being formed.

Ocean tides and ocean–ice shelf interactions are omitted or parameterized in most GCMs. They are not "small-scale" processes by definition, but a high resolution might be needed to represent the details of the bathymetry and ice shelf cavities that control tidal currents or ocean circulation outside and beneath the ice shelves. The effects of both processes on the atmosphere–sea ice–ocean interactions off coastal Antarctica, and in particular DSW formation, are still poorly understood.

One of the main freshwater sources for the coastal Southern Ocean is the melting of the ice shelves or icebergs. As such, the freshwater fluxes from the ice shelf melt could easily affect the production of DSW. Ice shelf melt was suggested to be one of the reasons for the absence of DSW formation off Sabrina coast or in the Amundsen Sea polynya, despite the intense sea ice production (Silvano et al., 2018). De Lavergne et al. (2014) also suggested that increased freshwater fluxes from ice shelf melt could increase the ocean stratification and suppress deep convection in the Weddell Sea. However, the role of ice shelf melt fluxes on DSW formation in Adélie Land remains poorly known. Cougnon et al. (2013) showed that accounting for ocean–ice shelf interactions in a model leads to a decrease in DSW formation in Adélie Land. But the Adélie Land sector has undergone a major reorganization following the breaking of the Mertz Ice Tongue in 2010, affecting the sea ice production and ocean circulation (Kusahara et al., 2011b; Tamura et al., 2012; Lacarra et al., 2014; Snow et al., 2018). The dynamics of the polynyas off Adélie Land and the basal melt are likely different now (Cougnon et al., 2017; Kusahara et al., 2017), leading to different implications for the ice shelf melt. Another way ice shelf melt could influence the DSW formation is via its impact on sea ice production. Depending on the sector, ice shelf melt was shown to increase (Bintanja et al., 2015; Jeong et al., 2020) or decrease (Jourdain et al., 2017; Mathiot et al., 2017; Merino et al., 2018) sea ice production. This dichotomy has to deal with the properties of the water masses upwelled by the melt-driven overturning circulation. The DSW formation could affect the ice shelf melt in return, as the presence of DSW could block the intrusions of warmer waters (CDW), or on the contrary, replace the colder ISW produced within the cavity. It is thus needed to account for the two-way interactions.

Tides have recently been suggested to play an important role in cross-shelf exchanges thanks to the mean tidal currents (Wang et al., 2013; Stewart et al., 2018). Tides were also shown to modulate the export of DSW (Padman et al., 2009) and are a source of vertical mixing, leading to water masses transformation in the World Ocean (Simmons et al., 2004) or in Antarctic coastal seas (Beckmann and Pereira, 2003). Tides could thus govern DSW circulation after its formation or modify the properties of the water column beneath polynyas by, for instance, advecting CDW. Finally, tides have been suggested to influence sea ice motion and production (Koentopp et al., 2005; Luneva et al., 2015), and could thus influence DSW production. However, the influence of tides on ocean circulation and water masses transformation, in particular DSW production, is poorly known. Besides, tides are thought to be an important driver of ice shelf basal melt (Padman et al., 2018; Jourdain et al., 2019; Hausmann et al., 2020), either through the friction of tidal currents at the ocean–ice shelf interface or by modulating the ocean circulation or water masses properties in

the neighborhood of ice shelves. The effect of tides on the ice shelf melt off Adélie Land is presently not known and could modify the response of DSW formation to ocean–ice shelf interactions.

The objectives of Chapter 1 are to evaluate the effect of tides on ocean–ice shelf interactions in the Adélie Land area and to understand how tides, ocean–ice shelf interactions, and the interplay between the two processes affect the formation of DSW off Adélie Land. To do so, I have developed a regional configuration of the NEMO-LIM ocean–sea ice model forced by an atmospheric reanalysis. In order to improve the representation of landfast ice compared to previous studies in the Adélie Land sector, a parameterization of landfast ice including tensile strength and taking into account the role of grounded icebergs has been introduced into the model. This configuration is the first one to represent the dynamics of landfast sea ice in coastal Antarctica. Compared to previous studies, the model also has a higher resolution of 1/24° (approximately 2 km), which might be important for the representation of the bathymetry, the ice shelf geometry, and small-scale currents. In order to specifically address the questions of the role of tides, whether on the formation of DSW or on ocean–ice shelf interactions, a series of experiments have been carried out where tides are omitted or accounted for. Besides, we also test how ocean–ice shelf interactions affects the formation of DSW to discriminate their effects from the ones arising from tides–ice shelf interactions.

1.4.4 Effects of the atmospheric forcing resolution on simulated sea ice and polynyas off Adélie Land

The production of DSW is tightly linked to the atmospheric forcing via the opening of polynyas. There is almost no direct observations of the interactions between the ocean, sea ice and atmosphere within polynyas, and most knowledge about polynyas dynamics is derived from remote sensing. GCMs struggle to represent coastal polynyas (Mohrmann et al., 2021) and coastal DSW formation (Heuzé et al., 2013; Heuzé, 2021), which can affect both their representation of the coastal ocean and of the MOC. A potential cause might be the misrepresentation of coastal winds, due to either misadapted atmospheric physics or to the coarse resolution of GCMs. The thermal inversion which occurs over the Antarctic continent plays an important role in the onset of katabatic winds (Parish and Waight, 1987) which are misrepresented in GCMs. The smoothing of the AIS slopes in coarse-resolution GCMs might lead to a negative bias in the simulated coastal wind intensity (Van den Broeke et al., 1997). The katabatic winds are by definition strongly controlled by the topography (Parish, 1988; Parish and Cassano, 2003; Parish and Bromwich, 2007), but they can also be

affected by local air-sea heat fluxes over polynyas in coastal regions (Gallée, 1997; Savijärvi, 2011). Thus, the representation of Antarctic katabatic winds is sensitive to the horizontal resolution. Bromwich et al. (2013) suggested that increasing the resolution of an atmospheric model resulted in better model performance. Petrelli et al. (2008) showed that refining the resolution of an atmospheric model down to 2 km leads to significant intensification of katabatic winds and sea ice production.

Antarctic coastal winds are of major importance for the coastal ocean and sea ice. In particular, katabatic winds are thought to be the main driver of Antarctic coastal polynyas (Adolphs and Wendler, 1995; Massom et al., 1998) and subsequent DSW formation. Barthélemy et al. (2017) highlighted that uncertainties in the atmospheric forcing lead to important modifications of sea ice production all around Antarctica. The representation of katabatic winds appears to be particularly crucial: Mathiot et al. (2012) showed that using outputs from a regional atmospheric model instead of a global reanalysis to drive a sea ice–ocean model produced more realistic winds and increased coastal sea ice production due to the increased resolution and to the representation of polar-specific processes. Correcting the wind fields from a global reanalysis or of a global climate model were shown to substantially affect the sea ice and ocean simulated by the NEMO-LIM or LOVECLIM models (Mathiot et al., 2010; Barthélemy et al., 2012). Besides sea ice, modifications of wind intensity were also shown to modify the intrusions of CDW and the ocean mixing in West Antarctica, impacting the basal melt of ice shelves simulated in the ROMS model (Dinniman et al., 2012).

The horizontal resolution of atmospheric models appears to be an essential factor controlling their ability to represent Antarctic coastal winds. However, it is unclear what resolution is actually needed to realistically simulate katabatic winds. Petrelli et al. (2008) simulated an intensification of katabatic winds by increasing the resolution down to 2 km, while van Wessem et al. (2015) attributed model errors to the poor resolution despite using 5.5 km resolution. Are such resolutions needed to represent katabatic winds elsewhere in Antarctica, such as the Adélie Land, where the topography is less complex than in the coastal Weddell Sea? In addition, it is unclear how coastal ocean and sea ice respond to the atmospheric grid refinement towards finer resolution than 20 km. If Mathiot et al. (2012) demonstrated a strong sensitivity to the representation of katabatic winds, they were still using a relatively low resolution (20 km) not much greater than the one of current global reanalyses (31 km for ERA5). Petrelli et al. (2008) suggested an increase in sea ice production with a grid refinement up to 2 km in the Terra Nova Bay region, but they used a relatively simple polynya model. It might be needed to include the interactions

of sea ice with ocean and ice shelves to understand how the ocean–sea ice system responds to the atmospheric forcing resolution. Dinniman et al. (2015) showed that increasing the forcing resolution with the PolarWRF model led to an increase in oceanic heat transport to the ice shelf simulated in the ROMS oceanic model. As will be shown in Chapter 1, ocean–ice shelf interactions significantly influence the DSW formation. So the response of ice shelf basal melt to the forcing resolution might affect DSW in return. Finally, as landfast ice governs the motion of coastal sea ice and the location of polynyas, testing the sensitivity of polynyas to the atmospheric forcing resolution might provide different results if landfast ice is simulated. Ebner et al. (2014) illustrated the different roles of katabatic and large-scale winds in forcing coastal polynyas using high-resolution models of the Weddell Sea, but they struggled to represent polynyas adequately, potentially due to the misrepresentation of landfast ice.

Knowing how to adequately simulate coastal winds and their effects on the coastal ocean-ice system off Antarctica is crucial to improve the representation of the Antarctic climate dynamics in models. In Chapter 3, I evaluate the sensitivity of coastal winds simulated by an atmospheric model to the resolution of this model and the impacts of increasing the atmospheric forcing resolution on the simulation of sea ice and polynyas in the Adélie Land sector. This work is based on a series of experiments performed using a regional atmospheric model and the regional ocean–sea ice model developed in Chapter 2, thus representing tides, ocean–ice shelf interactions, and landfast ice. To explore the role of the resolution, three atmospheric simulations are conducted at resolutions of 20, 10, and 5 km using the MAR model (Modèle Atmospherique Régional). These resolutions range from the horizontal resolution of high-resolution climate models or of high-resolution reanalyses (31 km for ERA5) to very high resolution rarely used in polar atmospheric models and out of reach for current global models. The atmospheric numerical experiments are designed such that horizontal resolution is the only difference between one another, i.e, the physical parameterizations are kept identical between the three experiments. These experiments serve to study the effect of resolution and to test whether the resolution of current atmospheric reanalyses is sufficient to represent coastal katabatic winds in the Adélie Land area. This study contributes to a better understanding of the role of resolution in simulating coastal winds off Antarctica.

The second part of the study consists of using the three atmospheric simulations presented earlier to force the ocean–sea ice model developed in Chapter 2. Our goal is to specifically study the sensitivity of coastal sea ice (polynyas or landfast ice) and the associated brine rejection to the resolution of the atmospheric forcing in

the Adélie Land sector. To our knowledge, it is the first time that the effect of the atmospheric forcing horizontal resolution on the Antarctic coastal ocean and sea ice is tested using a realistic ocean–sea ice regional model configuration including a realistic representation of landfast ice and a very high resolution.

1.4.5 Effects of ocean mesoscale eddies on atmosphere–sea ice–ocean interactions off Adélie Land

The first two chapters of this thesis emphasize the role of small-scale processes in the atmosphere–sea ice–ocean interactions in coastal regions, i.e. in the lower cell of the Southern Ocean MOC. But small-scale processes might also affect the atmosphere–sea ice–ocean interactions that drive the upper cell of the MOC. In the open ocean, one of the most fundamental small-scale processes currently parameterized in GCMs is the mesoscale ocean activity.

Over the past decades, mesoscale ocean eddies have become a key component in our understanding of the dynamics of the Southern Ocean. Mesoscale eddies are fundamental for the ocean dynamics, as they account for most of the ocean kinetic energy (Ferrari and Wunsch, 2009). They were shown to contribute to the Southern Ocean MOC and meridional heat fluxes (Volkov et al., 2008; Dufour et al., 2015). Eddies are also key features of the ACC circulation (Rintoul, 2018) and can temper the Southern Ocean response to climate change (Farneti et al., 2015) by partly compensating for the increase of the wind-driven northward Ekman drift. In addition, Stewart and Thompson (2015) and Stewart et al. (2018) also suggested that eddies play an important role in cross-shelf exchanges. The first Rossby radius of deformation, determining the size of mesoscale eddies, ranges from a few to a few 10s of kilometers in the Southern Ocean (Chelton et al., 1998), so that most GCMs cannot explicitly represent them. Parameterizations account for their effect on mixing (Gent and Mcwilliams, 1990) and thus provide a part of the eddies contribution to the Southern Ocean dynamics (Poulsen et al., 2018).

However, the parameterization of eddies does not account for the direct effect of these eddies on air-sea fluxes. Eddies drive the variability of surface ocean properties and thus affect the turbulent air-sea fluxes (Villas Bôas et al., 2015). Hausmann et al. (2017) showed that mesoscale eddies in the Southern Ocean have a marked imprint on the mixed layer depth, which could influence air-sea or ocean-ice fluxes. Due to eddy-driven anomalous air-sea fluxes, eddies were found to impact wind speeds or precipitations in the Southern Ocean (Chelton, 2013; Frenger et al., 2013). Outside the polar regions, mesoscale eddies were shown to modify the air-sea interactions

(Chelton et al., 2001; O'Neill et al., 2005; Chelton et al., 2007; Chelton and Xie, 2010a). Via their effects on the air-sea fluxes, eddies could affect the atmosphere. For instance, Foussard et al. (2019) highlighted the sensitivity of the storm tracks to the representation of eddy-induced surface temperature variability in an idealized simulation of the Southern Ocean. Another effect of mesoscale eddies is their modulation of air-sea momentum fluxes. Via a mechanism called the "eddy killing effect", eddies reduce the energy transfer from the winds to the ocean, weakening the ocean kinetic energy and energizing the winds (Renault et al., 2016). Such interactions were shown to strongly affect western boundary currents (Renault et al., 2019a) and to affect the stratification of the ACC (Song et al., 2020).

Recent studies have pointed out that eddies could also influence the sea ice. Eddies imprints on sea ice concentration and motion were observed in the Arctic sea ice (Kozlov et al., 2019, 2020; Cassianides et al., 2021). By simulating an idealized marginal ice zone, Manucharyan and Thompson (2017) have illustrated the importance of eddies in lateral sea ice transfer and ocean-ice heat fluxes. Gupta et al. (2020) demonstrated the importance of eddies in governing the ocean-ice heat fluxes and the sea ice melt rate via Ekman pumping driven by current friction on the sea ice. This modulation of sea ice production by eddies affected the depth of the mixed layer in return. The effects of the interactions of eddies with the sea ice are presently not directly accounted for in coarse-resolution models.

The understanding of the role of eddies in atmosphere–sea ice–ocean interactions in the Southern Ocean is at an early stage. The results of Manucharyan and Thompson (2017) concerning eddy-driven sea ice advection were obtained from a highly-idealized configuration, and the implication of this mechanism in a realistic model needs to be evaluated. Gupta et al. (2020) showed that eddies modulate ocean-ice heat fluxes, but they did not investigate how the eddies and in particular the ocean kinetic energy were affected in return. Moreover, neither Manucharyan and Thompson (2017) nor Gupta et al. (2020) accounted for the coupling with the atmosphere. The observations of eddies imprints on the atmospheric field by Chelton (2013) and Frenger et al. (2013) are limited to the ice-free regions, and it is important to understand if such processes are at play in the seasonally ice-covered region as it could impact the upper cell of the MOC. The dynamical and mechanical interactions of eddies with the atmosphere were shown to have important implications for the ocean or atmosphere dynamics (Ma et al., 2015; Renault et al., 2019a), but there is no evidence today that these processes are at play in the seasonally ice-covered Southern Ocean.

In Chapter 4, we aim at understanding how eddies affect atmosphere–sea ice–ocean interactions and the state of the ocean, sea ice, and atmosphere. For this study, we have developed a fully coupled ocean-sea ice-atmosphere regional model based on the ocean and atmosphere models built previously. To understand the role of eddies in atmosphere–sea ice–ocean interactions, it is important to incorporate the response of the atmosphere to the eddy-driven small-scale variability of the ocean surface and sea ice. Apart from the work of Jourdain et al. (2011), studies based on the use of high-resolution coupled models in coastal Antarctica have been missing for the past decade. Our model is unique in its design, its representation of specific processes (landfast ice or ocean–ice shelf interactions), and its very high horizontal resolution (1/24° for the ocean and 5 km for the atmosphere).

The high-resolution coupled model resolve ocean eddies which enables us to study their effects on the sea ice or the atmosphere. Previous studies revealed a strong coupling between small-scale surface temperature gradients and near-surface wind speeds in the subtropical regions. The first goal of our study is to see if this small-scale coupling also exists off Adélie Land and to explore how it is impacted by the presence of sea ice. Chelton (2013) and Frenger et al. (2013) showed that the imprint of eddies can be found in the atmospheric fields over the Southern Ocean. Following their method, we track the mesoscale eddies and evaluate their imprint on the atmosphere. The focus is then shifted to the imprint of eddies on the sea ice. Recent observations and modeling studies have indeed suggested that eddies could affect the sea ice. In the context of atmosphere–sea ice–ocean interactions driving the Southern Ocean overturning circulation, the role of eddies in the sector-averaged air-sea buoyancy and momentum fluxes is then assessed. To do so, a coupled experiment where the imprint of eddies on ocean surface conditions is filtered out is conducted.

With the development of a regional high-resolution coupled ocean–sea ice–atmosphere model, Chapter 4 fills an important shortcoming of the current research in polar climate modeling. In particular, it contributes to advance our understanding of the implications of eddies in atmosphere–sea ice–ocean interactions and the dynamics of the Southern Ocean and MOC in general.

Chapter 2

Influence of ocean tides and ice shelves on ocean-ice interactions and dense shelf water formation in the D'Urville Sea, Antarctica

This chapter is based on the article "Influence of ocean tides and ice shelves on ocean-ice interactions and dense shelf water formation in the D'Urville Sea, Antarctica" published in Ocean Modelling in 2021 (Huot, Fichefet, Jourdain, Mathiot, Rousset, Kittel and Fettweis, 2021a).

2.1 Summary

The D'Urville Sea, East Antarctica, is a major source of DSW, a precursor of AABW. AABW is a key water mass involved in worldwide ocean circulation and long-term climate variability. The properties of AABW in GCMs suffer from several biases, making climate projections uncertain. These models are potentially omitting or misrepresenting important mechanisms involved in the formation of DSW, such as tides and ocean–ice shelf interactions. Recent studies pointed out that tides and ice shelves significantly influence the coastal seas of Antarctica, where AABW originates from. Yet, the implications of these two processes in the formation and evolution of DSW are poorly understood, in particular in the D'Urville Sea. Using a series of NEMO-LIM numerical simulations, we assess the sensitivity of dense water formation in the D'Urville Sea to the representation of tides and ocean–ice shelf interactions during the years 2010–2015. We show that the ice shelves off Adélie Land are highly sensitive to tidal forcing, with a significant basal melt increase in the presence of tides. Ice shelf basal melt freshens and cools the ocean over significant portions of the coastal seas at the depth of the ice shelf draft. An opposite warming and increase in salinity

are found in the upper layers. The influence of ice shelf basal melt on the ocean is largely increased in the presence of tides. However, the production of sea ice is found to be mostly unaffected by these two processes. Water mass transport out of polynyas and ice shelf cavities are then investigated, together with their sensitivity to tides and ocean–ice shelf interactions. Ice shelf basal melt impacts the volume of dense waters in two ways: 1) Dense Shelf Water and Modified Shelf Water are consumed to form water masses of intermediate density inside the ice shelf cavities, and 2) the freshening of the ocean subsurface makes its transformation into dense water by sea ice formation more difficult. These results suggest that ice shelf basal melt variability can explain part of the observed changes of dense water properties, and may also affect the production of dense water in a future climate.

2.2 Introduction

As polar regions face changes at an alarming rate, concerns about their linkages with global climate emerge. It is indubitable that the reduction of the sea ice cover will affect the Earth's climate through changes in radiative balance (Curry et al., 1995), or that the ongoing melt of continental ice sheets will enhance sea-level rise (Alley et al., 2005). However, the future of polar regions is uncertain. In particular, the question of the evolution of AABW in a changing climate remains particularly challenging. AABW is the densest water mass found globally. Made of cold and saline water, it occupies a large portion of the World Ocean's seafloor (Johnson, 2008). AABW forms and sinks at high latitudes of the Southern Ocean, after mixing of cold and saline DSW and warmer CDW. Due to its long renewal time, AABW can store heat and CO_2 for several centuries (Pardo et al., 2014). As AABW occupies a large portion of the World Ocean, any warming of this water would be accompanied by a global sea-level rise due to thermal expansion (Purkey and Johnson, 2013). AABW also takes part in the low-frequency climate variability through its implication in the ocean thermohaline circulation (Stocker et al., 1992; Jacobs, 2004). Observations suggest that AABW has been undergoing significant changes in the recent past. For instance, Purkey and Johnson (2013) showed that the deep Southern Ocean has been warming and freshening over the past decades, in particular in the East Antarctic basins (Aoki et al., 2005; Rintoul, 2007), while Aoki et al. (2020) revealed a reversal of the trend after 2010. As modifications of AABW are expected to have far-reaching consequences, such changes illustrate the need for trustworthy projections of future polar climate.

Unfortunately, the current generation of GCMs presents several biases in the Southern Ocean. In particular, they struggle to represent the current AABW properties. Sallée et al. (2013b) found that the water masses of the Southern Ocean are too light and too warm in GCMs used in the CMIP5 exercise. Heuzé et al. (2013) concluded that only a few CMIP5 models are able to form DSW along the coast of Antarctica, where intense DSW formation has been observed (Ohshima et al., 2013; Williams et al., 2008). Heuzé (2021) showed that numerous models from the CMIP6 exercise while providing better results than their predecessors, produced most of the AABW through open-ocean convection. This questions the ability of GCMs to simulate the future of AABW and of the Earth's climate.

DSW (a precursor to AABW) forms when large amounts of salt are rejected during seawater freezing. The increase in surface water density destabilizes the water column and potentially leads to convection. High sea ice production required for DSW formation is mostly found in coastal seas of Antarctica (Tamura et al., 2008), where katabatic winds are frequent (Mathiot et al., 2010). The fine scales of polynyas

and coastal katabatic winds make their representation delicate in GCMs, which might be a cause for the lack of DSW formation. Besides, the importance of some processes occurring below the ocean surface may have been overlooked. The stratification of the ocean, and in particular the freshwater content in the water column are expected to interfere with the formation of DSW. For instance, De Lavergne et al. (2014) demonstrated that a surface freshening of the Southern Ocean could imply a cessation of deep convection in the Weddell Sea. Concerning the D'Urville Sea, Lacarra et al. (2014) proposed that ocean convection could also be reduced by the presence of a marked pycnocline following winters of intense DSW formation in areas of limited lateral exchange of bottom water properties. Finally, the properties of the dense water being produced would also depend on the state of the water masses being entrained during the winter convection. For instance, CDW is believed to be involved in DSW formation (Mantyla and Reid, 1983). However, the understanding of the processes governing the presence of CDW, the stratification, and the properties of water masses of coastal seas of Antarctica is still incomplete.

Tides and ice shelf cavities are often ignored or parameterized in studies based on GCMs. Models of the CMIP6 exercise do not explicitly represent tides and rely on parameterizations of tidal mixing. In several models, ocean–ice shelf interactions are either omitted, such as in GFDL-CM4 (Held et al., 2019) or simply parameterized: freshwater flux from the ice sheet is for instance applied at the surface of the ocean in MPI-ESM (Jungclaus et al., 2013; Mauritsen et al., 2019). More sophisticated representations exist in HadGEM3 or IPSL models (Storkey et al., 2018; Boucher et al., 2020), where the freshwater flux is applied in the subsurface to mimic the impact of ocean–ice shelf interactions. Few models, such as the AWI-CM (Wang et al., 2014; Semmler et al., 2019), represent ice shelf cavities. While this illustrates the effort put into accounting for this process in GCMs over the recent years, models with a realistic representation of ocean–ice shelf interactions remain uncommon. However, a growing body of evidence suggests that these two processes have a substantial impact on the coastal seas of Antarctica. Tides can notably modulate the export of DSW out of the continental shelf over the spring/neap tidal cycle in the Ross Sea (Padman et al., 2009). They favor the inflow of warm CDW onto the continental shelf, alongside the eddies (Stewart et al., 2018). They also influence DSW volume through an enhanced mixing between DSW and CDW (Wang et al., 2013). Simultaneously, tides can affect sea ice production through the periodic opening and closing of leads (Luneva et al., 2015) or sea ice motion (Koentopp et al., 2005). Tides are also a strong contributor to ice shelf basal melt (Makinson et al., 2011; Mueller et al., 2012; Arzeno et al., 2014; Padman et al., 2018; Jourdain et al., 2019; Hausmann et al., 2020). Besides, several studies emphasized the significant impact of ice shelves on ocean and sea

ice. Numerical studies suggested that increases in ice shelf meltwater could favor (Bintanja et al., 2015), have no significant effect (Pauling et al., 2016), or even reduce the sea ice cover in some regions (Jourdain et al., 2017; Mathiot et al., 2017; Merino et al., 2018). Furthermore, enhanced ice shelf melting induces a subsurface warming all around Antarctica, with effects on AABW formation and the global climate system (Menviel et al., 2010; Fogwill et al., 2015; Bronselaer et al., 2018; Golledge et al., 2019; Schloesser et al., 2019). Moreover, Silvano et al. (2018) suggested that freshwater from ice shelf melting might suppress DSW formation in the Amundsen Sea polynya (West Antarctica) and along the Sabrina coast (East Antarctica), but not in other regions such as the Cape Darnley polynya. The understanding of the mechanisms connecting tides and ice shelves to DSW formation is vague, in particular in other regions of the Southern Ocean.

The D'Urville Sea, located off Adélie Land in East Antarctica, is one of the major sources of DSW and AABW (Rintoul, 1998). This production is supported by the intense and persistent katabatic winds typical of the region (Wendler et al., 1997; Williams et al., 2008), favoring high rates of sea ice production (as shown by Mathiot et al., 2012). It has been the focus of several studies following the calving of the Mertz ice tongue in 2010, which led to a decrease in polynya activity and DSW production (Kusahara et al., 2011b; Lacarra et al., 2014; Cougnon et al., 2017; Snow et al., 2018). Despite these studies, several questions remain concerning the processes involved in DSW formation in the D'Urville Sea. The influence of ice shelf basal melt on ocean circulation, sea ice, and DSW production is not well understood yet, and no study has focused on the influence of tides on the cross-shelf exchange or ice shelf basal melt in this region.

The present study assesses the role of tides and ocean–ice shelf interactions in DSW formation in the d'Urville Sea. We investigate the influence of tides on ice shelf basal melt, the role of tides and ocean–ice shelf interactions on coastal seawater mass properties and circulation, and how these changes impact dense water. To do so, we run high-resolution ocean–sea ice simulations of the D'Urville Sea incorporating both tides and ocean–ice shelf interactions. The model used is NEMO-LIM 3.6 and it is forced by the ERA5 atmospheric reanalysis. The period of interest is 2010-2015. A series of sensitivity experiments are performed in which we turn off the representation of tides, ocean–ice shelf interactions, or both processes together. We analyze the sensitivity of the ice shelf to tides, and how both processes affect the ocean mean state and the dense water production off Adélie Land. The paper is organized as follows. The model configuration and forcing as well as the experimental design are presented in Section 2.3. Our reference simulation is evaluated in Section 2.4.

Sensitivity experiments to tides and ice shelves are analyzed in Section 2.5. A general discussion and conclusions are presented in sections 2.6 and 2.7, respectively.

2.3 The model, boundary conditions and experimental design

We developed a regional configuration of the NEMO platform (Nucleus for European Modelling of the Ocean, Madec, 2016) in its version 3.6 together with the sea ice model LIM3.6 (Louvain-la-Neuve sea Ice Model). The ocean component is based on primitive equations, assuming hydrostatic balance and using the Boussinesq approximation. Parameterizations include a Turbulent Kinetic Energy scheme (Bougeault and Lacarrere, 1989; Gaspar et al., 1990) for vertical mixing, convection is represented by enhancing vertical mixing, the surface pressure gradient is treated with a time-splitting approach together with a non-linear free surface. The grid is refined from the ORCA1 tripolar grid to obtain a locally isotropic resolution corresponding to $1/24^\circ$ longitude, i.e. from 1.7 to 2.3 km over the domain (130°E-150°E and 60°S-70°S, see Figure 3.1). This is not enough to fully resolve the eddies on the coastal seas where the 1st baroclinic radius ranges from 1 to 6 km (Hallberg, 2013). The vertical discretization consists of 75 levels of increasing thickness from top to bottom (1 m at the ocean surface, 200 m at depths larger than 3500 m), together with partial step of the bottom cells (and top cells under ice shelves). A no-slip lateral boundary condition is applied at the coast. The ocean time step is 150 s. We use a polynomial approximation of the reference Thermodynamic Equation Of Seawater (TEOS-10) [IOC, SCOR, APSO, 2010] optimized for a Boussinesq fluid by Roquet et al. (2015) (hence, we are using "conservative temperature" and "absolute salinity" instead of potential temperature and practical salinity). The sea ice component, LIM3.6, is a dynamic-thermodynamic model described in Vancoppenolle et al. (2009) and Rousset et al. (2015). The configuration of LIM in our model derives from the one of Rousset et al. (2015). A subgrid-scale distribution of sea ice thickness is used with 5 categories. The time step for the sea ice model is set to 900 s, with 600 subcycles to solve sea ice rheology. Sea ice–ocean and sea ice–atmosphere drag coefficients are 5.0×10^{-3} and 1.4×10^{-3}, respectively.

Surface boundary fluxes are computed every 900 s using the CORE bulk formulas (Large and Yeager, 2004). No salinity restoring is applied. At the domain boundaries, a flow relaxation scheme (Engedahl, 1995) is applied to the three-dimensional ocean variables and two-dimensional sea ice variables. A Flather scheme (Flather, 1994) is used for barotropic velocities and sea surface elevation. Ice shelf cavities with explicit ocean–ice shelf interactions are represented by the ice shelf module introduced in

NEMO by Mathiot et al. (2017), i.e. using the three-equations formulation from Jenkins (1991). Transfer coefficients are velocity dependent: $\gamma_{T,S} = \Gamma_{T,S} \times u_*$. The friction velocity is given by $u_* = C_d \times \sqrt{u_{TML}^2}$ and constant values of $\Gamma_{T,S}$ taken from Jourdain et al. (2017) are used ($\Gamma_T = 2.21 \times 10^{-2}$ and $\Gamma_S = 6.4 \times 10^{-5}$ for temperature and salinity, respectively), C_d is the top drag coefficient, set to 2×10^{-3}, and u_{TML} is the ocean velocity in the top boundary layer (Losch, 2008). The thickness of the top boundary layer equals the thickness of the top wet cell.

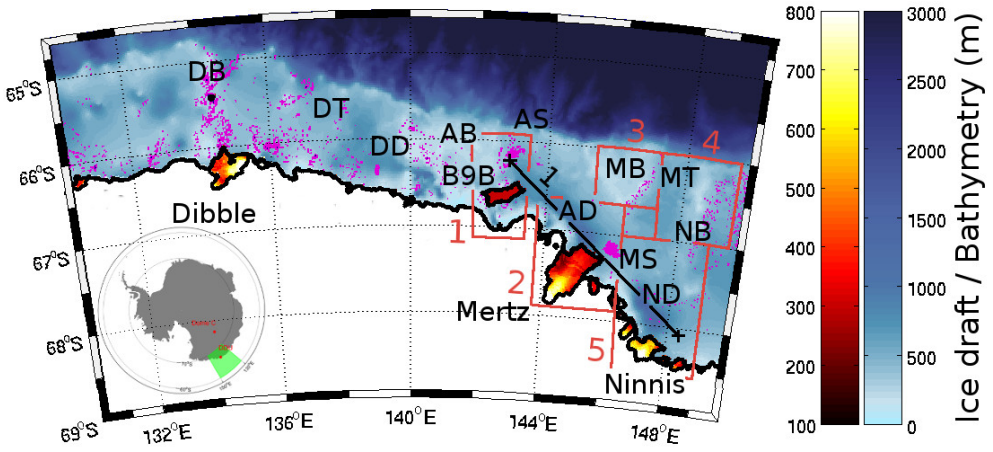

Figure 2.1: Map of the southern half of the model domain (D'Urville Sea). Blue shading corresponds to the bathymetry and yellow shading to the ice shelf draft. Purple dots represent grounded icebergs. From West to East, DB: Dibble Bank, DT: D'Urville Trough, DD: D'Urville Depression, AB: Adélie Bank, B9B: grounded iceberg, AS: Adélie Sill, AD: Adélie Depression, MB: Mertz Bank, MS: Mertz Sill, ND: Ninnis Depression, MT: Mertz Trough, NB: Ninnis Bank. The black line corresponds to transect 1 in Figure 2.10. Red squares indicate boxes for water mass transport computation (Figure 2.12). 1: B9B polynya, 2: Mertz Glacier Polynya, 3: Mertz Bank Polynya, 4: Ninnis Bank Polynya, 5: Ninnis Glacier Polynya.

Bathymetry is adapted from the GEBCO dataset (Weatherall et al., 2015), which includes the high-resolution measurements from Beaman et al. (2011). To ensure consistency with boundary conditions, the bathymetry at the boundaries is set to the bathymetry of the reanalysis used as lateral forcing. The B9B iceberg is mapped from LANDSAT8 images and added as an ice shelf. A second iceberg is added on the Dibble Bank, in the western part of the domain. Both iceberg locations appear to be almost unchanged over the period 2011-2015. B9B iceberg draft is set to 300 m following Mayet et al. (2013) and is treated as an ice shelf. We also set the Dibble iceberg draft to 300 m. Ice draft and bathymetry under ice shelves are adapted from Bedmap2 dataset (Fretwell et al., 2013). Bathymetry and ice draft are illustrated in Figure 3.1.

Tidal velocities and elevation of 18 tidal constituents from the Finite Element Solution 2012 (FES2012, Carrère et al. (2012)) are applied at the domain boundaries

as in Maraldi et al. (2013) and Jourdain et al. (2019). To compare the tides simulated by our NEMO configuration with those generated by the FES2012 barotropic model, we first run a pseudo-barotropic experiment as in Maraldi et al. (2013) and Jourdain et al. (2019). In this simulation (referred to as BARO hereafter), the ocean is set to a homogeneous salinity and temperature, and the atmospheric forcing and sea ice model are turned off together with the lateral boundary conditions to the exception of the tidal forcing from FES2012. The results are compared to FES2012 in Figure 2.2. The simulated tidal velocity is in good agreement with the external solution FES2012 for the semidiurnal component (here M2), with an RMSE of 0.49 cm/s and a mean bias of +0.12 cm/s over the continental shelf. The amplitude of the diurnal tidal velocities (here O1) is underestimated in BARO, especially at the shelf break, with a mean bias of -2.2 cm/s over the continental shelf.

The surface boundary conditions are derived from the 3-hourly ERA5 atmospheric reanalysis (Hersbach et al., 2020). The iceberg melt climatology of Merino et al. (2016) is used as an additional freshwater flux. Boundary conditions for the ocean and sea ice at daily frequency are derived from the 1/12° PSY4V3R1 ocean and sea ice analysis (https://www.mercator-ocean.fr/). It assimilates sea surface temperatures from OSTIA (Donlon et al., 2012), sea ice concentration from OSISAF (EUMETSAT, 2015), and temperature and salinity from the CORA4.1 dataset (Cabanes et al., 2013) and WOA13 (Zweng et al., 2013; Locarnini et al., 2013) below 2000 m depth. To reduce biases present on the coastal seas in the analysis used as lateral boundaries, we apply a correction towards the WOA18 climatology (Locarnini et al., 2018; Zweng et al., 2018). The temperature and salinity of the WOA18 climatology are imposed and daily anomalies from the PSY4V3R1 analysis with respect to their climatological values are added. The correction is only applied on the continental shelf (defined as the portions of the domain boundary where the bathymetry is shallower than 1000 m) because PSY4V3R1 shows better agreement with the observations in the open ocean and to reduce model instabilities. To minimize the mismatch between the surface water properties and sea ice conditions, the first ocean level is left unchanged, the correction is then linearly applied between z=1 m and z=10 m. To avoid a sharp lateral contrast between the shelf seas and the offshore ocean, the strength of the correction is linearly decreased on the 10 points following the shelf break. A constant sea ice salinity of 10 g/kg as well as a sea ice temperature of -3.15 °C are applied at the boundaries. A predefined sea ice thickness distribution is used for distributing the cell average thickness from PSY4V3R1 into the 5 categories of our simulations.

Large portions of the Adélie shelf seas are covered by patches of landfast ice (sea ice fastened to the coast, to the ice shelf tongues or grounded icebergs, see Fraser et al.

(2012)), often combined with the opening of polynyas on their lee side (Nihashi and Ohshima, 2015). Kusahara et al. (2010) successfully simulated the polynyas off Adélie Land by imposing barriers to sea ice advection as a way of mimicking the presence of icebergs. Fraser et al. (2012) suggested that landfast ice can form in a field of isolated grounded icebergs. This hypothesis is supported by the results of Olason (2016), who showed that the arching of sea ice anchored to several islands could lead to the formation of landfast ice, provided that the sea ice can offer tensile strength. This process was included in a viscous-plastic sea ice model by Lemieux et al. (2016) for the Arctic Ocean. The sea ice rheology from our model was adapted following Lemieux et al. (2016) to increase the sea ice tensile strength. The spatial distribution of small grounded icebergs off Adélie Land was obtained from the analysis of LANDSAT images taken between 2010 and 2015 (see Figure 3.1). These grounded icebergs are treated as land in the sea ice model and they mask air-sea fluxes. They do not produce freshwater as the contribution of icebergs to the freshwater budget is already accounted for in the runoff (as it includes the iceberg melt climatology of Merino et al., 2016) or is computed interactively in the case of the B9B iceberg (treated as an ice shelf). The ocean currents are free to cross grounded icebergs (as in Kusahara et al., 2017).

Our experimental design consists of a reference simulation and a set of sensitivity experiments. All simulations start from the WOA18 climatology in January 2007 and are run from 2007 to 2015. Years 2007-2009 are discarded from the analysis. The reference simulation (denoted REF) includes both tides and ocean–ice shelf interactions (open ice shelf cavities and interactive basal melt). In the noT simulation, the tidal forcing at the domain boundary is turned off. In noI, the under ice shelf cavities are masked and there is no freshwater or heat flux at the ocean–ice shelf interface. This is done to completely remove the effect of ocean–ice shelf interactions. Simulation noA has both tides and ocean–ice shelf interactions turned off, with the same methodology as noI and noT. Table 2.1 summarizes the simulations.

	Tides	Ice shelves
REF	yes	yes (cavity and flux)
noT	no	yes (cavity and flux)
noI	yes	no (closed and no flux)
noA	no	no (closed and no flux)
BARO	yes	yes (cavity and no flux)

Table 2.1: Names and descriptions of the simulations performed in the present study.

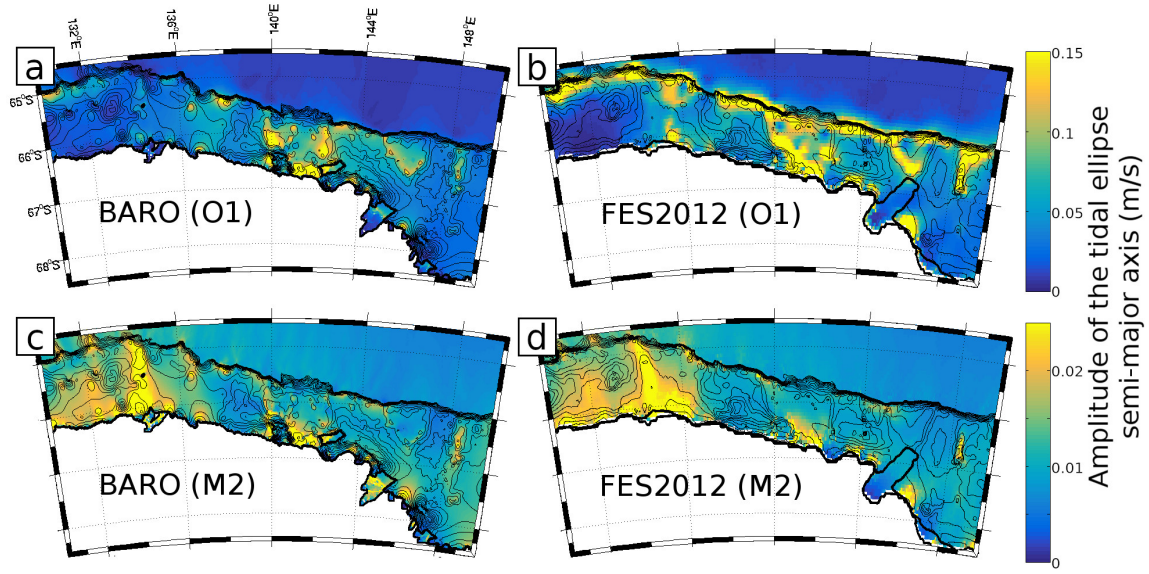

Figure 2.2: Amplitude of the semi-major axis of the tidal current ellipse for constituents O1 (panels a and b) and M2 (panels c and d) as simulated in BARO experiment (a and c) and in FES2012 solution (b and d). Note the different color scale for O1 and M2. The thick black line represents coastline or ice shelf grounding line/edge. The thin black lines corresponds to the bathymetric contours plotted every 200 m between 0 and 1200 m. DB: Dibble Bank, AB: Adélie Bank, AD: Adélie Depression, MB: Mertz Bank, ND: Ninnis Depression, NB: Ninnis Bank.

2.4 Model evaluation

2.4.1 Sea ice

In order to evaluate our simulation, two sea ice concentration datasets are used: the OSI450 (Lavergne et al., 2019) and ASI-SSMI products (Spreen et al., 2008; Kaleschke et al., 2001). The two datasets have different resolutions: 12.5 km for ASI-SSMI and 25 km for OSI450. We compare the simulated sea ice concentrations in REF with these satellite products over 2010-2015 (Figure 2.3). The simulated and observed sea ice extents in summer (January, February, March) are limited to the continental shelf (south of 65°S). The model represents the spatial distribution of sea ice concentration reasonably well but tends to underestimate the summer sea ice cover. It can be noted that a peninsula is present in the western part of the domain in ASI-SSMI, but not in the bathymetry and icescape dataset used for the model. LANDSAT-8 images covering 2010-2015 (Supplementary Figure 6.1) reveal that there is no such peninsula or ice tongue during our simulated period, but rather a large number of small grounded icebergs and associated landfast ice. The simulated sea ice extent in winter (May, June, July, August, September) is in good agreement with ASI-SSMI. Sea ice concentrations higher than 0.8 are found south of 64°S in both the model and observations and the average ice edge is located around 62°S. On

the continental shelf, our model tends to locally overestimate the sea ice concentration.

The temporal evolution of the total sea ice area as observed in OSI450 and ASI-SSMI and as simulated in REF is illustrated in panel E of Figure 2.3. The interannual variability of the total sea ice area is well captured by our model, with a correlation of 0.97 (significant at alpha = 5%) between REF and ASI-SSMI or OSI450. The absolute maximum of sea ice area is reached in both the model and observations in winter 2011, and the maximum high summer sea ice area observed in 2013 is also reproduced by the model. It can be noted that the interannual variability of sea ice area is large, with maximums ranging between 3.5×10^5 km^2 (in 2015) and 5×10^5 km^2 (in 2011).

To better evaluate the properties of the sea ice pack simulated in REF, we compare in Figure 2.4 the distribution of the normalized modeled sea ice concentration to the observations, i.e. as in Roach et al. (2018). The first thing to note is the discrepancy between the two observational datasets used: there is almost no weak sea ice (<10%) in ASI-SSMI compared to OSI-450 for all seasons, and a weaker amount of compact ice (>90%) in OSI-450 than in ASI-SSMI. The model shows high amounts of weak sea ice (<10%) in agreement with OSI-450 and also high amounts of compact ice (>90%), in agreement (but overestimating) the ASI-SSMI dataset. Overall, the modeled sea ice is either weak or compact, but intermediate sea ice concentrations (10-80%) are rare.

Thanks to the inclusions of grounded icebergs and to the modification of the sea ice rheology to account for its tensile strength, the model produces large areas of landfast ice and several polynyas. Landfast ice covers large portions of the continental shelf (Figure 2.5b). Patches of landfast ice form windward of grounded icebergs (on the Dibble, Adélie, Mertz, and Ninnis banks) or ice shelf tongues (Mertz and Ninnis Glaciers). The spatial distribution of landfast ice simulated by the model is in good agreement with the one described by Fraser et al. (2012). The largest difference between the model and Fraser's dataset is located on the eastern side of the D'Urville Sea: this is due to the calving of the Mertz Ice Tongue and the relocation of the B9B which blocked sea ice further upwind before 2010. The occurrence of polynyas (Figure 2.5a) closely matches the location of landfast ice patches. Six regions appear to be frequently free of sea ice during winter. They can be found on the lee side of the landfast ice patches. Only the Mertz Polynya is directly attached to the coast. Distinct processes might be at play for the formation of these polynyas, as suggested by Massom et al. (1998): the Mertz Polynya is driven by the katabatic winds while the other polynyas are forced by the prevailing easterly winds. The estimated and simulated amounts of sea ice produced in the polynyas off Adélie Land are indicated

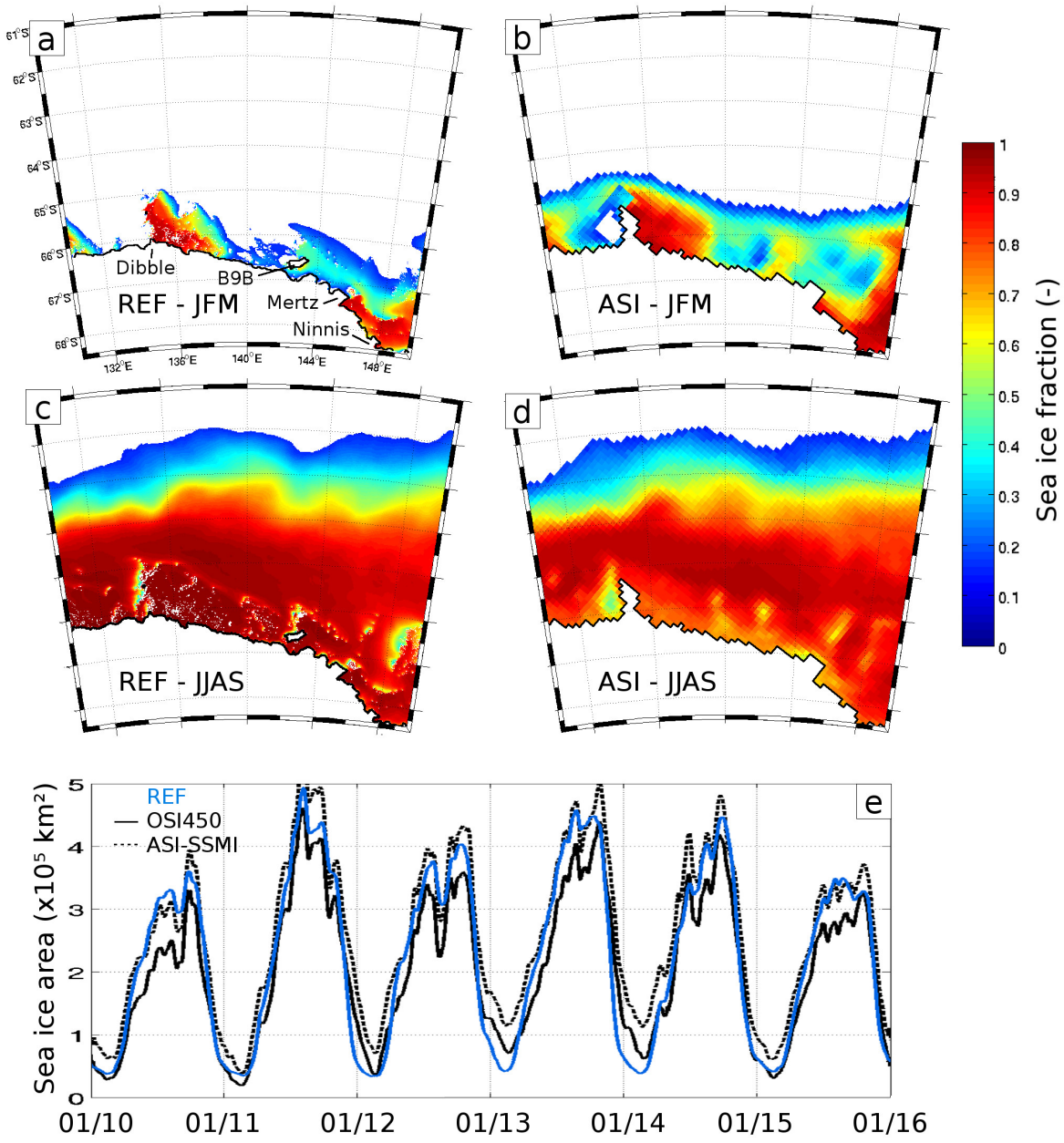

Figure 2.3: a-d: maps of sea ice concentration averaged on the 2010-2015 period. A and B: summer months (JFM) for REF and ASI-SSMI, respectively. (c) and (d): same as (a) and (b), but for winter months (JJASO). Sea ice concentrations below 15% have been removed in both the simulation and observational dataset. E: time series of total sea ice area (where sea ice concentration >15%) as simulated by REF and observed in OSI 450 (continuous line) and ASI-SSMI (dashed line).

in Table 2.2. We compare the simulated sea ice production to the estimates of Tamura et al. (2016). Tamura et al. (2016) combine an algorithm for the detection of thin sea ice from remotely sensed surface brightness temperature and the computation of surface heat loss using bulk formula and atmospheric reanalyses (NCEP-2 or ERA-Interim) to estimate sea ice production. The simulation underestimates the volume of sea

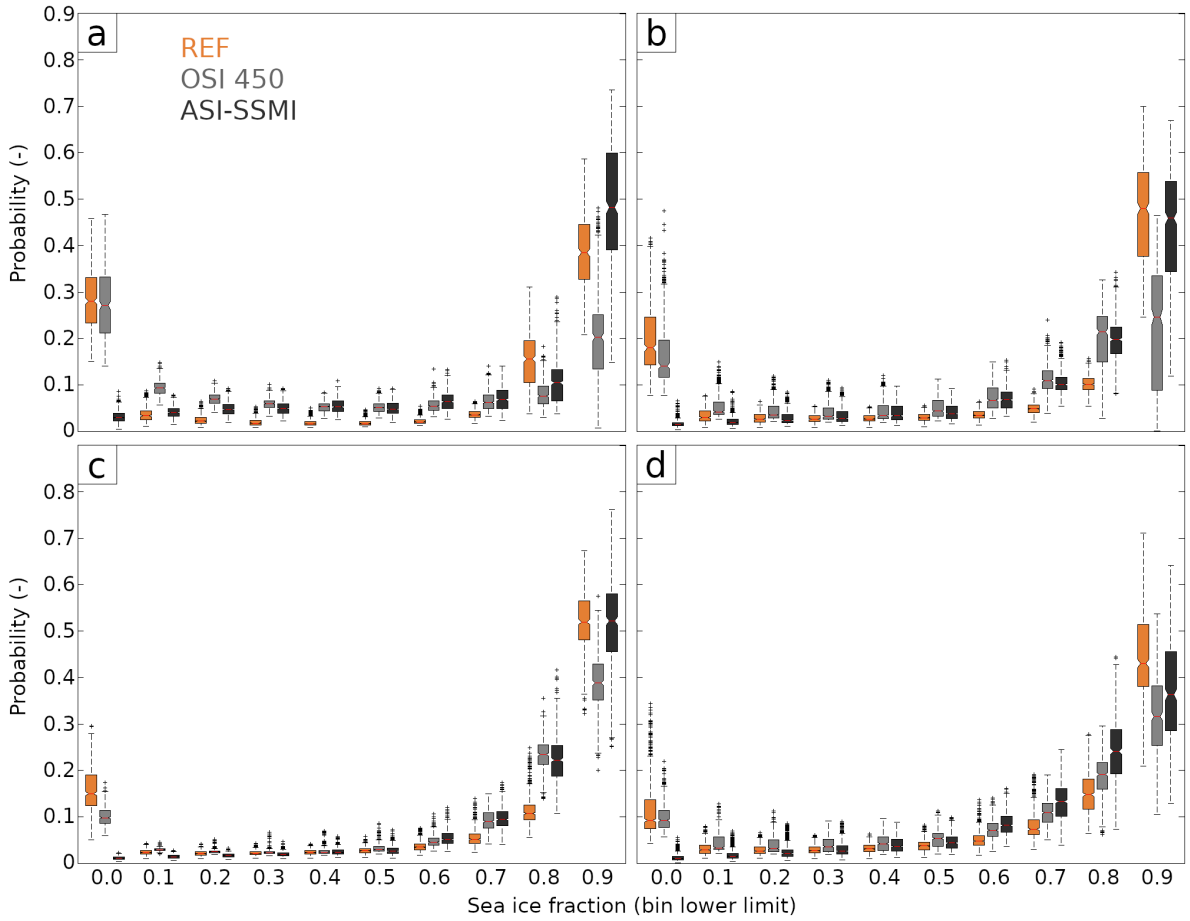

Figure 2.4: Distributions of the normalized sea ice concentration simulated in REF and observed in OSI-450 and ASI-SSMI for summer (a), fall (b), winter (c), and fall (d).

ice produced compared to Tamura et al. (2016), in particular, due to lower sea ice production in the Mertz Bank and Ninnis Bank polynyas (MBP and NBP) and to the absence of the polynya at 140^0 E. This might be due to a failure of the sea ice model to simulate certain polynyas, weak offshore winds, or to a potential overestimation of the sea ice production by Tamura et al. (2016), as they make the hypothesis that all the heat loss by the ocean is used for seawater freezing, and not to cool down the ocean. On the contrary, the model overestimates sea ice production in the Mertz and Ninnis Glacier polynyas.

2.4.2 Water masses

The simulated ocean properties on the continental shelf off Adélie Land are compared against CTD measurements from the World Ocean Database 2018 in Figure 2.6a,b. Only the measurements obtained after 2010 are taken into account as the simulation is performed with the post-calving ice shelf geometry (after the Mertz calving in 2010 and B9B relocation in 2011). The simulated temperatures are in good agreement with the observations down to 300 m, then the simulation exhibits a warm bias of 0.5°C.

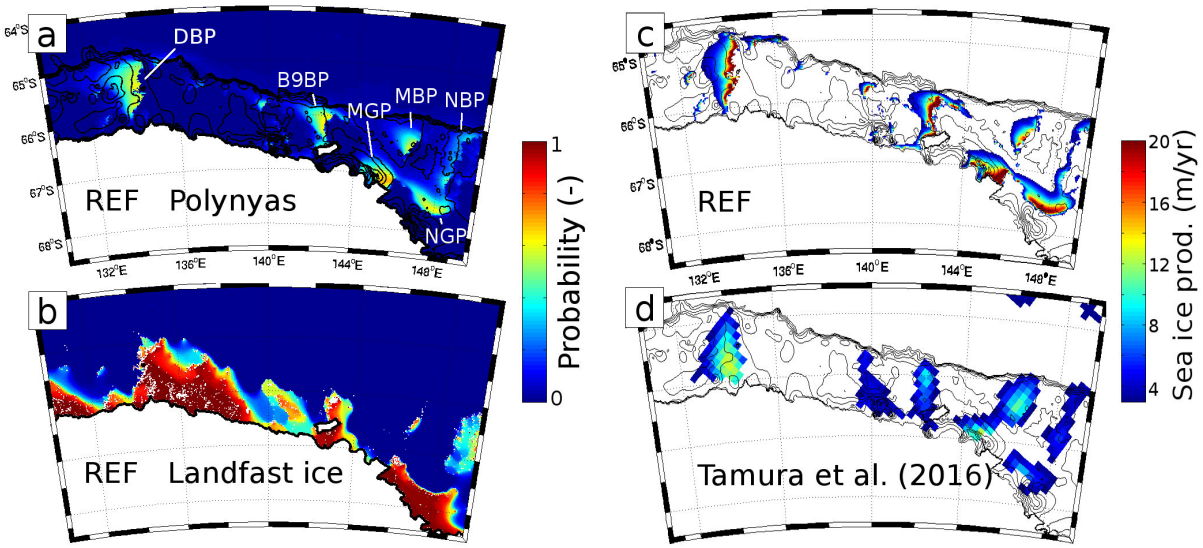

Figure 2.5: Polynya (a) and landfast ice probability (b) in REF simulation, averaged between 2010-2015. Polynyas are defined as an enclosed contour of sea ice with a concentration lower than 0.5 or a thickness lower than 0.2 m. Names of the polynyas: DBP: Dibble bank, B9BP: B9B iceberg, MGP: Mertz glacier, MBP: Mertz bank, NGP: Ninnis glacier, NBP: Ninnis bank. Landfast ice is defined as the sea ice with a two week-averaged velocity lower than 1 mm/s. Cumulated sea ice production (c) as simulated in REF and (d) estimated in Tamura et al. (2008) and Tamura et al. (2016) (using ERA-interim). Averaged between 2011 and 2013. Sea ice production rates lower than 3 m/yr have been masked. The simulated sea ice production rate is the sum of the freezing of open water and the growth of sea ice thinner than 0.2 m, as in Tamura et al. (2016).

Polynya	REF	Tamura et al. (2016)
DBP	72.10 ± 7.94	67.34 ± 4.48
B9BP	45.52 ± 1.75	38.94 ± 5.55
MGP	36.01 ± 1.99	14.55 ± 3.01
MBP	24.29 ± 3.01	36.69 ± 0.53
NGP	43.12 ± 3.97	31.50 ± 12.15
NBP	21.96 ± 1.05	36.78 ± 4.06
Shelf	337.73 ± 19.32	409.28 ± 41.69

Table 2.2: Yearly sea ice production (km^3) in the polynyas off Adélie Land (see Figure 2.5 for polynya locations) and over the entire continental shelf, as simulated in REF and as estimated by Tamura et al. (2016). Averaged between 2011 and 2013.

The simulated salinity is higher than the observed one in the top 200 m and slightly lower deeper in the water column.

The different water masses simulated in the d'Urville Sea are shown on the diagram of Figure 2.6c. Water masses can be divided into several poles with distinct properties. Antarctic surface water (AASW) corresponds to water with temperatures ranging from -1.7 to 1 °C and relatively low salinity. Winter Water (WW) is a relatively

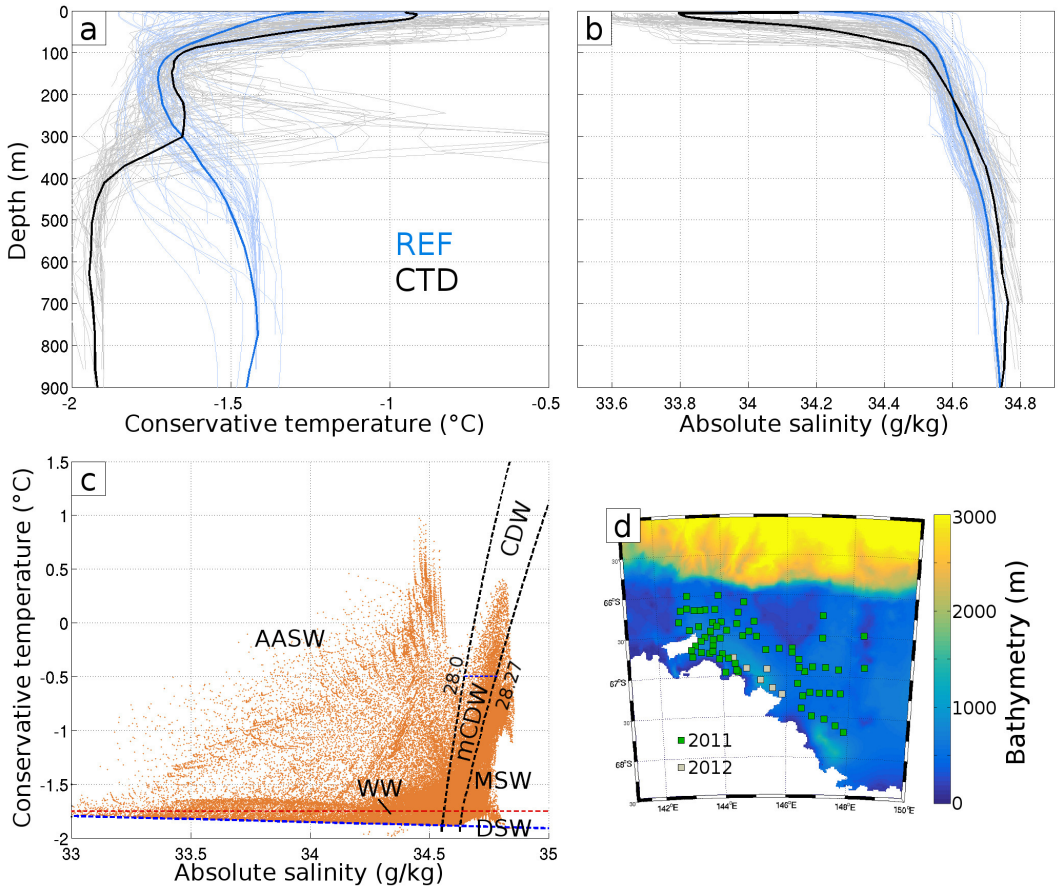

Figure 2.6: Vertical profiles of a) temperature and b) salinity on the continental shelves of Adélie Land. Black: CTD from the WOD18 database. Blue: as simulated in REF. Pale colors: individual profiles. Bright colors: basin average. Simulated profiles are taken at the same location and time as the CTD measurements. c) Temperature / salinity diagram on the continental shelf off Adélie Land as simulated in REF. Sampled between years 2010-2015. Dashed black contours: neutral density γ_n. Dashed blue line: surface freezing temperature. Dashed red line: temperature of -1.75°C. AASW: Antarctic Surface Water, WW: Winter Water, CDW: Circumpolar Deep Water, mCDW: modified CDW, DSW: Dense Shelf Water, MSW: Modified Shelf Water. d) locations of CTDs used in panels a) and b).

saline and cold (below -1.7°C) water mass, formed during the destratification in winter. Following Lacarra et al. (2014) and Whitworth III et al. (1998), we use the neutral density γ_n to discriminate the dense water masses. The pole of Circumpolar Deep Water (CDW) is defined as the water mass with γ_n between 28.0 and 28.27 kg/m^3, together with a relatively high temperature. We divide this pole into two water masses identified by their temperature: relatively pure CDW has a temperature above -0.5°C, while modified CDW (mCDW) is cooler. The densest WW forms the Dense Shelf Waters (DSW). We define Dense Shelf Water (DSW) as the water mass with $\gamma_n > 28.27$ kg/m^3 and a temperature below -1.75°C. Modified Shelf Water (MSW) is a water mass with $\gamma_n > 28.27$ kg/m^3 and a temperature above -1.75°C. We

also define the Shelf Waters (SW) as the water mass with $\gamma_n > 28.27$ kg/m^3 with no distinction on the temperature.

The volume of SW present in summer (January to March) in the WOA18 climatology (decade 2005-2017) is estimated to be 5.58×10^{12} m^3, with 3.95×10^{12} m^3 of DSW. In the REF simulation, there are 3.88×10^{12} m^3 of SW, which are made up of more than 90% of MSW (only 0.2×10^{12} m^3 of DSW). The DSW produced in winter in REF (see section 2.5.3) is quickly exported or converted in MSW after mixing with CDW. In addition, REF simulates frequent advection of MSW from the Mertz Trough into the Adélie Depression (Supplementary Figure 6.4). This MSW can fill the depressions as it is as dense as the simulated DSW. It is worth noting that the WOA18 climatology used here is built upon data from 2005 to 2017, thus incorporating measurements anterior to the 2010 calving and associated regime shift. Moreover, the simulated ocean had several years to adjust to the post-calving coastline and icescape thanks to the spin-up, while the actual ocean might still be adjusting to this event (CTD casts performed after 2015 suggest the replacement of some DSW by MSW in the Adélie Depression, see Supplementary Figure 6.3). The potential limitations emerging from this bias are presented and commented in Section 2.6.

2.4.3 Ice shelves

The averaged basal melt rate of the major ice shelves or icebergs off Adélie Land obtained in the REF simulation between years 2010 and 2015 are shown in Supplementary Figure 6.5 and compared to estimates of Rignot et al. (2013), Depoorter et al. (2013) and Adusumilli et al. (2020) (hereafter R13, D13 and A20 respectively) in Table 2.3. The simulated basal melt rates are lower than the estimates from R13 and D13 for the Dibble ice shelf and larger for the Mertz and Ninnis ice shelves. The simulated Mertz basal melt is however lower than the estimates of A20. The basal melt estimates of R13 and D13 were obtained using mostly data from the years 2000-2010. This limits direct comparison due to potential decadal variability. Moreover, the Mertz and Ninnis ice shelves have undergone drastic changes over the past decades. For instance, the Ninnis ice tongue calved in 2000 and the Mertz one in early 2010. These events had important repercussions for sea ice production, ocean circulation, and glacier dynamics, with possible consequences for the basal melt rates (Cougnon et al., 2017; Kusahara et al., 2017). Previous studies also suggested different basal melt rate values for these ice shelves: Berthier et al. (2003) and Rignot (2002) estimated the basal melt rate of the Mertz glacier to be 11 m/yr and 18 m/yr, respectively.

	REF					
	Avg.	Std.	Min. - Max.	R13	D13	A20
Dibble	3.08	0.94	1.82 - 4.04	5.5 ± 0.9	6.5 ± 2	-
Mertz	2.79	0.91	1.62 - 4.02	1.4 ± 0.6	0.8 ± 0.7	5.0 ± 2.4
Ninnis	3.35	1.09	2.10 - 4.52	1.2 ± 2	0 ± 1.5	-

Table 2.3: Basal melt rate (in m/yr) and its interannual standard deviation for major ice shelves as simulated in REF and as estimated from observations by Rignot et al. (2013), Depoorter et al. (2013) and Adusumilli et al. (2020) (R13, D13 and A20, respectively).

2.5 Sensitivity of ice, ocean and DSW to tides and ice shelves

2.5.1 Ice shelf melting induced by tides

In this section, we analyze the sensitivity to ocean–ice shelf interactions, which is in fact a sensitivity to the presence of an ice shelf cavity and the associated heat and freshwater fluxes (see Section 2.3). Tides and ocean–ice shelf interactions are closely linked processes, and part of their effects can arise from the interplay between each other. Therefore, we first evaluate the sensitivity of the basal melt of Adélie Land's ice shelves to tides.

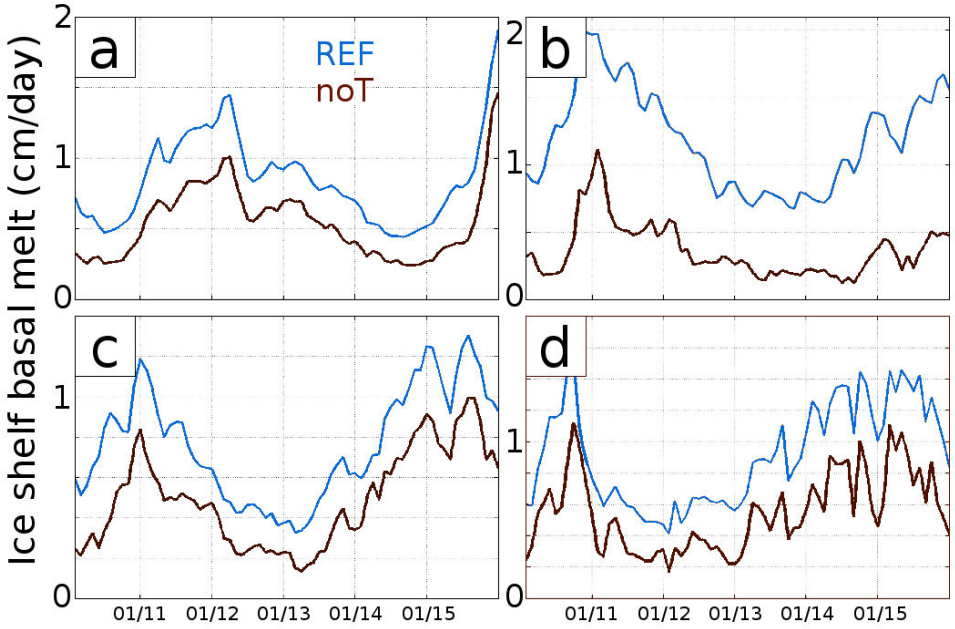

Figure 2.7: Monthly basal melt rate of the three largest ice shelves of Adélie Land and iceberg B9B. a: Dibble, b: B9B, c: Mertz and d: Ninnis. Dark red curve: without tides (noT), blue curve: with tides (REF).

Tides lead to an increase in ice shelf and iceberg basal melt rates (Figure 2.7). The relative increase in the basal melt is comparable between the three ice shelves (+62% for Dibble and Mertz and +72% for Ninnis). It reaches a much higher value of +250% for the B9B iceberg.

Tides can affect ice shelf basal melt through dynamical and thermodynamical effects (Jourdain et al., 2019). In the first case, tidal velocities enhance the turbulent heat flux at the ice-ocean interface. In the second case, tides induce changes in ocean temperature and salinity at the ice-ocean interface either through the mean tidal circulation or tidal mixing. In the simulations with ice shelves, the heat flux from the ocean to the ice shelf is computed as $\rho_w c_w \gamma_T (T - T_0)$, with ρ_w the density of seawater, c_w the specific heat of seawater, γ_T the transfer velocity, T the temperature of seawater and T_0 the freezing point of seawater computed at the depth of the ice shelf and using the salinity S_b at the ice-ocean interface (following Jenkins (1991)). Here, we define the tidal dynamical forcing as the difference in γ_T and the tidal thermal forcing as the difference in the term $T - T_0$ between simulations REF and noT. The two contributions are illustrated in the maps of Figure 2.8. Tides increase γ_T over most of the ice shelves (Figures 2.8b and 2.8d). γ_T is twice as large in REF than in noT for the Mertz, Ninnis, and Dibble ice shelves. Even larger changes are observed beneath the B9B iceberg, where γ_T is increased by a factor of 5. This strong sensitivity to tides arises from the large amplitude of tidal velocities found beneath B9B (Figure 2.2 and also Supplementary Figure 6.2). The thermal effect of tides (Figures 2.8a and 2.8c) partly compensates for the dynamical forcing, likely because more dynamically induced melting tends to cool the top boundary layer beneath ice shelves (Jourdain et al., 2019). The ice shelves indeed undergo a decreased thermal forcing in the presence of tides, with variable magnitude: almost null for Ninnis, less than 50% decrease for Mertz and Dibble, and slightly above 50% for the B9B, which may be related to the strength of the dynamical tidal forcing beneath the B9B.

2.5.2 Effect of tides and ocean–ice shelf interactions on the modeled ocean mean state

The ocean mean state, the mean circulation, and the mean sea ice production simulated in REF are shown in Figure 2.9. Relatively warm and saline mCDW occupies the northernmost part of the continental shelf, on the east of the Mertz and Ninnis banks. Cooler and relatively fresher water masses are found along the coast, in the southwestern half of the Adélie Depression and west of the Adélie Bank. The mean ocean circulation on the continental shelf consists of a westward current crossing the Adélie Depression from the east to the northwest. This current forms

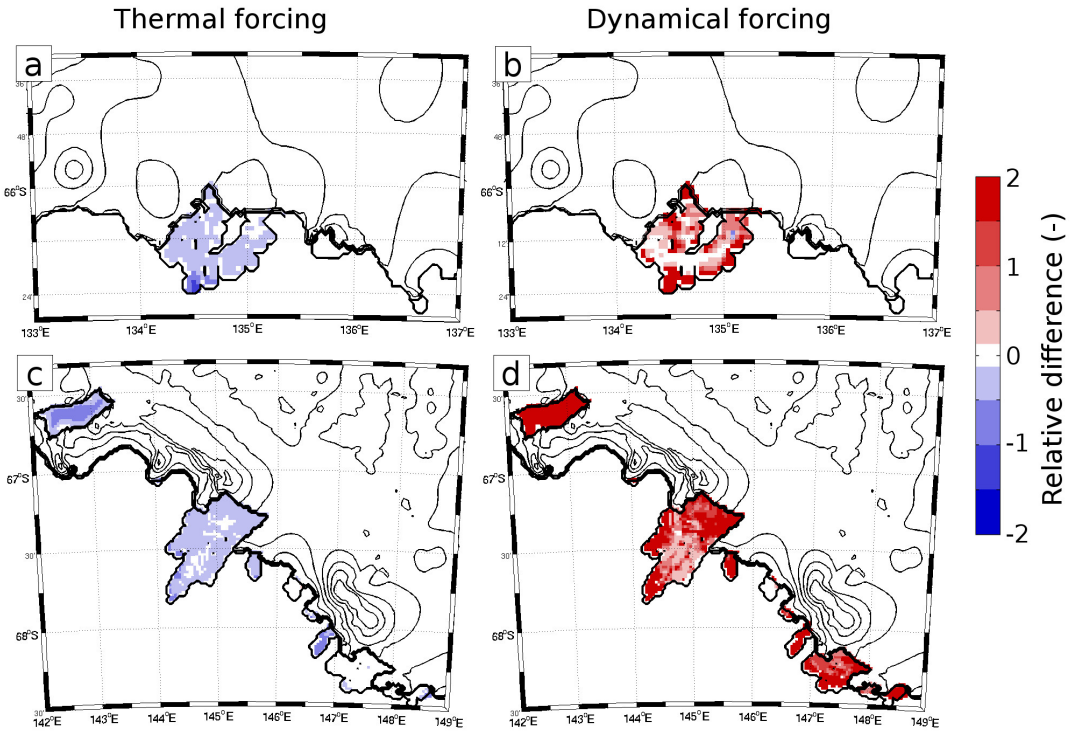

Figure 2.8: a and c: relative changes in thermal forcing at the ice shelf base between REF and noT $R_{th} = \frac{(T-T_0)_{REF}-(T-T_0)_{noT}}{(T-T_0)_{noT}}$. b and d: relative difference in ocean–ice shelf heat transfer velocity between REF and noT $R_{dyn} = \frac{(\gamma_{TREF}-\gamma_{TnoT})}{\gamma_{TnoT}}$. Dibble: a and b: B9B, Mertz and Ninnis: c and d. Averaged between 2013 and 2015.

east of the Mertz Sill, from the confluence of a cold and fresh coastal current from the south and the inflow of CDW from the north. This confluence leads to the sporadic inflow of mCDW into the Adélie Depression (intrusions of mCDW from the east were suggested by Snow et al. (2016) and Martin et al. (2017)).

As tides substantially influence ocean–ice shelf interactions, it can be of interest to differentiate the individual effect of each process and the effect of the interactions between tides and ice shelves. To isolate the effect of ocean–ice shelf interactions, we compute the differences between the simulations noT and noA (respectively noI and noA for the effect of tides). The effect of the interactions between tides and ice shelf (namely the tide-induced basal melt increase, hereafter tides–ice shelf interactions) can be obtained by subtracting the combination of the effects of tides and ocean–ice shelf interactions considered separately, namely noI-noA and noT-noA, to the total effect REF-noA.

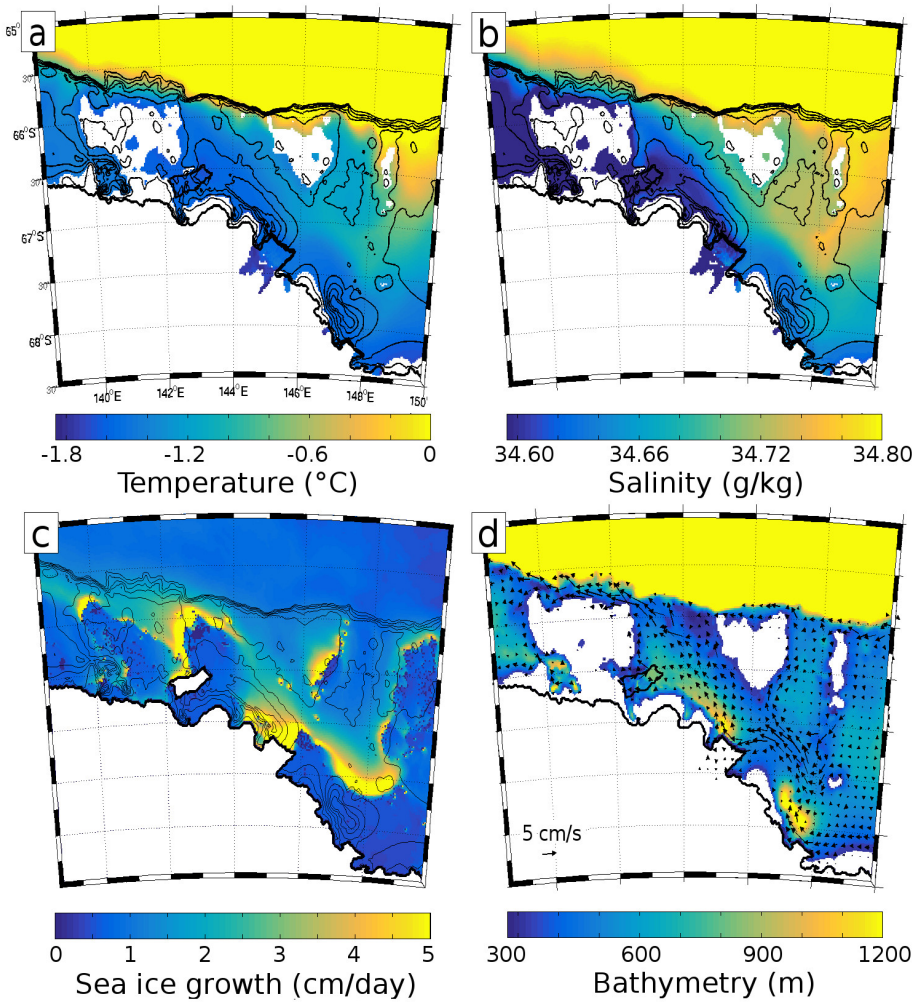

Figure 2.9: Mean state (2010-2015 averaged) of the ocean temperature (a), salinity (b) and ocean velocity (d) at 300 m depth simulated in REF. Average sea ice production during March-October simulated in REF (c). Bathymetry is indicated as black contours every 200 m in (a),(b),(c) and as color shading in (d).

To understand how ice shelf basal melt and tides affect the water column, we investigate the differences in ocean temperature and salinity between the sensitivity experiments as a function of depth along Section 1 of Figure 3.1. Results are displayed in Figure 2.10. This section is roughly parallel to the coastline and follows the mean westward current (see Figure 2.9). In simulation REF, the current first encounters the Ninnis ice shelf in the Ninnis Depression, where the ocean undergoes a first cooling and freshening. At the Mertz Sill, the confluence with the current from the northeast carrying CDW induces slight warming. A second cooling and freshening occur after passing by the Mertz ice shelf.

The influence of ocean–ice shelf interactions on the water column is illustrated on panels (b) and (g) of Figure 2.10. A subsurface cooling and freshening take place in the lee of the ice shelves (-0.1°C and -0.02 g/kg after Ninnis, -0.2°C and -0.05 g/kg after

Mertz and B9B). This signal is located at the depth of the ice shelf base (around 500 m for Ninnis, 400 m for Mertz, and 300 m for B9B). An opposite effect (warming and salinity increase) takes place in the top 200 m in the Adélie Depression. Tides (panels c and h of Figure 2.10) lead to a slight cooling below 200 m and a rise in salinity in the top 200 m of the Adélie Depression. The salinity and temperature anomalies described previously are also present with a stronger magnitude when both tides and ocean–ice shelf interactions are present (Figure 2.10d, i). The interactions between tides and ice shelves (Figure 2.10e, j) are computed following the methodology described in the previous paragraph. They further intensify the effect of the ice shelves on the ocean. The results presented here are also shown as maps in Supplementary Figures 6.7, 6.8 and 6.9.

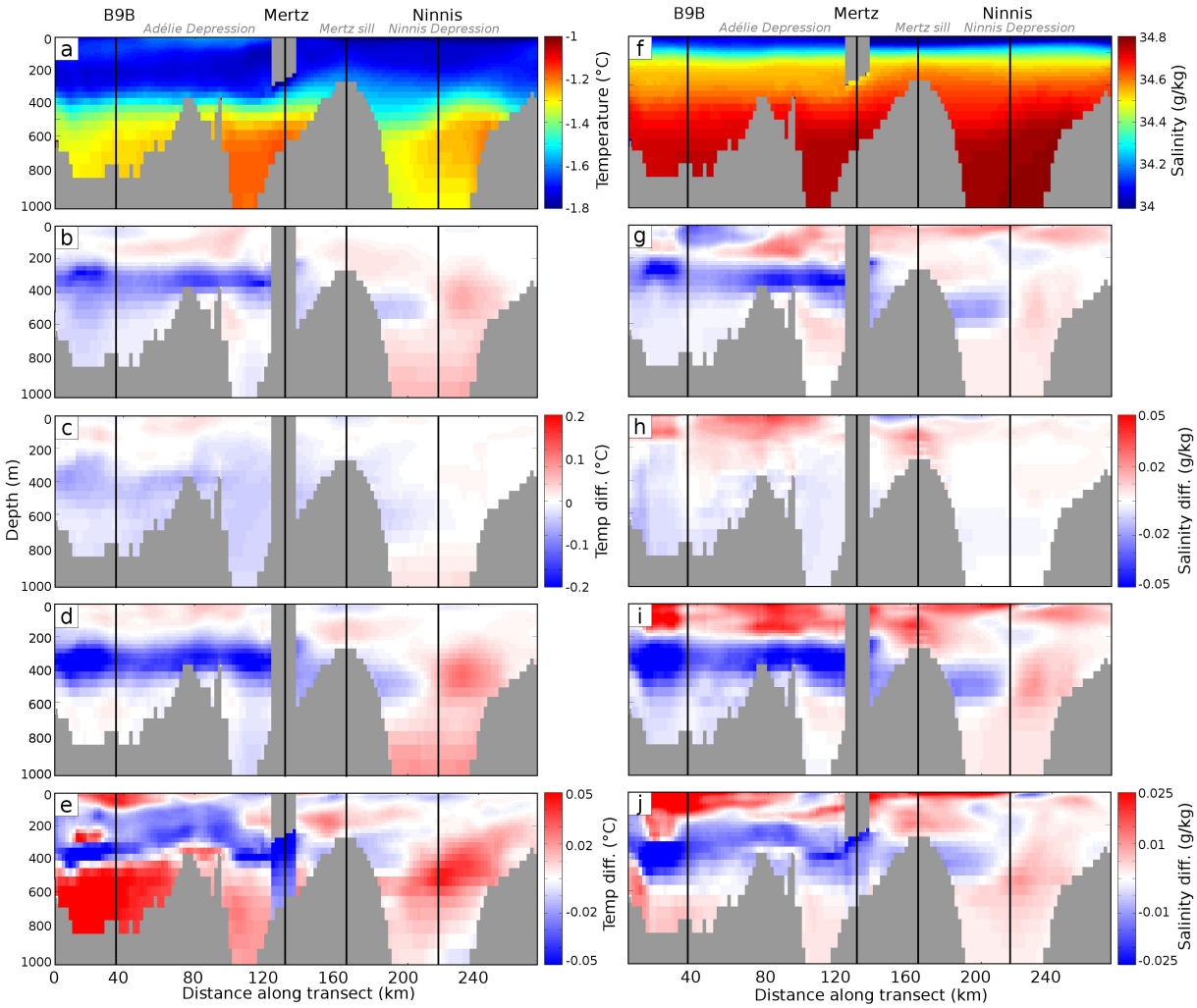

Figure 2.10: Averaged ocean temperature along section 1 of Figure 3.1 (from west to east). a) REF simulation, b) noT - noA, c) noI - noA, d) REF - noA, e) effect of tide–ice shelf interactions $REF - noA - (noI - noA + noT - noA)$) f) - j): same as a) - e) but for ocean salinity. Note the change in the color axis for panels e) and f). Black lines indicate the locations of ice shelves or the Mertz Sill.

2.5.3 Water mass transport and production of dense water

Dense water production and interannual variability

The temporal evolution of the salinity in the water column of each polynya simulated in REF is illustrated in Figure 2.11. Freshwater occupies the top of the water column in summer. As the surface salinity rises in response to sea ice formation, the water column destratifies. Eventually, the salinity becomes high enough to enable the production of dense water (DSW, potentially converted into MSW after mixing with CDW), suggested by the rise of the 28.27 kg/m^3 neutral density contour. Surface waters reach the dense water state almost every year in the MBP and NGP (Figure 2.11c,f), except for the year 2010 (and 2014 for the NGP). Despite the important sea ice growth rates in the MGP and B9BP, surface waters only reach the dense water state in 2012. The summer surface salinity is much lower in these two polynyas than in the three others, which can be one of the reasons for the limited dense water formation. Even if the surface water γ_n does not reach the dense water state, the γ_n=28.27 kg/m^3 contour shoals by 50 to 100 m in summer or late winter in the MGP and NBP. This indicates that dense water production is still possible thanks to mixing at the base of the mixed layer.

The interannual variability of sea ice production in the polynyas is displayed in panel a) of Figure 2.11. This variability explains an important part of the year-to-year difference in wintertime convection. Large volumes of sea ice are created in 2013 for the NBP, MBP, and MGP. During this year, surface water density reaches the density threshold in these polynyas. Similarly, 2010 is a year of low sea ice production for most of the polynyas, and the surface salinity remains below the dense water threshold. However, low sea ice production does not necessarily mean that dense water formation is not possible. In 2015, the sea ice production is particularly low for the NBP and NGP, but both polynyas form surface water with $\gamma_n > 27.28$ kg/m^3. In the same way, the high sea surface salinities reached in 2012 in the MGP and B9BP are not associated with particularly large volumes of sea ice being created in these polynyas. Another potentially important factor is the summer salinity which tends to be higher than average in these two polynyas before the 2012 convection event.

Sensitivity of dense water to tides and ocean–ice shelf interactions

Sea ice production plays a central role in the formation of dense water. Despite the changes in the mean ocean temperature and salinity described previously, the presence of tides and ocean–ice shelf interactions do not significantly affect the sea ice growth off Adélie Land (see Supplementary Figure 6.7). Changes in sea ice growth rates induced by tides and ocean–ice shelf interactions can locally increase or decrease

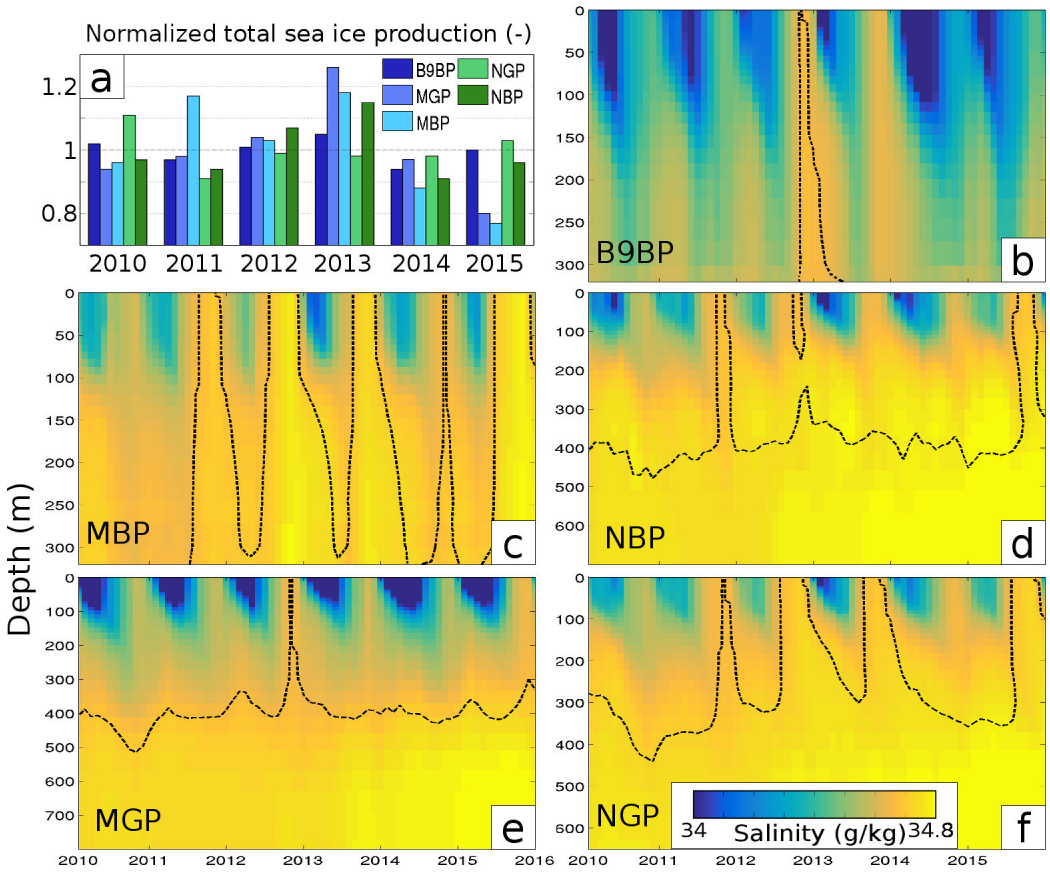

Figure 2.11: (a) Normalized total sea ice production in the polynyas off Adélie Land (refer to Figure 2.5 for polynya locations). Temporal evolution of the water column salinity simulated in REF for the B9BP (b), MBP (c), NBP (d), MGP (e) and NGP (f). Dashed black line represents $\gamma_n = 28.27$ kg/m^3 (used to define MSW and DSW).

sea ice production by up to 20%, but these differences compensate each other and are not sufficient to significantly impact the cumulated sea ice production in the polynyas (not shown).

To assess the sensitivity of the water masses budget off Adélie Land to tides and ocean–ice shelf interactions, we compute the transport budget of each water mass across the limits of the polynyas (the water masses used for this computation are those defined in Figure 2.6c). Following the methodology of Cougnon et al. (2013), we define the transport budget of a water mass as the difference between the inflow and the outflow of water with the properties of the considered water mass across the boundaries of the polynya. A positive transport budget indicates that the water mass is being exported out of the box (draining the volume of water mass which was either produced or stored in the box), and a negative one indicates either the storage or the destruction of the water mass in the box. Results for each polynya and each simulation are gathered in Figure 2.12.

In REF, pure CDW is imported in NGP, MBP, and NBP (panels c, d, and e of Figure 2.12, respectively). This CDW is potentially transformed in-situ and exported as mCDW, which can later feed the MGP. Winter Water is exported out of B9BP and MGP (panels a and b of Figure 2.12) but has a negative budget in NGP and NBP. The budget of WW in MBP is null, suggesting its direct transformation into other water masses. DSW is exported from MBP, with secondary sources in NBP and MGP. The other type of dense water, namely MSW, is formed in the MBP and NBP after the mixing of local DSW with intruding CDW. MSW is later exported and stored or consumed in MGP or B9BP.

In the B9BP, MSW has a negative budget in the REF simulation, but not in the other simulations. REF also shows higher export of lighter water masses such as mCDW and AASW than the simulations without tides and/or ocean–ice shelf interactions. REF stands out from the other simulation, indicating that the effect of the interplay between tides and ocean–ice shelf interactions overcomes the effect of each process taken individually. It can still be noted that noI (tides but no ocean–ice shelf interactions) and REF show little difference for the outflow of mCDW and WW, suggesting that tides significantly contribute to these exchanges. In MGP, the simulations with ocean–ice shelf interactions strongly differ from the two others. The import of MSW and mCDW and the export of AASW and WW only takes place in REF and noT. While the water mass transport budget shares the same sign between these two simulations, rates of export (or import) are higher in REF than in noT. This is in accordance with the intensification of the effect of ocean–ice shelf interactions by tides described earlier. The export of MSW in NGP is highly reduced in both simulations representing ocean–ice shelf interactions. Tides alone (noI) appear to inhibit the outflow of mCDW and the inflow of CDW. The effect of tides on mCDW is compensated when ocean–ice shelf interactions are also accounted for. The water mass transport budget in MBP and NBP are almost unaffected by ocean–ice shelf interactions. This could be expected by their relatively remote location from the ice shelves. When tides are absent (noT and noA), more CDW and WW are imported and the export of mCDW and MSW are slightly increased for MBP.

Tides and ocean–ice shelf interactions affect the water masses transport budget in different ways from one polynya to the other. In the B9B, the effect of ice shelves is weak in the absence of tides but becomes significant when both processes are taken into account. Ocean–ice shelf interactions have an important effect on the water mass transport budget in MGP, and this effect is strengthened when tides are accounted for. In NGP, tides and ocean–ice shelf interactions have independent effects which add up when both processes are considered. This analysis illustrates that ocean–ice

shelf interactions induce a net decrease of the export of dense waters out of the B9BP, NGP, and MGP and that tides amplify this effect in B9BP and MGP. Ice shelf melting appears to favor the inflow of mCDW, CDW, or MSW and to increase the outflow of WW or AASW. The budget of shelf water (DSW and MSW) cumulated over all polynyas is almost null in REF (6.89 mSv), and amounts to 80.1, 62.10, and 73.26 mSv in noI, noT, and noA, respectively. These results suggest that ocean–ice shelf interactions can limit the production of dense water or favor its transformation into lighter water masses (referred hereafter as dense water consumption).

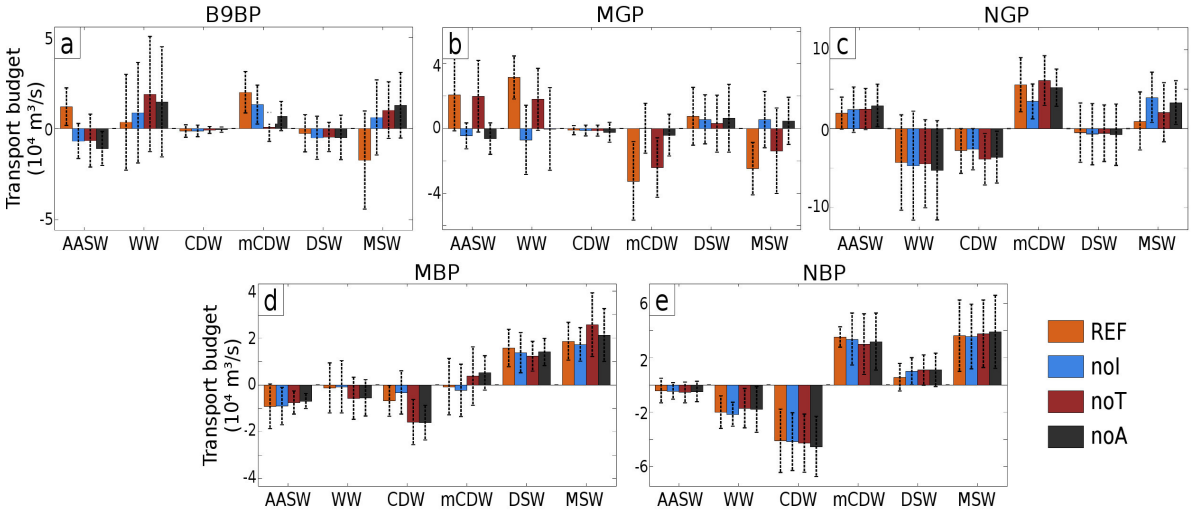

Figure 2.12: Mean yearly water mass transport budget in the B9BP (a), MGP (b), NGP (c), MBP (d) and NBP (e) simulated in REF and in the sensitivity experiments. Positive transport budget rates indicates net export. Black dashed lines indicate interannual standard deviation. Refer to Figure 2.5a for polynya locations and Figure 2.6c for water mass definitions.

The influence of ocean–ice shelf interactions on dense water can be separated into two distinct contributions. First, water masses are directly transformed inside the ice shelf cavity, either by mixing or by the heat and freshwater fluxes at the ice-ocean interface. Then, the water mass transformations can also be modified outside the cavity due to the changes in the water column properties (as described in Figure 2.10). To understand how ocean–ice shelf interactions impact the volume of dense water, we compute the water mass transport budget for ice shelf cavities. The average transport budgets in temperature and salinity space are shown in Figure 2.13 for the B9B iceberg and Mertz and Ninnis ice shelves. The temperature/salinity diagram is divided into intervals of temperature and salinity with bin widths of 0.08°C and 0.05 g/kg, respectively.

The water mass transport budget beneath the ice shelves consists of the import of mCDW and MSW (and lower amount of WW or AASW) and the export of a fresher

and cooler water mass. MSW is imported into the three cavities, while mCDW is only entering the Mertz ice shelf cavity. The water masses outflowing from the ice shelf cavities have the properties of high salinity AASW, mCDW, or WW for the B9B and Mertz, and MSW or mCDW for Ninnis. In REF, the average cooling amounts to 0.17°C for B9B and 0.11°C for Mertz and Ninnis, while the water masses are freshened by 0.12, 0.05, and 0.03 g/kg respectively. A small amount of DSW can also be imported into the Mertz and Ninnis cavities. The basal melt of ice shelves acts as a positive buoyancy flux as it reduces the density of the inflowing water masses, leaving the freshening signature observed in the Adélie Depression (see Figure 2.10). The total import is higher in the presence of tides, as ice shelf basal melt is higher. REF exhibits an increase in the basal melt-driven inflow of 45% for B9B, 21% for Mertz, and 16% for Ninnis with respect to noT. On average, dense water inflow and potential transformation beneath ice shelf cavities amount to 9.2 (6.7) mSv in B9BP, 28.6 (22.2) mSv in MGP, and 24.4 (11.1) mSv in NGP in REF (respectively noT).

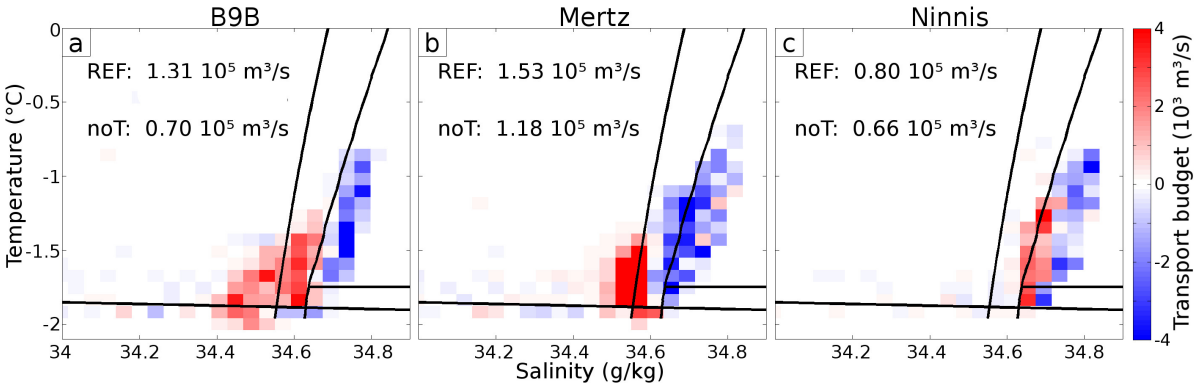

Figure 2.13: Transport budget (difference between inflow and outflow) under the ice shelves calculated for REF simulation using bin widths of 0.08°C and 0.05 g/kg for temperature and salinity, respectively. B9B iceberg (a), Mertz ice shelf (b) and Ninnis ice shelf (c) as simulated in REF. Positive transport budget indicates net export. Black numbers represent the overturning rate in REF and noT computed as the volume of water being imported in the cavity. Black contours indicate neutral density 28.0 kg/m^3 (left) and 28.27 kg/m^3 (right). Bottom black lines indicate freezing point of surface temperature and T=-1.75°C.

The changes in the water column properties or ocean circulation due to ocean–ice shelf interactions may affect the formation of DSW outside the cavities. To investigate this effect, the water mass transport budgets were computed in boxes 1, 2, and 5 (Figure 3.1) reshaped to exclude the ice shelves. In this way, we ensure that the water mass transformations accounted for are only the ones happening in the polynyas. The yearly transport budgets of dense water (DSW and MSW) are displayed in Figure 2.14.

When considering only the polynyas (and not the processes happening beneath the ice shelf cavities), the transport budget of dense water simulated in REF is almost null in B9BP, and a net export is found for MGP and NGP. In the B9BP, only noI shows a significant departure from REF, with an important inflow of dense water. As noT does not differ from noA, this indicates that ocean–ice shelf interactions alone have little impact. However, since REF includes tides and its dense water transport budget is almost null, it appears that the effect of the tide-induced basal melt counteracts the effect of tides alone. Dense water exports from the MGP are the lowest in REF and noT, i.e., when ocean–ice shelf interactions are present. REF shows a lower export than noT, indicating that the intensification of the effect of ice shelf basal melt by tides exceeds the slight positive effect of tides alone (noI vs noA). On the contrary, in the NGP, the dense water export in REF shows no difference with noA, indicating a compensation of the negative effect of ocean–ice shelf interactions (noT vs noA) by the positive effect of tides (noI vs noA).

Overall, the remote effect of ocean–ice shelf interactions slightly reduces dense water export from MGP and NGP. The water mass transport budget showed larger sensitivity to ocean–ice shelf interactions when the ice shelf cavities were included in the boxes used for the diagnostic. This indicates that most of the effect of ocean–ice shelf interactions on dense water transport budget takes place inside the ice shelf cavities.

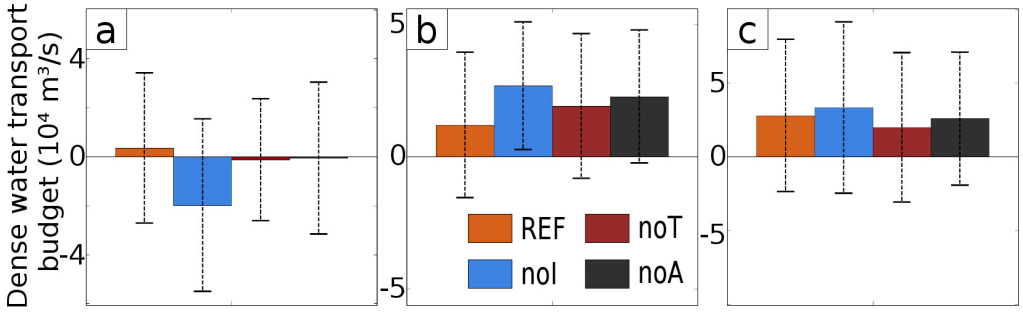

Figure 2.14: Yearly transport budget of dense water (DSW and MSW) in the B9BP (a), MGP (b) and NGP (c) adapted to exclude the under ice shelf cavities. Positive transport budget indicates net export. Black lines indicate the interannual standard deviation.

2.6 Discussion

The production of DSW off Adélie Land has undergone an important decline after the calving of the Mertz Ice Tongue in 2010 (Lacarra et al., 2014; Snow et al., 2018). While the diminution of sea ice growth is most likely the first driver of this decrease,

the potential role of other processes is not well understood. In this study, we tested the hypothesis that ocean–ice shelf interactions and tides can modify the water mass budget and the export of dense water. We show that ocean–ice shelf interactions destratify the upper 500 m of the water column, leaving a fresh and cold anomaly between depths of 200 and 500 m and a warming and salinity increase in the top 200 m. This effect is enhanced in the presence of tides, in response to higher ice shelf basal melt. Ocean–ice shelf interactions lower the volume of dense water off Adélie Land in two ways: through the conversion of dense water into water masses with intermediate density in the ice shelf cavities and by limiting the export of dense water out of the polynyas.

The basal melt of the ice shelves off Adélie Land is found to be highly sensitive to tides, with a positive dynamical forcing partly compensated by a negative thermal one. This sensitivity arises from the relatively high magnitude of tidal velocities in the region (especially for the B9B). Such results were already obtained in previous studies such as Jourdain et al. (2019) for West Antarctica and Hausmann et al. (2020) for the Ronne ice shelf. However, our results indicate that tides considered alone have little impact on the ocean and sea ice in the eastern D'Urville Sea. Stewart et al. (2018) suggested that tides play an important role in the intrusions of CDW onto the continental shelves. They showed, however, that this effect was highly variable from one place to the other and can be absent from several portions of the Antarctic continental shelf break. In our simulations, tides favor the cross-shelf intrusions of CDW west of the Adélie Bank (west of 140°E) but have little impact over the section studied here (between 140°E-150°E). Most of the effect of tides for the eastern D'Urville Sea resides in their interactions with ice shelves. An important implication of this result is that tides strongly amplify the effect of ocean–ice shelf interactions. The role played by tides in the coastal seas of Antarctica might thus have been overlooked in previous studies where ocean–ice shelf interactions were not considered.

Ice shelf–ocean interactions lower the export of dense waters (MSW or DSW) out of the polynyas of Adélie Land. While this result is in accordance with several previous studies (Cougnon et al., 2013; De Lavergne et al., 2014; Silvano et al., 2018), the mechanism being involved seems different in our simulations. These authors indeed argued that the input of fresh water led to a lowering of the maximum density of the winter water. In our simulations, this process seems to take place in the MGP, but not in the NGP and B9BP. A potential explanation for this difference is the rise in the salinity of the top 200 m of the ocean induced by ocean–ice shelf interactions. A similar increase in near-surface salinity was obtained by Mathiot et al.

(2017) and was attributed to the upwelling of mCDW or SW by the basal-melt-driven overturning. In our simulations, the principal factor for the decline in dense water formation appears to be the conversion of those dense waters (especially MSW) into lighter water masses at the ice shelf–ocean interface. We demonstrated here that ice shelf-induced conversion of dense water can substantially affect the dense water budget off Adélie Land. This illustrates the importance of representing under ice shelf cavities in climate models. Another approach consists of applying the freshwater flux from the ice shelf in the subsurface, to mimic the effect of the cavities without explicitly representing them. This methodology, proposed by Mathiot et al. (2017) is for instance used in some CMIP6 models (Storkey et al., 2018; Lurton et al., 2020) and might be able to reproduce the effect of the ocean–ice shelf interactions on dense water.

The influence of ocean–ice shelf interactions on the dense water export off Adélie Land confirms the hypothesis that changes in basal melt could be one of the driving mechanisms for dense water production variability. As mentioned earlier, the volume and density of dense water produced in Adélie Land underwent a significant decline following the Mertz calving and B9B relocation (Lacarra et al., 2014; Snow et al., 2016; Aoki et al., 2017). While the observed changes in sea ice production estimated by Tamura et al. (2012) are certainly the main driver of these modifications, we advocate that other processes might also be involved, such as changes in ice shelf basal melt. Modeling studies of Kusahara et al. (2017) and Cougnon et al. (2017) (hereafter K17 and C17) proposed a distinct response to the calving: K17 suggested a decrease in the Mertz basal melt, while C17 advocated the opposite. In our work, only the post-calving scenario is considered, but it can complement the two aforementioned studies. Both C17 and K17 found an increase in mCDW intrusions east of the Mertz Sill (east of 146°E), which lead to a warming in the Adélie depression in C17 but not in K17. K17 and C17 both represent ocean–ice shelf interactions, but only the model of C17 incorporates tides and a velocity dependant basal melt parameterization (similarly to our model). Another difference is the bathymetry and ice draft dataset used in these studies. The K17 model does not include the recent measurements of Beaman et al. (2011), and their ice shelf drafts show important differences with the recent dataset used in this study or in C17, especially for the Mertz ice shelf. The mean ocean state simulated here resembles the post-calving state of C17, especially considering the intrusions of mCDW in the Adélie depression. Our results seem to support the finding of C17, namely an increase in ice shelf basal melt, but this must be regarded with caution knowing the uncertainties that remain about the ice shelf draft and bathymetry of the region. The actual changes in ice shelf basal melt post-calving remain to be supported by observations. Under the hypothesis that the basal melt of the Mertz ice shelf increased following the calving, our results suggest that this might

be one of the reasons for the dense water production decrease.

The present study faces some limitations. The first one resides in the properties of the water masses simulated in the Adélie Depression. As depicted in Figure 2.6, our simulations exhibit a warm bias of 0.5°C with respect to in-situ CTD casts there. The presence of MSW instead of DSW in the deep Adélie Shelf Sea can affect the ice shelf basal melt and its effect on the SW production. In presence of colder DSW, the basal melt should be weakened, which could reduce the effect of the ocean–ice shelf interactions on the consumption of SW. The interannual variability of the simulated ice shelf melt can be used to explore the sensitivity of the ice shelf melt to the ocean forcing, and the impact on water masses. The basal melt of the ice shelves is 140% lower during the years 2008, 2009, and 2012 (1.37 Gt/yr for the Mertz in REF) than during the years 2010, 2014, and 2015 (3.32 Gt/yr for the Mertz). This is most likely due to the thermal forcing of the ocean since the averaged temperature in the cavity is below -1.7°C during years of low basal melt rate (Supplementary Figure 6.10a). During these periods, the basal melt-driven consumption of SW simulated in REF is 160% lower than during the periods of intense basal melt (Supplementary Figure 6.10b). The transformations of SW inside the cavity seem to be highly sensitive to the basal melt rate. Another effect of the presence of MSW instead of DSW is linked to the non-linearities of the seawater equation of state. The transformation of DSW by ocean–ice shelf interactions can be estimated to be 30% higher than the transformation of MSW for a similar basal melt rate (see Supplementary Figure 6.10c), due to the increase in seawater density with decreasing temperature. Additionally, the warm anomaly can limit the sea ice growth as the mixed layer deepens during winter, potentially responsible for the low sea ice production rate in MBP and NBP.

This warm bias might be induced by the mean circulation simulated by our model: the westward current crossing the Mertz Sill and Adélie Depression carries a large amount of relatively warm mCDW. Such intrusions of mCDW have been suggested by Snow et al. (2016) and Martin et al. (2017) before the calving, but the amount of mCDW entering the Adélie Depression through the Mertz Sill is unknown in the current state. Summer observations, however, indicate intrusions of CDW east of the Mertz Sill (Aoki et al., 2017), without entering the Adélie Depression. Understanding the driving mechanism of the CDW intrusions east of the Adélie Depression is beyond the scope of this study. It also appears that the destratification in the Adélie Depression remains incomplete by the end of winter. One could expect to obtain different ocean–ice shelf interactions and impact on polynyas if the stratification is entirely eroded each winter. One potential cause resides in the atmospheric forcing resolution: despite the relatively high resolution of the ERA5 dataset (31 km), it is

probably not enough to catch the detailed topography which leads to the exceptional intensity of katabatic winds in Adélie Land (as do most of the global atmospheric reanalysis (Jones et al., 2016; Jonassen et al., 2019)). This can have the effect of underestimating the actual sea ice production in coastal polynyas. In addition to the low sea ice production, the presence of the B9B iceberg during our simulated period potentially further limits the formation of DSW (K17 simulated sustained sea ice growth over larger portions of the Adélie Depression as the B9B is absent). One could expect a higher DSW formation rate now that the B9B has left the Adélie Depression. Finally, the method used here to analyze the influence of ocean–ice shelf interactions on dense water (namely the transport budget) presents some limitations. It is not suited to discriminate between thermodynamical water mass transformation and local convergence/divergence of water mass. Other methods, such as the one proposed by Abernathey et al. (2016) could solve this issue.

2.7 Conclusion

In this study, we analyzed the sensitivity of ice shelf basal melt, ocean mean state, and dense water transport to the representation of tides and ice shelves. We run a series of high-resolution simulations of the ocean and sea ice using an ocean–sea ice model driven by atmospheric reanalysis. Our experiments revealed that ice shelves of the D'Urville Sea are highly sensitive to tidal forcing, with a basal melt increase ranging from +62% to +250% depending on the ice shelf considered. This response is attributed to the dynamical forcing of tides near the ocean–ice shelf interface. Ocean–ice shelf interactions yield a cooling and a freshening of the subsurface ocean, and a warming and salinity increase concentrated in the top 200 m of the water column, and to the onset of a basal-melt–driven circulation. The investigation of water mass transport in polynyas revealed that the Mertz Glacier Polynya hosts very little dense water formation, but that DSW can be formed in other polynyas off Adélie Land (Mertz or Ninnis Bank Polynyas). The heat and freshwater fluxes between ice and ocean beneath ice shelves yield a freshening and cooling of the water masses involved (mCDW, CDW, MSW, or DSW). This results in the production of a relatively light water mass from the consumption of dense water (mostly MSW). This way, ocean–ice shelf interactions lead to a decrease in the amount of dense water being formed off Adélie Land, as part of the dense water formed in situ is consumed beneath ice shelves. This effect is further strengthened by tide-induced ice shelf basal melt increase. Moreover, the subsurface freshening induced by ice shelf melting inhibits the conversion of surface waters into dense waters as sea ice forms. This suggests that ocean–ice shelf interactions could have played a role in recent changes in dense water formation.

Tides and ocean–ice shelf interactions are two important processes that have to be accounted for in numerical models dedicated to the study of the formation of dense water. Furthermore, we argue that both processes have to be represented together as the absence of interactions between them might alter results from studies involving tides or ice shelves in coastal Antarctica. The importance of ice shelves for dense water transformation raises the question of the formation of DSW in a future climate. Our results suggest that an increase in ice shelf basal melt could lead to a diminution of dense water production. The important interactions between ice shelf basal melt in the presence of tides stress the need to take these processes into account in climate models.

Chapter 3

Effects of the atmospheric forcing resolution on simulated sea ice and polynyas off Adélie Land, East Antarctica

This chapter is based on the article "Effects of the atmospheric forcing resolution on simulated sea ice and polynyas off Adélie Land, East Antarctica" under review for publication in Ocean Modelling (authored by Huot P.-V., Kittel C., Fichefet T., Jourdain N. C., Sterlin J., Fettweis X.).

3.1 Foreword

In the previous chapter, the ocean–ice shelf interactions, amplified by the tides, were shown to reduce the formation of dense waters and later lead to its consumption. This implies that small-scale processes of coastal seas taking place beneath the surface can affect the budget of dense waters. However, the first driver of dense water production remains the high sea ice production rates in coastal polynyas. The interactions of the ocean and sea ice with the atmosphere likely explain most of the dense waters formation and its variability. The goal of the next chapter is to assess the role of small-scale processes in these interactions with the atmosphere. In particular, the next chapter focuses on the role played by the small-scale variability of the atmosphere in driving polynyas activity. In a modeling framework, the spatial variability of the atmosphere is partially defined by the horizontal resolution of the atmospheric forcing. Increasing the resolution could affect the local winds driving the activity of polynyas and thus affect dense water production. In addition, as discussed in the introduction, polynyas can also affect ice shelf basal melt as they deeply modify the properties of water masses in coastal seas. Thus, changes in polynya activity

could affect the production of dense waters in several ways, directly by surface transformation, or indirectly by modulating ice shelf basal melt.

3.2 Summary

Coastal polynyas of the Southern Ocean play a central role in the ventilation of the deep ocean and affect the stability of ice shelves. It appears crucial to incorporate them into climate models, but it is unclear how to adequately simulate them. In particular, there is no consensus on the atmospheric forcing resolution needed to appropriately model the sea ice in coastal Antarctica. A high resolution might be required to represent the local winds such as katabatic winds which are key drivers of coastal polynyas. To fill in this gap, we have tested the sensitivity of sea ice and atmosphere–sea ice–ocean interactions to the resolution of the atmospheric forcing in a high-resolution ocean–sea ice model . A set of regional atmospheric simulations at horizontal resolutions of 20, 10, and 5 km are performed with an atmospheric regional model and used to force three ocean–sea ice simulations in the Adélie Land sector, East Antarctica. Due to the better representation of topography with a refined grid, the offshore component of coastal winds becomes stronger at increased resolution. The wind intensification is particularly strong down valleys channelizing the katabatic flow, with an increase in wind speed ranging between 1 and 3 m/s. Under a higher resolution forcing, polynyas open more frequently and are wider. This fosters the growth rate of sea ice in polynyas, while landfast ice and pack ice are weakly affected. In polynyas, the production of sea ice is increased by up to 30% at 5 km resolution compared to 20 km resolution. Polynyas downstream of the katabatic wind pathway are more affected than the ones driven by easterly winds, highlighting the importance of the local wind conditions. Brine rejection associated with these higher sea ice production rates affects the salinity budget of the ocean and enhances both the volume and density of the dense Shelf Water produced off Adélie Land. These results underpin the need to better account for local coastal winds and polynyas in ocean and climate models.

3.3 Introduction

Sea ice growth usually acts as a negative feedback to ocean cooling, as the ice insulates the ocean from the cold atmosphere. However, some processes can inhibit the onset of ice cover, leaving areas of low sea ice concentration called polynyas. These polynyas are often divided into two categories: the sensible heat polynyas, which are forced by anomalously high ocean temperatures inhibiting sea ice freezing, and the latent heat polynyas, which are formed by the local divergence of the sea ice (Morales Maqueda et al., 2004). Most Antarctic coastal polynyas belong to the second category (Massom et al., 1998). They form in recurrent locations, where coastline, grounded icebergs, or ice shelf tongues in combination with the wind favor the local divergence of sea ice. Latent heat polynyas host continuous sea ice freezing, which is balanced by wind-driven sea ice export. As polynyas are places of intense air-sea fluxes, they have important effects on the ocean, the ice shelves, and the fauna of coastal Antarctica. Indeed, brine rejection in polynyas fosters ocean convection and sometimes leads to the formation of Dense Shelf Water (DSW). DSW can later be transformed into Antarctic Bottom Water (AABW) and thus contribute to the global ocean thermohaline circulation. DSW formed in polynyas can also affect the melting of ice shelves, due to the depletion of the ice melting point at high pressure (Jacobs et al., 1992). Besides, polynyas are often described as 'life oases' supporting the planktonic activity (Liniger et al., 2020) and helping Antarctic fauna to endure the harsh winter (Labrousse et al., 2018).

Approximately two thirds of the Antarctic coastal polynyas appear to be driven by katabatic winds (Massom et al., 1998). These winds blow offshore over most of the Antarctic coastline and originate from surface air cooling over the slopes of the Antarctic ice sheet (Parish and Bromwich, 1987). They are particularly persistent during winter and can reach astonishing velocities such as the yearly mean wind speed of 20 m/s measured by Wendler et al. (1997) at Cape Denison, East Antarctica. Such conditions are favored by the topography which channelizes the katabatic flow. The representation of katabatic winds in atmospheric models relies on their ability to represent the topography and the very stable surface boundary layer over the ice sheet. Polar-oriented regional atmospheric models have been shown to simulate realistic katabatic winds (Jourdain and Gallée, 2011), or to produce stronger coastal winds than a coarse-resolution global atmospheric reanalysis (Mathiot et al., 2012). The ability of atmospheric models to simulate coastal winds is also improved at higher horizontal resolution (Bromwich et al., 2013). Coarse-resolution models (above 1° or 100 km) struggle to represent realistic coastal winds, which can have important implications for the representation of polar climate. The use of high-resolution winds modifies the ocean heat transport towards the Antarctic ice shelves (Dinniman et al.,

2015). Introducing katabatic winds in an atmospheric reanalysis modifies the coastal and deep ocean properties (Mathiot et al., 2010; Barthélemy et al., 2012). Besides, Zhang et al. (2015) showed that different treatments of the orographic drag in two atmospheric reanalyses have important repercussions for the simulation of coastal offshore winds and for the coastal sea ice production.

The coarse representation of coastal winds in global climate models might be one of the reasons for their weak convection in coastal areas and biases in AABW properties (Heuzé et al., 2013; Heuzé, 2021). Meanwhile, coarse atmospheric reanalyses are commonly used to force ocean–sea ice models of the Southern Ocean. The new generation of atmospheric reanalyses has a higher horizontal resolution (roughly 30 km in ERA5, Hersbach et al. (2020)), with grid size approaching the 20 km horizontal resolution of the regional atmospheric model used in Mathiot et al. (2012) for instance. While this improves the representation of small-scale atmospheric variability in Antarctica (Tetzner et al., 2019), it remains unclear if this resolution is sufficient to produce realistic coastal ocean and sea ice when used as a forcing for ocean–sea ice models. Gossart et al. (2019) showed that ERA5 underestimated the intensity of coastal winds. Petrelli et al. (2008) or Ebner et al. (2014) showed that increasing the atmospheric resolution below 10 km intensifies the katabatic winds and the polynya activity in the Ross Sea sector, but their studies did not involve an ocean–sea ice model. Moreover, the complex topography of the Transantarctic Mountains or the Antarctic Peninsula imposes the use of very high resolution in these regions (2 km in Petrelli et al. (2008)), while it might not be needed elsewhere in Antarctica. The choice of the atmospheric forcing is a primordial question for polar ocean modelers. As high-resolution atmospheric models can be expected to produce more realistic coastal winds and in particular stronger katabatic winds, we expect that increasing the atmospheric forcing resolution could increase the frequency of coastal polynyas and the associated sea ice production.

The Adélie Land sector (East Antarctica) is known for the intensity of its katabatic winds (Wendler et al., 1997). This area is recognized as a major source of AABW (Rintoul, 1998) thanks to the activity of the Mertz Glacier Polynya (see Figure 3.1), despite its abrupt decline after the major calving event of the Mertz ice tongue in 2010 (Kusahara et al., 2011b; Tamura et al., 2012; Lacarra et al., 2014; Aoki et al., 2017; Snow et al., 2018). The calving event raised a lot of interest (Cougnon et al., 2017; Kusahara et al., 2017) as the polynya and the ice tongue were suggested to apply strong control on the ocean circulation (Martin et al., 2017). These studies, however, relied on coarse-resolution atmospheric forcing which might underestimate the intensity of katabatic winds. In addition, the representation of sea ice and in particular landfast

ice (thick and immobile sea ice fastened to the coastline, to the seafloor, to ice shelf front, or to grounded icebergs) remains relatively crude in these models. This is problematic given that landfast ice is thought to be related to the development of coastal polynyas (e.g., Fraser et al. (2012); Nihashi and Ohshima (2015); Fraser et al. (2019)). The blocking of sea ice on obstacles is indeed often a prerequisite for sea ice divergence and the opening of a latent heat polynya. Another interest of the Adélie Land is that it is representative of the majority of Antarctic coastlines, with a relatively smooth topography compared to mountainous areas of Antarctica.

In this study, we aim at investigating whether increasing the resolution of atmospheric forcing beyond the resolution of present global atmospheric reanalyses would affect the activity of coastal polynyas off Adélie Land. To separate the effect of resolution, we use a set of regional atmospheric simulations based on the MAR (Modèle Atmospherique Régional) model at resolutions of 20, 10, and 5 km with identical physics (every aspects and parameters of the model are held constant). These simulations are used to force a regional ocean–sea ice configuration of the NEMO-LIM model (Nucleus for European Ocean Modeling and Louvain-la-Neuve sea Ice Model), including a parameterization of landfast ice. The atmosphere, ocean–sea ice, and ice shelf models are described in Section 3.4. In Section 3.5, we analyze how the resolution of the atmospheric model affects the near-surface forcing fields. The sensitivity of sea ice and polynyas to the atmospheric forcing resolution is assessed in Section 3.6. In Section 3.7, we investigate the effects of forcing resolutions on salt fluxes and water mass transformations. We finally discuss the implications of fine-scale atmospheric processes for the coastal Southern Ocean and indicate which resolution appears the most suitable for the atmospheric forcing of polar ocean–sea ice models in Sections 3.8 and 3.9.

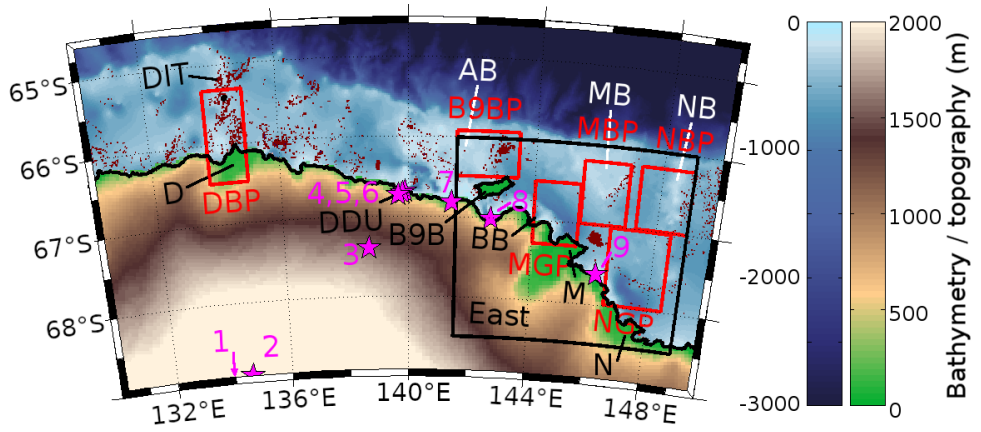

Figure 3.1: Bathymetry (in the NEMO-LIM model) and topography (in the AM5 simulation) of Adélie Land and the D'Urville Sea. Dark red dots indicate the locations of small grounded icebergs in the model. Red boxes represent the polynyas of the Dibble Bank (DBP), B9B iceberg (B9BP), Mertz Glacier (MGP), Mertz Bank (MBP), Ninnis Glacier (NGP), and Ninnis Bank (NBP). The black box indicates the area for water mass transformation computation. Pink stars indicate Automatic Weather Stations, 1: D85 (out of the map) 2: E-66, 3: D47, 4: D17, 5: D10, 6: DDU, 7: Port Martin, 9: Cape Denison, 9: Penguin Point. DIT: Dibble iceberg tongue, D: Dibble ice shelf, DDU: Dumont D'Urville base, B9B: tabular iceberg, AB: Adélie Bank, BB: Buchanan Bay, M: Mertz ice shelf, MB: Mertz Bank, N: Ninnis ice shelf, NB: Ninnis Bank.

3.4 The model and forcing

3.4.1 MAR atmospheric model

The MAR model is used to produce the atmospheric forcing of the ocean-sea ice model. MAR is a hydrostatic polar-oriented model (Gallée and Schayes, 1994) that has often been used to study the climate over the Antarctic ice sheet (Amory et al., 2015; Kittel et al., 2018; Agosta et al., 2019; Donat-Magnin et al., 2020; Mottram et al., 2020). The model includes a cloud microphysics module solving conservation equations for five water species: snow particles, cloud ice crystals, raindrops, cloud droplets, and specific humidity (Gallée, 1995). The cloud microphysics module is based on Kessler (1969) parameterizations latter improved following Lin et al. (1983). The MAR radiative scheme has been adapted from the European Centre for Medium-Range Weather Forecasts ERA-40 reanalysis (Morcrette, 2002; Uppala et al., 2005). The transfer of energy and mass between the atmosphere and the surface is simulated by the one-dimensional surface scheme SISVAT (Soil Ice Snow Vegetation Atmosphere Transfer) module (De Ridder and Gallée, 1998). In particular, the module represents the evolution of snow (Gallée and Duynkerke, 1997; Gallée et al., 2001) and ice (Lefebre et al., 2003), partly based on an old version of the snow model CROCUS (Brun et al., 1992). In the surface layer, the turbulence is resolved using the

Monin-Obukhov similarity theory, while above the surface layer, it is resolved with a local closure scheme adapted for representing stable conditions in the boundary layer enabling a better representation of katabatic winds (Gallée et al., 2015). The MARv3.10 configuration used in this study is similar to the one without drifting snow evaluated by Le Toumelin et al. (2020) over Adelie Land. MAR describes the atmosphere using a stretched grid with 24 vertical sigma levels, the lowest being at 2 m and 5 are located in the lowest 100 m of the atmosphere. MAR is forced by 6-hourly outputs of ERA5 (Hersbach et al., 2020) at its atmospheric lateral boundaries (pressure, wind, specific humidity, and temperature) and at its sea surface over 2000-2015. The temperature and wind velocity at the top of the atmosphere are constrained by ERA5 following van de Berg and Medley (2016). As MAR is not coupled to an ocean model, it does not simulate sea surface temperature or sea ice concentration, so both are prescribed from ERA5. However, MAR represents the thermodynamical evolution of sea ice energy budget and thickness (with a prescribed minimal value of 10 cm that can be covered by snow). We performed MAR simulations at three resolutions (20, 10, and 5 km) over the same domain covering the NEMO grid (see next section) and using exactly the same parameters for the three runs. In this way, the three simulations share identical physical settings and surface boundary conditions. The results of the three MAR simulations are described and evaluated in Section 3.5. Finally, the Antarctic topography and ice and rock fractions are derived from the 1 km resolution digital elevation model Bedmap2 (Fretwell et al., 2013), but unlike previous studies with MAR in Adélie Land (Le Toumelin et al., 2020), the coastline in the three simulations has been corrected to match as much as possible the one from NEMO. This results in adjustments in the ice mask, notably the removal of the Mertz ice tongue and the addition of grounded icebergs (see below).

3.4.2 Ocean–sea ice model

We make use of a regional configuration of the NEMO platform (Madec, 2016) in its version 3.6 which includes the sea ice model LIM3.6 (Louvain-la-Neuve sea Ice Model). NEMO-LIM is commonly used to study the whole Southern Ocean (Lecomte et al., 2016; Merino et al., 2016; Marchi et al., 2019) or specific sectors (Jourdain et al., 2017; Donat-Magnin et al., 2017; Hausmann et al., 2020; Huot et al., 2021a). The ocean component solves the primitive equations, assuming hydrostatic balance and using the Boussinesq approximation. Parameterizations include a Turbulent Kinetic Energy scheme (Bougeault and Lacarrere, 1989; Gaspar et al., 1990) for vertical mixing. Convection is represented by enhancing vertical mixing. The surface pressure gradient is treated with a time-splitting approach together with a non-linear free surface. The present configuration was used and evaluated against observations in Huot et al. (2021a). The grid is refined from the eORCA1 tripolar

grid to a resolution of $1/24^\circ$ in longitude, i.e. from 1.8 to 2.3 km over the domain (130°E-150°E and 60°S-70°S, see Figure 3.1). The vertical discretization consists of 75 levels of increasing thickness from 1 m at the top to 200 m at the bottom of the ocean. The thickness of the bottom cells or of the top cells beneath ice shelves is adjusted to match the bathymetry or ice draft. We use a polynomial approximation of the reference Thermodynamic Equation Of Seawater (TEOS-10) [IOC, SCOR, APSO, 2010] optimized for a Boussinesq fluid (Roquet et al., 2015). The sea ice component, LIM3.6, is a dynamic-thermodynamic model described in Vancoppenolle et al. (2009) and Rousset et al. (2015). A subgrid-scale distribution of sea ice thickness with 5 categories is used. Drag coefficients are 5.0×10^{-3} and 1.4×10^{-3} for sea ice–ocean and sea ice–atmosphere, respectively. The simulation of landfast sea ice is achieved following the methodology of Van Achter et al. (2021), also used in Huot et al. (2021a). The elastic-viscous-plastic (EVP) rheology was modified to include both isotropic and uniaxial tensile strength based on the works of König Beatty and Holland (2010) and Dumont et al. (2009), combined in Lemieux et al. (2016). The isotropic tensile strength parameter k_t is set to 0.2, the eccentricity of the elliptical yield curve e to 1.5, and the number of sub-iterations of the EVP solver to 900. These modifications of the sea ice rheology are not sufficient to adequately represent landfast sea ice off Antarctica. The role of grounded icebergs also needs to be incorporated as suggested by Fraser et al. (2012, 2019) and Van Achter et al. (2021). In the model, grounded icebergs are added as anchoring points for the sea ice in the following way: icebergs are treated as land points in the sea ice model and for the surface flux module, but they do not interact dynamically nor thermodynamically with the ocean. The locations of small grounded icebergs (see Figure 3.1) were manually extracted from LANDSAT (Landsat image courtesy of the U.S. Geological Survey) images between 2011 and 2015 to build a constant iceberg mask used in the landfast sea ice parameterization.

Surface boundary fluxes are computed every 900 s from the 3 hourly MAR outputs using the CORE bulk formulas (Large and Yeager, 2004). An additional freshwater flux representing the melting of icebergs is applied at the ocean surface using the climatology of Merino et al. (2016). No salinity restoring is applied. At the domain boundaries, a flow relaxation scheme (Engedahl, 1995) is applied to the three-dimensional ocean variables and two–dimensional sea ice variables. A Flather scheme (Flather, 1994) is used for barotropic velocities and sea surface elevation. The model simulates under-ice shelf cavities with explicit ocean–ice shelf interactions as implemented in NEMO by Mathiot et al. (2017). The bathymetry of the domain (see Figure 3.1) is adapted from the GEBCO dataset (Weatherall et al., 2015), which includes the high-resolution measurements from Beaman et al. (2011). Tides are applied at the lateral boundaries of the domain using the FES2012 dataset (Carrère et al., 2012), as in

Maraldi et al. (2013) and Jourdain et al. (2019). The bathymetry and icescape used in the model correspond to the state of the Adélie Land region after the Mertz calving in 2010. More precisely, in our configuration, the Mertz ice tongue is calved and the B9B iceberg is located in the Commonwealth Bay (see Figure 3.1). The B9B iceberg is mapped from LANDSAT8 images and represented as a flat ice shelf. B9B iceberg draft is set to 300 m following Mayet et al. (2013). Ice draft and bathymetry under ice shelves are adapted from the Bedmap2 dataset (Fretwell et al., 2013).

3.4.3 Experimental design

MAR simulations are conducted on three grids with different resolutions (20, 10, and 5 km, respectively simulations AM20, AM10, and AM5). The computational costs of these three simulations are indicated in Figure 3.2. The 3-hourly outputs from MAR are then interpolated on the ocean–sea ice model grid using a bilinear interpolation for scalar atmospheric fields and bicubic interpolation for wind vectors. Before the interpolation, MAR outputs were "drowned", i.e. values over the ice sheet and land points were extrapolated from the nearest ocean points, which limits the effects of mismatch between the ocean model coastline and the coastline in MAR at three different resolutions. These datasets constitute the atmospheric fields used to compute the surface boundary conditions of the ocean–sea ice model via the bulk CORE formulas. Three ocean–sea ice experiments are carried out using the set of atmosphere simulations, namely OM20, OM10, and OM5 (NEMO-LIM forced by AM20, AM10, and AM5, respectively). The simulations start in January 2007 and end in December 2015. The first three years serve as spin-up and are discarded for the sea ice and ocean analysis.

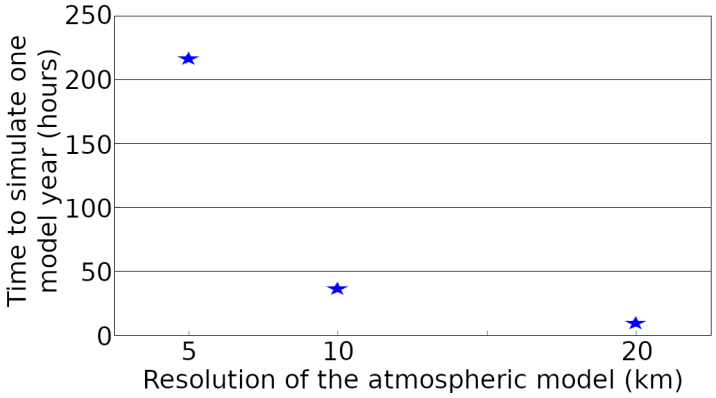

Figure 3.2: Time needed to compute one model year for the three MAR simulations at 20, 10 and 5 km resolutions (using 8 AMD EPYC 2.9 GHz CPUs). AM5 is 6 times slower than AM10, itself being 4 times slower than AM20.

Changing the resolution of the atmospheric model impacts the spatial variability of the atmospheric fields, but also modifies the atmospheric model dynamics. In addition, the ocean and sea ice might exhibit different sensitivities to the resolution for each atmospheric variable. To explore in more detail these questions, we ran two additional shorter (2007-2010) simulations. OM20W5 is an ocean–sea ice simulation forced by AM20 apart from the wind speeds, which are those of AM5. OM5x20 is forced by AM5 but the high-resolution atmospheric fields were averaged onto the 20 km grid of AM20. The first of these simulations is used to discriminate the sensitivity to the wind resolution from the sensitivity to the resolution of other atmospheric fields, while the second serves to disentangle the dynamical effects from the resolution effects of grid refinement.

3.5 Atmospheric forcing and effects of resolution

In this section, we describe the differences between the near-surface fields obtained from the three atmospheric simulations AM20, AM10, and AM5. We also compare them to the ERA5 reanalysis to evaluate the atmospheric simulations above the ocean and show the differences between the global reanalysis and the regional polar-oriented atmospheric model. ERA5 has a resolution of 0.28°, which corresponds to approximately 12x31 km near Dumont D'Urville.

Simulated surface air temperatures and wind speeds in AM20, AM10, AM5, and ERA5 are compared to those observed by the Automatic Weather Station (AWS) network in Adélie Land in Figure 3.3. On every coastal station (Penguin point to Dumont D'Urville (DDU), points 4 to 9 in Figure 3.1), MAR exhibits a cold bias, which is slightly reduced in AM5. Inland (E-66 and D-85), MAR simulations show a +1°C bias compared to the AWS. Compared to MAR, ERA5 better represents the mean temperature, which likely results from the assimilation of near-surface temperatures and of radiance and cloud products. The wind speeds simulated by MAR are in better agreement with the AWS observations than winds of ERA5. Both the mean bias and the correlation are improved in MAR. ERA5 exhibits particularly poor correlation and a negative bias reaching 10 m/s for the coastal stations Penguin point and Cape Denison. Increasing the resolution of the atmospheric model tends to improve the simulated wind speeds. Yet, it seems to only partially explain the better performance of MAR compared to ERA5. Indeed, AM20 and ERA5 have similar resolutions, yet AM20 presents more realistic winds. Other source of improvement might be related to the specific treatment of the polar atmospheric boundary layer and surface roughness in MAR(Gallée et al., 2015; Agosta et al., 2019). Coastal winds are better represented in MAR, highlighting the interest of using an atmospheric model developed for the

representation of the polar atmosphere to force ocean–sea ice models.

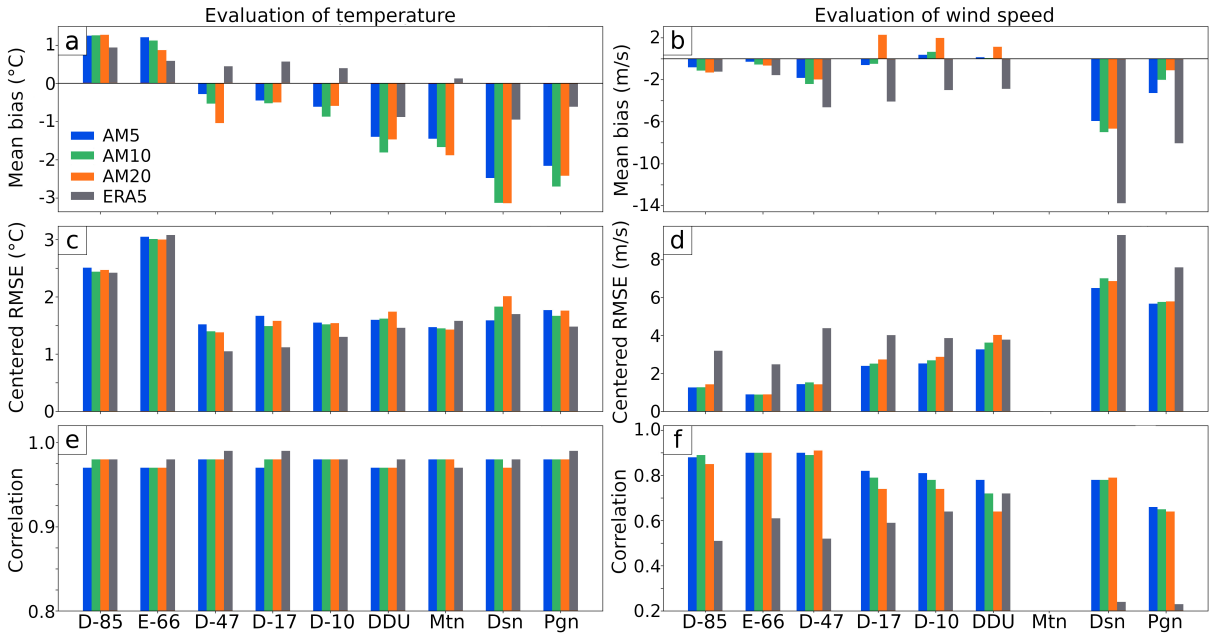

Figure 3.3: Mean bias (a) and root mean-square error (RMSE; c) of surface air temperatures simulated in AM20, AM10, AM5, and ERA5 with the measurements performed by the Automatic Weather Station (AWS) network (see Figure 3.1 for station locations). (e) Correlations between the surface air temperatures simulated in AM20, AM10, AM5, and ERA5 and the ones measured by the AWS network. (b), (d), (f): same as (a), (c), (e) but for wind speed. DDU: Dumont D'Urville, Mtn: Port Martin, Dsn: Cape Denison, Pgn: Penguin Point. Note that no wind data were available for Port Martin.

The typical wind conditions of coastal Adélie Land simulated in the MAR runs and ERA5 are shown in Figure 3.4. To illustrate the variability of wind conditions blowing over polynyas off Adélie Land, we make the distinction between the easterlies and southerlies cases. To do so, we compute the area-averaged wind direction over the eastern coastal seas (pink box in Figure 3.4, corresponding to the area of most intense polynya activity, see Section 3.6) and use it to discriminate between the easterlies (winds are oriented left of the median wind) and southerlies (winds are oriented right of the median wind). During easterlies periods in AM5 (Figure 3.4g), strong winds parallel to the coastline blow over the coastal seas. The mean wind speed intensifies from east to west between 150°E and 140°E, peaking at values of 11 m/s, before weakening west of 132°E. Locally, the mean winds can also show a component perpendicular to the coast in the southeast of the domain, near the Mertz ice tongue, Ninnis ice tongue, or B9B iceberg. The winds perpendicular to the coastlines are of katabatic origin, and the mean wind speeds locally reach 13 m/s there. The average wind conditions during easterlies are similar for the three MAR simulations and for the ERA5 reanalysis (Figure 3.4a,c,e,g). Yet, winds tend to be weaker when the

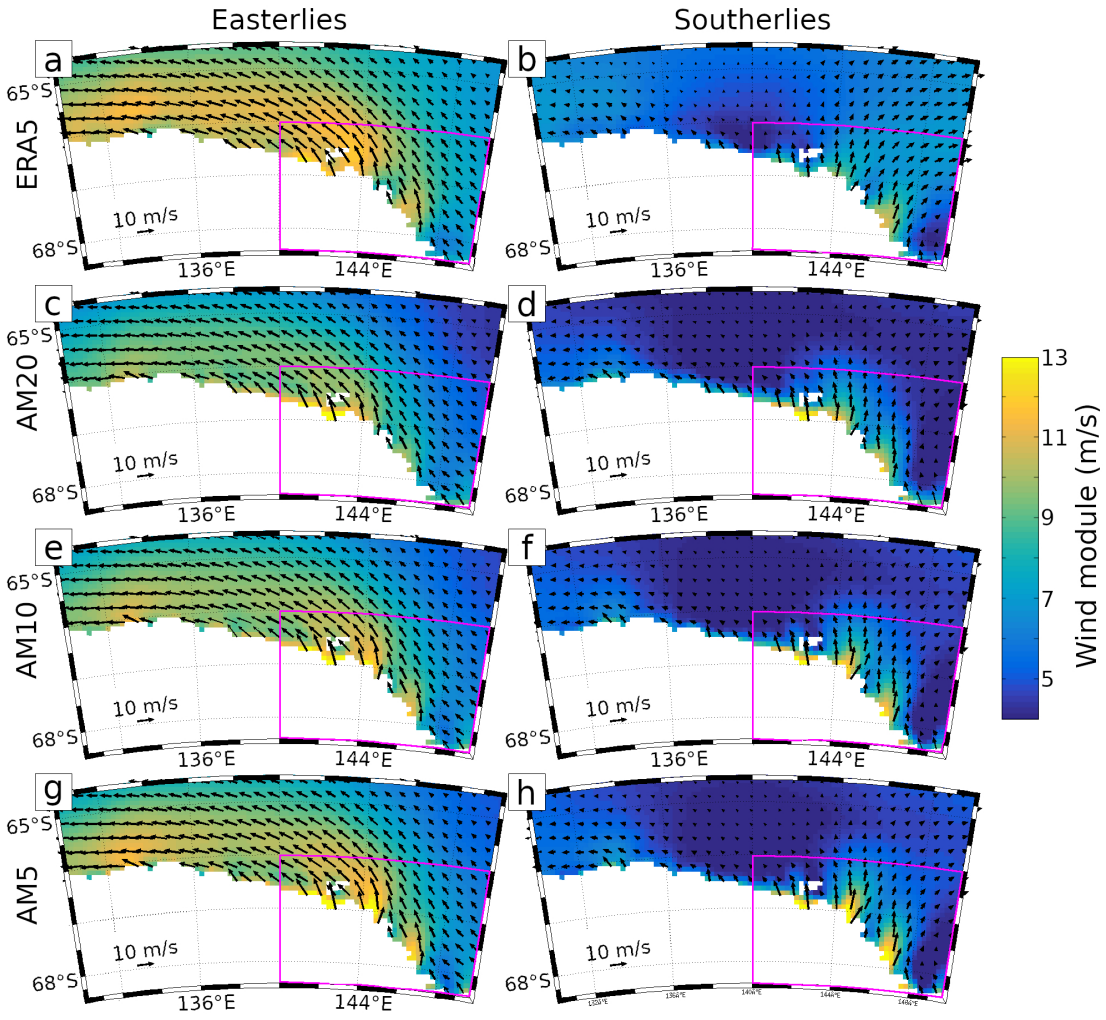

Figure 3.4: Mean wind speed during easterlies (left column) events and southerlies (right column) events in winter (May to September), averaged over 2010-2015. (a) and (b): ERA5, (c) and (d): AM20, (e) and (f): AM10, (g) and (h): AM5. Easterlies and southerlies events are defined using the distribution of the area-averaged wind direction over the pink box. Easterlies (southerlies) are defined as events when the area-averaged wind direction is lower (higher) than the median wind direction.

resolution is coarsened in MAR. For instance, the easterlies blowing north of the B9B iceberg are slower in AM20 than in AM10, the latter being slower than those of AM5. Katabatic winds near the Mertz or Ninnis ice tongues are also weakened at lower resolution. The coastal winds of katabatic origin in the Commonwealth Bay, off the Mertz Glacier, and off the Ninnis glacier are stronger in the three MAR simulations than in ERA5. On the contrary, offshore easterlies in ERA5 are stronger than those simulated in the three MAR experiments. Winds in ERA5 are overall stronger than those of MAR, with the exception of the coastal offshore winds in AM10 and AM5. The second mode of wind conditions corresponds to southerlies in the eastern coastal sea (Figure 3.4b,d,f,h). During southerlies, the easterlies previously described vanish, and the mean wind speeds over the ocean are lower than in the easterlies case.

Despite the overall calm wind conditions, strong winds perpendicular to the coast are encountered near the Ninnis and Mertz ice shelves and in the Commonwealth Bay. There, the wind speeds reach 13 m/s in AM5. The intensity of the local southerlies weakens with decreasing resolution (AM10 and AM20; Figure 3.4d,f). Southerlies are weaker in ERA5 than in the three MAR simulations. However, the winds away from the coast are stronger in ERA5 than in the MAR simulations during the southerlies regime. ERA5 near-surface winds are on average stronger everywhere above the ocean away from the coastline. As an increase of resolution tends to strengthen coastal winds but does not affect the winds away from the coast, the difference of resolution between ERA5 and the MAR experiments should not explain the changes in wind speeds over the ocean. The stronger winds in ERA5 might come from differences in the turbulent mixing parameterizations or to the treatment of surface roughness lengths between the atmospheric model of ERA5 and the MAR model. Yet, MAR produces stronger katabatic winds even at low resolution which is probably linked to the specific adaptation of MAR for the modeling of polar climate. The increase in resolution is a second factor explaining the higher katabatic wind speeds in MAR than in ERA5, and also explains the intensification of winds between AM20, AM10, and AM5. In summer (not shown), the wind conditions are similar, with two preferential wind directions (easterlies and southerlies). Summer winds are on average weaker than winter winds. The same differences between the three simulations and reanalysis are found (i.e. in general stronger winds over the ocean in ERA5, but stronger southerly winds along the coast in the MAR simulations).

The intensification and change of direction of coastal winds when comparing ERA5 to the MAR simulations or MAR simulations with different resolutions can be related to the differences in topography. The topographies of ERA5 and of the three MAR simulations are shown in Figure 3.5a,c,e,f. The refinement of resolution between ERA5 and MAR, and between AM20, AM10 and AM5 enable a more realistic representation of small-scale structures such as the valleys associated with the Dibble, Mertz, or Ninnis Glaciers. A better representation of valleys favors the channelization of the katabatic flow and the subsequent local intensification of those winds (as can be seen in Figure 3.4). The peak of katabatic wind intensity observed in Figure 3.4 coincides with the location of the Mertz and Ninnis glacier valleys. The increase of resolution to 10 km allows for a much better representation of the valleys compared to AM20 or ERA5, the additional refinement to 5 km leading to minor changes. Besides the representation of valleys, a higher resolution enables to better capture the steep slopes of the Antarctic Ice Sheet (Figure 3.5 b,d,f,h). The slopes of the Antarctic Ice Sheet are much smoother in the ERA5 topography than in the one of AM5. The gradual grid refinement between AM20 and AM5 is also accompanied

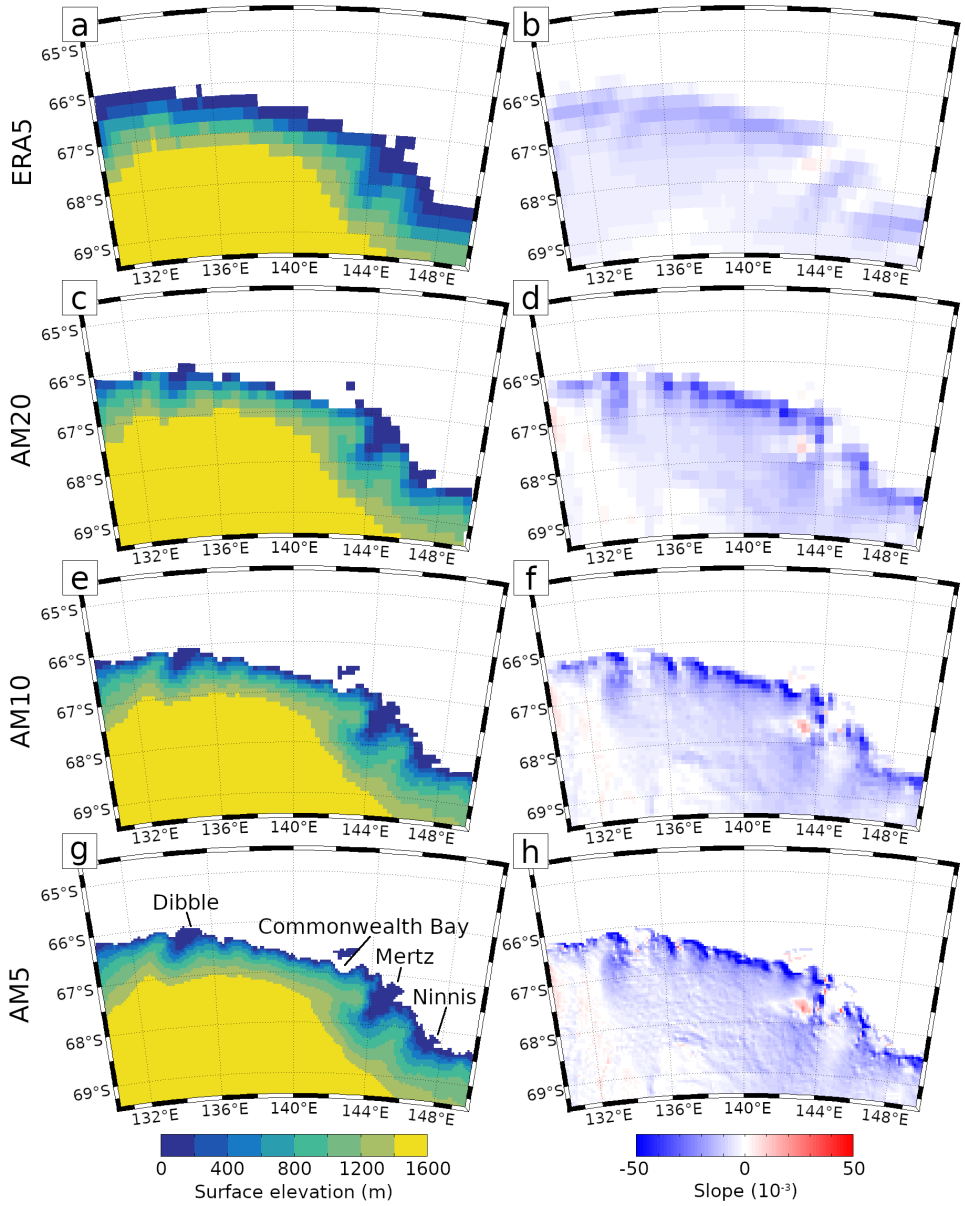

Figure 3.5: Topography (left) and terrain slope (right) in ERA5 (a and b), AM20 (c and d), AM10 (e and f), and AM5 (g and h). The terrain slope is counted positive when the surface elevation increases eastward / northward.

by a steepening of the slopes along the coastline. Steep slopes are important for the acceleration of the gravitational flows such as katabatic winds.

Topography applies a strong control on the coastal winds as can be seen in Figure 3.6. In the MAR simulations, the zonal distribution of the intensity of the meridional (offshore) and zonal components coastal winds presents a large variability between 142°E and 150°E. The most notable maximums are found in regions where the topography channelizes the katabatic flow, i.e in the Commonwealth Bay and off the Mertz or Ninnis valleys (see Figure 3.5). The imprint of the Dibble ice shelf also

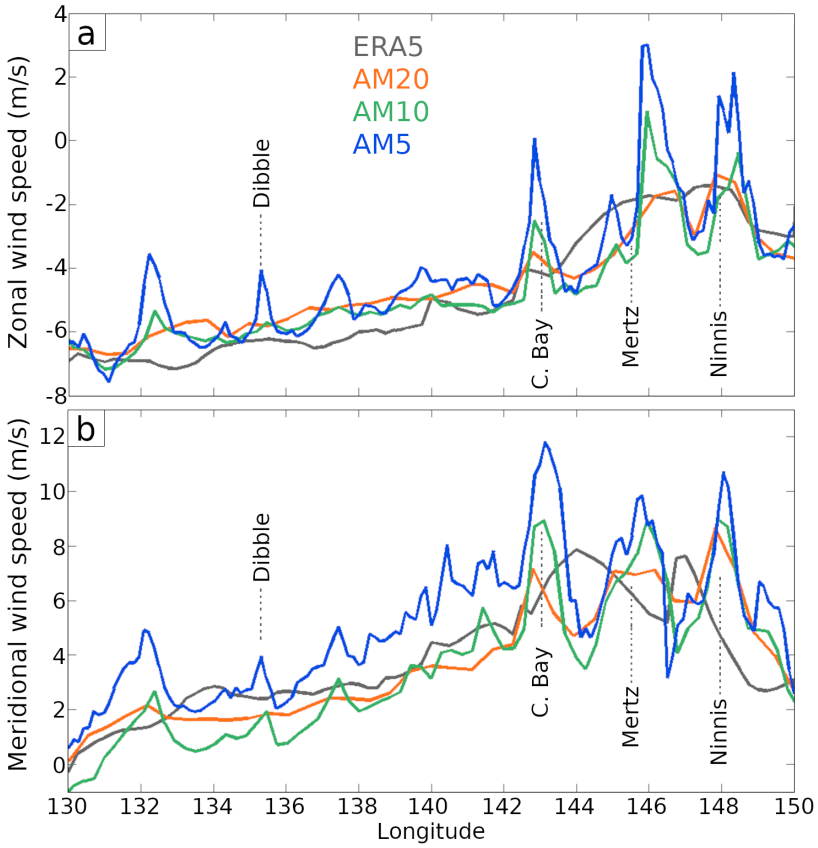

Figure 3.6: Zonal (a) and meridional (b) wind speeds at the coast (defined as the first ocean point after the continent) averaged between 2010-2015 (all seasons). Note that the location of the first ocean points varies with the representation of the coastline in the different models. C. Bay: Commonwealth Bay.

appears on the wind speeds. The intensity of the zonal (easterlies) winds decreases in front of these valleys as the component of katabatic winds that is parallel to the coast is weak. As can be seen in Figure 3.4, the intensity of the coastal meridional or zonal winds increase with the resolution: AM5 meridional winds are 1 to 3 m/s faster and zonal winds 1 to 4 m/s faster than those of AM20. The imprint of remarkable topographic features (Mertz and Ninnis valleys or Commonwealth Bay) is much weaker or absent in the ERA5 coastal winds. Two peaks can be seen east of the Commonwealth Bay and Mertz valley, but are of weaker magnitude than those of AM10 or AM5. The control applied to coastal winds by small-scale topographic features is increased with the resolution and is particularly weak in the ERA5 reanalysis.

Increasing the MAR forcing resolution has nearly no effects on the near-surface air temperature and humidity, as illustrated by the seasonal cycles shown in Figures 3.7a and 3.7c. The three MAR experiments have similar air humidities over the coastal ocean, and AM5 exhibits moderate warming (up to 1°C) compared to AM10 and

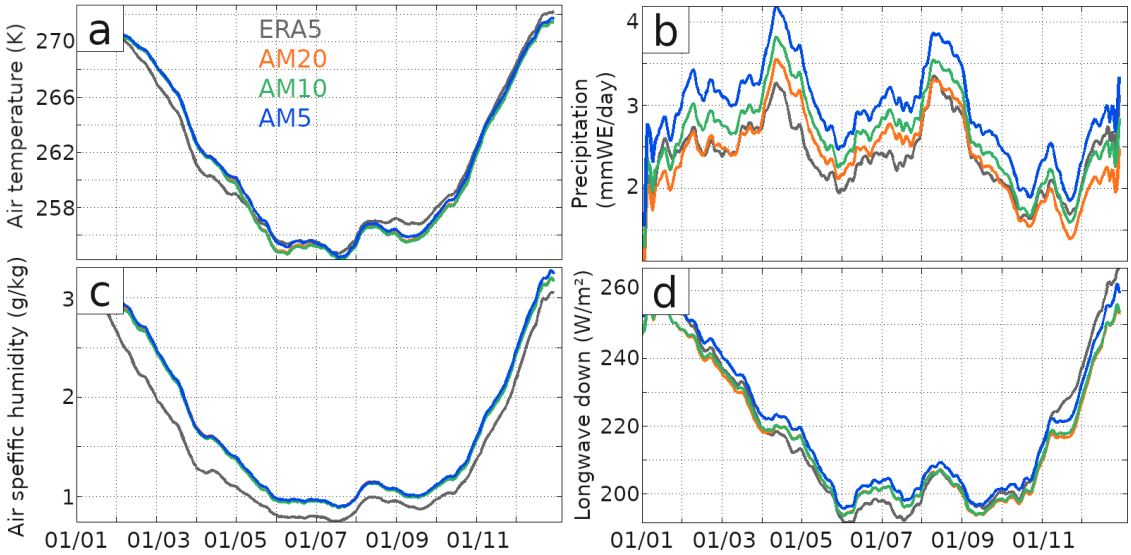

Figure 3.7: Seasonal cycle (averaged between 2007 and 2015) of (a) 2 m air temperature, (b) total precipitation, (c) 2 m air specific humidity, and (d) downward longwave radiation simulated in ERA5 global reanalysis and in AM5, AM10, and AM20, averaged over the ocean between 131 to 149°E and 64.5 to 68.5°S.

AM20 in winter. The seasonal cycles of temperature simulated in the three MAR experiments are similar to the one of the ERA5 reanalysis. The atmosphere simulated over the coastal ocean in MAR is moister than ERA5 (from +0.22 g/kg in AM20 to +0.25g/kg in AM5). The precipitation rate simulated in MAR over the coastal sea increases with the resolution (+0.22 mmWE/day between AM10 and AM20, +0.52 mmWE/day between AM5 and AM20) and are overall higher than those of ERA5 in winter for AM20 and year-round for AM10 and AM5. The downward longwave radiation is higher by 2 to 5 W/m² between AM5 and AM10 or AM20. Simulated downward longwave radiations are on average higher in winter (+3 W/m in AM20 and AM10, +5 W/m² in AM5) and lower in summer in MAR compared to ERA5.

Increasing the resolution of the atmospheric model leads to an intensification of the coastal offshore winds and of easterly winds. Other atmospheric fields are less impacted apart from the precipitation which increases with resolution. The three MAR simulations present several differences with the ERA5 reanalysis that do not originate from changes in resolution (higher air humidity, slower winds above the ocean). As our goal is to understand the role of forcing resolution on the simulation of the ocean and sea ice, we will only use the three MAR experiments as atmospheric forcing. A comparison between an ocean–sea ice simulation forced by ERA5 and the OM20 and OM5 simulations is presented in Section 6.2.1 (supplementary material).

3.6 Sensitivity of the sea ice to the atmospheric forcing resolution

3.6.1 Effects of the atmospheric forcing resolution on sea ice

In this section, we describe the mean sea ice state in OM5 and show how it is affected by the atmospheric forcing resolution in simulations OM20 and OM10.

First, we evaluate the state of the sea ice cover simulated in OM5 with respect to observations. The observed sea ice concentrations are obtained from the 6.25 km resolution ASI-AMSR-E dataset (ARTIST sea ice dataset developed using data from the Advanced Microwave Scanning Radiometer - Earth Observing System (Spreen et al., 2008)). The time coverage is limited to one year but its high resolution enables the visualization of small-scale features such as polynyas. A comparison between the OM5 simulation and observations on a longer period is proposed in Supplementary Figure 6.11. The mean sea ice covers simulated in OM5 for summer and winter of 2011 are displayed in Figures 3.8a and 3.8c, respectively. The simulated sea ice concentration shows good agreement with the observations depicted in Figures 3.8b and 3.8d. In summer, the model tends to underestimate the sea ice cover in the eastern part of the domain. The landfast ice patches (areas with high sea ice concentration in summer) persist throughout the melt season due to their high thickness. They are well distributed thought being larger in the simulation than in the observations. In winter, several polynyas appear over the continental shelf. The model is able to represent their location but underestimates their extent, especially for the DBP and for the polynya off the Dumont D'Urville base (140°E). The misrepresentation of polynyas might be due to the iceberg mask built in this study, as the iceberg distribution is assumed to be constant during the simulated period. The simulated winter sea ice thickness is compared to the sea ice thickness retrieved using a combination of Cryosat-2 and AMSR2 altimeters in the LEGOS/CTOH dataset (Guerreiro et al., 2017) (LEGOS: Laboratoire d'Etude en Géophysique et Océanographie Spatiale, CTOH: Center for Topographic studies of the Ocean and Hydrosphere). The range of sea ice thickness and its spatial variability are well captured by the OM5 simulation (Figures 3.8e and 3.8f). For instance, the landfast ice patches can be identified by sea ice thicker than 2 m. The thickness of the landfast ice patch at 136°E is overestimated in the model with values reaching 6 m and even 8 m locally. Such thick sea ice can also be observed in the LEGOS/CTOH dataset but it covers smaller areas.

The heterogeneity of the coastal sea ice off Adélie Land is a major driver of the spatial variability of air-sea heat fluxes. The simulated sea ice cover can be

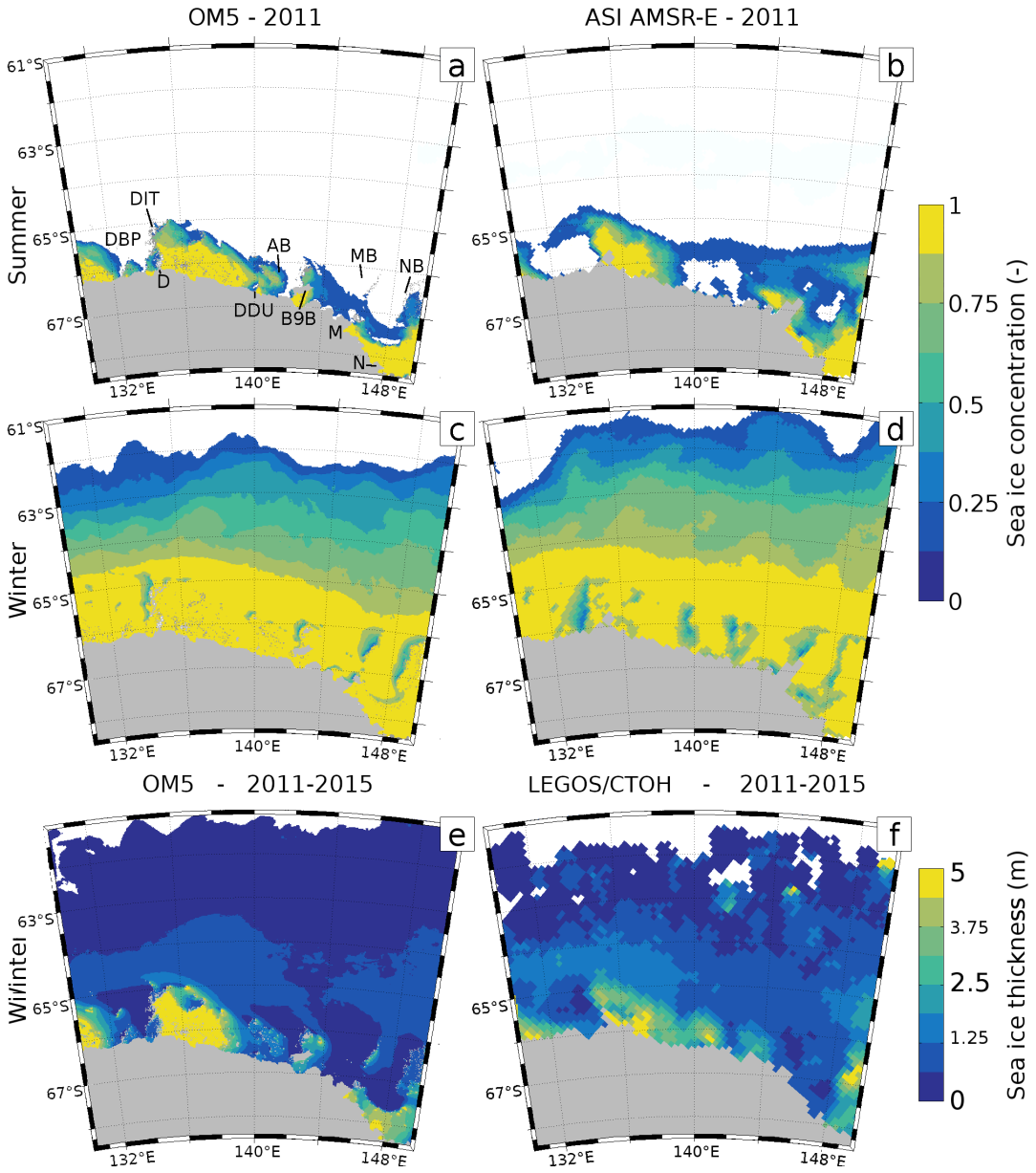

Figure 3.8: Sea ice concentrations simulated in OM5 and observed in ASI AMSR-E during summer (a and b) and winter (c and d) of 2011. Sea ice thickness averaged during winters of 2011-2015 as simulated in OM5 (e) and observed in the LEGOS/CTOH Cryosat-2 AMSR2 dataset (Guerreiro et al., 2017) (f). Year 2010 is discarded as we use the post-calving (after 2010) ice scape in our model. DIT: Dibble iceberg tongue, D: Dibble ice shelf, DDU: Dumont D'Urville base, AB: Adélie Bank, B9B: tabular iceberg, M: Mertz ice shelf, MB: Mertz Bank, N: Ninnis ice shelf, NB: Ninnis Bank.

decomposed in two distinct types of sea ice: landfast ice and polynyas (Figures 3.9a and 3.9b). The thick sea ice cover inhibits air-sea fluxes in landfast ice patches, which is not the case in polynyas. In the OM5 simulation, landfast ice patches are found year-round east of the Dibble iceberg tongue (east of 135°E), south of the B9B iceberg (142°E), or east of the Mertz glacier tongue. The landfast ice cover is intermittent in

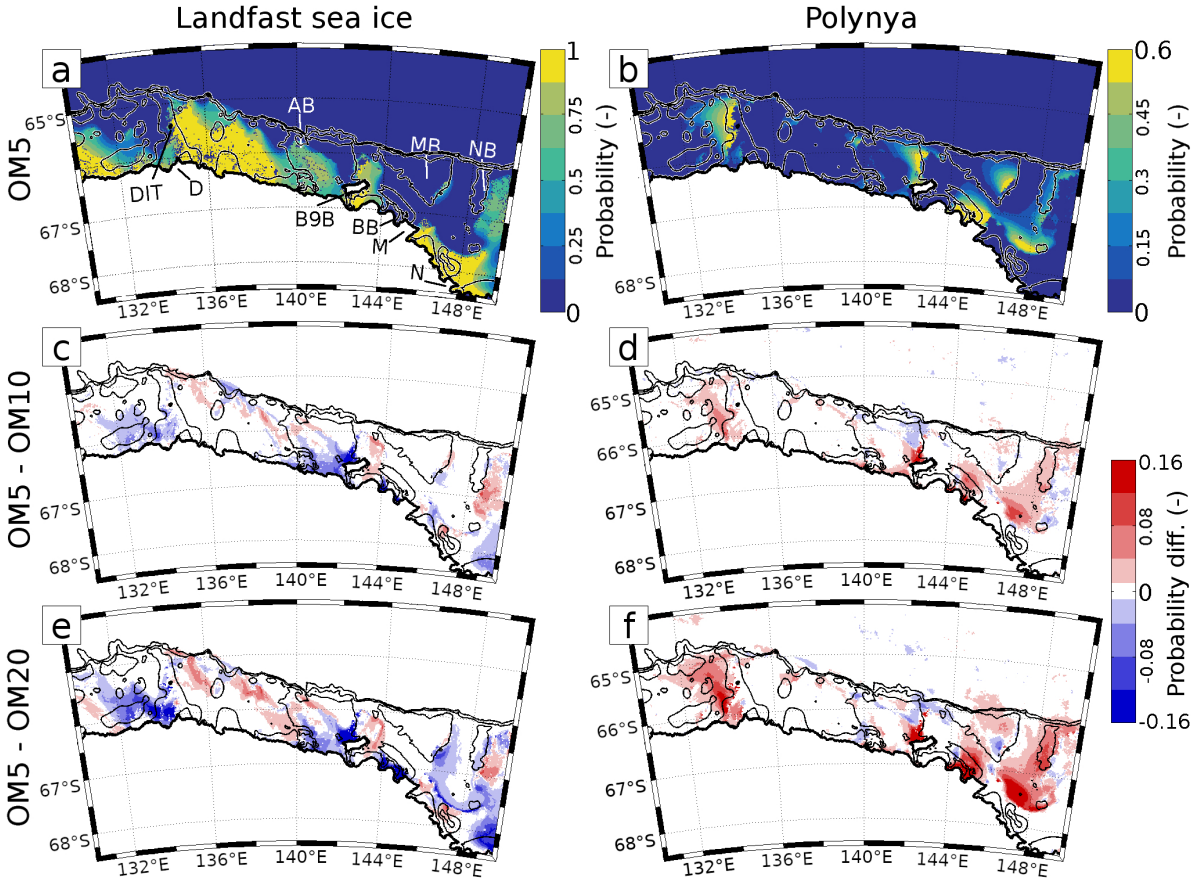

Figure 3.9: Probability of lanfast ice (a) and polynya (b) occurrence in OM5 averaged between years 2010 to 2015. Difference of landfast ice (c) and polynya (d) probability between OM5 and OM10. Difference of landfast ice (e) and polynya (f) probability between OM5 and OM20. Landfast ice is defined as sea ice with a 15 day averaged velocity lower than 0.1 cm/s. Polynyas are defined as closed contours within the ice pack with a daily sea ice concentration lower than 15% or a daily thickness lower than 0.2 m. Bathymetry is represented as black contours every 400 m. Legends for the panel (a) DIT: Dibble iceberg tongue, D: Dibble ice shelf, AB: Adélie Bank, B9B: tabular iceberg, BB: Buchanan Bay, M: Mertz ice shelf, MB: Mertz Bank, N: Ninnis Glacier, NB: Ninnis bank. Legends for panel b): DBP: Dibble Bank polynya, B9BP: B9B iceberg polynya, MGP: Mertz glacier polynya, MBP: Mertz Bank polynya, NGP: Ninnis glacier polynya, NBP: Ninnis Bank polynya.

other regions such as the Adélie or Ninnis Banks. Polynyas frequently open in the lee of obstacles and landfast ice patches. Six important polynyas can be identified: west of the Dibble iceberg tongue (DBP), north of B9B iceberg (B9BP), north of the Mertz Glacier (MGP) or Ninnis Glacier (NGP), and above the Mertz Bank (MBP) and Ninnis Bank (NBP) (see Figure 3.1 for polynya names used throughout the manuscript). These polynyas can also be seen in the observations of sea ice concentration of Figure 3.8d.

Increasing the resolution of the atmospheric forcing from 10 to 5 km (Figures 3.9c

and 3.9d) leads to a localized decrease in landfast ice probability and to an enhanced probability of polynya opening. Areas where landfast ice cover is intermittent undergo a decrease in landfast ice cover probability, while persistent patches are unaffected. Polynyas become more frequent under higher resolution forcing, with strongest changes in coastal polynyas. The differences between OM20 and OM5 show the same spatial distribution as the differences between OM10 and OM5, but the magnitude of the changes is increased. Areas frequently occupied by landfast ice are replaced by polynyas, such as the lee of the B9B iceberg or the Buchanan Bay (west of the Mertz ice tongue). Increasing the forcing resolution locally reshapes the contours of the sea ice cover in coastal seas, reducing the landfast ice cover and favoring the development of polynyas due to the strengthening of winds. Increasing the resolution thus improves the representation of polynyas, as the OM5 simulation tends to underestimate their extent (Figure 3.8).

The simulated sea ice production (Figure 3.10a) closely matches the locations of polynyas. In addition, the shelf break appears to be a favorable place for sea ice production, which can be attributed to the frequent openings of leads (Reiser et al., 2019). Compared to the AM10 forcing, the AM5 one leads to enhanced sea ice growth rates inside the polynyas (Figure 3.10b). This can be attributed to the increase in polynya extent and frequency, but also to the intensification of turbulent surface heat fluxes due to the increase in wind speed. The sea ice growth rates of OM5 are much higher than those of OM20 inside the polynyas (Figure 3.10c). Moreover, in OM5, sea ice growth rates also appear higher in landfast ice patches. On the contrary, the sea ice production north of the shelf break is lower in OM5 than in OM20. The lower offshore sea ice production in OM5 can be a consequence of the higher ice production rates on the shelf seas which inhibits air-sea exchanges downwind.

The effects of the atmospheric forcing resolution on individual sea ice growth processes are illustrated in Figures 3.10d to 3.10o. The open-water freezing term (Figures 3.10d to 3.10f) refers to the formation of new sea ice in ice-free ocean. Open-water freezing is responsible for intense sea ice formation concentrated on the upwind sides of the polynyas and vanishes after a few kilometers. This process is strongly affected by the forcing resolution: switching from AM10 to AM5 or from AM20 to AM5 both yields an intensification of the open-water sea ice production (though being larger in the second case). Open-water ice formation is lower at high resolution in a few places (Figure 3.10f), which can be explained by the displacement of the landfast ice edges under higher-resolution forcing (see the previous section). After its formation, sea ice can grow through several mechanisms. The dominant term is the bottom growth through the freezing of seawater (Figures 3.10g to 3.10i).

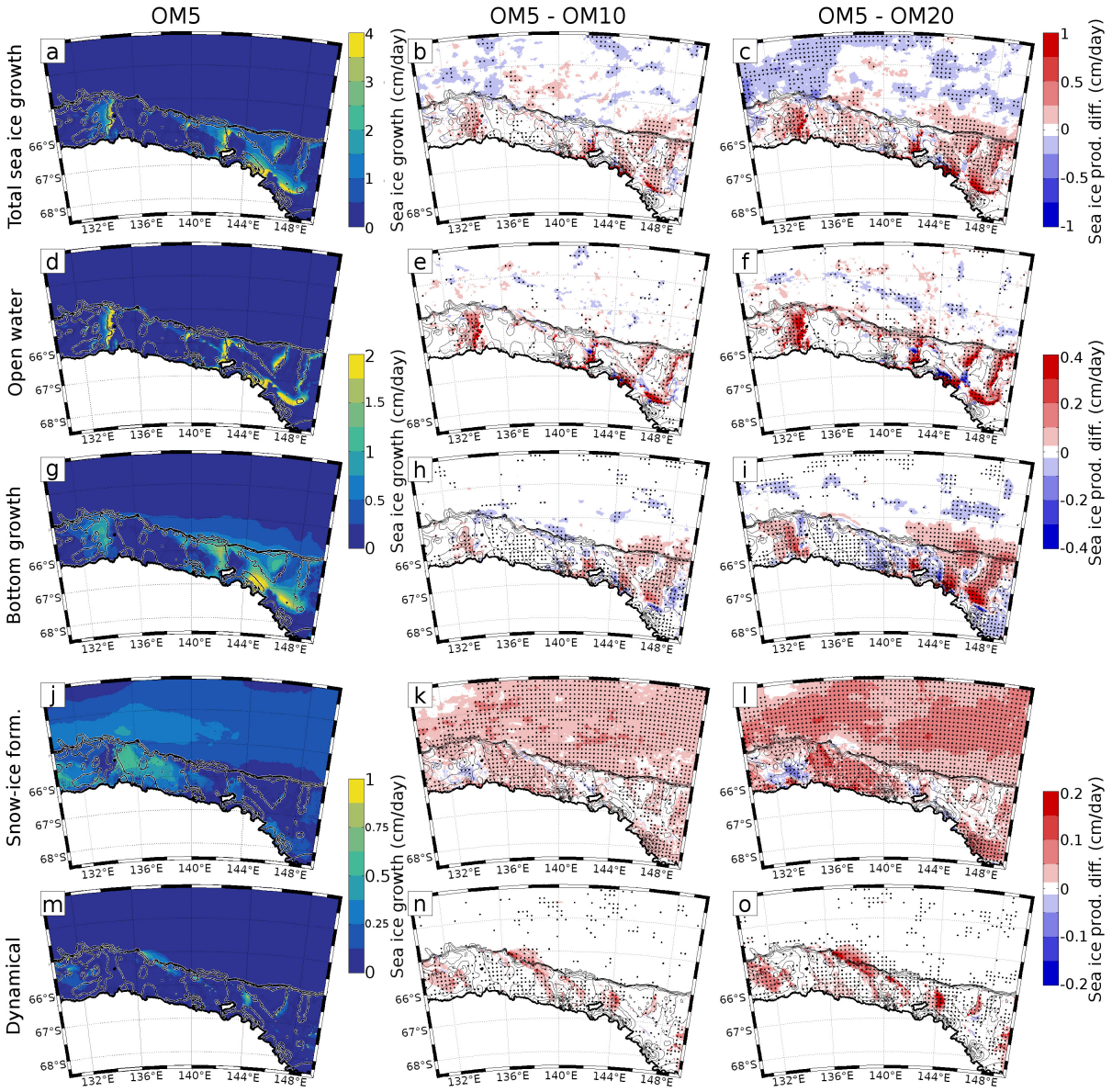

Figure 3.10: Mean daily total sea ice production in OM5 (a), difference with OM10 (b), and with OM20 (c). d), e) and f): same as a), b) c) but for open water sea ice production; g), h) and i): bottom sea ice growth; j), k), l): snow-ice formation. m), n), o): dynamical (ridging and rafting) growth. Note the changes in the color axis range as sea ice growth mechanisms have distinct magnitudes. The maps were produced by averaging the sea ice production terms over fall and winter (April-September) 2010-2015. Black crosses indicate statistical significance (2σ). Thin black contours indicate bathymetry (every 200 m).

This process is more intense for the newly-formed, thin sea ice than for thicker sea ice as the latter inhibits the ocean heat loss. Bottom growth is responsible for important rates of sea ice production in polynyas, downwind the areas of open water formation, and also significantly contribute to sea ice growth at the shelf break. Bottom freezing inside polynyas is enhanced under higher resolution forcing. On the contrary, it is reduced in AM5 compared to AM20 in landfast ice patches. Another mechanism of

sea ice growth is snow-ice formation (Figures 3.10j to 3.10l). When the snow load on top of sea ice becomes too heavy, the snow-ice interface is depleted beneath the sea surface. Seawater then floods the porous snow and freezes in situ. Sea ice growth by snow-ice formation is dominant for landfast ice patches and sea ice north of the shelf seas, but almost null in polynyas (since newly formed sea ice has not accumulated snow yet). Snow-ice formation is enhanced when the forcing resolution increases, both between OM5 and OM10 and between OM5 and OM20. Higher snow-ice formation rates are found in landfast ice and in offshore pack ice. This enhancement certainly results from the lower precipitation in the low-resolution version of MAR (Figure 3.7). Finally, the ridging and rafting induced by sea ice convergence can also lead to sea ice formation. During its deformation, the porosity of the sea ice increases enabling the entrapment of seawater. The entrapped seawater can later freeze in situ, leading to an increase in sea ice volume. This process is referred to as 'dynamical growth' and is illustrated in Figures 3.10m 3.10o. The dynamical growth is maximum upwind of landfast ice patches or grounded icebergs. Its contribution to sea ice growth is small, but it is increased when using high-resolution forcing. This might be one of the reasons for the slight increase in landfast ice probability found at the edges of the landfast ice patches under higher-resolution forcing (Figures 3.9c and 3.9e).

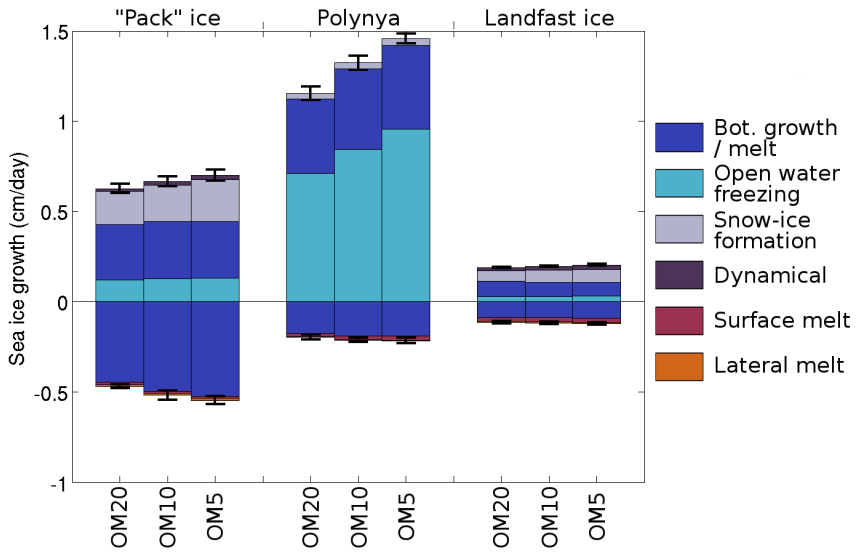

Figure 3.11: Yearly mean sea ice production and melting terms simulated in OM20, OM10, and OM5 for three types of sea ice cover. Landfast ice and polynyas are defined in the same way as in Figure 3.9. "Pack ice" consists of ice-covered regions that are neither polynyas nor landfast ice. The period is 2010-2015. The interannual standard deviation of the yearly sea ice growth and melt rates are indicated on the top and bottom of each bar.

The contributions of individual sea ice growth terms (i.e., open-water freezing, bottom freezing, snow-ice formation, and dynamical growth) and melting terms to

the yearly sea ice budget are shown in Figure 3.11. As the sea ice cover is highly heterogeneous, the distinction is made between landfast ice, polynya sea ice, and "pack" ice. Landfast ice and polynya ice are defined as in Figure 3.9 (i.e. using a velocity criteria for landfast ice and a concentration and thickness criteria for polynya ice). The "pack" ice represents all the sea ice which is neither landfast ice nor polynya ice. Sea ice growth in polynyas is dominated by new sea ice formation in open water, with a non-negligible contribution of bottom sea ice growth. The latter is the dominant term in pack ice production, followed by snow-ice formation and open-water freezing. Snow-ice formation and bottom growth are the main contributors to landfast sea ice vertical growth. Sea ice melt is governed by basal melting in the three types of sea ice cover, with a secondary contribution of surface melt. Lateral melt is only effective in the pack ice. Increasing the forcing resolution enhances the dynamical, snow ice, and open water production terms, and also strengthens the basal melt (as overall, more sea ice is available for melting in summer). In polynyas, the increase in forcing resolution boosts the open water freezing term, whilst leaving the other terms unchanged. Landfast ice growth slightly increases under high-resolution forcing due to an increase in snow-ice formation and dynamical growth. Changes in snow-ice formation on landfast ice or "pack" ice can be imputed to the higher precipitation rates as the resolution of the atmospheric forcing increases.

3.6.2 Polynya dynamics and sensitivity to atmospheric forcing resolution

Increasing the atmospheric forcing resolution mostly affects the sea ice production inside polynyas, as shown in Figures 3.10 and 3.11. Moreover, the coastal polynyas seem more sensitive to an increase in forcing resolution than the polynyas located farther offshore. To understand this difference, we compare a coastal polynya and an offshore polynya, namely the MGP and the MBP. The seasonal and interannual variability of sea ice production in these two polynyas is displayed in Figure 3.12. Sea ice production is increased in OM5 compared to OM10 and OM20, and this throughout all the freezing period and for every year. The MGP (Figure 3.12b) shows higher sensitivity to forcing resolution than the MBP (Figure 3.12a). The annual sea ice production is 25.8% (8.7%) higher for the MGP and 12.4% (6.6%) higher for the MBP in OM5 compared to OM20 (respectively OM5 and OM10). The higher sensitivity of the MGP to forcing resolution can be explained by its proximity to the coast, where the katabatic winds are particularly intensified at high resolution. The estimates of Tamura et al. (2016) are also shown for the period 2010–2013. The estimated yearly sea ice productions are higher than the simulated ones for the MBP and lower for the MGP. Sea ice production estimated by Tamura et al. (2016) shows two peaks in early

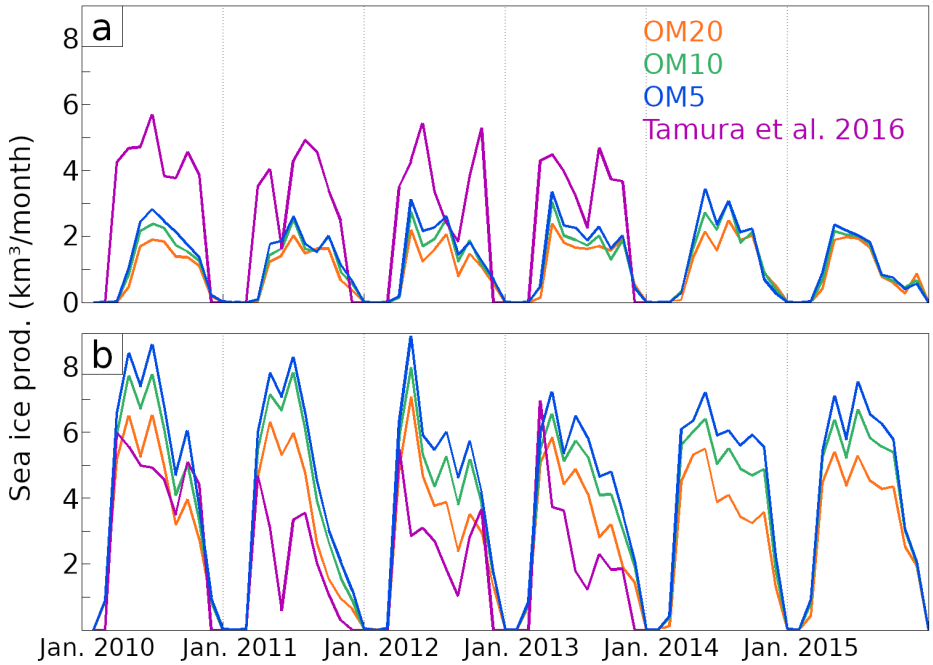

Figure 3.12: Sea ice production summed over (a) the MBP (see Figure 3.1) and (b) the MGP as simulated in OM20, OM10, and OM5, and as estimated by Tamura et al. (2016) (computed using ERA-interim). Simulated sea ice production is the sum of open-water freezing and bottom growth of sea ice thinner than 0.2 m to approach the methodology of Tamura et al. (2016).

fall and late spring for the MBP which are absent from the simulations. The peaks of sea ice production in the early or late freezing season can be related to the hypothesis made by Tamura et al. (2016) who assume that seawater is at freezing temperature, which is probably not the case in late spring and early fall, i.e. when shortwave radiation is non-zero. In the core of winter, estimated and simulated production rates are in better agreement for the MBP, while the MGP produces more sea ice in the simulations.

The distinct sensitivities of the coastal (MGP) and shelf (MBP) polynyas are mainly due to the strengthening and change in direction of the winds in AM10 and AM5 compared to AM20. Figures 3.13c and 3.13d illustrate the probability density distribution of the wind direction θ averaged over the MBP and MGP boxes (θ is the angle between the wind vector and the north, counted positive towards the east). In all experiments, southeasterlies are the most frequent winds over the MBP, with a preferential direction of $\theta = -45°$ and a secondary peak towards 10°. Over the MBP, the wind direction distribution is quite homogeneous between $-45°$ and 15°, suggesting an equal influence of the easterlies and katabatic winds. Winds show a shift towards the east in AM5 compared to AM20. Associated with the change in direction, the intensity of the wind increases with the forcing resolution for both

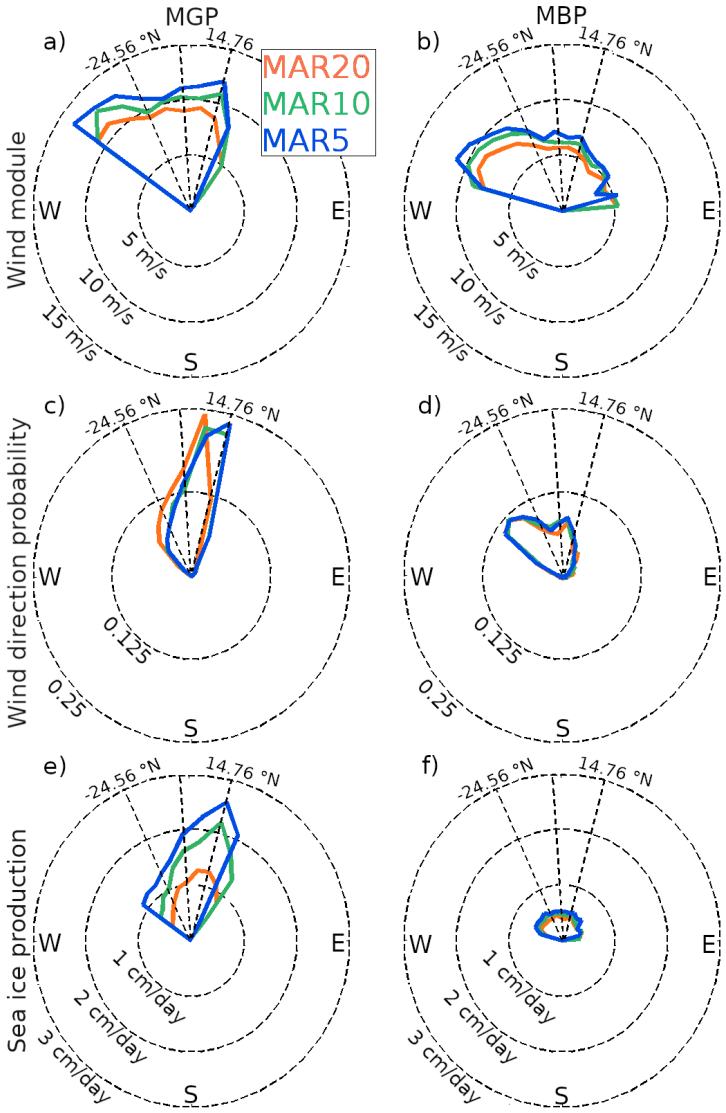

Figure 3.13: Averages of the 3-hourly 10 m wind speeds as a function of wind direction simulated in AM20, AM10, and AM5 during winters of 2010-2015, (a) and (b). Normalized probability density function of the 3-hourly 10 m wind direction θ over the MBP (c) and NBP (d). A direction of 0°N denotes a southerly wind. Sea ice production averaged in the MBP (e) and MGP (f) as a function of wind direction. The distribution are computed using a bin width of 5°. Bins representing less than 0.5% of the events were removed from the panels a, b, e and f for clarity.

polynyas (Figures 3.13a and 3.13b). Winds are intensified with resolution regardless of their direction. The sea ice production in polynyas (hereafter polynya productivity) is depicted in Figures 3.13e and 3.13f. The productivity of the MBP peaks during easterly wind events, while it is maximum for southerly winds in the MGP ($\theta = 15°$). The intensification of winds at high resolution leads to enhanced sea ice production in polynyas. However, this effect is stronger for the MGP than for the MBP as winds favorable to the MGP productivity are more frequent in the high-resolution forcing.

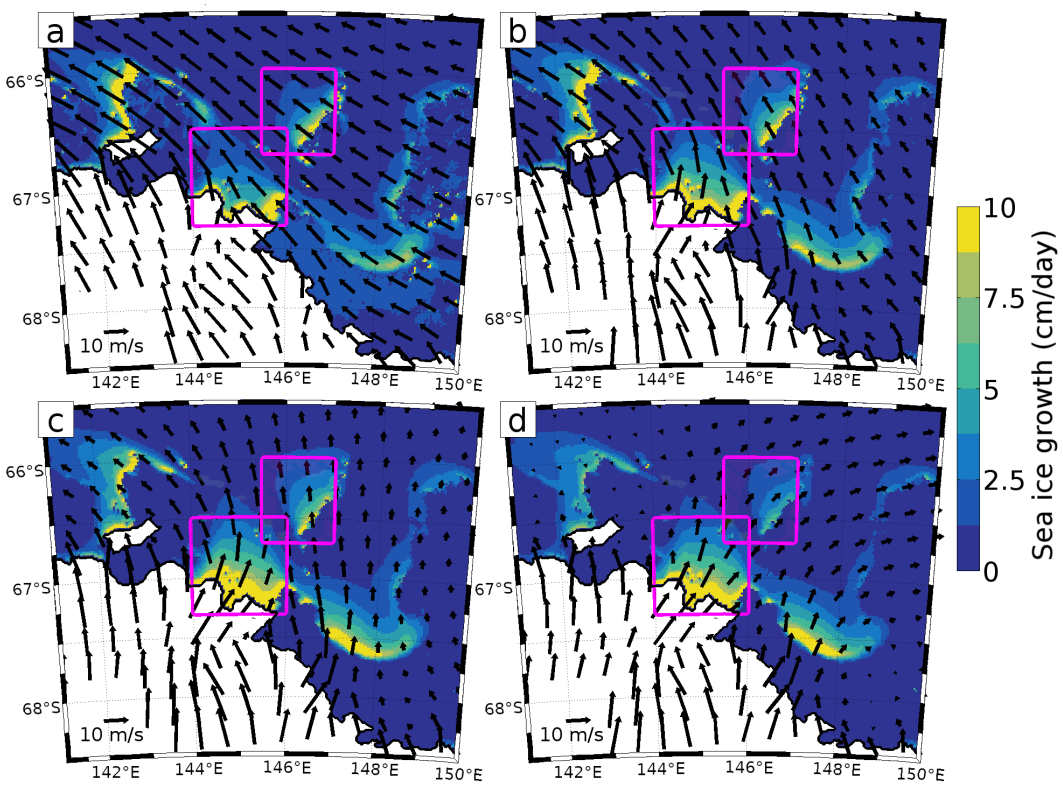

Figure 3.14: 10 m daily wind vectors and sea ice growth rates averaged over each quartile of the wind direction distribution of the MGP in AM5/OM5. The maps and quartiles are built using fall-winter (May to September) data from years 2010 to 2015. (a) 1st quartile ($\theta < -24.56°$N), (b) 2nd quartile ($-24.56°$ N $< \theta < -3.89°$ N), (c) 3rd quartile ($-3.89°$ N $< \theta < 14.76°$ N) and (d) 4th quartile ($\theta > 14.76°$ N). Pink boxes indicate the MBP (north) and MGP (south).

The different wind regimes over the eastern D'Urville Sea are illustrated in Figure 3.14. Each wind regime is defined as the mean wind pattern averaged for one quartile of the wind direction distribution over the MGP in AM5 (Figure 3.13b). The transition from the easterlies case (1st quartile) to the westerlies case (4th quartile) is accompanied by an overall decrease in area-averaged wind speed, a decrease of northern polynyas productivity (B9BP, MBP, and NBP), and an increase in southern polynyas productivity (MGP and NGP). Easterly winds are indeed less favorable to the opening of coastal polynyas, as they push sea ice towards the coast. Southerlies or westerlies, however, support the northward expansion of the MGP and NGP. In the 3rd and 4th quartiles, katabatic winds dominate the weaker large-scale winds, favoring the opening of the southern polynyas. This suggests that the MGP and NGP are primarily driven by katabatic winds, while the B9BP, MBP, and NBP are rather driven by the easterlies. In addition to the increase in wind speed at high resolution, the shift in direction might also explain the local increase in sea ice production, particularly strong for the MGP and NGP.

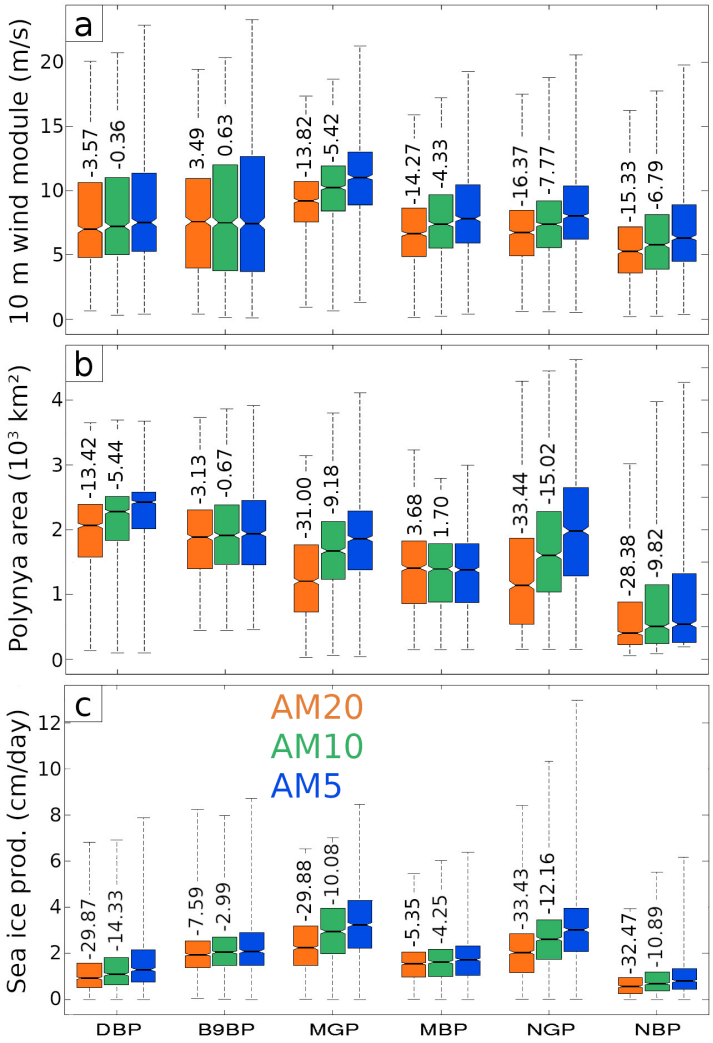

Figure 3.15: Distribution of (a) daily 10 m wind speed, (b) polynya area and (c) sea ice growth rate averaged over polynyas off Adélie Land (see Figure 3.9b for polynya definition), as simulated by OM20, OM10, and OM5 (respectively AM20, AM10 and AM5 for atmospheric fields) during winters of 2010-2015. Horizontal black lines indicate the median values; the top and bottom of the bars corresponds to the 75th and 25th percentiles, respectively. The maximum to minimum range is depicted by the dashed whiskers. The averages of the relative difference between coarse-resolution experiments and OM5 (resp. AM5 for winds) are listed as percentages above the boxes.

Figure 3.15 sums up the sensitivity of the wind and sea ice production for the main polynyas off the Adélie Land coast (see Figure 3.1). While the winds over the DBP and B9BP are only slightly sensitive to the atmospheric model resolution, all four eastern polynyas (MGP, MBP, NGP, and NBP) undergo an approximate 15% wind increase between the AM20 and AM5 forcings. The MGP, NGP, NBP, and DBP have a strong sensitivity to the atmospheric forcing resolution, with a sea ice production and polynya extent increase by up to 30% between OM20 and OM5. On the contrary, the B9BP and the MBP experience a weaker sensitivity to the forcing resolution with an intensification of sea ice production by 10%. The lower sensitivity of the B9BP

to the increase of resolution can be explained by the weaker increase in wind speed over the B9BP than for the other polynyas. For the MBP, the wind increase has the same magnitude as for the MGP, but the intensification of wind with resolution is accompanied by an increase in southerly wind frequency, which is detrimental to sea ice production in the MBP (see Figures 3.13 and 3.14). Higher sea ice advection from southern polynyas can also inhibit the sea ice growth in polynyas located downwind, limiting the sensitivity of northern polynyas to a wind intensification. Coastal polynyas (MGP and NGP) forced by katabatic winds are more sensitive to the change in wind intensity and direction associated with the refinement of the atmospheric model grid than polynyas located further offshore. The comparison of the sea ice production in polynyas and of the polynya extent between the three simulations reveals that the use of AM10 instead of AM5 has a weaker impact than the use of AM20 instead of AM5. The sea ice production is decreased by 3 to 10% (except the 15% of the NGP) between OM10 and OM5, and by 5 to 33% between OM20 and OM5 suggesting a limitation of the effect of the forcing resolution below 10 km.

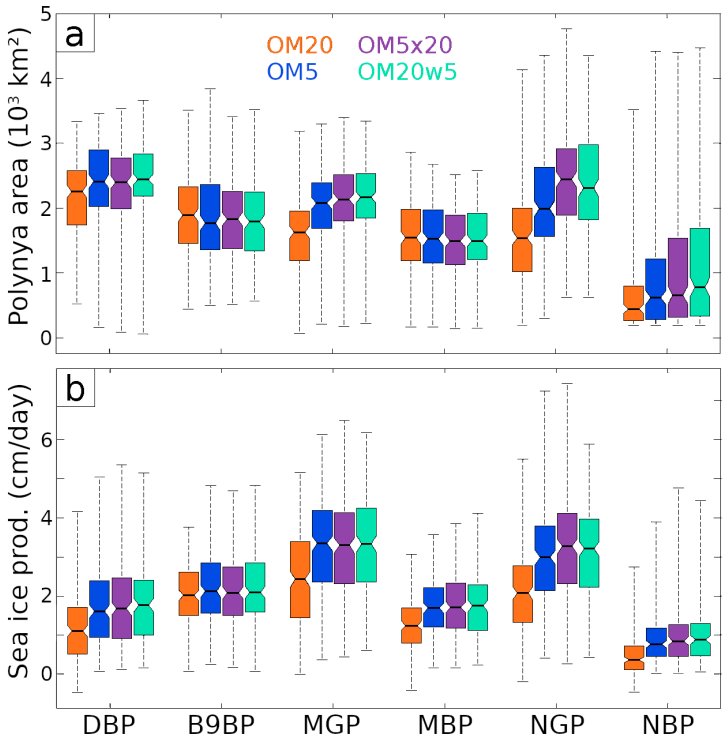

Figure 3.16: Same as Figures 3.15 b and 3.15c for years 2009-2010, including sensitivity experiments OM20w5 and OM5x20.

Increasing the atmospheric model resolution affects the spatial variability of the forcing fields and the atmosphere dynamics. To disentangle these two effects, the experiment OM5x20 is used (ocean–sea ice simulation forced by AM5 averaged on the AM20 grid). In addition, the sensitivity of the polynyas to the forcing resolution

may differ from one atmospheric field to the other. The sensitivity of the polynyas to an increase in the resolution of the wind is tested in OM20w5 (simulation forced by the winds of AM5 and other atmospheric fields from AM20). The polynya area and productivity simulated in these two experiments are compared to those of simulations OM20 and OM5 in Figure 3.16. For most polynyas, the sea ice production and polynya area in OM5x20 and OM20w5 are similar to those of OM5. The fact that OM5x20 does not strongly differ from OM5 suggests that most of the effect of the resolution arises from the modification of the atmospheric model dynamics, i.e., from the intensification and change of direction of the coastal winds. It can be noted that the size and the sea ice production of the NGP vary quite substantially between these experiments. The NGP appears to be sensitive to the small-scale winds (smoothed in OM5x20) or to the increase of resolution for other atmospheric fields than the winds. The NGP is subjected to intrusions of warm modified Circumpolar Deep Water from the east. Slight changes in the local wind divergence or curl due to the coarsening of the AM5 winds onto the AM20 grid might affect the transport of mCDW into the NGP but not in the other polynyas.
Increasing only the resolution of the wind and not that of the other atmospheric fields (simulation OM20w5) yields similar results than OM5. These results show that very high resolution matters less than simulating adequate wind speed and direction, although a high-resolution atmospheric model may be required to produce adequate winds.

The increase of air-ice momentum transfer resulting from the intensification of the winds with a refined resolution could also be simulated by adjusting the transfer coefficients. The transfer coefficients are indeed poorly constrained by observations and likely varies with the properties of sea ice, and adapting them could be an approach to better simulate polynyas in coarse-resolution models. In Figure 3.17, we compare simulations OM20 and OM5 to the simulation OM20Cd1.3. OM20Cd1.3 is identical to OM20 (i.e. it is forced by AM20) but the air-ice drag coefficient has been increased by 30% (i.e. from 1.4×10^{-3} to 1.82×10^{-3}). Increasing the air-ice drag coefficient has a similar effect on polynyas size and sea ice production as increasing the forcing resolution: compared to OM20, OM20Cd1.3 simulates higher polynya extent (between +4% and +43%) and sea ice production (from +13.88% to +48.05%). The response of coastal polynyas is also stronger than for the offshore ones, as obtained from an increase in resolution. However, despite the strong (+30%) increase of the air-ice drag coefficient compared to the intensification of wind speeds (up to +15% between AM20 and AM5), the polynya extent and sea ice production simulated in OM20Cd1.3 do not reach the ones of AM5. If increasing the air-ice transfer coefficient can mimic the effects of wind speed intensification due to model

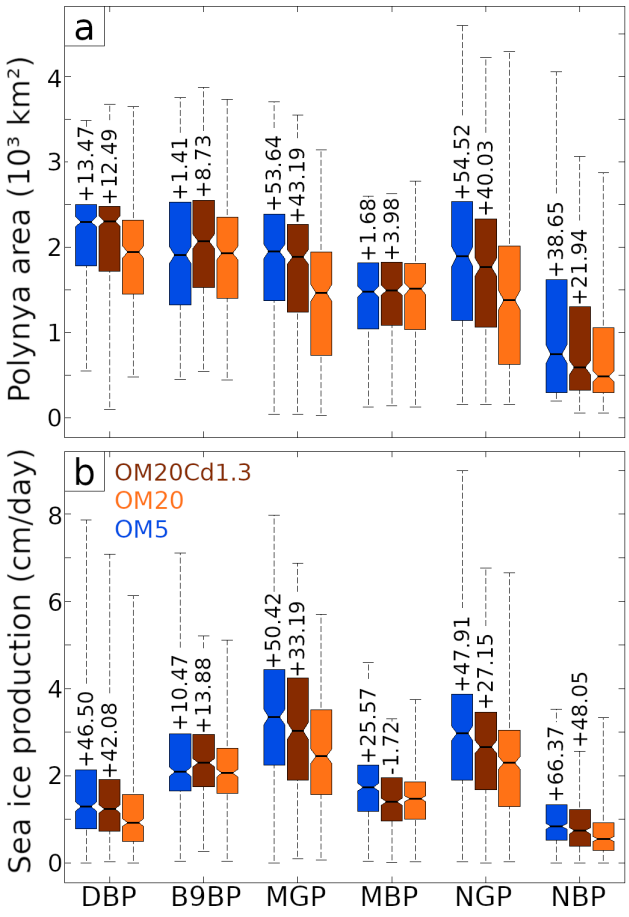

Figure 3.17: Same as Figures 3.15 b and 3.15c for years 2010-2011, including sensitivity experiment OM20Cd1.3

grid refinement, it presents several limitations. The momentum transfer from winds to sea ice is increased regardless of the wind orientation (although offshore winds are more affected by the model resolution) and the dependence of air-sea turbulent heat fluxes on wind speed is not accounted for. Besides, modifying the air-ice drag coefficient might affect the simulated sea ice and ocean far beyond coastal polynyas, as it will alter the large-scale sea ice advection and momentum transfer from the ice to the ocean. Parameterizing the effects of intense, small-scale winds on coastal polynyas by adapting the transfer coefficients as it has been done here is likely too crude to improve coarse-resolution models. A more tailored approach, targeting only the offshore components of the wind velocity in areas of intense sea ice divergence and accounting for the effects on air-sea exchanges could be a better solution.

3.7 Effects of atmospheric forcing resolution on salt flux and water mass transformations

The increase in atmospheric forcing resolution enhances the sea ice production in the coastal seas off Adélie Land, thanks to the increase in polynya frequency. Due to the brine released during sea ice freezing, such changes might have important repercussions for the salt budget and water mass transformations off Adélie Land. Figure 3.18a shows the salt budget associated with sea ice freezing or melting cumulated over the entire Adélie Land sector. The simulations exhibit a positive salt budget in the first 200 km from the coastline. Several peaks corresponding to the polynyas and the shelf break can be identified. Further offshore, the salt budget is negative. The Adélie Land sector is a region of net production and export of sea ice, as the positive salt flux is not entirely compensated by the negative one. Increasing the atmospheric forcing resolution substantially affects the amount of salt being rejected into the ocean in the first 200 km from the shore. Switching from AM20 to AM5 and from AM10 to AM5 increases the near-shore salt flux by 17% and 5.9%, respectively.

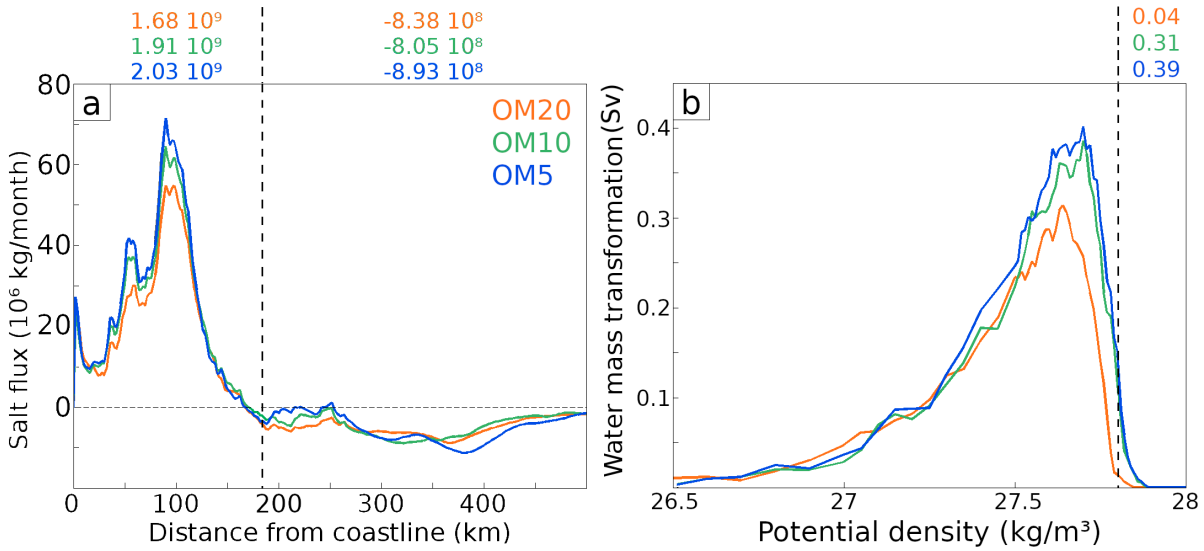

Figure 3.18: (a) Meridional section of the yearly salt fluxes due to brine rejection or sea ice melting, averaged between 2010-2015. The vertical dashed line indicates the transition between positive (left) and negative (right) salt fluxes used to compute the total salt fluxes (numbers on top, in kg/month). (b) Mean water mass transformation rates by surface buoyancy fluxes per potential density class (referenced to the surface). The dashed line indicates potential density anomaly $\sigma_0 = 27.80$ kg/m³, i.e. the lowest density for Shelf Waters (which includes Dense Shelf Water) set following Kusahara et al. (2011b) . Total shelf water transformation rates are listed on top of the diagram (in Sv). The diagnostics are computed from OM20, OM10, and OM5 outputs on the whole sector for panel (a) and in the box "east" (see Figure 3.1) for panel (b).

Another key process associated with polynyas is the production of Dense Shelf Water, potentially feeding the deepest limbs of the global ocean circulation. The water mass transformation rates are computed in the box "east" of Figure 3.1 for the experiments OM20, OM10, and OM5. To calculate these rates of transformation, we follow the methodology of Abernathey et al. (2016), also used in Jeong et al. (2020). A potential density scale is defined, ranging from 24.9 kg/m^3 to 28 kg/m^3, with decreasing density step from 0.1 kg/m^3 to 0.01 kg/m^3 to refine the resolution on the high-density end. The buoyancy flux associated with brine rejection is used to derive a water mass production rate for each density class previously defined. The transformation of Dense Shelf Waters (waters with a potential density of 27.80 kg/m^3) is 0.39 Sv in OM5 (Figure 3.18b). Williams et al. (2008) estimated that 0.1 to 0.5 Sv of Dense Water outflow the Adélie Depression at the Adélie Sill. Note that our estimate integrates a broader area than the Adélie Depression and that Williams et al.'s estimates were performed before the breaking of the Mertz ice tongue.

The production of water masses with a potential density above 27.5 kg/m^3 is considerably increased in OM10 and OM5 with respect to OM20 (see Figure 3.18b). The distribution of water masses being transformed in OM10 and OM5 is shifted towards higher density waters. The transformation of Dense Shelf Water (waters denser than 27.80 kg/m^3, as in Kusahara et al. (2011b)) is much lower in OM20 (0.04 Sv) compared to OM10 and OM5 (0.31 Sv and 0.39 Sv, respectively). Under higher-resolution forcing, there is a clear shift towards higher rates of dense water production, and towards the production of denser waters. A notable result from this analysis is the similarity between OM10 and OM5 regarding water mass transformation rates. This is in line with the fact that the increase in sea ice production is weaker between OM10 and OM5 compared to that between OM10 and OM20.

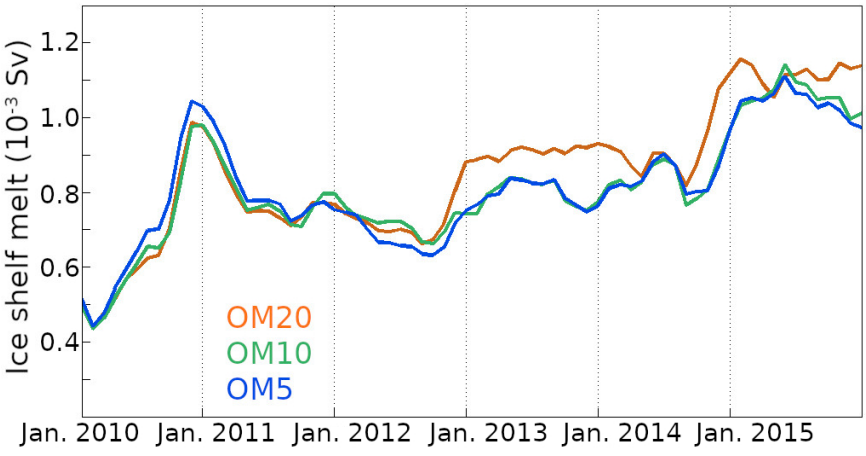

Figure 3.19: Total ice shelf basal melt in the Adélie Land sector simulated in OM20, OM10 and OM5.

A second important contributor to the salinity budget in the coastal seas of Antarctica is the freshwater flux from ice shelf melt. Ocean–ice shelf interactions at the ice shelf base can for instance transform Shelf Waters into lighter water masses (Huot et al., 2021a). The total ice shelf basal melt simulated in the OM20, OM10, and OM5 simulations are shown in Figure 3.19. The three experiments have similar ice shelf basal melts between 2010 and 2013. After 2013, the ice shelf melt is increased by 1×10^{-4} Sv in OM20 compared to OM10 and OM5, while OM10 and OM5 have identical basal melts. Ice shelf basal melt is linked to the polynya activity as the ice shelf melt rate depends on the temperature of the water entering the ice shelf cavities. The production of cold and saline waters in polynyas can thus limit the basal melt of the neighboring ice shelf. As OM20 produces less sea ice and less Shelf Waters, less cold waters enter the ice shelf cavities and the ice shelf basal melt is higher than in OM10 and OM5. The similarities of ice shelf basal melt between OM10 and OM5 can be related to their similar rate of production of Shelf Waters (Figure 3.18b). The increase of production of Shelf Waters in OM10 or OM5 compared to OM20 is reinforced by the weaker consumption of these water masses via ocean–ice shelf interactions. Increasing the atmospheric forcing resolution affects the Dense Water budget in two ways: it increases the production of Dense Water thanks to the intensification of polynya activity and it decreases the consumption of Dense Water through ocean–ice shelf interactions by decreasing the ice shelf melt rate.

3.8 Discussion

This study examined the sensitivity of winds, sea ice, and ocean salt fluxes off Adélie Land to an increase in resolution of the atmospheric model and forcing beyond the resolution of present global reanalyses. To do so, we have performed a set of regional atmospheric simulations at 20, 10, and 5 km resolutions. These experiments revealed that katabatic winds are intensified and extend further offshore when the atmospheric resolution is increased. At higher resolution, the offshore component of the winds (perpendicular to the coastline) is intensified. The changes in wind speed and direction were attributed to the better representation of the steep continental slopes and of the valleys channelizing the katabatic flow. The three atmospheric simulations were then used to force a $1/24^\circ$ resolution regional ocean–sea ice model. Due to the higher wind speed and wind-driven sea ice divergence, sea ice production is substantially increased under higher-resolution forcing, especially in polynyas. Polynyas are larger and produce up to 30% more sea ice when using a 5 km instead of a 20 km forcing resolution. Yet, each polynya presents a distinct sensitivity to forcing resolution depending on the local wind conditions, with coastal polynyas being more

sensitive than those located further offshore. The increase in sea ice production with higher resolution forcing affects the salinity budget over the whole Adélie Land sector and intensifies the production of Dense Shelf Water. These results demonstrate the sensitivity of coastal sea ice to small-scale atmospheric processes.

The results presented here suggest that simulated coastal polynyas are highly sensitive to the resolution of the atmospheric forcing. The use of coarse-resolution forcing might be a limitation for sea ice and ocean modeling off Antarctica. As mentioned earlier, many regional high-resolution models are forced by relatively coarse-resolution global atmospheric reanalyses (Marsland et al., 2004, 2007; Kusahara et al., 2011a; Cougnon et al., 2013; Kusahara et al., 2017; Cougnon et al., 2017; Donat-Magnin et al., 2017; Huot et al., 2021a). Despite the recent increase in horizontal resolution of these reanalyses, our results indicate that the use of higher-resolution forcing intensifies the activity of coastal polynyas, which are crucial for the atmosphere–sea ice–ocean exchanges in the coastal Southern Ocean. It has to be noted that using ERA5 as atmospheric forcing leads to similar sea ice production rates than our experiment OM5 (see the supplementary material, Section 6.2.1), but this was attributed to differences in the physics of both models and does not undermine our conclusions about the effects of the resolution. However, it is worth mentioning that most of the impact of the forcing resolution is already achieved at a horizontal resolution of 10 km. We found that the intensification of wind speeds and sea ice production in response to an increase in the atmospheric model resolution are higher between 20 km and 10 km resolution than between 10 km and 5 km resolution. The increase in dense water production with forcing resolution becomes even insignificant between OM10 and OM5. Dividing the resolution of the atmospheric by a factor 2 has a stronger impact from 20 to 10 km resolution than from 10 to 5 km resolution.

The Adélie Land sector has a relatively smooth topography compared to mountainous regions of Antarctica, suggesting that our conclusion about the role of forcing resolution can be extended to other sectors of Antarctica with similar topography. The 10 km resolution appears as a reasonable compromise between realism and computational cost for the forcing of coastal sea ice and ocean models. The use of higher resolutions could remain necessary for the study of certain areas, such as the coastal polynyas off the Mertz and Ninnis glaciers, or in mountainous areas of Antarctica such as the Antarctic Peninsula (Petrelli et al., 2008; Ebner et al., 2014). Another way of accounting for these locally intense winds is to correct global reanalyses using a higher-resolution regional model, as proposed by Mathiot et al. (2010). Such a method is supported by the results from our experiment OM5x20, as coarsening the high-resolution atmospheric forcing yields only minor changes.

Finally, the sensitivity of the ocean and sea ice to atmospheric forcing resolution would also most likely depend upon the resolution of the ocean grid itself, and on the representation of grounded icebergs and landfast ice.

Under higher wind speeds, the sea ice production in coastal polynyas drastically increases (e.g., +30% for the MGP and NGP for a +15% intensification of the wind speed). This implies some precautions for the estimation of the sea ice production in polynyas from remote sensing data. Tamura et al. (2016) constructed a valuable dataset gathering the sea ice growth rates in coastal polynyas off Antarctica. However, their estimates rely on coarse-resolution atmospheric reanalyses, probably simulating too weak winds down katabatic corridors. Our results suggest that their sea ice growth rates might be significantly underestimated for some polynyas, such as the Mertz and Ninnis glacier polynyas as MAR produces stronger and more realistic winds than the ERA5 global reanalysis in these areas.

The katabatic winds of Adélie Land appear to be highly sensitive to the resolution of the atmospheric model. However, our experiments only consider part of the response of the atmosphere to an increase in resolution. Indeed, the sea ice concentrations and sea surface temperatures are identical in the three atmospheric simulations. The role of small-scale spatial heterogeneity of the sea ice cover is for instance not accounted for. In addition, the atmosphere only partially responds to the increased air-sea heat flux in polynyas due to the wind intensification, as the sea ice conditions are prescribed in MAR. The intensification of heat, moisture, and momentum exchanges due to the enlargement of the polynyas would warm and moisten the air, potentially destabilizing the air column and thus affecting atmospheric convection (Weijer et al., 2017). Air-sea interactions above polynyas have been shown to produce breeze-like circulations that can intensify the downslope katabatic winds (Gallée, 1997; Savijärvi, 2011), but would also warm and saturate the air with water vapor, further increasing the snow accumulation over the ice sheet (Kittel et al., 2018). The impact of these processes on the activity of polynyas can be significant (Jourdain et al., 2011) but are not accounted for in our forced experiments.

3.9 Conclusion

Our results show that the representation of small-scale coastal winds, essential for the activity of coastal polynyas, strongly depends upon the atmospheric model resolution in the Adélie Land sector. At higher resolution, katabatic winds are shown to be significantly swifter and to extend further offshore. These changes increase the size of

polynyas and enhance sea ice production by up to 30%. Larger volumes of sea ice are produced in coastal seas under high-resolution forcing, affecting the salinity budget of the Southern Ocean and the production of Dense Shelf Water. Thus, we conclude that atmosphere–sea ice–ocean interactions in coastal Antarctica are highly sensitive to the resolution of the atmospheric forcing. Our results suggest that a resolution of 10 km might be needed to force an ocean–sea ice model off Adélie Land and potentially other sectors of Antarctica. Further resolution refinement yields locally significant impacts but has minor effects on the sector-averaged salt budget and water mass transformations.

While the importance of polynyas for the polar climate is indubitable, further work is needed to understand their driving mechanisms and to find a suitable approach to incorporate them in global climate models. The high sensitivity of polynya activity and dense water formation to the local wind questions their response to future atmospheric circulation changes in Antarctica such as the projected shift in Southern Ocean westerlies (Spence et al., 2014) which could affect the evolution of katabatic or easterlies (Hazel and Stewart, 2019) in a warmer climate. The response of polynyas to the modification of the atmospheric conditions with climate change is an important question, as changes in polynya activity would have far-reaching consequences for the global ocean circulation and ice sheet mass balance. In parallel, the importance of feedbacks between the ocean, ice, and air above polynyas remains mostly unknown and would require further work using high-resolution coupled atmosphere–sea ice–ocean models.

Chapter 4

Effects of ocean mesoscale eddies on atmosphere–sea ice–ocean interactions off Adélie Land, East Antarctica

This chapter is based on the article "Effects of ocean mesoscale eddies on atmosphere–sea ice–ocean interactions off Adélie Land, East Antarctica" submitted to Climate Dynamics (by Huot P.-V., Kittel C., Fichefet T., Jourdain N. C., Fettweis X.).

4.1 Foreword

The first two chapters were focused on small-scale processes affecting the atmosphere–cryosphere–ocean interactions in coastal seas. In these chapters, I have shown that ocean–ice shelf interactions, tides, and small-scale winds were impacting the production of dense waters. Thus, the lower cell of the Southern Ocean overturning circulation could be partially controlled by small-scale processes. It is indubitable that coarse-resolution global climate models would struggle to represent these processes, as the continental shelves are usually not wider than a few 100s of kilometers. However, it is less clear that small-scale processes would have such an impact on the upper cell of the overturning circulation. As the ocean is much deeper there, it is likely less crucial to represent the small-scale variability of the bathymetry than in coastal seas. An increase in resolution, however, would deeply affect the dynamics of the ocean circulation by enabling the representation of mesoscale eddies. Mesoscale eddies have the potential to affect the interactions of the ocean with the atmosphere or sea ice due to their characteristic imprint on surface currents, temperature, salinity, or stratification. The effects of eddies on atmosphere–sea ice–ocean interactions in the seasonally ice-covered Southern Ocean are mostly unknown, but if eddies could affect the momentum, heat, or salt exchanges between the ocean, sea ice, or atmosphere, they would possibly have an impact on

the upper cell of the Southern Ocean MOC. Understanding how mesoscale eddies can modulate atmosphere–sea ice–ocean interactions and the momentum or buoyancy fluxes at the ocean surface is the subject of the present chapter.

4.2 Summary

Mesoscale eddies are responsible for most of the ocean surface variability at horizontal scales ranging from 1 to 100 km. However, their influence on the interactions between the ocean and the atmosphere or sea ice is poorly known. Here, we explore how eddies influence air–sea ice–ocean interactions off Adélie Land, in East Antarctica. We use a high-resolution regional atmosphere–sea ice–ocean coupled model based on the NEMO-LIM and MAR models. The model represents known features of mesoscale air-sea coupling such as the response of near-surface winds to surface temperature gradients or ocean currents vorticity, but here, we can investigate how it is affected by the sea ice. The presence of sea ice is found to either have no influence or to amplify the response of the atmosphere to the small-scale variability of surface conditions. We then investigate how eddies affect the sea ice and atmosphere. Through the modulation of air-sea or ocean-ice heat and momentum fluxes, eddies mark the sea ice and the near-surface atmosphere. Eddies are found to drive sea ice advection and melting or freezing at small scale, with sea ice growth anomalies of +0.5 cm/day over cyclonic eddies (-0.5 cm/day for anticyclonic eddies). Anticyclonic eddies are associated with warmer sea surfaces and lower sea ice concentrations while cyclonic eddies have the opposite signature. The atmosphere response to ocean eddies is weak in the absence of sea ice, but becomes more significant over partially ice-covered eddies: the air is up to 0.2°C warmer above anticyclonic eddies, winds up to 0.1 m/s faster, and the turbulent heat fluxes up to 10 W/m² stronger (the sign is reversed for cyclonic eddies). These results suggest that eddies can affect air-sea interactions in the polar oceans via their imprint on the sea ice cover. Then, we assess how the eddy-driven air–sea ice–ocean interactions affect the sector-averaged surface momentum and buoyancy fluxes. We conduct a numerical experiment in which the imprint of eddies on ocean surface conditions is filtered out. We find that eddies weaken the momentum input into the ice-free or ice-covered ocean by approximately 10% due to their friction on the atmosphere or sea ice. The additional friction of eddies leads to a decrease in the regional ocean kinetic energy by 8%. In addition, we find that eddies are important contributors to the northward sea ice advection. When eddies are allowed to interact with sea ice, the freshwater flux north of the seasonal ice zone is increased by 15%, impacting the ocean stratification and the transformation of water masses. Our model shows that ocean eddies affect the ocean, atmosphere, sea ice, and their interactions in the seasonally ice-covered Adélie Land sector.

4.3 Introduction

The exchanges of heat, freshwater, and momentum at the air-sea interface are primordial drivers of the ocean circulation and especially, of the Southern Ocean circulation. The Southern Ocean is a central component of the Earth's climate: it contributes to isolate Antarctica from meridional heat transport (Martinson, 2012) and hosts a large part of the exchanges between the surface and the deep ocean thanks to winter deep convection (Orsi et al., 1999). The Southern Ocean is also closely tied to the AIS: ice–shelf basal melt was found to be the main cause of Antarctic ice mass loss during the past decades (Rignot et al., 2019). To understand how the Earth's climate will evolve, it is necessary to better comprehend the drivers the evolution of the Southern Ocean. The ACC is suggested to be forced by surface momentum (Allison et al., 2010) or buoyancy fluxes (Hogg, 2010). Coupled with the ACC, the Southern Ocean hosts a meridional thermohaline circulation which is driven by surface heat and freshwater fluxes (Walin, 1982; Abernathey et al., 2016). The wind curl above the Southern Ocean also drives upwelling which closes the global meridional overturning circulation (Marshall and Speer, 2012). The drivers of the ACC or the Southern Ocean thermohaline circulation are still discussed, though. Besides the role of surface fluxes, other mechanisms were advanced (Thompson and Garabato, 2014; Marshall et al., 2017). Yet, it is indubitable that the interactions between the ocean and the atmosphere or the sea ice play a substantial role in the Southern Ocean dynamics. But the understanding of the processes affecting the atmosphere–sea ice–ocean interactions in the Southern Ocean remains incomplete. For instance, the role of processes taking place at small scales (below 100 km) is mostly unknown. This is due to the lack of high-resolution observations and to the cost of high-resolution models. These small-scale processes include the ocean mesoscale eddies.

Ocean mesoscale eddies are swirling circulation patterns in quasi-geostrophic equilibrium with scales ranging from 10 to 100 km. Eddies are ubiquitous in the World Ocean, observed almost everywhere except for the equatorial oceans (Faghmous et al., 2015). They are particularly active in the energetic currents such as Western Boundary Currents or the ACC, where they are generated by baroclinic instabilities of the flow or through flow-topography interaction. Eddies play an important role in the ocean dynamics as they represent most of the ocean kinetic energy (Ferrari and Wunsch, 2010) and potentially contribute to the transport and mixing of temperature, salinity, or carbon (Moreau et al., 2017).

Eddies can also modulate the interactions between the ocean and the atmosphere. Indeed, eddies often have a typical imprint on the sea surface temperature, salinity, and ocean currents, which can affect the turbulent fluxes at the air-sea interface

(Villas Bôas et al., 2015). Their effects on air-sea interactions have been extensively studied in the past two decades. It appears that, at small scales, the sea surface temperature variability can drive the variability of air-sea heat fluxes. For instance, O'Neill et al. (2005) observed a linear relationship between surface temperature gradients and wind stress curl over the Aghulas Current. This relationship was confirmed by modelling studies (Song et al., 2009) and other observations (Chelton et al., 2007; Chelton and Xie, 2010a). The underlying mechanisms, described in Small et al. (2008), involve a modification of the near-surface atmosphere stability, vertical momentum transfer, and surface pressure in response to air temperature changes. Eddies also affect air-sea momentum fluxes via their imprint on surface currents. The friction of ocean eddies on the atmosphere generates a wind stress curl (Renault et al., 2017a), reducing the eddy kinetic energy and lifetime (Renault et al., 2016), and affecting large-scale currents (Renault et al., 2017b). Eddy-induced stress curl also generates small-scale Ekman pumping (Gaube et al., 2015). The modulation of air-sea fluxes by eddies however seems to be variable in space and time. Small et al. (2019) showed that the drivers of the air-sea fluxes small-scale variability vary from one region to another.

In the Southern Ocean, Frenger et al. (2013) observed the imprint of eddies on wind speeds, cloud cover, and precipitation. Eddies also influence the mixed-layer depth, potentially affecting air-sea interactions (Hausmann et al., 2017). The interactions are two ways, as winds dampen the submesoscale activity (Du Plessis et al., 2019). The impact of eddies on air-sea momentum fluxes was found to impact the ACC energy budget and stratification (Song et al., 2020). Through this mechanism, eddies were suggested to drive Southern Ocean multi-decadal variability (Le Bars et al., 2016). Though it is clear that eddies influence air-sea exchanges, it is unclear whether these processes are at play in the ice-covered Southern Ocean. High-latitude eddies are often smaller than elsewhere in the ocean, limiting the possibility for the atmosphere to respond to their presence. Average winds over the Southern Ocean are particularly strong, with very frequent storms, which may reduce the relative importance of ocean currents with respect to wind velocity compared to other eddy-prone regions. The low sea ice temperature may lead to the development of temperature inversions making the low-level atmosphere very stable, inhibiting the atmosphere's sensitivity to surface conditions. Besides, thermal contrast between sea ice and leads or polynyas may induce mesoscale convective features (Gryschka et al., 2008). Finally, thick sea ice insulates the ocean from the atmosphere and could shut down mesoscale air-sea interactions during winter. Whether eddies impact air-sea interactions to a significant extent over the Southern Ocean regions remains an open question.

The imprint of eddies on the atmosphere can arise from their imprint on sea ice. Recent observations suggest that eddies affect the sea ice concentration and drift. By detecting the imprint of eddies on sea ice concentration, Kozlov et al. (2019) described the eddy activity in the Arctic. Cassianides et al. (2021) proposed a method to detect eddies beneath sea ice via their imprint on the sea ice vorticity. Eddy-like swirls can also be found in the sea ice (see Figure 1 of Manucharyan and Thompson (2017)). The interactions of eddies with sea ice have already been simulated in several models. Manucharyan and Thompson (2017) suggested that eddies and sea ice interact in the development of the Marginal Ice Zone (MIZ). They showed that eddies spontaneously appear in the MIZ where they affect sea ice advection and ocean-ice heat fluxes. Besides, the curl of eddies currents leads to sea ice divergence or convergence, affecting the air-sea and ocean-ice heat exchanges. Similar to the friction of eddies on the atmosphere (Renault et al., 2016), eddies also rub on the sea ice, which drives Ekman pumping or eddy-ice pumping (EIP) in the ocean. This process is described in Gupta et al. (2020), who showed that EIP reduced sea ice thickness by 10% and mixed layer depth by 60% due to increased sea ice melt in an idealized Southern Ocean simulation. Sea ice can also affect the eddy activity, either through eddy friction on it or by controlling lateral density gradients through melting and brine rejection. Horvat et al. (2016) showed that sea ice melting at the edges of ice floes drives submesoscale circulation. As mesoscale eddies influence sea ice, they could as well affect the air-sea interactions and the atmosphere in ice-covered regions. Observations of small-scale atmosphere–sea ice–ocean interactions are however too scarce to evaluate the role of eddies.

With the present study, our goal is to explore how mesoscale eddies influence air-sea interactions in the presence of sea ice. To do so, we have developed a high-resolution regional coupled model of the ocean, sea ice, and atmosphere based on the NEMO-LIM (ocean and sea ice) and MAR (atmosphere) models (Section 4.4). This model enables the study of atmosphere–sea ice–ocean interactions at scales where observations are missing and coupled models are rarely used. Due to the high cost of such a high-resolution coupled model, we limit our study to the Adélie Land sector, East Antarctica. We expect that the same interactions between eddies, sea ice, and atmosphere are at play elsewhere in the Southern Ocean. Our regional coupled model is presented in Section 4.4. We then analyze to what extent individual eddies affect the overlying sea ice and atmosphere properties (Section 4.5) and we describe the overall effect in the entire simulated region (Section 4.6). The results are discussed in Section 4.7, followed by our conclusions in Section 4.8.

4.4 The model, experimental design, and analysis strategy

4.4.1 The NEMO ocean–sea ice model

The ocean–sea ice model is adapted from the one used in Huot et al. (2021a) and Huot et al. (2021b). It is a regional configuration of the NEMOv3.6 platform (Nucleus for European Modelling of the Ocean, Madec (2016)), including the sea ice model LIM3 (Louvain-la-Neuve sea Ice Model). The ocean domain extends from 70°S to 59°S and from 129°E to 151°E. The grid is derived from the eORCA1 global tripolar grid which was refined to a resolution of $1/24°$. The grid spacing ranges from 1.8 to 2.3 km, which is enough to resolve eddies away from the continental shelves (Hallberg, 2013). The vertical discretization consists of 75 levels of increasing thickness from top to bottom (from 1 m to 200 m). The vertical mixing is treated via a TKE scheme (Bougeault and Lacarrere, 1989; Gaspar et al., 1990). Convection is parameterized by enhanced vertical mixing. LIM3 is a dynamic-thermodynamic model described in Vancoppenolle et al. (2009) and Rousset et al. (2015). We make use of a subgrid-scale distribution of sea ice thicknesses with 5 categories. We have increased the ocean-ice drag coefficient to 6.8×10^{-3} (instead of 5×10^{-3} in Huot et al. (2021a)), to maintain a constant ratio between the ocean-ice stress computed by NEMO-LIM and the atmosphere-ice stress computed by MAR. The parameterization of landfast sea ice (Van Achter et al., 2021; Huot et al., 2021b) was modified: sea ice experiences a bottom stress where a grounded iceberg is present, instead of treating icebergs as land points. The bottom stress is set to $\tau_{lfs} = a_i \tau_{icb}$ (with a_i the sea ice concentration and τ_{icb} a constant stress of 10 $\mathrm{N/m^2}$). The two methods produce similar results, but the one used here does not require adapting the land-sea mask. The ocean-sea ice model is forced at its lateral boundaries by the PSY4V3R1 1/12° global reanalysis as in Huot et al. (2021b). Tides are applied at the lateral boundaries using the FES2012 dataset (Carrère et al., 2012), as in Maraldi et al. (2013) and Jourdain et al. (2019).

4.4.2 The atmospheric model MAR

MAR (Modèle Atmosphérique Regional) is a hydrostatic polar-oriented model originally developed by Gallée and Schayes (1994). This model has often been used to study the climate over the AIS (eg., Amory et al. (2015); Kittel et al. (2018); Agosta et al. (2019); Donat-Magnin et al. (2020)). We refer to Kittel et al. (2021) for a description and evaluation of MAR all over Antarctica. The MAR configuration used in this study was adapted from the one utilized in Huot et al. (2021b), but MAR was updated to version 3.11. The model uses the $E - \epsilon$ scheme of Duynkerke (1988) for the subgrid-scale vertical fluxes. MAR is coupled to the surface model SISVAT from De Ridder and

Gallée (1998) (part of which is based on a former version of the CROCUS model for snow-covered surfaces (Brun et al., 1992)). Each grid cell of MAR in our configuration is either a land cell, possibly including a nunatak fraction (summit or ridge of a mountain that protrudes from an ice field), or an ocean cell, possibly including a fraction of sea ice. Sea sprays enhance evaporation acting as a moisture source over the ocean and decreasing the air potential temperature (Andreas and Decosmo, 2002). The atmospheric model is forced at its lateral boundaries and nudged in the top troposphere by 6-hourly outputs of ERA5 (Hersbach et al., 2020). The horizontal resolution is set to 5 km (same grid as the AM5 simulation of Huot et al. (2021b)). The vertical discretization consists of 24 sigma levels, with the first level at approximately 2 m. The atmospheric domain is larger than the one covered by the ocean model and MAR takes its surface conditions from the OSTIA reanalysis (Donlon et al., 2012) outside of the common area. A relaxation zone of 5 grid points is used between the coupled and uncoupled surfaces.

4.4.3 NEMO-MAR coupling

We have revised the coupling interface originally developed by Jourdain et al. (2011), by updating all model components, including the OASIS3-MCT3 coupler (Craig et al., 2017), by coupling at a higher frequency, and by revisiting some of the flux formulations. MAR computes the fluxes for NEMO-LIM, and NEMO-LIM sends its surface conditions to MAR. The coupling time step is 600 s (equal to 4 oceanic time steps and 30 atmospheric time steps). Every coupling time step, NEMO-LIM sends its 600-s averaged sea surface temperature, sea surface velocities, sea ice concentration, sea ice and snow thicknesses, sea ice albedo, sea ice surface temperature, and sea ice velocities. Sea ice albedo is a function of ice surface temperature, ice, and snow depth (Shine and Henderson-Sellers, 1985). The ocean albedo is recomputed in MAR and is a function of the zenithal angle and cloud cover. MAR sends net shortwave radiation, the non-solar heat flux (sum of net longwave, latent and sensible heat fluxes), and the turbulent momentum flux distinctively for the sea ice and the ocean to NEMO-LIM. In addition, MAR sends rainfall and snowfall, ice sublimation, and total evaporation. MAR also sends the non-solar heat flux sensitivity to surface temperature. The latter (computed as in Jourdain et al. (2011)) is used to adjust the fluxes to the actual sea ice temperature in NEMO-LIM to avoid large-amplitude noise of sea ice temperature. The ice thermodynamics module of MAR is not turned off, meaning that the ice temperature in MAR is free to evolve in between two coupling time steps. It is however brought back to the NEMO-LIM ice surface temperature at each coupling time step. All exchanged fields are interpolated bi-linearly in the longitude-latitude space between the two grids. Though the sea ice component LIM has a subgrid-scale ice thickness distribution, it is not the case for the atmosphere. NEMO-LIM, therefore,

sends the fraction-weighted average of the distributed variables (ice and snow thicknesses, ice temperature). The same air-ice fluxes are then applied to each sea ice category.

As in Renault et al. (2016), we use relative winds for the wind stress computation over ocean or sea ice. The relative zonal wind speed U_{rel} is defined as: $U_{rel} = (U_{10m} - U_{oce})(1-a) + (U_{10m} - U_{ice})a$, with U_{10m} the 10 m zonal wind speed component, U_{oce} the surface zonal ocean current speed, U_{ice} the zonal sea ice speed and a the sea ice concentration, and similarly in the meridional direction. The surface roughness length used for the air-sea or air-ice fluxes is computed as: $z0 = z0_{oce}(1-a) + z0_{ice}a$, with $z0_{oce}$ and $z0_{ice}$ the ocean and sea ice surface roughness lengths, respectively. $z0m_{oce}$, the ocean roughness length for momentum, is a function of the local wind speed after Wang (2001): $z0m_{oce} = 0.016\frac{(U*)^2}{g} + 0.11\frac{\nu}{U*}$, with $U*$ the friction velocity, ν the air kinematic viscosity (1.35×10^{-5} m^2/s) and g the gravitational acceleration. The roughness lengths for the sea ice latent, sensible, and momentum fluxes are constant and set to 1×10^{-3} m as in Cassano et al. (2001) and Bromwich et al. (2001).

4.4.4 Experimental design: REF and SMOOTH experiments

The reference (REF) simulation starts on the 1st of January 2011 and ends on the 31st of December 2013, using the outputs of a stand-alone ocean simulation forced by MAR outputs as an initial state (OM5 in Huot et al. (2021b)). The first year serves as a model spin-up and is discarded from the analyses. A comparison of the mean state of the ocean and atmosphere with the WOA18 climatology (Zweng et al., 2018; Locarnini et al., 2018) and with the ERA5 reanalysis (Hersbach et al., 2020) is proposed in Section 6.3 (supplementary material). In REF, the sea ice and the atmosphere feel the presence of the oceanic mesoscale activity which is at least partly resolved north of the continental shelf given that the effective ocean model resolution is generally estimated as 2 to 10 times the grid resolution i.e. 4 to 20 km in our configuration (Hallberg, 2013; Soufflet et al., 2016). The 5 km horizontal resolution of the atmospheric model seems to be enough to capture the oceanic mesoscale.

The time series of the sea ice area simulated in REF is compared to the observed sea ice area in Figure 4.1. The REF simulation offers a satisfying representation of the sea ice area (Figure 4.1) when compared to the OSI-450 dataset (Lavergne et al., 2019). REF underestimates the sea ice extent by 15% in the winters of 2011 (considered as a spin-up year hereafter) and 2012 while doing a better job in 2013. This negative bias may lead to an underestimation of the imprint of eddies on the sea ice pack as the eddy activity increases northwards.

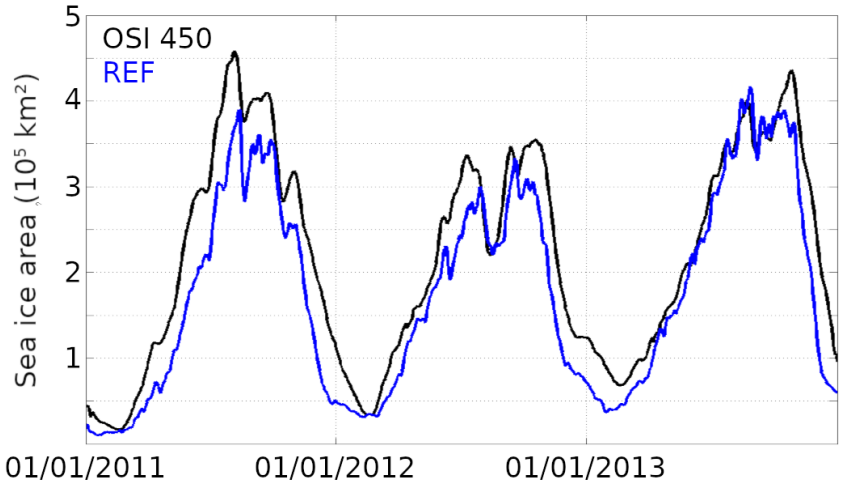

Figure 4.1: Time series of sea ice area integrated over the Adélie Land sector simulated in REF and derived from the observations OSI-450 (OSI SAF Global Sea Ice Concentration Climate Data Record).

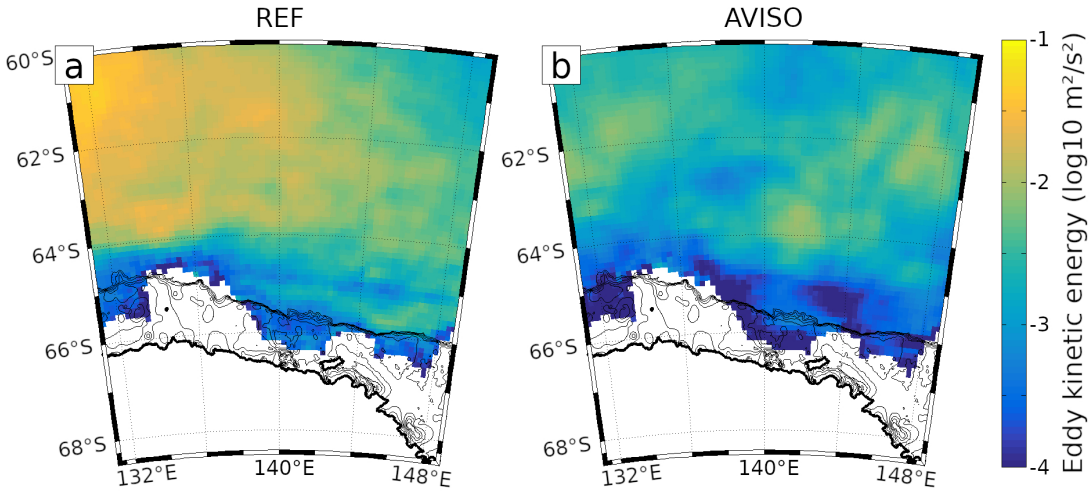

Figure 4.2: Eddy kinetic energy obtained from geostrophic currents simulated in REF (a) and estimated from AVISO (b), averaged over 2011 and 2012.

The eddy kinetic energy simulated in REF and estimated from the AVISO sea level anomaly dataset are illustrated in Figure 4.2. The spatial and temporal resolutions of the modeled (1/24° and daily) and observed SLA (function of track density, Ballarotta et al. (2019)) are too different to permit direct comparison and some adaptation is needed to compare observations and model on an even ground (as was for instance done in Amores et al. (2018)). Here, we have reconstructed the SLA of AVISO from the along-track SLA using the interpolation algorithm developed by Garcia (2010) (this algorithm showed good capabilities when applied to geophysical datasets in Wang et al. (2012)). The reconstructed SLA compares well with the AVISO interpolated field, with an averaged root mean squared error of 0.69 cm. The same methodology is applied to the modeled field: "along-track" SLA are obtained using the real tracks

of the altimeter used in AVISO, and the SLA is interpolated. Before the interpolation, we have masked the locations with an observed sea ice concentration (in the OSI-450 dataset) higher than 0%. The model overestimates the ocean EKE in the northwestern part of the domain (where the simulated values can be four times higher than the ones estimated from AVISO) but shows reasonable values of EKE in the eastern part. The simulated EKE is however similar to the one simulated by Stewart et al. (2018).

To test the effects of the ocean eddies on the atmosphere–sea ice–ocean interactions, we perform a second experiment named SMOOTH. SMOOTH starts on the 1st of January 2012, using a snapshot of the ocean and sea ice states from REF as initial conditions. In SMOOTH, we remove the modulation of atmosphere–sea ice–ocean heat and momentum fluxes by ocean eddies. To do so, we smooth the oceanic fields before their use in the sea ice model and before their exchange with the atmosphere model. The filter (inspired from Renault et al. (2019b)) is a 2D Gaussian with a standard deviation of 40 km. It is applied online to the sea surface temperature (SST), salinity (SSS), and meridional and zonal currents (SSU and SSV). We mirrored the oceanic fields across the lateral limits to avoid nonphysical boundary effects. We also masked land points and adapted the filter weights in the neighborhood of coastlines. The filter width is set to 6 times the standard deviation of the Gaussian. In this experiment, the atmosphere and the sea ice do not feel the small-scale heterogeneity of ocean surface conditions. Note that the sea ice fields are not filtered before the exchange with the atmosphere. The same filter is used offline to isolate the mesoscale variability of a given field. We decompose a field F into its mesoscale part F_{meso} and large-scale part F_{large} such as $F = F_{meso} + F_{large}$. F_{large} is obtained by filtering F by the Gaussian filter described above.

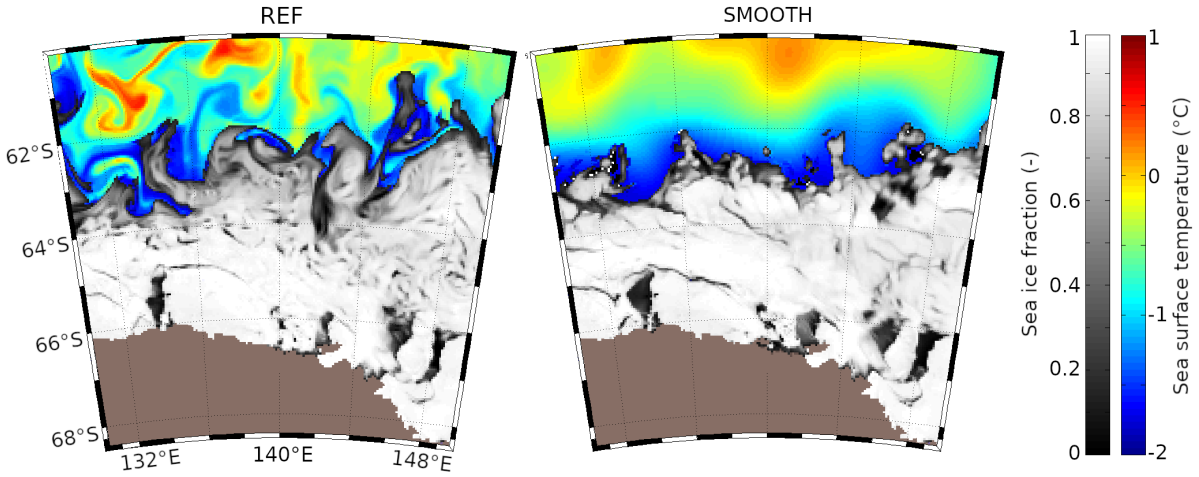

Figure 4.3: Snapshots of sea ice concentration (black and white shading) and SST (red-green-blue shading) seen by MAR in REF (left) and SMOOTH (right) on 27th Aug. 2013.

The effects of smoothing are illustrated by the snapshots of sea ice concentration and sea surface temperature in Figure 4.3. The imprint of mesoscale activity is manifest on the SST of REF, with circular or swirling warm and cold anomalies. The SST of SMOOTH is exempt from these eddies and filaments (note that the eddies of both simulations are not in phase). As explained before, the sea ice fields are not smoothed in SMOOTH. The ice pack presents small-scale heterogeneity due for instance to the opening of leads and polynyas in both simulations. Yet, the ice edge has a distinct shape between both simulations: between 64°S and 62°S, the eddies are deforming the ice pack. Swirling shapes in the sea ice concentration are found in REF but not in SMOOTH. This study aims to understand the mechanisms at play and their implications for the exchanges with the atmosphere. The ocean kinetic energy and SST power spectrums before and after filtering (Figure 4.4) show how different wavelengths are filtered. The filter effectively reduces the variability of the SST for length scales lower than 150 km.

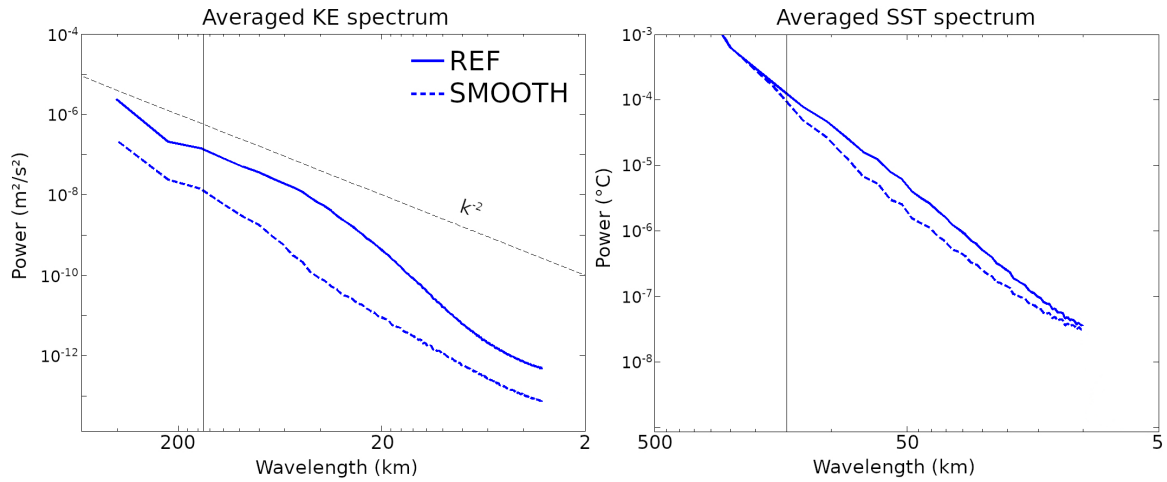

Figure 4.4: Radially averaged power spectrums of the ocean kinetic energy (left) and SST simulated in REF and SMOOTH over the period 2012-2013. The SST is the one seen by MAR and has a resolution of 5 km, while the ocean kinetic energy was recomputed offline and has a resolution of 2 km. The dashed black line indicates the k^{-2} slope, and the vertical black line a wavelength of 150 km.

Caution must be exercised when analyzing the results from the SMOOTH experiment. As described above, the filter dampens the imprint of small-scale processes on the sea surface. This includes the effects of the eddies but also the imprint of other processes (such as heterogeneous surface fluxes). Filtering the surface fields thus also dampens the small-scale feedbacks between surface fluxes and the ocean. In other words, while the ocean is free to adjust to surface fluxes, the sea ice and atmosphere see a diluted response due to the spatial filtering. This can have the effect of inhibiting the small-scale atmosphere–sea ice–ocean interactions which are

not associated with ocean mesoscale activity. We carried out another experiment where the filter is applied to surface currents only (not to SST or SSS). This did not impact the results presented here (not shown). Therefore, we can confidently attribute the effects of the filtering described hereafter to the mesoscale dynamical structures (eddies, meanders).

4.4.5 Eddy tracking and compositing

As we are particularly interested in understanding the mechanisms of atmosphere–sea ice–ocean interactions induced by mesoscale ocean eddies, it is important to analyze the simulations at the scale of those eddies. To do so, we produced a series of sea surface and atmosphere composites above eddies. We use the eddy tracking algorithm proposed by Faghmous et al. (2015). It was originally developed for remotely sensed data but can be applied to outputs from numerical models as well. The algorithm localizes the local extremums of SLA (maximum for anticyclonic eddies, minimum for cyclonic eddies) within squares of 9x9 pixels. Then, it finds the largest closed contour of SLA that contains a single SLA extremum. The eddy consists of all the pixels enclosed within the largest SLA contour. Closed contours of SLA with an area lower than 300 grid points (a circle with a radius of approximately 10 grid points in our configuration) are discarded. Eddies with an SLA anomaly lower than 3 cm were also discarded. Note that one eddy can be detected several days in a row. The daily sea surface, sea ice, and atmospheric conditions within 3 eddy radius from the eddy center were gathered and averaged to produce composite images. These composites represent the mean state of the ocean, atmosphere, or sea ice in the eddies referenced frame. Before averaging, the eddies were scaled according to their individual eddy radius. Additionally, atmospheric fields were rotated to be aligned with the local wind direction (as in Frenger et al. (2013)) averaged over one eddy radius from the eddy center. For each variable, we make separate composites for cyclonic and anticyclonic eddies.

4.5 Atmosphere–sea ice–ocean interactions at the mesoscale

In this section, we investigate how eddies affect air-sea interactions at small scales and the mesoscale variability of the sea ice, atmosphere, and ocean. First, the response of the small-scale wind to the mesoscale surface temperature variability is assessed. Then, we describe the imprint of individual eddies on the sea ice, atmosphere, and ocean.

4.5.1 Small-scale atmosphere–sea ice–ocean coupling

In this section, we analyze how the atmosphere responds to mesoscale anomalies of surface conditions (i.e. not only eddies but all mesoscale heterogeneities).

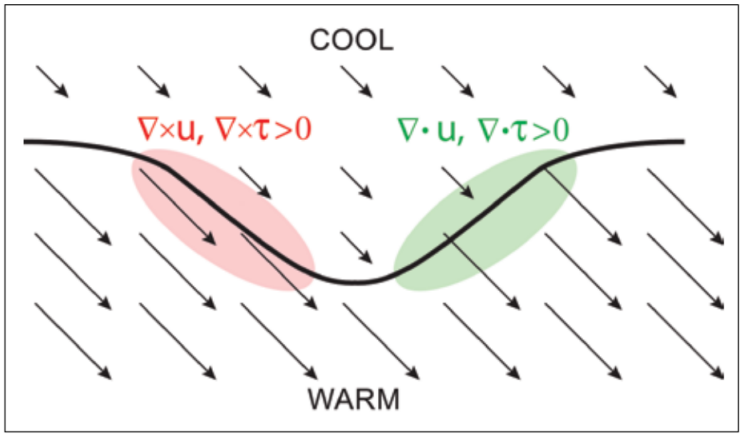

Figure 4.5: Schematic view of the response of a surface wind field (black arrows) to a surface temperature front (thick black line), adapted from Chelton and Xie (2010a). Surface winds are weaker over the cool side of the SST front and stronger over its warm side. Winds blowing along the surface temperature front start to curl (orange shaded area) while winds blowing across the surface temperature front diverges (green shaded area).

We first focus on the thermal feedback, i.e. the anomaly of wind or stress divergence across surface temperature gradients and of wind or stress curl along surface temperature gradients (O'Neill et al., 2005; Chelton and Xie, 2010a). Small-scale positive or negative surface temperature anomalies induce an associated warming or cooling of the near-surface air, potentially intensifying or weakening the near-surface winds (Small et al., 2008). As a result, winds blowing across a positive surface temperature gradient will gradually intensify, thus generating surface wind divergence. Similarly, winds blowing along a surface temperature gradient will start to curl. These two cases are illustrated in Figure 4.5 and details about the mechanisms can be found in Chelton and Xie (2010a). We compute the relationships between the cell-averaged surface temperature (weighted average of the ocean and sea ice surface temperatures, hereafter ST) gradient and wind curl or divergence using the outputs of REF. For the ice-covered cells, we use the cell-averaged surface temperature of the ocean and sea ice instead of the SST. We compute the surface temperature downwind and crosswind gradients as in O'Neill et al. (2005). The downwind ST gradient is defined as: $\overrightarrow{\nabla_{down}}ST = ||\overrightarrow{\nabla}ST||.cos(\Theta)$ and the crosswind gradient as: $\overrightarrow{\nabla_{cross}}ST = ||\overrightarrow{\nabla}ST||.sin(\Theta)$ with ST the surface temperature and Θ the angle between the ST gradient and the wind. We extract the mesoscale anomalies of these fields and of the wind curl and divergence as described in Section 4.4.4. We then derive

the relationship between surface conditions and the wind for ice-free ($SIC = 0$) and ice-covered ($SIC > 0.05$) cases.

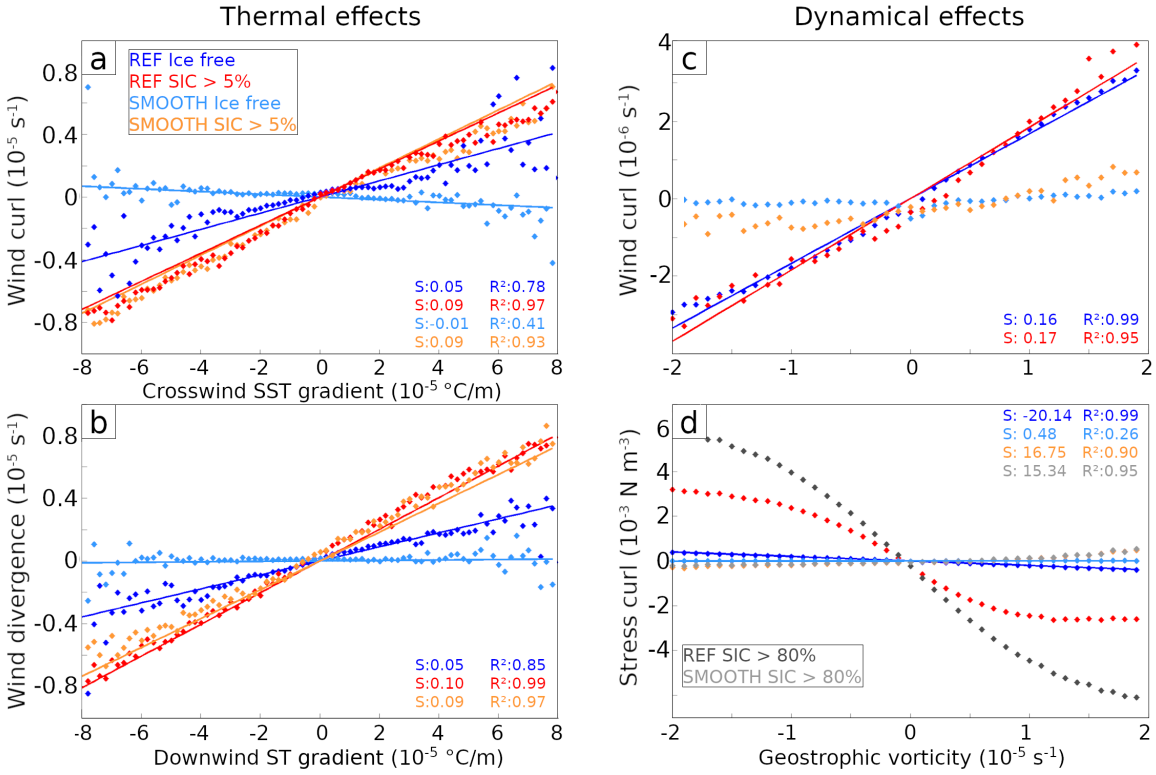

Figure 4.6: Binned scatterplots of the small-scale anomalies of: a) the crosswind surface temperature (ST) gradient and the wind curl, b) the downwind ST gradient and the wind divergence, c) the geostrophic current vorticity and the wind curl, d) the geostrophic currents vorticity and the ocean stress curl. Bin widths are 1×10^{-6} °C/m for temperature gradients and 1×10^{-6} s^{-1} for the geostrophic vorticity. Each marker corresponds to the average of all simulated points within the bin range. The binned scatter plots are built from daily outputs over the period 2012-2013. For the "ice free" relationships, only the pixels with a sea ice concentration (SIC) equal to zero are considered. Linear regressions on the bin averages are indicated when such a relationship exists. The slopes (S) and regression coefficients (R) are indicated on each panel.

The resulting binned scatterplots are displayed in Figures 4.6a and 4.6b. For the ice-free ocean, there is a positive relationship between the crosswind gradient of surface temperature and the wind curl. A positive relationship is also found between the downwind surface temperature gradient and the wind curl. These positive relationships are in agreement with previous work (Chelton and Xie, 2010a; Song et al., 2009). The relationships are also positive for the ice-covered ocean, but the coupling is stronger. The slopes of the crosswind ST - wind curl relationship and of the downwind ST - wind divergence relationship are indeed increased by a factor of 2 in the presence of sea ice. This indicates that the atmospheric response to small-scale

changes in temperature is stronger in the presence of sea ice.

Then we focus on the so-called current feedback (Renault et al., 2016), which depends on the relative velocity of wind and ocean currents. This feedback induces wind stress curl over ocean vorticity, which tends to extract vorticity from the ocean and therefore to weaken ocean eddies. Renault et al. (2016) defined the dynamical coupling as the relationship between the surface currents vorticity and the wind or surface stress curl. The relationships between the mesoscale anomalies of these fields are depicted in Figures 4.6 c and d. As for the thermal effect, we compute one relationship for the ice-free ($SIC = 0$) and one for the ice-covered ($SIC > 0.05$). Note that the "stress" is the cell average of the wind stress and ice stress on the ocean (hereafter "ocean stress"). In the ice-covered ocean, it thus also incorporates the dynamical interactions between the ocean and the sea ice. For the ice-free case, REF simulates a positive relationship between the current vorticity and the wind curl, in agreement with previous results (Renault et al., 2016). This can be explained by the negative relationship between the current vorticity and the ocean stress curl. The friction of eddies against the atmosphere leads to a stress curl opposed to the ocean currents. This results in a modification of the air-sea stress and induces a wind curl in the same direction as the ocean currents vorticity. The presence of sea ice does not affect the relationship between the surface current vorticity and the wind curl. But, the one with the stress curl is amplified. Two reasons can be given to explain the strength of the vorticity-stress curl relationship in the ice-covered ocean. First, the ocean-ice drag coefficient is larger than the air-ice one. Also, ocean currents and sea ice velocities have the same order of magnitude, making sea ice more sensitive to ocean currents. Yet, the relationship gets weaker for a high absolute current vorticity. This suggests that ocean currents drive sea ice motion in intense eddies, which leads to a saturation of the ice-ocean stress. By taking only the pixels where $SIC > 0.8$ (dark gray markers of Figure 4.6d) likely representing more resistant sea ice, the effect of currents vorticity on stress curl weakens for high absolute vorticity but does not saturate anymore. The alignment of sea ice velocities with ocean currents can also explain why the vorticity-wind curl relationship (Figure 4.6c) is not affected by the presence of weak sea ice. With strong sea ice ($SIC > 0.8$) however, the relationship becomes insignificant (not shown).

In the SMOOTH simulation, the dynamical effect vanishes, as illustrated by the flat curves of Figure 4.6 c. This is due to the removal of the contribution of small-scale currents to ocean stress. For the ice-covered ocean, SMOOTH represents a positive relationship between the vorticity and the stress curl, which might indicate the forcing of the ocean circulation by the large-scale sea ice curl. The relationships between

ice-free surface temperature gradients and wind divergence become null, and the one with the wind curl becomes negative (Figures 4.6a and 4.6b). It is not the case for the coupling between surface temperature gradient and wind divergence or curl in the presence of sea ice (orange markers in Figures 4.6a and 4.6b). In SMOOTH, small-scale heterogeneities in the sea ice cover are not filtered out. Thus, there are still small-scale surface temperature gradients that can drive small-scale interactions in the ice-covered regions.

4.5.2 Imprint of eddies on the sea ice and atmosphere

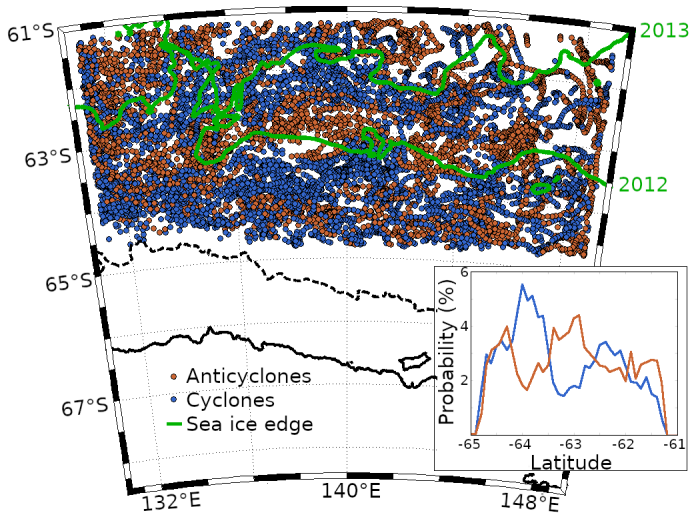

Figure 4.7: Location of eddies detected in REF between 1st of January 2012 and 31st of December 2013. The green lines indicate the maximum sea ice extent for years 2012 and 2013. The coastline is indicated as a thick black line and the 1200 m isobath as a dashed black line. The insert represent the meridional distribution of eddies.

In the previous section, we have described the mechanisms of atmosphere–sea ice–ocean coupling for general mesoscale structures. The origins of small-scale heterogeneity in the ocean surface and sea ice characteristics can be diverse (eddies, leads, local air-sea fluxes). Here, we focus on the imprint of ocean eddies. To do so, we apply the eddy tracking and analysis method described in Section 4.4.5 to the daily SSH of the REF simulation. Between the 1st of January 2012 and 31st of December 2013, we detected ∼5100 cyclonic eddies and ∼3400 anticyclonic eddies (approximately 7 cyclonic eddies and 5 anticyclonic eddies each day). As illustrated in Figure 4.7, anticyclonic and cyclonic eddies are relatively uniformly distributed apart from the peak in cyclonic eddy frequency near 64°S and the peak of anticyclonic eddy frequency near 63°S. The differences between anticyclonic and cyclonic eddies should not arise from a difference in spatial distribution.

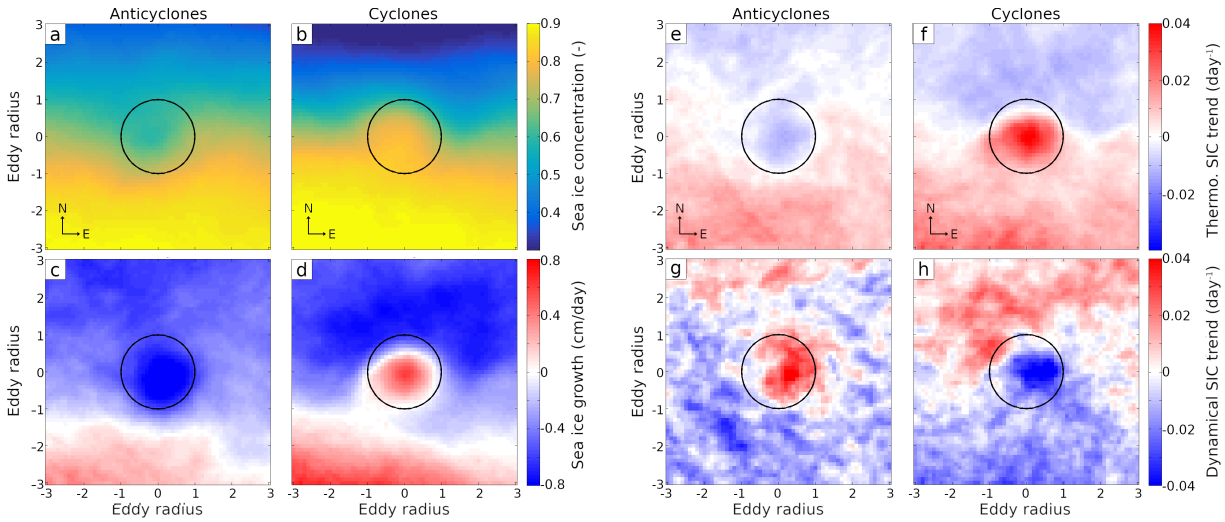

Figure 4.8: Composites of the eddies imprint on the sea ice concentration (a-b), sea ice growth rate (c-d), sea ice concentration thermodynamical (e-f), and dynamical (g-h) tendencies simulated in REF. Only the eddies with a sea ice concentration averaged within 3 eddy radius larger than 0.4 are accounted for. Anticyclonic eddy (warm core) and cyclonic eddy (cold core) are shown on the left and right columns of each sub-figure, respectively. Each eddy has been scaled with respect to its radius but the orientation of eddies is not modified. Composites are built from 01/01/12 to 31/12/13. A circle of one eddy radius is drawn on each panel.

First, we investigate the effects of eddies on sea ice. To do so, we consider here only the eddies with a mean sea ice concentration of 0.4 within 3 eddy radius. Most of the ice-covered eddies are encountered close to the ice edge, as shown by the northward decrease in sea ice concentration (Figure 4.8a-b). Anticyclonic eddies are associated with negative SIC anomalies, while cyclonic eddies are associated with positive ones. The mean sea ice production rate north and alongside the eddies is negative, as ice-covered eddies are mostly encountered in the north of the ice pack (Figure 4.8c-d). The imprint of eddies is overlaid on this large-scale trend. There is a stronger melt (-1 cm/day within the eddy core compared to -0.2 cm/day outside) in anticyclonic eddies and a lower melt or even freezing (+0.6 cm/day on average) above cyclonic eddies. Cyclonic eddies thus enable the formation of sea ice further north where sea ice should normally melt, but this is compensated by increased melt on the north of cyclonic eddies.

We separate the sea ice concentration tendencies into its thermodynamical and dynamical components in Figure 4.8 e-f and g-h. As for the sea ice growth rate anomalies, cyclonic and anticyclonic eddies have an opposite imprint on the thermodynamical SIC trend. The thermodynamical SIC trend is negative above anticyclonic eddies and positive above cyclonic eddies. These anomalies are

compensated by the imprint of eddies on the dynamical SIC trend. The sea ice converges above anticyclonic eddies (as previously described by Manucharyan and Thompson (2017)) and diverges above cyclonic eddies. Cyclonic eddies are also associated with a northward sea ice advection, as seen by the positive dynamical SIC trend in Figure 4.8h. The advected sea ice likely encounters warmer waters north of the ice edge, leading to intensified melt (Figure 4.8 d and f).

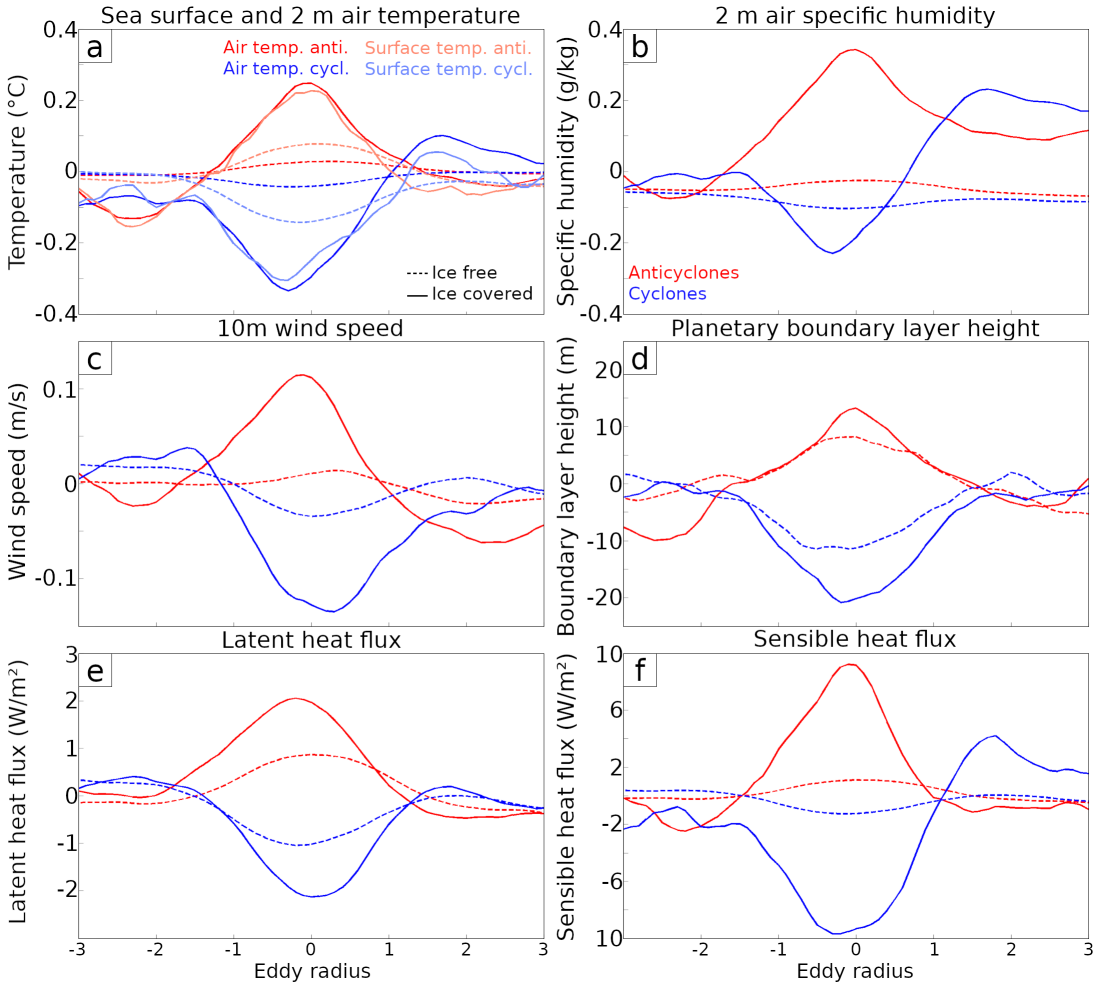

Figure 4.9: Downwind transects of the imprint of eddies on the surface conditions, heat fluxes and atmosphere. a) Surface temperature (weighted average of ocean and sea ice temperatures, light blue and pink) and 2 m air temperature (red and blue), b) 2 m air specific humidity, c) 10 m wind speed, d) planetary boundary layer height, e) latent heat flux, and f) sensible heat flux. A positive heat flux means an energy loss by the surface. The mesoscale part of each field was first extracted following the method described in Section 4.4.4. Eddies were resized with respect to their radius and rotated to be aligned with the local wind. Separated downwind transects are computed for anticyclonic eddies (red or pink) and cyclonic eddies (blue or light blue). The distinction is also done between ice-free (dashed line) and ice-covered ($SIC > 0.4$, solid line) eddies. The composite are computed using daily outputs from REF between 2012 and 2013.

We apply the same diagnostics to detect the imprint of eddies on air-sea fluxes and on surface air properties (Figure 4.9) in the REF simulation. On average, the imprint of ice-free eddies on near-surface air temperature or humidity is almost indistinguishable (< 0.05°C and < 0.05 g/kg). The imprint of eddies becomes significant for ice-covered eddies, the atmosphere is warmer (+0.3°C) and moister (+0.3 g/kg) over ice-covered anticyclonic eddies. The sign of the anomalies is reversed for ice-covered cyclonic eddies. These stronger anomalies are coherent with the negative (positive) sea ice concentration anomalies of anticyclonic (cyclonic) eddies, but could also illustrate the stronger sensitivity of the atmosphere to small-scale heterogeneity of surface conditions in ice-covered regions described earlier (Figure 4.6). The temperature and moisture anomalies originate from the imprint of eddies on latent and sensible heat fluxes (Figure 4.9e,f).

The influence of eddies can also be observed on the winds. The presence of anticyclonic eddies leads to wind intensification, while cyclonic eddies lead to the opposite response (Figure 4.9c). As with air temperature, the imprint is stronger for ice-covered than for ice-free eddies, which can be related to the stronger changes in air temperature for ice-covered eddies. Two mechanisms are often proposed to explain the modulation of wind speed by mesoscale eddies. The first one involves a modification of the vertical momentum transfer due to changes in atmosphere stability associated with the warming/cooling effect of eddies. The second one is a modification of local pressure (due to changes in air density), which can drive local winds. The imprint of eddies on surface pressure (not shown) is either null or uncorrelated to the simulated changes in wind speed. The effects of eddies on wind speed simulated in REF are most likely imputable to changes in vertical momentum transfer. This is in agreement with the imprint of eddies on the planetary boundary layer (Figure 4.9d). The planetary boundary layer (PBL) is on average thicker above anticyclonic eddies than above cyclonic eddies. Thicker PBL enables a stronger downward momentum transfer and stronger winds above anticyclonic eddies.

The coupled model shows that mesoscale eddies affect air temperature and wind speed off Adélie Land. The imprint on air temperature or wind speed remains relatively weak, but the latter is in agreement with the imprint on wind speed observed by Frenger et al. (2013). However, the influence of eddies on the atmosphere quickly vanishes as we move away from the surface. Despite the imprint on the height of the PBL, we have not detected any imprint on the cloud cover or precipitation rates in our simulation. The atmospheric response to eddies suggests the existence of small-scale feedbacks. Air warming (cooling) above anticyclonic (cyclonic) eddies reduces the air-surface temperature contrast and thus, the turbulent heat fluxes. The

modification of wind speeds due to the presence of eddies can amplify or on the contrary dampen the temperature contrast diminution effect, as stronger (weaker) winds would intensify (lower) the heat loss above anticyclonic (cyclonic) eddies.

An interesting result is the higher sensitivity of the atmosphere to eddies in ice-covered areas which might be related to the stronger air-sea coupling in presence of sea ice described in Section 4.5.1. As sea ice limits air-sea fluxes, the anomalies of sea ice concentration associated with mesoscale eddies likely intensify the atmosphere's response to the presence of a mesoscale eddy. In addition, sea ice can reach lower temperatures than the sea surface, leading to stronger surface temperature gradients than over ice-covered than over ice-free eddies. However, it seems that the difference between surface temperature and near-surface air temperature is similar between ice-covered and ice-free eddies in the REF simulation (not shown). The higher sensitivity of the atmosphere to ice-covered eddies could arise from the differences in heat transfer coefficient between the ocean and sea ice. Another potential cause might be the presence of a thermal inversion over the sea ice, increasing the sensitivity of surface air to surface heat fluxes.

4.5.3 Eddies imprint on the ocean

In this subsection, we investigate whether the mesoscale interactions between ocean eddies and the atmosphere or sea ice feedback to the ocean properties within eddies. To do so, we analyze eddy-composites of sea surface temperature, salinity, and Ekman pumping, in the presence or absence of sea ice, and the presence or absence of mesoscale feedback (Figure 4.10).

In REF and SMOOTH, anticyclonic eddies have a warm and fresh core and cyclonic eddies a cold and saline core, whether they are covered by sea ice or not (Figure 4.10a-d). This signature differs from the warm and saline / cold and fresh anomalies observed by Frenger et al. (2015), and the SST signature of eddies simulated is approximately half the one observed by Frenger et al. (2015) (they however consider eddies in the whole Southern Ocean and likely do not detect eddies as small as the one accounted for here). In the absence of sea ice, the interactions of eddies with the atmosphere act to dampen their thermal and saline structure. The signature of ice-free eddies on surface temperature or salinity is indeed weaker by 20% in REF than in SMOOTH. For ice-covered eddies, the temperature anomaly is also dampened in REF compared to SMOOTH, but the salinity anomaly is enhanced. This can be related to the increase (decrease) of sea ice production over cyclonic (anticyclonic) eddies. In addition, eddy-driven stress curl generates Ekman suction in anticyclonic eddies and Ekman pumping in cyclonic ones (Figure 4.10e,f). The Ekman

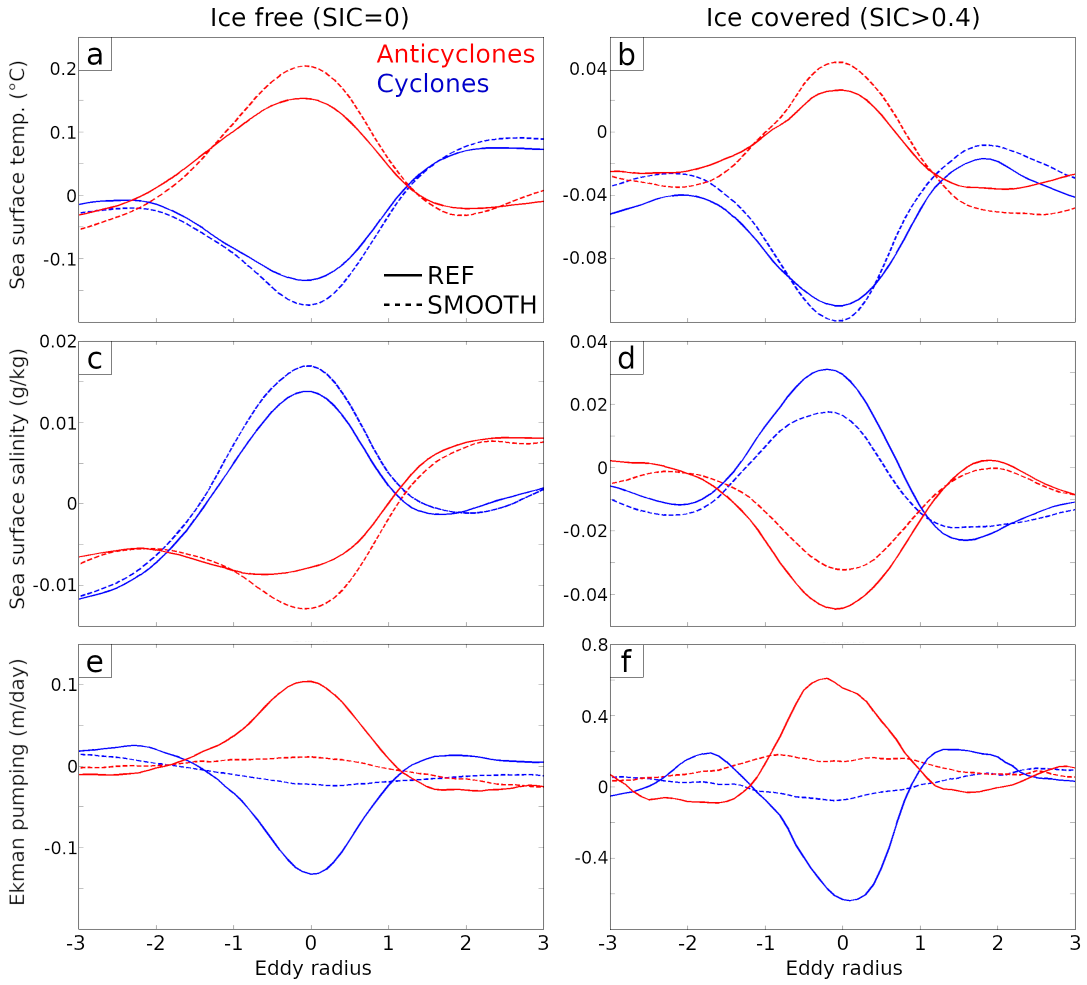

Figure 4.10: Mean zonal sections of the mesoscale anomalies of the sea surface temperature (top row), sea surface salinity (middle row), and Ekman pumping (bottom row) simulated in REF and SMOOTH. The sections are computed for ice-free (left) and ice-covered (SIC > 0.4, right) eddies.

suction/pumping is stronger over ice-covered eddies (up to 0.6 m/day) compared to ice-free eddies (0.1 m/day) and is close to the values obtained by Gupta et al. (2020). Eddy-driven atmosphere–sea ice–ocean interactions thus contribute to vertical exchanges, especially in the ice-covered ocean.

We now investigate how eddy-driven atmosphere–sea ice–ocean interactions affect the properties of eddies below the surface (Figures 4.11 and 4.12). On average, anticyclonic eddies are associated with a warm and fresh anomaly (Figures 4.11a,e and Figures 4.12a,e), whether we consider ice-free or ice-covered eddies. The thermal anomaly is found down to 200 m, while the fresh anomaly is bounded to the upper 80 m. Within cyclonic eddies, the ocean is cooler and has a higher salinity than in the surroundings. The temperature anomalies of ice-covered eddies are consistent with their imprint on the surface (Figure 4.10) and on the sea ice freezing and melting

(Figure 4.8).

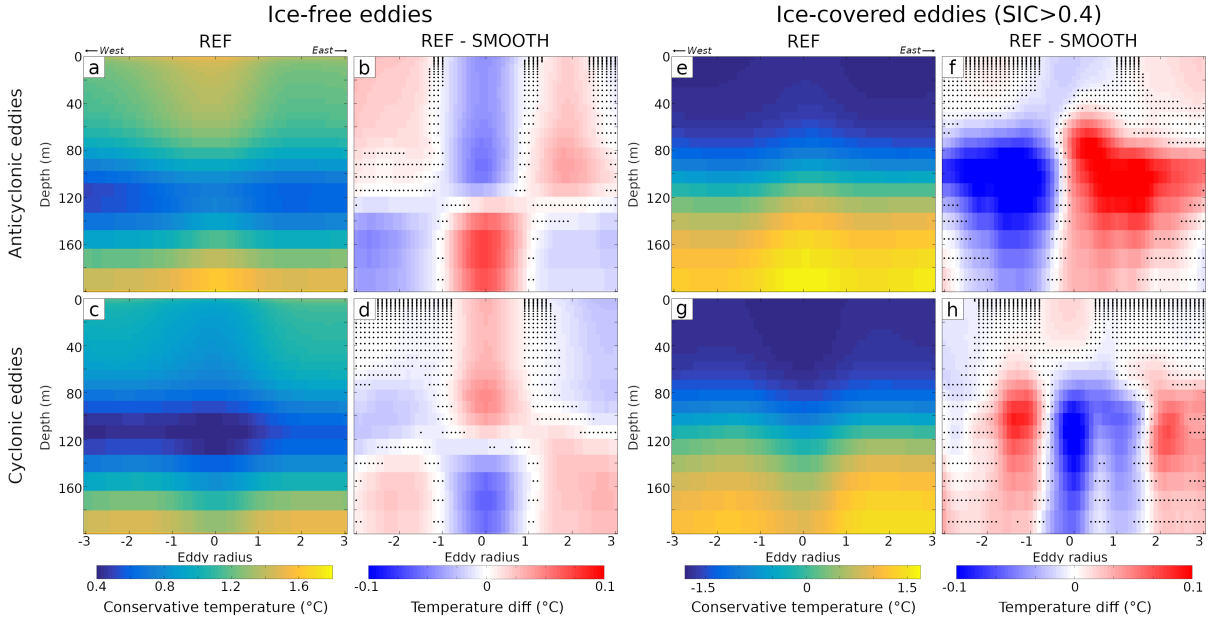

Figure 4.11: Mean zonal section of ocean temperature across mesoscale eddies. a) Ocean temperature across ice-free anticyclonic eddies in REF, b) difference of ocean temperature between REF and SMOOTH, e) ocean temperature across ice-covered anticyclonic eddies in REF, and f) difference in ocean temperature between REF and SMOOTH. c), d), g), h): same as a), b), e), f) but for cyclonic eddies. For panels b), d), f) and h), the difference between REF and SMOOTH is statistically significant (2σ) in the undotted areas. To remove the difference in the mean state between REF and SMOOTH, the mean temperature was subtracted at each level for the computation of the differences between REF and SMOOTH.

To examine the influence of eddy-mediated air-sea and ocean-ice interactions on the properties of eddies, we compare the ocean temperature and salinity structures within eddies between REF and SMOOTH (Figures 4.11b,f,d,h and Figures 4.12b,f,d,h). Eddy-mediated air-sea interactions weaken the signature of eddies on ocean temperature and salinity in the ice-free case. Ice-free anticyclonic (cyclonic) eddies are cooler (warmer) and have higher (lower) salinity in REF than in SMOOTH. This is coherent with the stronger (weaker) heat loss above anti-cyclonic (cyclonic) eddies described in Figure 4.9, but could also result from changes in vertical motion through Ekman pumping (see Figure 4.10e,f) or from the decrease of the eddy intensity via the eddy-killing effect. Eddy-driven Ekman suction upwells the warmer and more saline subsurface waters in anticyclonic eddies, which can explain the difference between REF and SMOOTH (Figure 4.11b and 4.12b). The picture is reversed for cyclonic eddies, where the curl of surface stress induces Ekman pumping. For ice-covered eddies, the Ekman suction/pumping is intensified (see Figure 4.10e,f) but it is partly compensated by eddy-driven ocean-ice heat and salt fluxes, leading to a

more complex picture (see panels f,h of Figures 4.11 and 4.12). The higher (lower) sea ice freezing rate in cyclonic (anticyclonic) eddies have an opposite effect on ocean salinity and mixed layer depths than the stress-driven vertical motion.

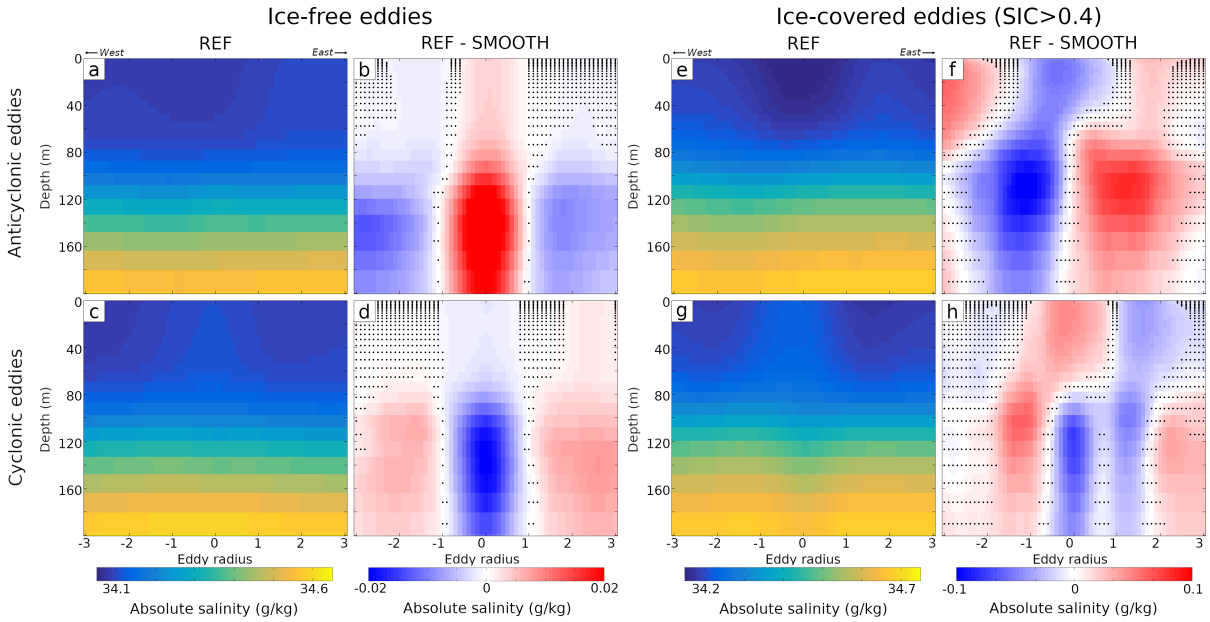

Figure 4.12: Same as Figure 4.11 but for ocean salinity.

4.6 Effects of eddies on momentum and buoyancy fluxes at the ocean surface

4.6.1 Momentum transfer and kinetic energy budget

In the previous section, we have shown that eddies were associated with small-scale variability of ocean, sea ice, and atmosphere properties. We now investigate how the aforementioned interactions affect the large-scale atmosphere–sea ice–ocean buoyancy and momentum fluxes.

The friction of mesoscale ocean currents on the atmosphere or sea ice harms the eddy intensity. This process is at play in REF (as illustrated in Figure 4.6) but not in SMOOTH, and can affect the oceanic kinetic energy budget. The ocean kinetic energy (KE) time series in REF and SMOOTH are shown in Figure 4.13. Total KE in REF experiences a strong variability at the sub-annual time scale. It has two maxima, one in May and one in November (though being weaker in 2013). The total ocean kinetic energy is higher in SMOOTH, and the seasonal variability is less pronounced. We compute the KE source originating from the eddying component of the surface stress following Renault et al. (2016), i.e. as $FeKe = \frac{1}{\rho_0}(\tau_x U_{oce} + \tau_y V_{oce})$,

with $\rho_0 = 1035\text{kg/m}^3$ the reference density of seawater, τ_x and τ_y the eddy surface stress zonal and meridional components (average of wind stress and sea ice stress) and U_{oce} and V_{oce} the eddying components of the zonal and meridional ocean surface current velocities. As in Renault et al. (2016), the eddying component of the surface stress or surface current velocities is computed as the departure from the two-year average (without filtering the seasonal cycle). The work exerted by friction at the top of eddies (hereafter eddy stress work) in REF and SMOOTH are shown in Figure 4.13b. There is a clear seasonal cycle with a maximum kinetic energy input during the winter season, as wind speeds are generally stronger. The eddy stress work is higher during winter in SMOOTH than in REF, especially in 2012. This might be one of the reasons for the lower total KE in REF. The eddy-killing effect is equally efficient over the ice-free ocean than over the ice-covered ocean with a 10.2% and 12.8% of eddy stress work decrease between REF and SMOOTH, respectively. Overall, the energy input through eddy stress work is decreased by 11%, and the ocean KE by 8.2% when eddy-driven atmosphere–sea ice–ocean interactions are turned off.

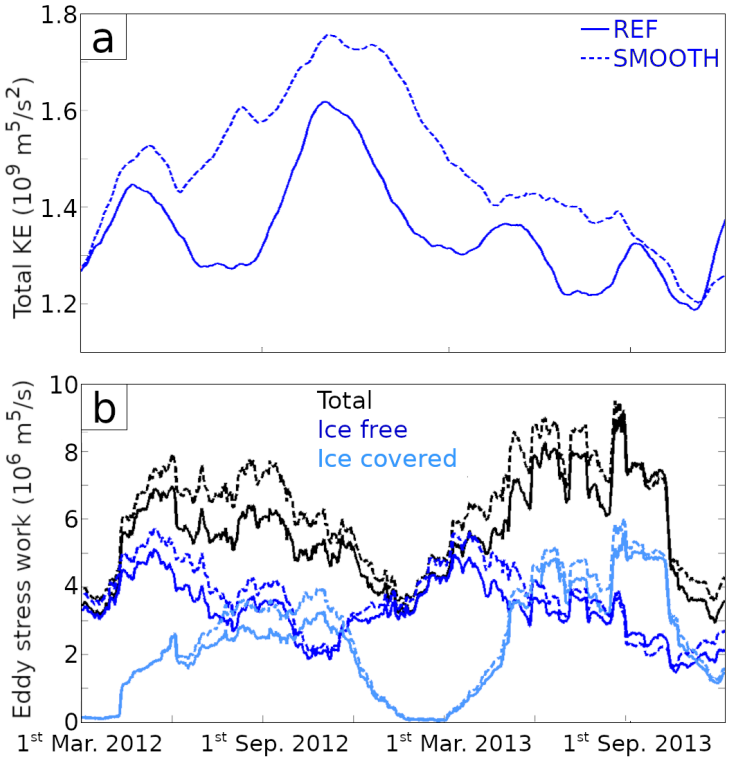

Figure 4.13: a) Upper 200 m ocean kinetic energy north of 65°S in REF and SMOOTH. b) Eddy stress work north of 65°S for the whole area (black), the ice-free (SIC=0) area (red), and the ice-covered ($SIC > 0.05$) area (blue). REF and SMOOTH are denoted with solid and dashed lines, respectively. A common sea ice mask is used for the computation of the eddy stress work for ice-free and ice-covered oceans in REF and SMOOTH. A 60 days moving average was applied to the time series.

4.6.2 Freshwater and buoyancy fluxes

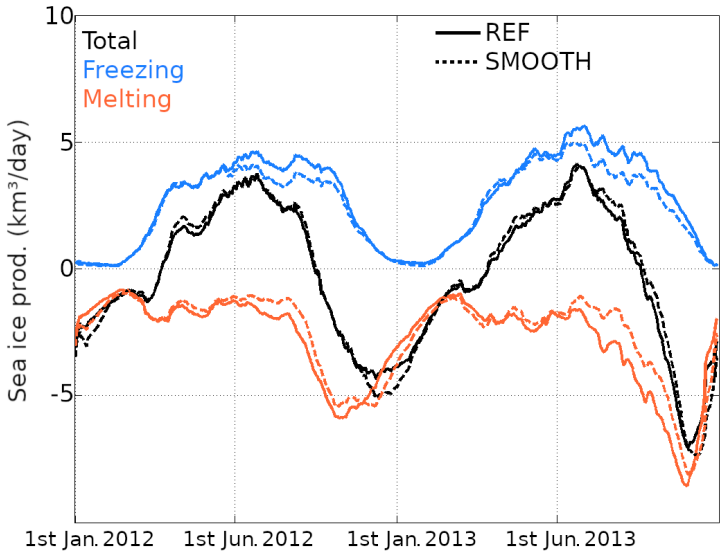

Figure 4.14: Time series of the total thermodynamical sea ice volume trend (black), sea ice freezing (teal) and melting (orange) simulated in REF and SMOOTH.

By forming close to the coast and melting offshore, the sea ice redistributes freshwater at the Southern Ocean surface. As eddies affect the ocean interactions with the sea ice and the atmosphere, they can also affect the freshwater budget of the ocean. The total sea ice production (Figure 4.14, black curve) and the total sea ice volume (not shown) are not affected by the presence of eddies. But, this hides compensating changes in sea ice growth and melt. Indeed, REF produces more sea ice than SMOOTH (Figure 4.14), which is compensated by larger melt. The lowering of sea ice freezing and melting in SMOOTH occurs from early July to September, or between the maximum sea ice extent and the summer. Eddies have no clear effect during the onset of the seasonal ice cover (from March to June). It is only when sea ice advances far enough offshore that it can encounter mesoscale eddies. If the total freshwater flux associated with sea ice melt/freeze is similar between the two simulations, its effects on the ocean are not necessarily compensated. The brine rejection due to seawater freezing destratifies the water column and impacts the subsurface ocean, which is not the case for sea ice melting. In addition, melting and freezing do not occur at the same place, thus the spatial distribution of the freshwater fluxes may be modified.

The meridional distribution of the sea ice melting differs between the two simulations (Figure 4.15a). The amount of sea ice melting north of 62.5°S is increased by 15% in REF compared to SMOOTH. To support the larger melt rates north of 63°S in REF, additional sea ice transport is required. There is indeed an increased northward

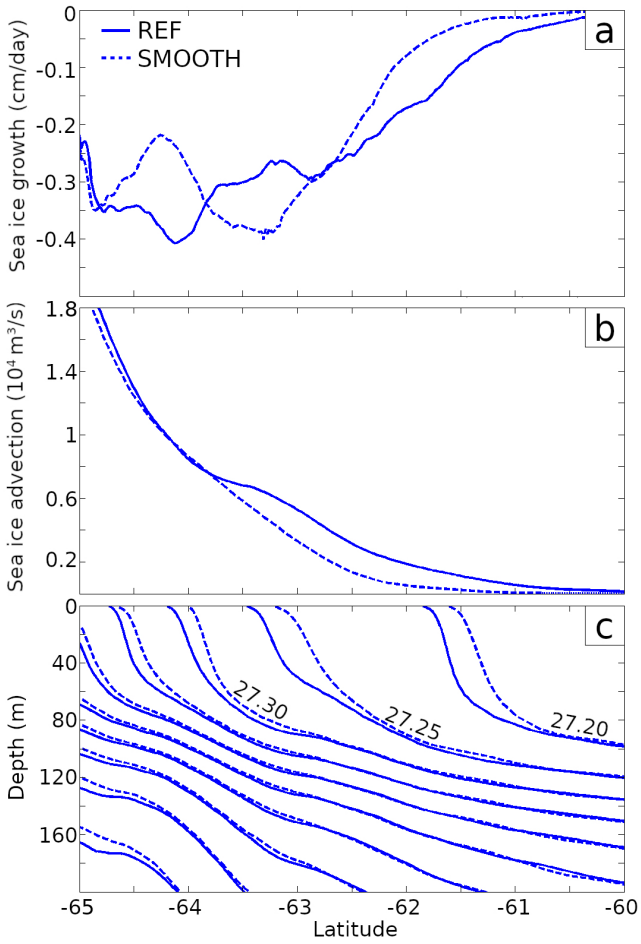

Figure 4.15: Meridional profiles of: a) mean sea ice growth rate, b) total meridional sea ice advection (positive northward), and c), ocean potential density (referenced to the surface) contoured every 0.05 kg/m^3 as simulated in REF and SMOOTH over the year 2013.

sea ice advection in REF (Figure 4.15b): starting from 63.5°S, the northward sea ice volume advection is higher by 2×10^3 m^3/s in REF. The stronger sea ice advection is due to higher meridional sea ice velocities in REF than in SMOOTH (see Figure 4.16). This results in higher melting in the northern half of the domain, leading to stronger ocean stratification (Figure 4.15c). Another effect of the lower northward sea ice export in SMOOTH is its accumulation inside the ice pack, leading to the intensified melt near 63.5°S.

The redistribution of sea ice and the modulation of air-sea heat fluxes by eddies can affect the surface buoyancy fluxes and the transformation of water masses off Adélie Land. Water masses undergoes two types of transformation in the Southern Ocean: either an increase in density dominated by brine rejection and ocean cooling, or an opposite density decrease dominated by sea ice melt, ocean warming, and precipitations. We compute the water mass transformations by surface fluxes

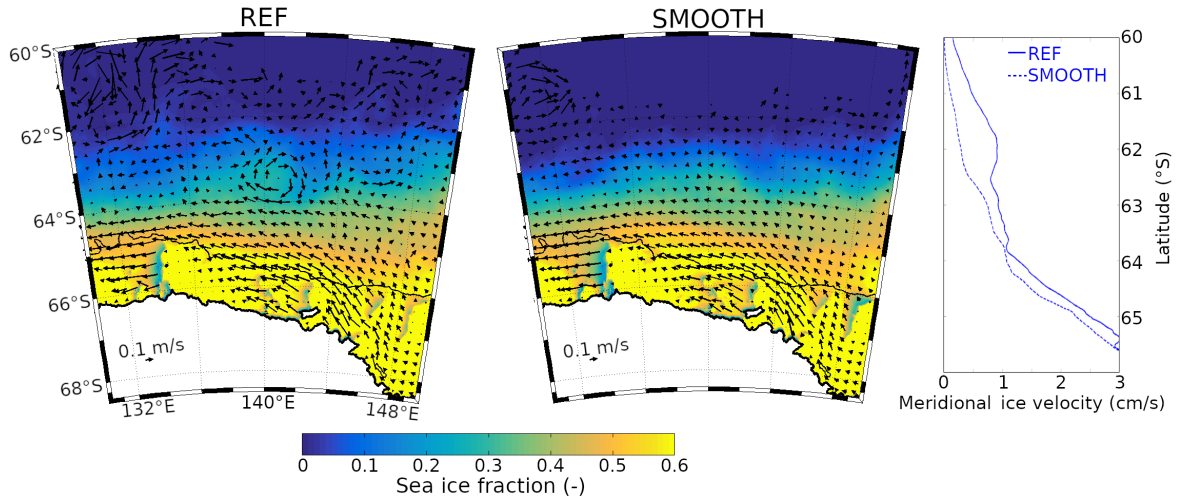

Figure 4.16: Mean sea ice velocities (black arrows) overlayed over the mean sea ice concentration (color shading) averaged over 2013 in REF (left) and SMOOTH (middle). Zonal average of the mean sea ice velocity in REF and SMOOTH (right).

following the method proposed by Walin (1982) and used for the Southern Ocean in Abernathey et al. (2016) and Jeong et al. (2020). The water mass transformation rate Ω is defined as $\Omega(\sigma,t) = \frac{1}{\sigma_{k+1}-\sigma_k}\int\int_A(\frac{\alpha Q}{C_p\rho_0}+\frac{\beta SF}{\rho_0})dA$. σ is the seawater potential density referenced to the surface, α and β the thermal expansion and haline contraction coefficients, Q the surface heat flux, C_p the thermal capacity of seawater at constant pressure ($C_p = 3994 J/kg^\circ C$), S the surface salinity, F the freshwater flux, ρ_0 the reference density of seawater, and A the area of the ocean surface with $\sigma_k < \sigma < \sigma_{k+1}$. We use a σ scale with a bin width of 0.1 kg/m^3 below 26.9 kg/m^3, 0.05 kg/m^3 between 26.9 kg/m^3 and 27.5 kg/m^3, and 0.01 kg/m^3 above 27.5 kg/m^3 to increase the resolution for the high density water masses. We compute a transformation rate for the freshwater flux associated with sea ice melting or freezing and for E-P (evaporation minus rainfall and snowfall). We also compute a transformation rate due to heat fluxes, which is separated into the ice-free and ice-covered ($SIC > 0.05$) cases.

The water mass transformation rates simulated in REF and SMOOTH are illustrated in Figure 4.17. The total transformation (black curves) shows the expected buoyancy loss by dense waters ($\sigma > 27.4\ kg/m^3$) and the buoyancy gain of lighter waters ($\sigma < 27.4\ kg/m^3$). The buoyancy loss of dense waters is dominated by the brine flux, with a secondary role of heat loss in the ice-covered ocean for relatively lighter waters. The gain of buoyancy is distributed between the freshwater and heat fluxes from sea ice melting, the surface warming for the ice-free ocean, and precipitation. The surface transformation of water masses denser than $\sigma > 27.4\ kg/m^3$ is weakly affected by the eddies. Most of the surface transformation of dense waters takes place on the continental shelf, where the model is not eddy-resolving. The transformation of intermediate waters ($27 < \sigma < 27.4\ kg/m^3$) is reduced in SMOOTH compared to

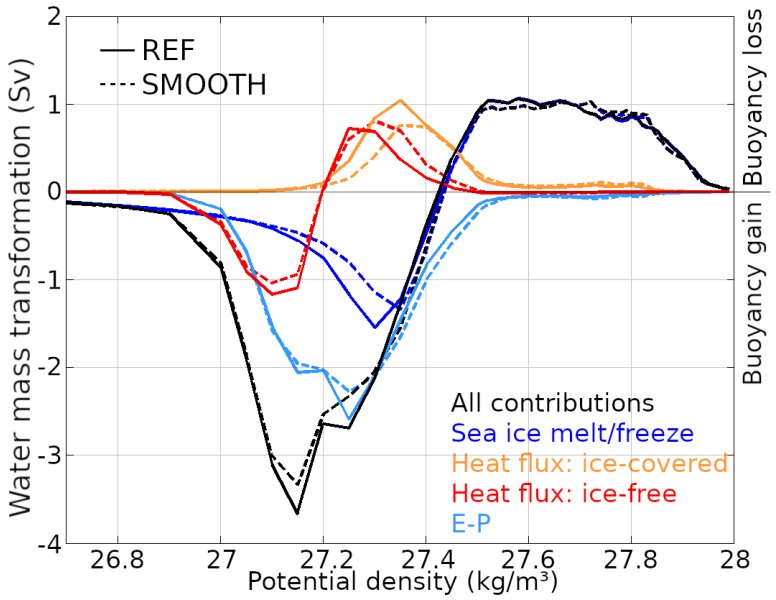

Figure 4.17: Water mass transformation rate per density class in REF (solid lines) and SMOOTH (dashed lines). The total contribution (black line) is the sum of: the buoyancy flux due to sea ice freezing or melting (blue), the buoyancy flux associated with heat fluxes (latent, sensible, longwave and shortwave) for the ice-free (red) and ice-covered (orange) cases, and the precipitation over the ocean (teal).

REF. This means that intermediate density waters receive weaker buoyancy fluxes in SMOOTH than in REF. Buoyancy loss due to heat fluxes in the ice-free ocean is higher in SMOOTH than in REF. There is an opposite effect for the ice-covered ocean. This results from the lowering of the sea ice extent in response to weaker northward sea ice advection in SMOOTH. Buoyancy gain through heating in the ice-free ocean is slightly decreased in SMOOTH. The contribution of sea ice melt to water masses transformation is also lowered. We note a slight decrease in buoyancy gain due to E-P. As seen in Figure 4.15, eddies contribute to the northward export of sea ice. In SMOOTH, less sea ice is available for melting in the intermediate density waters encountered in the north of the Adélie Land sector. This leads to a weaker freshwater flux and buoyancy gain. The combined effect of eddies is an increase of buoyancy loss or water mass transformation for the intermediate to low density waters. Thus, by redistributing the sea ice, eddies act to restratify the ocean and transform water masses in the upper branch of the thermohaline circulation.

4.7 Discussion

The present results reveal that eddies can affect the air-sea fluxes and the atmosphere in high latitudes of the Southern Ocean, even in the presence of sea ice. To our

knowledge, it is the first time that the modulation of atmosphere–sea ice–ocean interactions by mesoscale eddies is described in a coupled model. Our results confirm the possibility for eddy–sea ice interactions through the mechanisms described by Manucharyan and Thompson (2017) and Gupta et al. (2020). As in those studies, the imprint of eddies on the sea ice originates from the dynamical and thermal forcing of eddies. The sea ice also affects the eddies in return, via the modulation of surface buoyancy fluxes or the mechanical slow down of eddies. We found that the eddy-driven sea ice advection explains most of the large-scale effects of eddies. The mechanism of Manucharyan and Thompson (2017) might be a key process governing the evolution of the MIZ and the ocean stratification in the Southern Ocean. Eddies are thought to contribute to ocean restratification by flattening tilted isopycnals (McWilliams, 2008; Chanut et al., 2008). The eddy-driven sea ice advection can be a second mechanism by which eddies restratify the Southern Ocean. Gupta et al. (2020) suggested that eddy-ice pumping in anticyclonic eddies leads to upward heat flux and sea ice thickness reduction. The EIP seems to have a weaker effect in our simulations, which might be due to the higher proportion of cyclonic compared to anticyclonic eddies simulated off Adélie Land. Besides, we showed that the stress curl response to an increase of current vorticity saturated for eddies covered by weak sea ice. As we do not detect many eddies in the strong ice pack, the EIP simulated in our experiments is likely weaker than the one of Gupta et al. (2020).

Besides the imprint of eddies on the sea ice, we also explored how eddies modulate air-sea interactions with and without sea ice. For the ice-free ocean, we found that the dynamical and thermal mesoscale air-sea coupling are at play in our simulation (Chelton and Xie, 2010a; Renault et al., 2016). This illustrates a tight coupling between the ocean and atmosphere at the mesoscale despite the small eddy radius and swift winds. One of our most striking results is the existence of mesoscale air-sea interactions despite the presence of sea ice. In our model, the atmosphere–sea ice–ocean coupling is even intensified. Through both mechanisms, ice-free and ice-covered eddies affect the near-surface atmosphere. This opens the possibility of feedback. The air cooling above ice-covered cyclonic eddies likely increases the sea ice lifetime, increasing the potential for eddy-driven advection. A proper quantification of the atmosphere–sea ice–ocean feedback remains to be done. Our findings suggest that the eddy imprint on the atmosphere observed by Frenger et al. (2013) could be extended to the ice-covered ocean. However, we did not find imprints of eddies on the atmosphere away from the surface. The cooler surface or stronger atmosphere stratification in the southernmost Southern Ocean might inhibit the upward propagation of the surface anomalies in the atmosphere (Bailey and Lynch, 2000; van Lipzig et al., 2002; Kittel et al., 2018). This could also be due

to model limitations such as the hydrostatic approximation or the use of a vertical mixing scheme designed for the ice sheet. Further sensitivity experiments have to be carried out to clarify this issue.

The effects of eddies on atmosphere–sea ice–ocean interactions have several implications for the modeling and understanding of the polar climate and Southern Ocean dynamics. Most current GCMs do not explicitly resolve mesoscale eddies. While several effects of eddies on the ocean are parameterized in GCMs, no parameterization exists to represent the effects of eddies on the atmosphere–sea ice–ocean interactions. We showed that eddies affect the freshwater redistribution by the sea ice and the ocean surface momentum fluxes. Freshwater fluxes are essential for the dynamics of the Southern Ocean, as they condition the ocean stratification and the rate of water masses transformation. Changes in freshwater fluxes could induce a modification of heat and carbon storage in the Southern Ocean, affect the sea ice (Bintanja et al., 2015), and modulate the thermohaline circulation (De Lavergne et al., 2014; Abernathey et al., 2016). On the other hand, the effects of eddies on momentum fluxes can have repercussions for the Southern Ocean dynamics. The modulation of air-sea momentum fluxes by eddies was suggested to drive multidecadal variability of the Southern Ocean (Le Bars et al., 2016). Finally, the effects of eddies on the polar atmosphere are mostly unknown. Foussard et al. (2019) suggested that eddies affect the large-scale atmospheric circulation in an idealized polar vortex. As we have shown, eddies also affect the atmosphere in an ice-covered ocean. However, the imprint of eddies on the sea ice or atmosphere described in the present study remains relatively weak. There is no change in the total sea ice production if the interactions of eddies with the sea ice are turned off, the imprint on air-sea flux is lower than 10 W/m^2 leading to a temperature response of the order of 0.2°C, and the effect on the atmosphere is limited to the lowermost layers. The role of eddies on air-sea momentum fluxes and sea ice advection is more important and might have large-scale consequences, but the effects remain of second-order compared to other sources of error in GCMs. Some of our conclusions might have, however, been underestimated due to the prescription of lateral boundary conditions. A similar experiment other the whole Southern Ocean would enable us to better quantify the importance of the processes described in this study.

We expect that the mesoscale atmosphere–sea ice–ocean interactions simulated here off Adélie Land are at play elsewhere in the Southern Ocean. Yet, one of the particularities of the Adélie Land sector is the proximity of ACC jets to the continental shelf (Sokolov and Rintoul, 2009). This likely explains the high eddy activity found in this region (Hausmann et al., 2017) and also the relatively low sea ice extent in

this sector of Antarctica. High-resolution coupled models of the whole Southern Ocean would be needed to understand how the processes described here affect the large-scale ocean, sea ice, and atmosphere. Besides, even higher resolution models would be needed to understand the role of eddies in the lower-cell of the thermohaline circulation and the formation of Dense Shelf Waters (Stewart et al., 2018). The results presented here might be sensitive to modeling choices. An assessment of the sensitivity of mesoscale atmosphere–sea ice–ocean interactions to the model parameters is also needed. For instance, the treatment of the sea ice rheology might influence the ability of sea ice to deform due to small-scale ocean currents. The choice of transfer coefficients for the atmosphere–sea ice–ocean fluxes could also affect small-scale atmosphere–sea ice–ocean interactions. In our experiments, the sea ice roughness lengths for air-ice or sea ice momentum fluxes are assumed to be constant. But they may vary with the sea ice concentration or the sea ice morphology (Lüpkes et al., 2012). We compute the sea surface roughness as a function of wind speed, but this relationship does not hold when waves interact with sea ice (Boutin et al., 2018). Finally, the choice of vertical mixing scheme in the atmosphere possibly impacts the small-scale air-sea interactions (Song et al., 2009). It is unclear now how to represent the boundary layer turbulence above the sea ice. MAR is adapted for the representation of the stable boundary layer over the Antarctic Ice Sheet and thus potentially underestimates the turbulence over the ocean. The response of the atmosphere to the eddies might also be different with a non-hydrostatic model as shallow convection may occur over sea ice leads or polynyas (Gryschka et al., 2008).

4.8 Conclusion

The Southern Ocean is a region of intense atmosphere–sea ice–ocean interactions with global repercussions. It is also a hotspot of mesoscale activity. Yet, the role of eddies in modulating atmosphere–sea ice–ocean interactions is poorly understood. In this work, we have assessed how mesoscale eddies affect atmosphere–sea ice–ocean interactions in the Adélie Land sector using a regional ocean–sea ice–atmosphere model. We found that eddies affect the sea ice motion and melting/freezing. For the first time, we showed that eddies also imprint the near-surface air temperature and wind speed in ice-covered regions. These imprints are due to the modulation of atmosphere–sea ice–ocean heat and momentum fluxes by the eddies. Contrary to the general assumption, the sea ice intensifies the small-scale atmosphere–sea ice–ocean interactions. At the scale of the Adélie Land sector, the modulation of atmosphere–sea ice–ocean interactions by eddies has two major effects for the ocean and sea ice. First, eddies dampen the energy input to the ocean by surface stress,

reducing the large-scale kinetic energy. Secondly, eddies redistribute the sea ice and contribute to its northward advection. This leads to higher freshwater fluxes favoring ocean restratification in the seasonal ice zone. These results suggest that there is a tight coupling between the atmosphere, ocean, and sea ice at the mesoscale which can impact the large-scale behavior of these two media.

The recent research about ocean eddies in polar regions suggests that they play a bigger role than previously thought. This represents an important issue for the modeling of climate. Most global climate models do not resolve mesoscale eddies (let alone eddies in polar regions), and the parameterizations of eddy effects are not accounting for the specific processes of polar regions. The knowledge gap is yet a great opportunity for scientific research, as it opens many questions. Understanding the effects of the mesoscale atmosphere–sea ice–ocean interactions on the whole Southern Ocean is crucial. It may impact the dynamics of the ACC, the storm track, the thermohaline circulation, and the ocean carbon and heat uptake. Further work is needed to understand how to simulate mesoscale atmosphere–sea ice–ocean interactions. Such effort would benefit from the development of observational capabilities at small spatial scales.

Chapter 5

Conclusions and perspectives

5.1 Main achievements

Owing to the scarcity of observations in the Southern Ocean, the small-scale interactions between the ocean, cryosphere, and the atmosphere are poorly understood. At the same time, GCMs do not explicitly represent several small-scale processes that can have important implications for the climate. It is therefore needed to identify the relevant air-sea-ice interactions taking place at small scales, how their misrepresentation in climate models can hamper the realism of climate simulations and how to address this issue. The sector of Adélie Land, in East Antarctica, constitutes an interesting region to investigate the importance of small-scale processes on ocean–sea ice–atmosphere interactions as it hosts the formation of AABW, a water mass involved in the global oceanic thermohaline circulation. By using high-resolution regional ocean–sea ice and ocean–sea ice–atmosphere models, we have tried to bridge this knowledge gap and to answer the question: 'What are the effects of small-scale processes on the atmosphere-cryosphere-ocean interactions in the Adélie Land sector, East Antarctica?'.

In Chapters 2 and 3, we explored how tides, ocean–ice shelf interactions, and small-scale winds affect the production of DSW in coastal seas. The first question that was addressed is: "How do tides and ocean–ice shelf interactions affect the formation of DSW off Adélie Land?". To address this issue, we have developed a 1/24° regional configuration of the NEMO-LIM model capable of simulating landfast ice, polynyas, and small-scale ocean circulation within ice shelf cavities or in the shelf seas. We performed a set of simulations in which ocean tides, ocean–ice shelf interactions, both of them or neither of them are accounted for. Our results pointed out that ocean–ice shelf interactions transform dense waters into lighter water masses within the cavities leading to a lowering of the DSW production rate. The effects of ice shelf basal melt on DSW formation highlighted in our study corroborate recent findings which suggested

a potential suppression of deep convection in the Weddell Sea or DSW production in the Amundsen Sea due to ice shelf meltwater (De Lavergne et al., 2014; Silvano et al., 2018). The mechanism involved is, however, slightly different. Our results suggest greater importance of the consumption of dense waters within the cavities compared to the indirect effect on the sea ice production or the freshwater content within polynyas. This is in a sense in agreement with the impact of ice shelves on water masses transformation simulated by Jeong et al. (2020), but our model does not indicate a sea ice production increase that can compensate the consumption of DSW within cavities. This conclusion might, however, be specific to the Adélie Land area and is potentially sensitive to the model mean state. It should thus be confirmed by future work. One important implication of the effects of ice-shelf melt on DSW is that the projected increase in AIS freshwater discharge for the 21st century could diminish or suppress DSW production. In this regard, we state that ocean–ice shelf interactions have to be accounted for in climate models. Concerning the role of tides, our results point out that they have little influence on the DSW production or ocean circulation around the Mertz Glacier Polynya if ocean–ice shelf interactions are not accounted for. However, tides increase the basal melt of Adélie Land's ice shelves as simulated in the Weddell Sea (Hausmann et al., 2020) or West Antarctica (Jourdain et al., 2019). As a result, tides amplify the effects of ocean–ice shelf interactions on DSW. From our simulations, it seems that the effects of tides could be represented by parameterizing their influence on ice shelf basal melt, for instance following the method of Jourdain et al. (2019). Our conclusion about the absence of effects of tides alone is yet likely specific to the sector investigated here, and could not hold for other regions (Stewart et al., 2018). Besides, the importance of tides on ice shelf basal melt suggests that the role of tides might have been overlooked in previous studies. Stewart et al. (2018) obtained an important effect of tides on cross-shelf and on-shelf ocean circulation, but they did not account for ocean–ice shelf interactions in their model.

In Chapter 2, we investigated the implication of subsurface processes on the formation of DSW, but this should not overshadow the importance of the atmosphere through its effects on polynyas. In Chapter 3, we assessed the sensitivity of sea ice and polynyas to small-scale atmospheric variability and questioned the benefits of increasing the atmospheric forcing resolution. The second question that was addressed in this thesis is: "What is the sensitivity of sea ice and polynyas to the resolution of the atmospheric forcing in the region of Adélie Land?". This work is based on a set of atmospheric simulations performed with the MAR model at varying horizontal resolutions which are used to force our ocean–sea ice model. We have shown that refining an atmospheric model grid leads to a large increase in katabatic wind speed in coastal regions and a local redirection of the coastal winds.

We attributed this to a better representation of topography and valleys of the AIS in coastal regions, as also suggested by Petrelli et al. (2008). Sea ice production in polynya increases together with DSW production as the forcing resolution gets finer. These results confirm the high sensitivity of coastal Antarctic sea ice to the representation of katabatic winds simulated by Mathiot et al. (2010) or Barthélemy et al. (2012). However, we showed that a resolution higher than 20 km might be needed to represent the local intensification of katabatic winds. As the effect of resolution is linked to the representation of topography, the choice of the atmospheric resolution should be guided by the complexity of the terrain under investigation. The importance of resolution for the simulation of coastal winds points to a shortcoming of coarse-resolution GCMs. The weaker coastal and katabatic winds simulated at low resolution could partially explain the poor representation of DSW and polynyas in these models (Heuzé, 2021; Mohrmann et al., 2021). Particular attention should be given to the representation of Antarctica coastal winds in GCMs in the future. If increasing the resolution of the atmospheric component of climate models might not be feasible yet, other approaches can be envisioned such as a fine tuning of the orographic drag (Jourdain and Gallée, 2011). In addition, we showed that coastal polynyas are more sensitive to the atmospheric forcing resolution than the offshore ones. Indeed, polynyas are either forced by the local katabatic winds or by large-scale easterlies, as was suggested by Massom et al. (1998). This could influence the way polynyas and DSW respond to the future evolution of winds and illustrate the need to understand how will katabatic winds and easterlies evolve in the future. Our simulations also allowed us to pinpoint a weakening of the effects of increasing the atmospheric forcing resolution below 10 km. The added value of increasing the atmospheric model resolution further appears limited. Finally, we found that increasing the atmospheric forcing resolution leads to a lowering of ice shelf basal melt, in contradiction with the effects of forcing resolution simulated by Dinniman et al. (2015). Their results are for the whole Southern Ocean and thus mask regional variability. For regions such as Adélie Land where katabatic winds prevail, the effects of the forcing resolution on polynyas activity likely exceed the potential effects on ocean heat transport suggested by Dinniman et al. (2015). Via the mechanisms presented in Chapter 2, the response of ice shelves to an increase in atmospheric forcing resolution tempers the effects of a sea ice production increase on DSW production. This illustrates the importance of the interactions between polynyas and ice shelves.

In Chapter 4, we switched the focus to processes taking place in the open ocean and affecting the upper cell of the Antarctic MOC. We tried to elucidate the role played by ocean eddies by addressing the following question: "How do mesoscale ocean

eddies affect the atmosphere–sea ice–ocean interactions?". Besides exploring the role of poorly documented processes, one of the main originality of this chapter is the development and application of a high-resolution regional coupled atmosphere–sea ice–ocean model. We found that eddies have a remarkable imprint on sea ice, by impacting its motion and growth rate as suggested by Manucharyan and Thompson (2017) and Gupta et al. (2020). The imprint of eddies is also found on the near-surface atmosphere, whether the ocean is covered by sea ice or not. Actually, the imprint of eddies on the atmosphere is stronger in presence of sea ice. Our model suggests that the observations of ocean eddies imprint on the atmosphere reported by Chelton (2013) and Frenger et al. (2013) could be extended to the ice-covered parts of the Southern Ocean, thought direct observations are needed to confirm this. The coupled model simulates a divergence (positive curl) of the wind across (along) small-scale surface temperature gradients, as found at lower latitudes (Chelton and Xie, 2010b). As it is the first time that the existence of such a relationship is suggested for the ice-covered Southern Ocean, we wanted to explore how the presence of sea ice affects the small-scale air-sea interactions. We found that the winds response to surface temperature changes is stronger in the presence of sea ice, suggesting a stronger sensitivity of the near-surface atmosphere to small-scale heterogeneity above sea ice than above the ocean. However, we could not investigate the effects on the atmosphere at a large scale due to the limited spatial coverage of our model. These results might also be sensitive to model parameter choices, which are poorly constrained by observations. As ocean eddies influence the heat and momentum transfer at the ocean–sea ice–atmosphere interface, they might also impact the Southern Ocean circulation and water masses transformations. To investigate these effects, we conducted a simulation in which eddies do not affect atmosphere–sea ice–ocean heat or momentum exchanges. This simulation revealed that eddies interactions with the sea ice or atmosphere reduce the ocean kinetic energy due to the friction of eddies on the surface, which weaken the momentum transfer from the winds to the ocean. Renault et al. (2016) already showed this mechanism for lower latitudes, but it is the first time that the effect is simulated in the ice-covered Southern Ocean. However, understanding the extent of the kinetic energy sink would require simulating the whole Southern Ocean. Furthermore, we found that eddies are important contributors to the northward advection of sea ice. This way, eddies contribute to the northward expansion of the sea ice cover, increase the freshwater flux in the north of the sea ice zone, and act to restratify the ocean. While eddies are known to contribute to ocean transport within the Antarctic MOC (Volkov et al., 2008; Dufour et al., 2015), we demonstrated that they also intervene in the MOC via their effect on surface fluxes. This effect is however limited, as the total sea ice production is similar whether eddies affect ocean-ice interactions or not. The positive influence of cyclonic

eddies on sea ice growth likely compensates for the negative effect of anticyclonic eddies suggested by Gupta et al. (2020). Yet, the influence of eddies on the surface water mass transformations and ocean kinetic energy might be underestimated in our model, due to the strong control applied at the boundary conditions. To unravel the influence of eddies on the sea ice and freshwater budget, it would also be needed to represent the Southern Ocean entirely. Our experiments suggest that eddy-driven atmosphere–sea ice–ocean interactions could affect the mean ocean circulation (by acting as a kinetic energy sink) and the thermohaline circulation (by redistributing the sea ice–driven buoyancy flux). These effects are missing from GCMs, but large-scale simulations would be needed to prove the need to incorporate them.

From the results of our three studies, we suggest the following path of improvements for climate models:
- including ice shelf basal melt in climate models appears important for its influence on the DSW formation demonstrated in Chapter 3 and impact on global sea level (not investigated here). In particular, interactive basal melt (accounting for the ocean state) might be crucial to simulate the response of the ice sheet to a potentially warming ocean and for the coupling between the ice sheet, ocean and polynyas illustrated in Chapters 3 and 4.
- efforts should be put into representing polynyas more realistically. This could be done by including the effects of landfast sea ice, the role of grounded icebergs, and by improving the representation of coastal winds (Chapter 4). A cheap approach could be to statistically correct coastal winds (using the information of high-resolution numerical models or in-situ wind measurements) or to increase the air-ice transfer coefficient in polynyas (discussed in Chapter 4) in order to intensify the activity of coastal polynyas.
- though we have demonstrated the importance of ocean mesoscale eddies in air-sea-ice interactions (Chapter 5), the simulated effects remained weak (no net effect on total sea ice production, 10% decrease of ocean kinetic energy while low-resolution models already underestimate it). The modulation of air-sea-ice interactions by mesoscale eddies simulated in our experiments appears to be of second-order compared to the other known impacts of eddies on the ocean (horizontal mixing, contribution to the meridional overturning circulation, ocean currents transport and pathways ...).

One of the principal limitations of the work presented here is its limited spatial and temporal coverage. Investigating the sensitivity of the Antarctic MOC, ACC, or the atmospheric circulation to small-scale processes (small-scale winds, ocean-ice shelf interactions or mesoscale eddies in our case) would require representing the

whole Southern Ocean. Extrapolating our results to other sectors of Antarctica might also be delicate. For instance, in the Weddell Sea, the ocean interactions with the immense Ronne ice shelf are likely different than in the Adélie Land sector. In West Antarctica, the warmer coastal ocean could respond differently to ocean–ice shelf interactions, tides, or small-scale winds. Besides, local processes can have remote effects due to the advection by the mean circulation. Another caveat is the short period of time covered by our simulations. The Antarctic climate exhibits important modes of variability on interannual to decadal time scales, which could affect the response of the atmosphere-cryosphere-ocean system to small-scale processes. Furthermore, large-scale ocean circulation such as the MOC need several years to adjust to forcing modifications, illustrating the need for longer simulations. Another limitation resides in the realism of the models used. Despite their very high resolution and the multitude of processes represented, the models used here remain idealized representations of reality. The fundamental dynamics of our model is adapted to represent the large-scale, global ocean and sea ice. Several processes are still missing or parameterized, such as eddies in the coastal seas and oceanic or atmospheric convection. Due to limited observations, tuning high-resolution models is delicate and it is unclear how well is the model represents small-scale processes. The results presented in this thesis are theoretical and likely sensitive to model choices.

With the ability to represent processes at smaller scales, high-resolution GCMs were shown to outperform coarse-resolution ones in several aspects of their representation of the climate dynamics (Roberts et al., 2018; Hewitt et al., 2020). The polar regions, and particularly Antarctica, have been missing from these analyses. This thesis contributed to filling in this gap. I have shown that the exchanges of heat, freshwater, and momentum between the components of the polar climate system are sensitive to the representation of small-scale processes presently missing from GCMs. By enlightening current GCMs limitations, this thesis can support the development of the next generation of GCMs. This thesis also revealed how the ocean, cryosphere, and atmosphere interact with one another at small spatial scales. Through the spectrum of small-scale processes, the atmosphere-cryosphere-ocean system reveals a new level of complexity that will have to be taken into account to predict the future of polar regions.

5.2 Perspectives

The first perspective of the work presented here would be to increase both the spatial and temporal coverage of the model. The processes investigated in this thesis affect the atmosphere–sea ice–ocean interactions in a certain manner, but they

might act differently in other sectors subjected to different forcings. Performing similar sensitivity experiments but at the scale of the entire Southern Ocean would be needed to obtain the zonally-cumulated effects of small-scale processes. Having a peri-Antarctic model would also allow us to study the response of the ACC and the Antarctic MOC that can only be "guessed" from our regional models, as large-scale oceanic currents are prescribed at the model boundaries. Taking into account the whole Southern Ocean would also enable us to study the effects of mesoscale eddies or polynyas on the atmospheric circulation, which is for the most part prescribed in our models, even in coupled mode. Apart from the spatial scale, increasing the time window of the simulations would permit us to better understand the implications of the processes studied here in the interannual variability of the Antarctic climate. We showed that small-scale processes significantly affect atmosphere–sea ice–ocean interactions under present-day climate conditions, it is natural to wonder how accounting for coastal polynyas, ocean–ice shelf interactions or mesoscale eddies could affect the climate projections made using GCMs. Experiments designed to study the effects of resolution in GCMs have already been performed, but these studies did not focus on the Southern Ocean. Exploring how the resolution affects the ACC, the Antarctic MOC or coastal water and sea ice properties in models of the HighResMIP (High-Resolution Model Intercomparison Project (Haarsma et al., 2016)) or PRIMAVERA (PRocess-based climate sIMulation: AdVances in high-resolution modeling and European climate Risk Assessment, https://www.primavera-h2020.eu/) projects would be highly instructive. Besides, small-scale processes can also evolve in a changing climate. The mesoscale activity of eddy-rich regions of the World Ocean (such as the Southern Ocean) has been rising over the past decades (Martínez-Moreno et al., 2021), which might be related to the global acceleration of ocean currents under strengthening winds (Hu et al., 2020). The intensification of mesoscale activity is also simulated by high-resolution climate models (Farneti et al., 2010), and could affect the response of the Southern Ocean meridional heat transport under climate change. In coastal seas, the effects of climate change could profoundly affect the ocean-ice-atmosphere system: ocean warming would increase ice shelf basal melt, potentially limiting DSW production (Silvano et al., 2018), while it is unclear how the Antarctic coastal winds (easterlies and katabatic winds) will evolve (Hazel and Stewart, 2019). Understanding how global warming will affect these processes would greatly improve our capacity to predict the future of the Antarctic Climate.

The role of small-scale processes in the Antarctic climate appears to be more important than previously thought, but GCMs with resolution approaching the one of our models are currently out of reach. There is therefore a need to develop methods

and parameterizations to account for the small-scale processes investigated in this thesis in GCMs. Several parameterizations already exist, but to our knowledge, there is currently very little effort to improve the representation of polynyas, landfast ice, or DSW production in coastal seas of Antarctica in GCMs. Similarly, specific attention should be brought to the representation of coastal winds. Several ways might be followed to improve coastal wind intensity simulated by GCMs in Antarctica: finely tune the orographic drag to account for the channelizing effect and the steep slopes that cannot be represented at low resolution, use statistical relationships obtained by comparing coarse and high-resolution models or adapt the air-sea and air-ice drag coefficients in polynyas. Besides the parameterizations in climate models, correcting the coastal winds of a global reanalyses such as ERA5 (as was for instance done by Mathiot et al. (2010)) could be a way to improve the forcing of ocean–sea ice models of Antarctica. The role of eddies on air-sea or ocean-ice interactions is presently not entirely accounted for in models. If eddies were found to significantly affect the ocean-ice interactions at the scale of the Southern Ocean, then it could be necessary to incorporate this effect in coarse-resolution models.

Despite the scarcity of high-resolution observations in the Southern Ocean, it is already possible to gain some information about small-scale processes from existing data and it will become easier in the near future. Such observations are desperately needed to evaluate the capabilities of models such as the one used here to simulate small-scale processes. High-resolution radars or altimeters (ICESat-2, SWOT) are now or will be able to observe the imprint of processes taking place at kilometric scales. New technologies such as Unmanned Aerial Vehicles (see Cassano et al. (2016)) or sea gliders (see Giddy et al. (2021)) could provide precious information about small-scale atmosphere–sea ice–ocean interactions. Besides, high-resolution remote sensed data can already be used to explore the role of small-scale processes, such as the eddies imprint on sea ice (Kozlov et al., 2020; Cassianides et al., 2021) or the distribution and frequency of sea ice leads (Reiser et al., 2019, 2020). Using the coupled model developed during this thesis in coordination with an observation campaign could be highly instructive to evaluate the capabilities of the model and understand the mechanisms at play. For instance, the YOPPsiteMIP initiative (Year of Polar Prediction site Model Intercomparison Project, https://www.polarprediction.net/key-yopp-activities/yoppsitemip/) aims at improving the understanding of polar processes with locally intensified measurements coupled to the use of numerical models around selected sites, such as the Dumont D'Urville base in Adélie Land. In the absence of high-resolution observations, a first approach could be to investigate the sensitivity of small-scale processes to modeling choices.

Finally, our study was limited to specific processes, but many other small-scale processes might be of interest. Despite its high resolution, our model is not capable of resolving submesoscale ocean activity or mesoscale eddies in the shelf seas. Increasing the resolution even further could unravel new interactions between the ocean, sea ice, and atmosphere at those scales. Coupling the atmosphere, sea ice, and ocean at high resolution offers possibilities that were not exploited in this thesis. For instance, the role of sea ice heterogeneity on the atmosphere or air-sea interactions has not been investigated in detail. The atmospheric response to polynyas or leads could affect the air-sea heat fluxes and the sea ice production and is thus important to understand. Performing longer simulations would also enable to study the coupling between the ocean and the ice sheet. The past variability of the Mertz Glacier Polynya is thought to be tightly coupled to the advance of the Mertz Ice Tongue (Campagne et al., 2015). Elucidating how the ocean, sea ice, and ice sheet interact together in the Adélie Land sector is crucial to understand how the formation of DSW will evolve in the upcoming century.

Chapter 6

Appendix

6.1 Supplementary material for Chapter 2

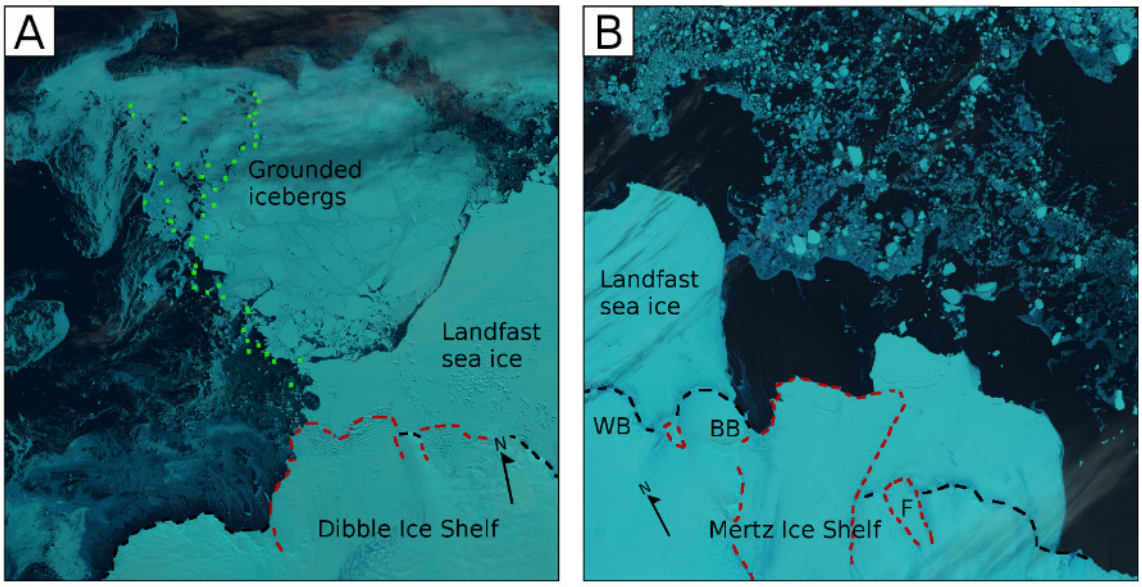

Figure 6.1: LANDSAT natural color images (USGS/NASA Landsat Program) of A) Dibble Ice Shelf region taken on 23 March 2015 and B) Mertz Ice Shelf region taken on 23 November 2014. The black dashed line illustrates the coastline and the red dashed line illustrate the ice shelves front or grounding line. Green dots indicate the location of potentially grounded icebergs. WB: Watt Bay and Ice Shelf, BB: Buchanan Bay, F: Fisher Ice Shelf.

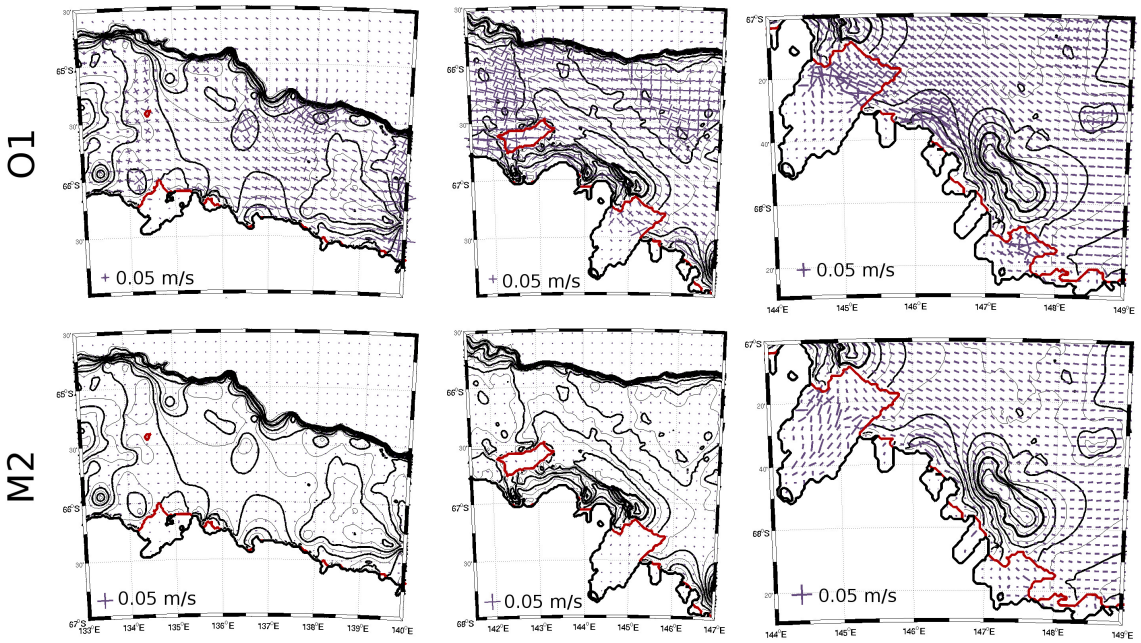

Figure 6.2: Tidal ellipses for constituents O1 and M2 in simulation BARO overlaying bathymetric contours. Red lines indicates the ice shelf or iceberg edges. Zoom over Dibble Ice Shelf (left), Adélie Depression (middle), Mertz and Ninnis Ice Shelves (right). Note the scale difference between O1 and M2.

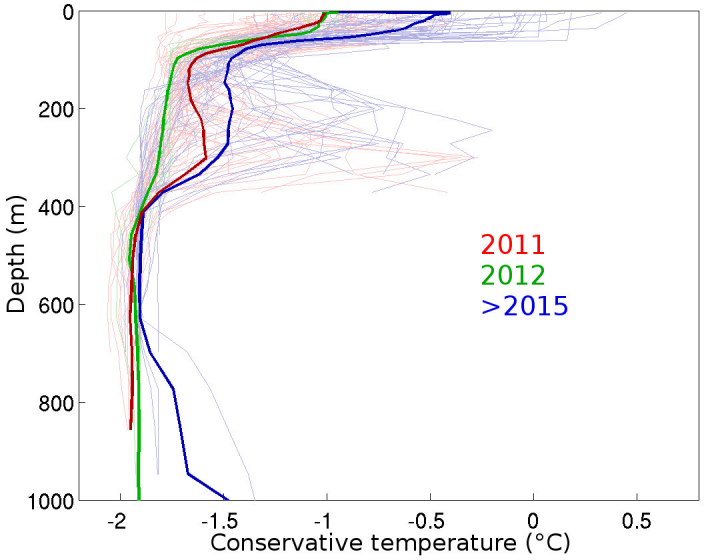

Figure 6.3: Ocean temperatures in the Adélie Depression from the CTD casts performed after 2010 used in the WOA18 climatology.

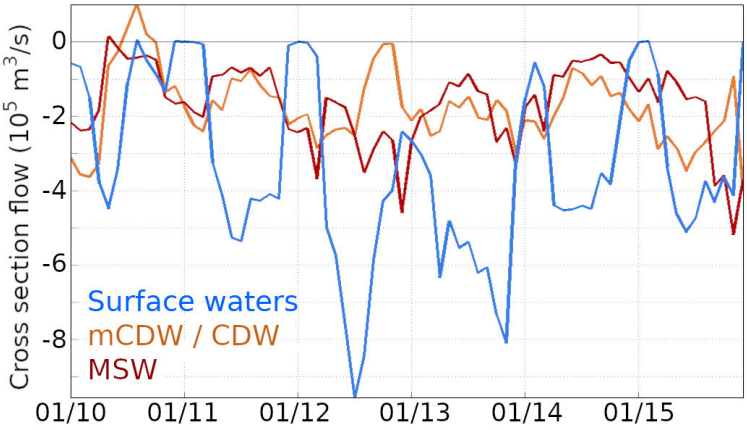

Figure 6.4: Ocean transport (counted positive eastward) across the Mertz Trough (Figure 3.1) simulated in REF for: surface waters ($\gamma_n < 28.0$ kg/m^3), mCDW/CDW ($28.0 < \gamma_n < 28.27$ kg/m^3 , T > -1.75°C), and MSW ($\gamma_n > 28.27$ kg/m^3, T >-1.75°C).

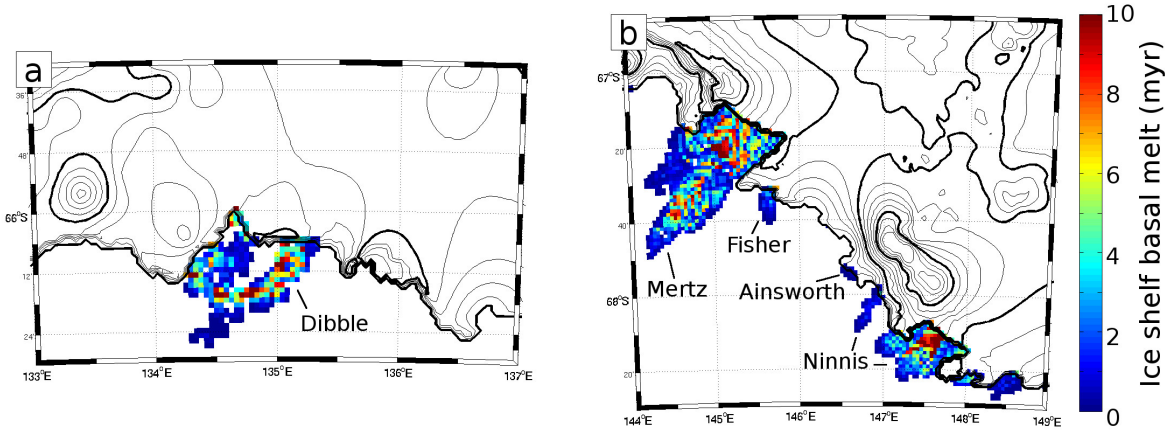

Figure 6.5: 2010-2015 averaged basal melt of ice shelves in Adélie Land. a) Dibble ice shelf; b) Mertz and Ninnis ice shelves. Black contours: bathymetry (every 100 m for thin lines, 500 m for thick lines).

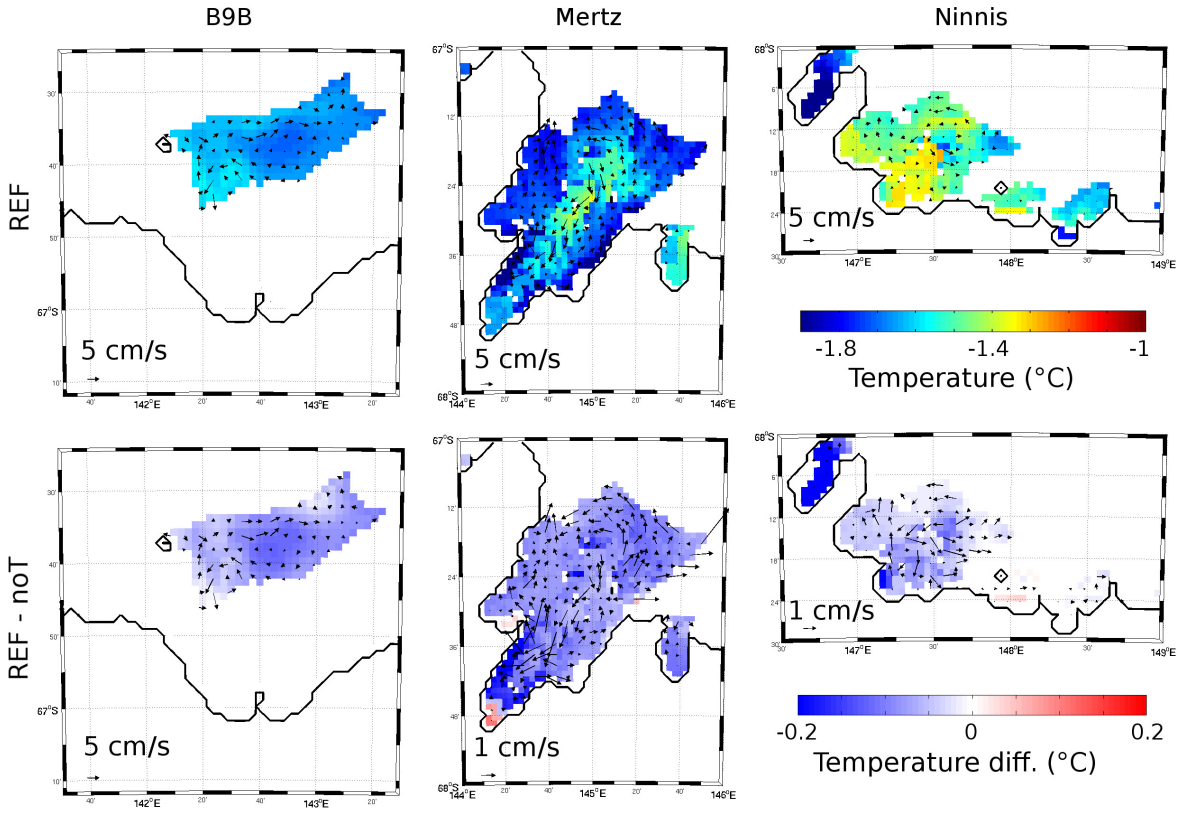

Figure 6.6: Average ocean temperature and velocity in the boundary layer at the ice-ocean interface beneath B9B (left), Mertz (middle) and Ninnis (right) Ice Shelves, simulated in REF (top). Difference between REF and noT (bottom row).

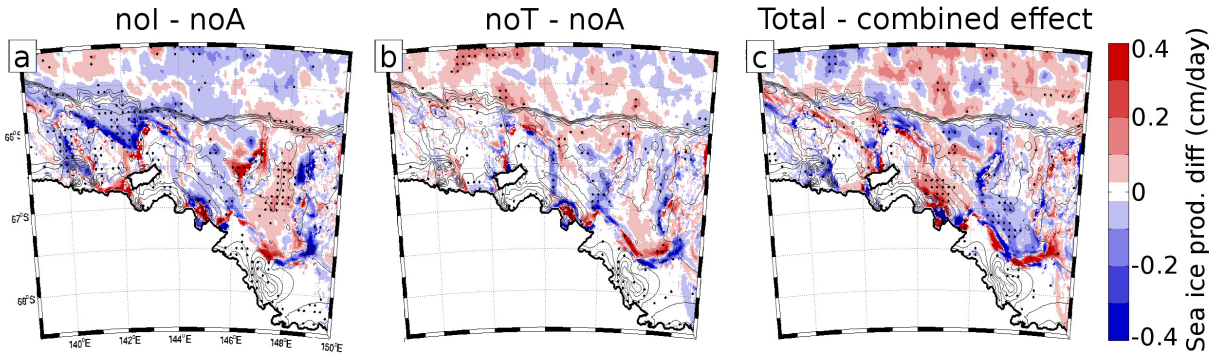

Figure 6.7: Differences in sea ice production (cumulated during freezing period: April to October), between noI and noA (a) and noT and noA (b). Effect of the interactions between tides and ice shelf (c). 2010-2015 averaged. Black crosses on color shading indicate statistical significance (2σ)

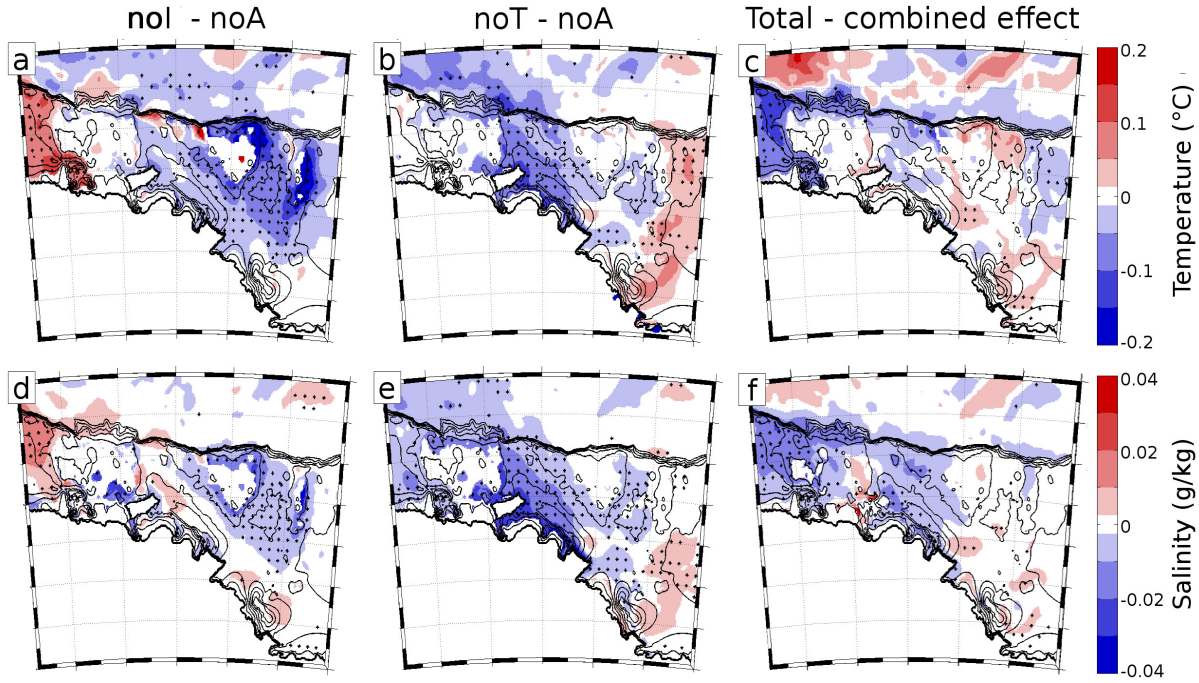

Figure 6.8: Temperature difference averaged between 200 m and 400 m (2010-2015 average) between noT and noA (a) and noI and noA (b). Temperature changes due to tide–ice shelf interactions (c). (d), (e) ,(f): as for (a), (b), (c) but for ocean salinity. Black crosses on color shading indicate statistical significance (2σ). Bathymetry is indicated as black contours every 200 m.

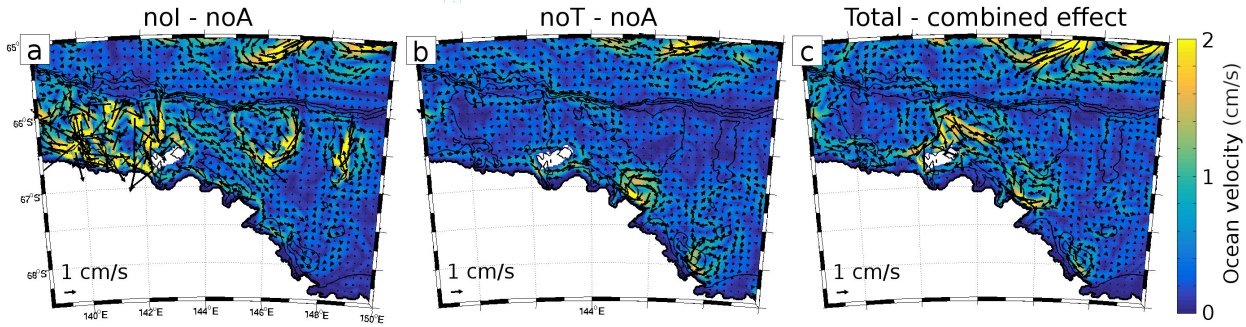

Figure 6.9: Same as figure 6.8 but for ocean velocities.

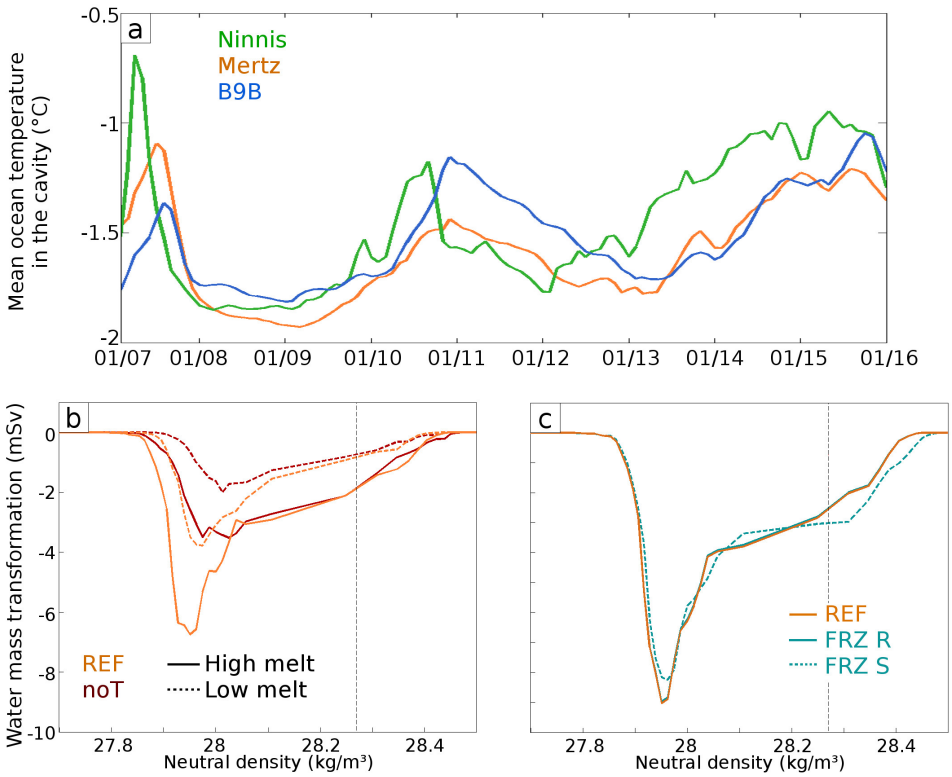

Figure 6.10: a) Ocean temperature averaged inside the Mertz, Ninnis and B9B cavities in the REF experiment. b) Water mass transformations from ocean–ice shelf interactions (computed following Jeong et al. (2020)) simulated in REF and noT for the years with low basal melt (2008, 2009 and 2012, dashed line) and for the years with high basal melt (2010, 2014 and 2015, solid line). Vertical dashed line indicates the 28.27 neutral density threshold. c) Water mass transformations from ocean–ice shelf interactions simulated in REF and estimated if the ocean temperature was -1.8°C: using the density of REF (FRZ R, solid line), or using the salinity of REF (FRZ S, dashed line).

6.2 Supplementary material for Chapter 3

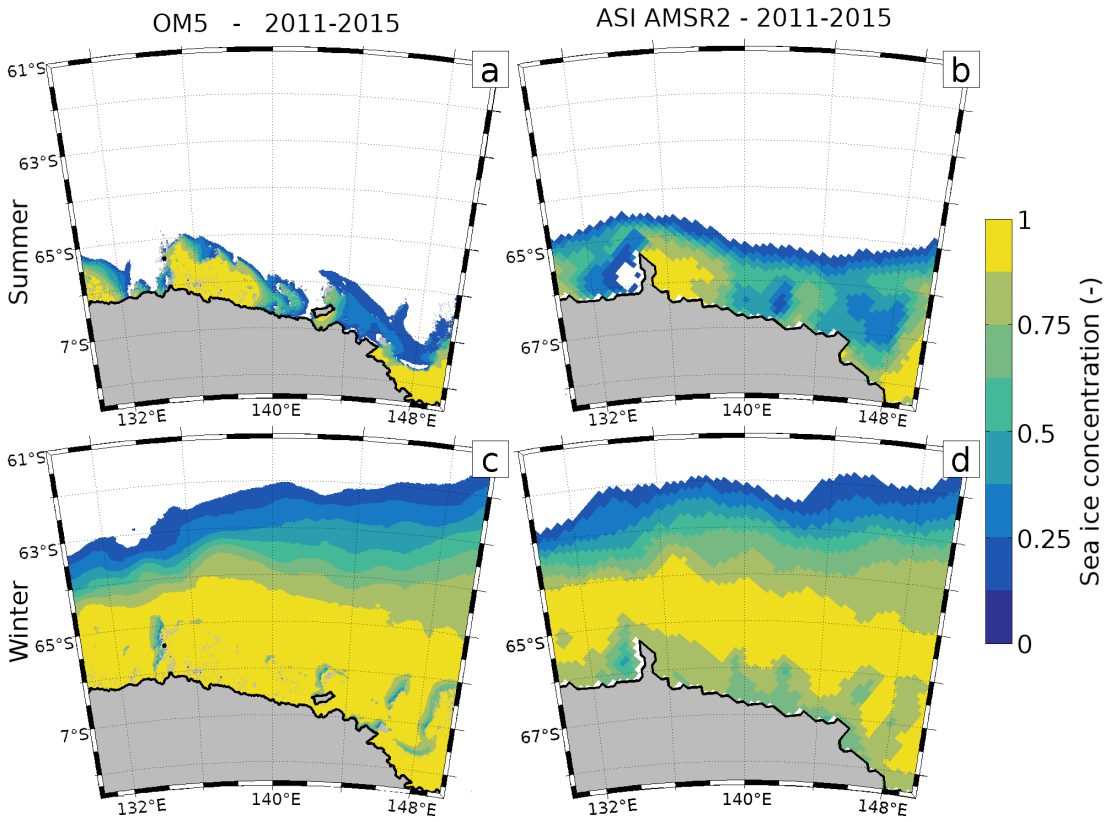

Figure 6.11: Mean sea ice concentration simulated in OM5 and observed in the ASI-AMSR 2 dataset in summer (a and b) and winter (c and d) of years 2011 to 2015.

6.2.1 Comparison between ERA5 and MAR simulations when used as forcing

In this appendix section, we compare the simulations OM20 and OM5 to an additional experiment (OERA5) sharing identical setup but using the ERA5 reanalysis as atmospheric forcing. OM10 is discarded for clarity, as its added value is limited here.

In Figure 6.12, we compare the mean sea ice production during winter for the OERA5 simulation and the OM20 or OM5 simulations. Compared to OM20, the sea ice production on the shelf seas is increased in OERA5. Sea ice production in OERA5 is higher than the one in OM20 for all the polynyas, with increases of more than 1 cm/day. The intensification of sea ice production is particularly large in the NGP and DBP. Sea ice production is also larger in OERA5 than in OM20 at the shelf break. The lower production rates found north in OERA5 likely arise from the melting of the larger volume of sea ice produced in the south. The sea ice production rates are closer between OERA5 and OM5. OERA5 still produces more sea ice at the shelf break or in the B9BP, DBP or off Dumont D'Urville (140°E). However, OM5 produces more sea

ice in the MGP (and locally in the NGP or B9BP). Sea ice formation rate in the MGP is up to 1 cm/day larger in OM5 than in OERA5.

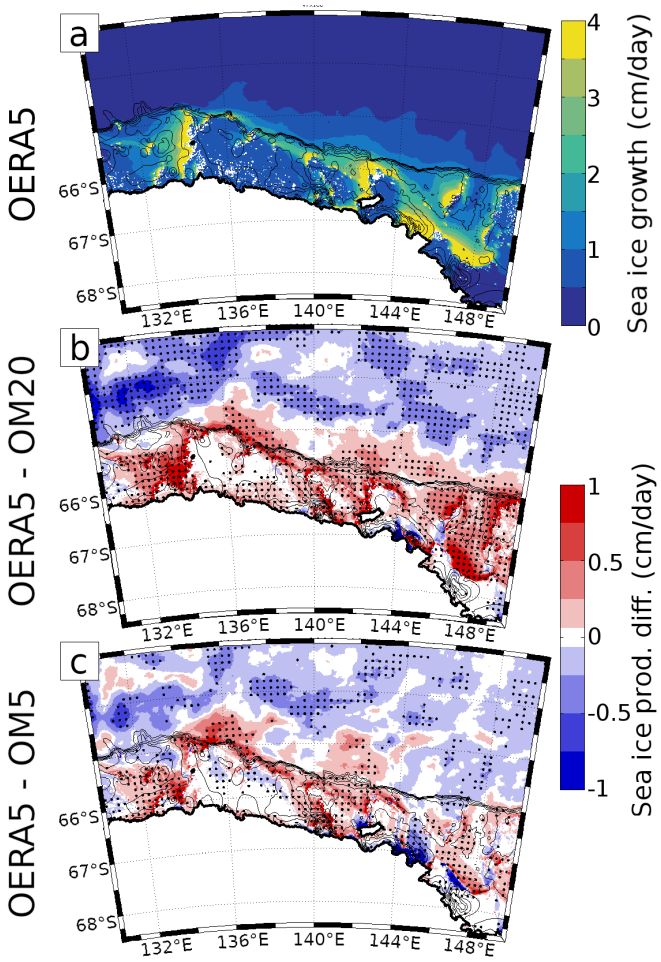

Figure 6.12: Mean sea ice production averaged over winters of 2010-2015 simulated in OERA5 (a). Differences of the mean sea ice production between OERA5 and OM20 (b) or OERA5 and OM5 (c). Dotted regions indicate statistical significance. Black contours represent the model bathymetry (every 200 m).

The rates of transformation of water masses due to brine rejection for the three simulations are shown in Figure 6.13. These rates of transformation are similar in OERA5 and OM5. The transformation rate is slightly shifted towards denser water in OERA5 compared to OM5 (weaker transformation below 27.5 kg/m^3, higher transformation rate above 27.7 kg/m^3). The transformation rate of water masses with density higher than 27.4 kg/m^3 is higher in OERA5 than in OM20, despite the lower resolution of the ERA5 reanalysis.

As shown in Sections 3.5 and 3.7 of the manuscript, increasing the forcing resolution between OM20, OM10, and OM5 leads to an increase in sea ice and dense water production. Despite the fact that ERA5 has a lower resolution than the three MAR experiments, the simulation OERA5 produces more sea ice and more

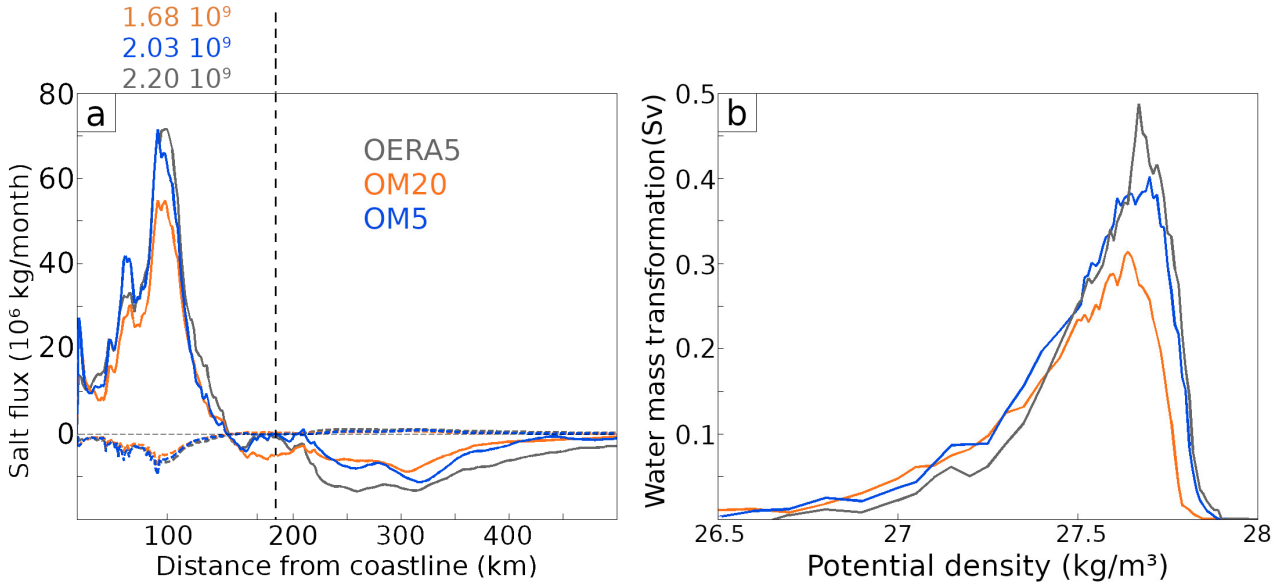

Figure 6.13: Same as Figure 3.18 but for simulations OERA5, OM20, and OM5.

dense waters than the OM5 simulation. A notable exception is the MGP, which opens more frequently and hosts stronger sea ice production in OM5 (Figure 6.14f). Another important difference between the OERA5 simulation and the OM20 or OM5 simulation is the distribution of landfast ice (Figure 6.14). Landfast ice occupies larger areas in the OM20 or OM5 simulation than in OERA5, and this has for effect to lower the extent of polynyas and the sea ice production in coastal seas. The causes explaining the higher sea ice production and lower landfast ice areas in OERA5 than in the simulations forced by MAR despite the weaker offshore winds of ERA5 remains to be elucidated and this question is out of scope of this paper. The dryer air of ERA5 implies stronger evaporation over the ocean and sublimation over sea ice that can boost the sea ice production. The stronger winds over the ocean favor the opening of offshore polynyas and the turbulent air-sea heat fluxes. Substantial differences are found between the precipitation rates of ERA5 and of the MAR simulations (Figure 3.7), which can affect the landfast ice (Figure 3.10). The comparison presented in this appendix suggests that using ERA5 instead of the MAR simulations does not imply an underestimation of the sea ice production, apart from specific coastal polynyas.

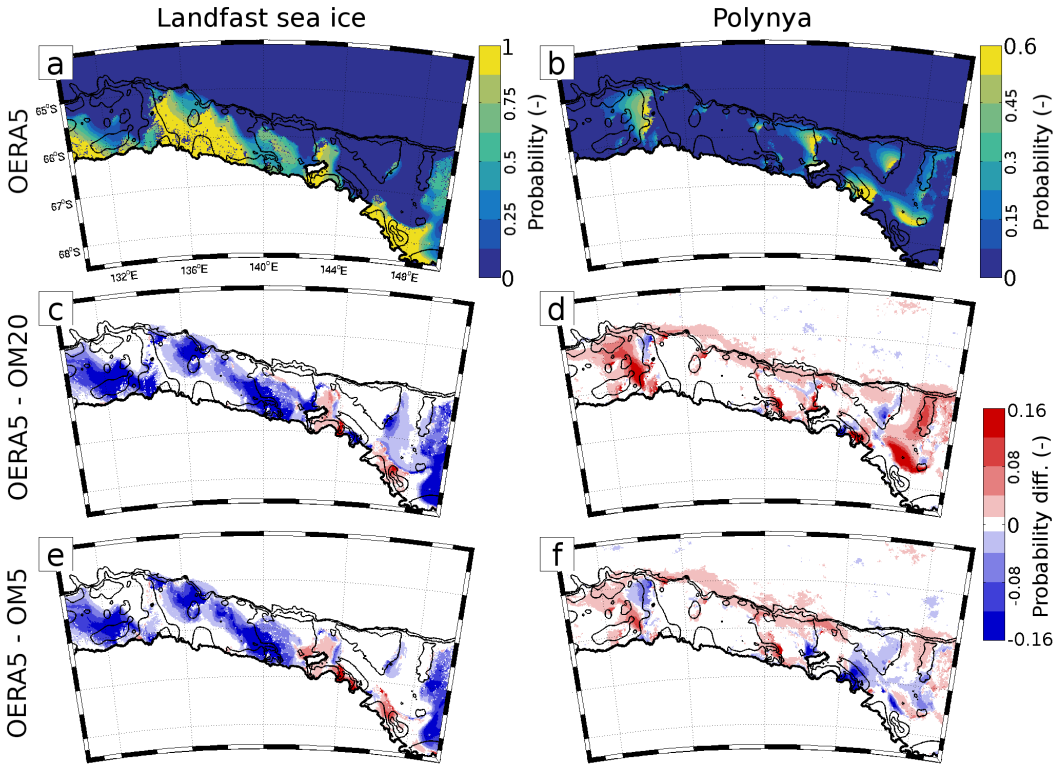

Figure 6.14: Same as Figure 3.9, but for OERA5 (a and b), OERA5 - OM20 (c and d), and OERA5 - OM5 (e and f).

6.3 Comparison of the coupled model with atmospheric reanalysis and ocean climatology

6.3.1 Atmosphere

Here, we compare the mean state of the atmosphere component in REF to the ERA5 reanalysis (European Center for Medium-Range Weather Forecast ERA5 Hersbach et al. (2020)). Observations are too scarce to perform a proper evaluation of the atmospheric model above the ocean. But, by comparing the model to ERA5, we ensure that the simulation of the atmosphere is satisfactory. Note that ERA5 is a reanalysis with its own biases and which has, to our knowledge, not been evaluated above the ocean or sea ice off Adélie Land. The mean summer and winter near-surface air temperatures, wind speeds, and downward longwave radiative fluxes simulated in REF are shown in Figure 6.15. On average, westerlies/northerlies blow in the northern part of the domain, and easterlies/southerlies in the southern one. The easterlies/southerlies intensify in winter as the polar front migrates northwards. In response, the westerlies are also shifted northwards. The differences between MAR and ERA5 are displayed on the two bottom rows of Figure 6.15. The 2 m air temperature is up to 2°C too high over the ocean in MAR, both in winter and summer. This bias can be related to the weaker sea ice cover in REF than in the

observations. South of 65°S, in winter, MAR is in general colder than ERA5 apart from some places along the coast, or downwind of obstacles (grounded icebergs or ice shelf tongues). Above the coastal seas, the sea ice model simulates thick landfast sea ice and polynyas (Van Achter et al., 2021; Huot et al., 2021b). Both are most likely absent from the surface boundary conditions of ERA5. As landfast sea ice can reach thicknesses of several meters, its surface temperature is lower than the one of thinner ice. Thus, the air temperatures above landfast sea ice in the coupled model are colder than in ERA5. The areas where MAR is colder than ERA5 in summer are also linked to the presence of landfast ice due to its higher albedo than thin sea ice. On the contrary, strong air-sea fluxes in polynyas warm the overlying atmosphere in winter, explaining the higher temperature in MAR in several places along the coastline (134°E, 140°E, and 145.5°E). The coastal easterlies are weaker in MAR than in ERA5 during winter. The southerlies are also weaker, apart from some specific areas along the coast where valleys channelize the katabatic winds. Differences in wind speed between MAR and ERA5 can have several origins, such as different treatment of surface drag or atmospheric boundary layer physics, higher-resolution topography in MAR, or different surface boundary conditions (winds in stand-alone MAR simulations are also weaker than those of ERA5, (Huot et al., 2021b)). Finally, the downward longwave radiations are weaker in MAR, especially in winter, when the difference reaches -20 W/m^2. This is a recurrent bias in MAR, also present in forced runs (Huot et al., 2021b) and discussed in Le Toumelin et al. (2020).

6.3.2 Ocean

The mean state of the ocean simulated in REF is presented and compared to the WOA18 (World Ocean Atlas 2018) climatology (Locarnini et al., 2018; Zweng et al., 2018) in Figure 6.16. The WOA18 climatology used here is built upon data from the past decade (2010-2020), and thus covers a longer period than the two years of simulation described here (2012-2013). It has to be noted that WOA18 is an optimal interpolation which does not directly represent the observations. The vertical profiles of temperature and salinity simulated in REF are in overall good agreement with the WOA18 climatology. In summer, the simulation are warmer than WOA18 between 50 and 130 m, peaking at 0.8 °C at 80 m, and fresher below 100 m. The amplitude of the seasonal cycle of surface salinity is lower than 0.03 g/kg while it reaches 0.1 g/kg in WOA18. By contrast, the seasonal cycle of temperature is well represented. The averaged mixed layer depth, indicated by the depth at which salinity starts to increase, is deeper in the simulation than in the observations. The fresh and warm anomalies in REF compared to WOA18 are general to the whole sector, as illustrated by the meridional sections of the ocean temperature and salinity of Figures 6.16c-f.

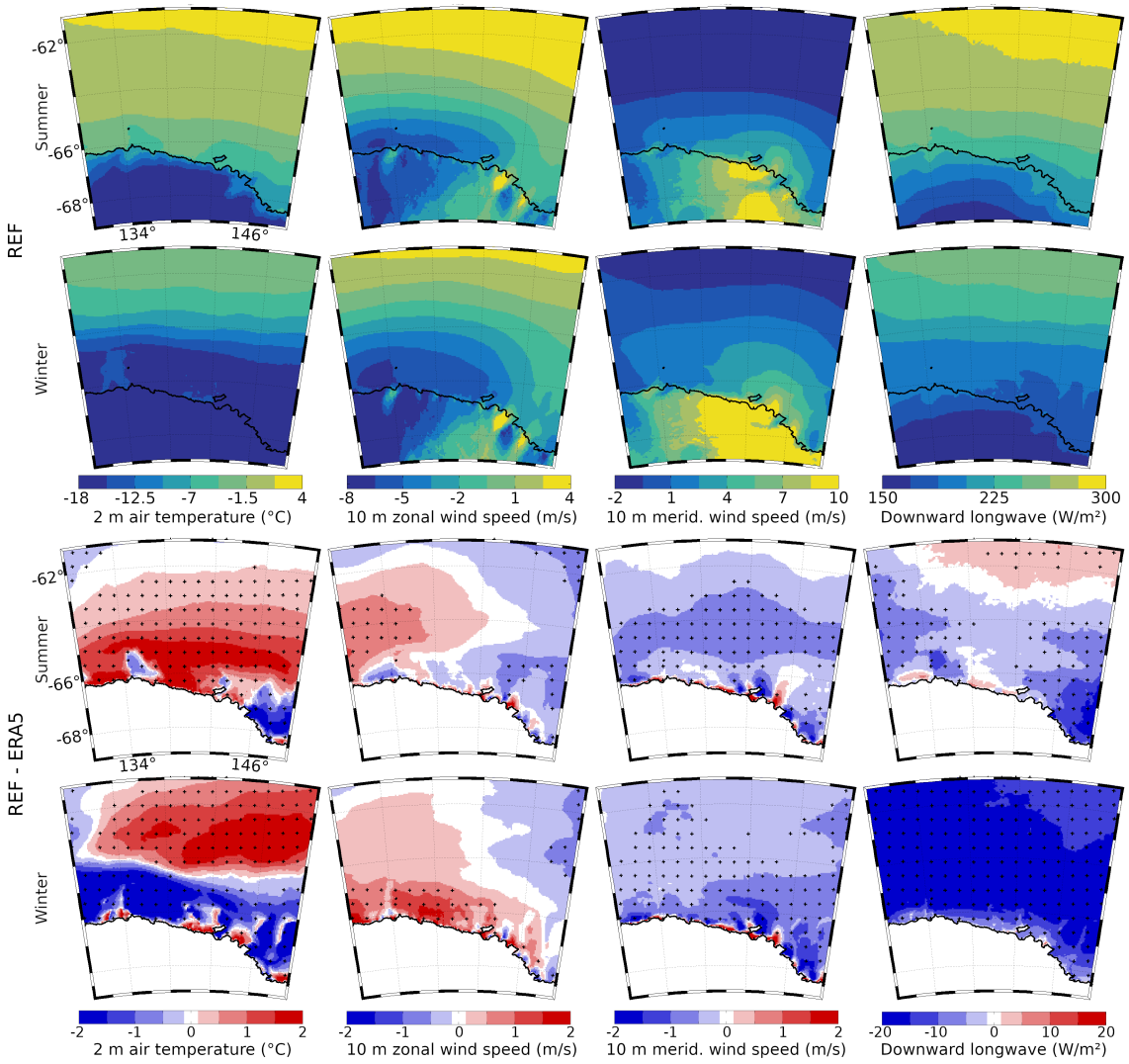

Figure 6.15: Average 2 m air temperature (1st column), 10 m zonal wind speed (2nd column), 10 m meridional wind speed (3rd column) and downward longwave radiation (4th column) simulated by MAR in REF, for summer (January to March, 1st row) and winter (May to October, 2nd row). The differences between REF and ERA5 are presented in the two bottom rows, for summer and winter. Black crosses indicate significant differences (2σ). ERA5 data were formerly interpolated on the MAR grid. Average over the 2011-2013 period.

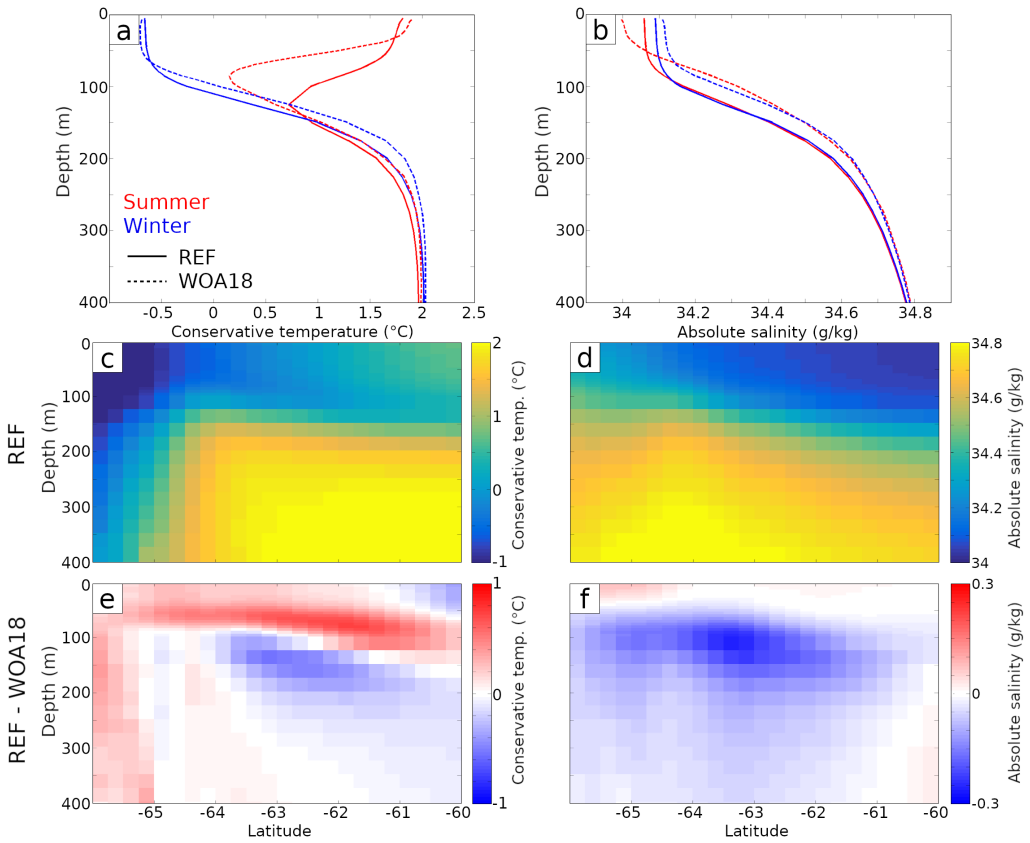

Figure 6.16: Ocean conservative temperature and absolute salinity simulated by REF (2012-2013) and from the WOA18 climatology (2010-2020). Top: vertical profiles of temperature (left) and salinity (right) averaged between 65°S and 60°S for summer (January-April) and winter (May-October). Bottom: meridional section (averaged over the whole sector) of the mean temperature (left) and salinity (right) as simulated in REF (middle row) and difference with WOA18 (REF-WOA18, bottom row).

List of Figures

1.1 Topography, bathymetry and ice draft (thickness of the ungrounded ice) of Antarctica and the Southern Ocean (in meters). The pink box indicate the location of the Adélie Land sector studied in this thesis. The topography is the one of ERA5 (Hersbach et al., 2020) i.e., using the Radarsat Antarctic Mapping Project Digital Elevation Model, Version 2 (RAMP2) dataset (`https://nsidc.org/data/nsidc-0082`). The bathymetry is obtained from ETopo1 (Amante and Eakins, 2009) and from IBCSO (Arndt et al., 2013) for the coastal seas of Antarctica. . . 6

1.2 Schematic view of the generation and flow of katabatic winds along a cross-slope section of Antarctica. https://commons.wikimedia.org/wiki/File:Katabatic-winds-antarctica.png 7

1.3 Schematic representation of the Southern Ocean depth-averaged circulation, prevailing winds, sea ice extents and DSW production location. The path of the ASC was reproduced from Thompson et al. (2018). Summer and winter sea ice extents are obtained from the 2000-2010 climatology of sea ice concentration from the OSI-450 dataset (Lavergne et al., 2019). 9

1.4 Schematic view of a meridional section of the Southern Ocean. AIS: Antarctic Ice Sheet, ASC: Antarctic Slope Current, ACC: Antarctic Circumpolar Current. 10

1.5 Schematic view of a meridional section of an Antarctic coastal sea illustrating the atmosphere-cryosphere-ocean interactions. ISW: Ice Shelf Water, AASW: Antarctic Surface Water, DSW: Dense Shelf Water, CDW: Circumpolar Deep Water, AABW: Antarctic Bottom Water, ASC: Antarctic Slope Current. 11

1.6 Schematic view of the Southern Ocean MOC, adapted from Speer et al. (2000). LCDW: Lower Circumpolar Deep Water, UCDW: Upper Circumpolar Deep Water, AAIW: Antarctic Intermediate Waters, SAMW: Sub-Antarctic Mode Water, AABW: Antarctic Bottom Water. . . 14

1.7 Section of ocean potential temperature and ocean salinity measured between Tasmania and Adélie Land. From the WOCE Southern Ocean Atlas (Orsi and Whitworth, 2005). 16
1.8 Representation of typical atmospheric and oceanic processes in a diagram of time and spatial scales adapted from Steele (1995) 19
1.9 Illustration of the evolution of GCMs horizontal resolution between the First (FAR) and the 4th Assessment Report of the Intergovernmental Panel on Climate Change (IPCC). The figure was adapted from Figure 1.4 of the 4th Assessment Report of the IPCC (Solomon et al., 2007). . . . 22
1.10 Simplified representation of the interactions of the ocean-sea ice model LIM with the atmosphere in a) the forced mode (by the global atmospheric reanalysis ERA5 or outputs from MAR) and b) the coupled mode with the MAR model. 29

2.1 Map of the southern half of the model domain (D'Urville Sea). Blue shading corresponds to the bathymetry and yellow shading to the ice shelf draft. Purple dots represent grounded icebergs. From West to East, DB: Dibble Bank, DT: D'Urville Trough, DD: D'Urville Depression, AB: Adélie Bank, B9B: grounded iceberg, AS: Adélie Sill, AD: Adélie Depression, MB: Mertz Bank, MS: Mertz Sill, ND: Ninnis Depression, MT: Mertz Trough, NB: Ninnis Bank. The black line corresponds to transect 1 in Figure 2.10. Red squares indicate boxes for water mass transport computation (Figure 2.12). 1: B9B polynya, 2: Mertz Glacier Polynya, 3: Mertz Bank Polynya, 4: Ninnis Bank Polynya, 5: Ninnis Glacier Polynya. 44
2.2 Amplitude of the semi-major axis of the tidal current ellipse for constituents O1 (panels a and b) and M2 (panels c and d) as simulated in BARO experiment (a and c) and in FES2012 solution (b and d). Note the different color scale for O1 and M2. The thick black line represents coastline or ice shelf grounding line/edge. The thin black lines corresponds to the bathymetric contours plotted every 200 m between 0 and 1200 m. DB: Dibble Bank, AB: Adélie Bank, AD: Adélie Depression, MB: Mertz Bank, ND: Ninnis Depression, NB: Ninnis Bank. 47
2.3 a-d: maps of sea ice concentration averaged on the 2010-2015 period. A and B: summer months (JFM) for REF and ASI-SSMI, respectively. (c) and (d): same as (a) and (b), but for winter months (JJASO). Sea ice concentrations below 15% have been removed in both the simulation and observational dataset. E: time series of total sea ice area (where sea ice concentration >15%) as simulated by REF and observed in OSI 450 (continuous line) and ASI-SSMI (dashed line). 49

2.4 Distributions of the normalized sea ice concentration simulated in REF and observed in OSI-450 and ASI-SSMI for summer (a), fall (b), winter (c), and fall (d). 50
2.5 Polynya (a) and landfast ice probability (b) in REF simulation, averaged between 2010-2015. Polynyas are defined as an enclosed contour of sea ice with a concentration lower than 0.5 or a thickness lower than 0.2 m. Names of the polynyas: DBP: Dibble bank, B9BP: B9B iceberg, MGP: Mertz glacier, MBP: Mertz bank, NGP: Ninnis glacier, NBP: Ninnis bank. Landfast ice is defined as the sea ice with a two week-averaged velocity lower than 1 mm/s. Cumulated sea ice production (c) as simulated in REF and (d) estimated in Tamura et al. (2008) and Tamura et al. (2016) (using ERA-interim). Averaged between 2011 and 2013. Sea ice production rates lower than 3 m/yr have been masked. The simulated sea ice production rate is the sum of the freezing of open water and the growth of sea ice thinner than 0.2 m, as in Tamura et al. (2016). 51
2.6 Vertical profiles of a) temperature and b) salinity on the continental shelves of Adélie Land. Black: CTD from the WOD18 database. Blue: as simulated in REF. Pale colors: individual profiles. Bright colors: basin average. Simulated profiles are taken at the same location and time as the CTD measurements. c) Temperature / salinity diagram on the continental shelf off Adélie Land as simulated in REF. Sampled between years 2010-2015. Dashed black contours: neutral density γ_n. Dashed blue line: surface freezing temperature. Dashed red line: temperature of -1.75°C. AASW: Antarctic Surface Water, WW: Winter Water, CDW: Circumpolar Deep Water, mCDW: modified CDW, DSW: Dense Shelf Water, MSW: Modified Shelf Water. d) locations of CTDs used in panels a) and b). 52
2.7 Monthly basal melt rate of the three largest ice shelves of Adélie Land and iceberg B9B. a: Dibble, b: B9B, c: Mertz and d: Ninnis. Dark red curve: without tides (noT), blue curve: with tides (REF). 54
2.8 a and c: relative changes in thermal forcing at the ice shelf base between REF and noT $R_{th} = \frac{(T-T_0)_{REF}-(T-T_0)_{noT}}{(T-T_0)_{noT}}$. b and d: relative difference in ocean–ice shelf heat transfer velocity between REF and noT $R_{dyn} = \frac{(\gamma_{T_{REF}}-\gamma_{T_{noT}})}{\gamma_{T_{noT}}}$. Dibble: a and b: B9B, Mertz and Ninnis: c and d. Averaged between 2013 and 2015. 56

2.9 Mean state (2010-2015 averaged) of the ocean temperature (a), salinity (b) and ocean velocity (d) at 300 m depth simulated in REF. Average sea ice production during March-October simulated in REF (c). Bathymetry is indicated as black contours every 200 m in (a),(b),(c) and as color shading in (d). 57
2.10 Averaged ocean temperature along section 1 of Figure 3.1 (from west to east). a) REF simulation, b) noT - noA, c) noI - noA, d) REF - noA, e) effect of tide–ice shelf interactions $REF - noA - (noI - noA + noT - noA))$ f) - j): same as a) - e) but for ocean salinity. Note the change in the color axis for panels e) and f). Black lines indicate the locations of ice shelves or the Mertz Sill. 58
2.11 (a) Normalized total sea ice production in the polynyas off Adélie Land (refer to Figure 2.5 for polynya locations). Temporal evolution of the water column salinity simulated in REF for the B9BP (b), MBP (c), NBP (d), MGP (e) and NGP (f). Dashed black line represents $\gamma_n = 28.27$ kg/m^3 (used to define MSW and DSW). 60
2.12 Mean yearly water mass transport budget in the B9BP (a), MGP (b), NGP (c), MBP (d) and NBP (e) simulated in REF and in the sensitivity experiments. Positive transport budget rates indicates net export. Black dashed lines indicate interannual standard deviation. Refer to Figure 2.5a for polynya locations and Figure 2.6c for water mass definitions. . . 62
2.13 Transport budget (difference between inflow and outflow) under the ice shelves calculated for REF simulation using bin widths of 0.08°C and 0.05 g/kg for temperature and salinity, respectively. B9B iceberg (a), Mertz ice shelf (b) and Ninnis ice shelf (c) as simulated in REF. Positive transport budget indicates net export. Black numbers represent the overturning rate in REF and noT computed as the volume of water being imported in the cavity. Black contours indicate neutral density 28.0 kg/m^3 (left) and 28.27 kg/m^3 (right). Bottom black lines indicate freezing point of surface temperature and T=-1.75°C. 63
2.14 Yearly transport budget of dense water (DSW and MSW) in the B9BP (a), MGP (b) and NGP (c) adapted to exclude the under ice shelf cavities. Positive transport budget indicates net export. Black lines indicate the interannual standard deviation. 64

3.1 Bathymetry (in the NEMO-LIM model) and topography (in the AM5 simulation) of Adélie Land and the D'Urville Sea. Dark red dots indicate the locations of small grounded icebergs in the model. Red boxes represent the polynyas of the Dibble Bank (DBP), B9B iceberg (B9BP), Mertz Glacier (MGP), Mertz Bank (MBP), Ninnis Glacier (NGP), and Ninnis Bank (NBP). The black box indicates the area for water mass transformation computation. Pink stars indicate Automatic Weather Stations, 1: D85 (out of the map) 2: E-66, 3: D47, 4: D17, 5: D10, 6: DDU, 7: Port Martin, 9: Cape Denison, 9: Penguin Point. DIT: Dibble iceberg tongue, D: Dibble ice shelf, DDU: Dumont D'Urville base, B9B: tabular iceberg, AB: Adélie Bank, BB: Buchanan Bay, M: Mertz ice shelf, MB: Mertz Bank, N: Ninnis ice shelf, NB: Ninnis Bank. 75
3.2 Time needed to compute one model year for the three MAR simulations at 20, 10 and 5 km resolutions (using 8 AMD EPYC 2.9 GHz CPUs). AM5 is 6 times slower than AM10, itself being 4 times slower than AM20. 78
3.3 Mean bias (a) and root mean-square error (RMSE; c) of surface air temperatures simulated in AM20, AM10, AM5, and ERA5 with the measurements performed by the Automatic Weather Station (AWS) network (see Figure 3.1 for station locations). (e) Correlations between the surface air temperatures simulated in AM20, AM10, AM5, and ERA5 and the ones measured by the AWS network. (b), (d), (f): same as (a), (c), (e) but for wind speed. DDU: Dumont D'Urville, Mtn: Port Martin, Dsn: Cape Denison, Pgn: Penguin Point. Note that no wind data were available for Port Martin. 80
3.4 Mean wind speed during easterlies (left column) events and southerlies (right column) events in winter (May to September), averaged over 2010-2015. (a) and (b): ERA5, (c) and (d): AM20, (e) and (f): AM10, (g) and (h): AM5. Easterlies and southerlies events are defined using the distribution of the area-averaged wind direction over the pink box. Easterlies (southerlies) are defined as events when the area-averaged wind direction is lower (higher) than the median wind direction. 81
3.5 Topography (left) and terrain slope (right) in ERA5 (a and b), AM20 (c and d), AM10 (e and f), and AM5 (g and h). The terrain slope is counted positive when the surface elevation increases eastward / northward. . . 83
3.6 Zonal (a) and meridional (b) wind speeds at the coast (defined as the first ocean point after the continent) averaged between 2010-2015 (all seasons). Note that the location of the first ocean points varies with the representation of the coastline in the different models. C. Bay: Commonwealth Bay. 84

3.7 Seasonal cycle (averaged between 2007 and 2015) of (a) 2 m air temperature, (b) total precipitation, (c) 2 m air specific humidity, and (d) downward longwave radiation simulated in ERA5 global reanalysis and in AM5, AM10, and AM20, averaged over the ocean between 131 to 149°E and 64.5 to 68.5°S. 85
3.8 Sea ice concentrations simulated in OM5 and observed in ASI AMSR-E during summer (a and b) and winter (c and d) of 2011. Sea ice thickness averaged during winters of 2011-2015 as simulated in OM5 (e) and observed in the LEGOS/CTOH Cryosat-2 AMSR2 dataset (Guerreiro et al., 2017) (f). Year 2010 is discarded as we use the post-calving (after 2010) ice scape in our model. DIT: Dibble iceberg tongue, D: Dibble ice shelf, DDU: Dumont D'Urville base, AB: Adélie Bank, B9B: tabular iceberg, M: Mertz ice shelf, MB: Mertz Bank, N: Ninnis ice shelf, NB: Ninnis Bank. 87
3.9 Probability of lanfast ice (a) and polynya (b) occurrence in OM5 averaged between years 2010 to 2015. Difference of landfast ice (c) and polynya (d) probability between OM5 and OM10. Difference of landfast ice (e) and polynya (f) probability between OM5 and OM20. Landfast ice is defined as sea ice with a 15 day averaged velocity lower than 0.1 cm/s. Polynyas are defined as closed contours within the ice pack with a daily sea ice concentration lower than 15% or a daily thickness lower than 0.2 m. Bathymetry is represented as black contours every 400 m. Legends for the panel (a) DIT: Dibble iceberg tongue, D: Dibble ice shelf, AB: Adélie Bank, B9B: tabular iceberg, BB: Buchanan Bay, M: Mertz ice shelf, MB: Mertz Bank, N: Ninnis Glacier, NB: Ninnis bank. Legends for panel b): DBP: Dibble Bank polynya, B9BP: B9B iceberg polynya, MGP: Mertz glacier polynya, MBP: Mertz Bank polynya, NGP: Ninnis glacier polynya, NBP: Ninnis Bank polynya. 88
3.10 Mean daily total sea ice production in OM5 (a), difference with OM10 (b), and with OM20 (c). d), e) and f): same as a), b) c) but for open water sea ice production; g), h) and i): bottom sea ice growth; j), k), l): snow-ice formation. m), n), o): dynamical (ridging and rafting) growth. Note the changes in the color axis range as sea ice growth mechanisms have distinct magnitudes. The maps were produced by averaging the sea ice production terms over fall and winter (April-September) 2010-2015. Black crosses indicate statistical significance (2σ). Thin black contours indicate bathymetry (every 200 m). 90

3.11 Yearly mean sea ice production and melting terms simulated in OM20, OM10, and OM5 for three types of sea ice cover. Landfast ice and polynyas are defined in the same way as in Figure 3.9. "Pack ice" consists of ice-covered regions that are neither polynyas nor landfast ice. The period is 2010-2015. The interannual standard deviation of the yearly sea ice growth and melt rates are indicated on the top and bottom of each bar. 91
3.12 Sea ice production summed over (a) the MBP (see Figure 3.1) and (b) the MGP as simulated in OM20, OM10, and OM5, and as estimated by Tamura et al. (2016) (computed using ERA-interim). Simulated sea ice production is the sum of open-water freezing and bottom growth of sea ice thinner than 0.2 m to approach the methodology of Tamura et al. (2016). 93
3.13 Averages of the 3-hourly 10 m wind speeds as a function of wind direction simulated in AM20, AM10, and AM5 during winters of 2010-2015, (a) and (b). Normalized probability density function of the 3-hourly 10 m wind direction θ over the MBP (c) and NBP (d). A direction of 0°N denotes a southerly wind. Sea ice production averaged in the MBP (e) and MGP (f) as a function of wind direction. The distribution are computed using a bin width of 5°. Bins representing less than 0.5% of the events were removed from the panels a, b, e and f for clarity. 94
3.14 10 m daily wind vectors and sea ice growth rates averaged over each quartile of the wind direction distribution of the MGP in AM5/OM5. The maps and quartiles are built using fall-winter (May to September) data from years 2010 to 2015. (a) 1st quartile ($\theta < -24.56$°N), (b) 2nd quartile (-24.56° N $< \theta < -3.89$° N), (c) 3rd quartile (-3.89° N $< \theta <$ 14.76° N) and (d) 4th quartile ($\theta >$ 14.76° N). Pink boxes indicate the MBP (north) and MGP (south). 95
3.15 Distribution of (a) daily 10 m wind speed, (b) polynya area and (c) sea ice growth rate averaged over polynyas off Adélie Land (see Figure 3.9b for polynya definition), as simulated by OM20, OM10, and OM5 (respectively AM20, AM10 and AM5 for atmospheric fields) during winters of 2010-2015. Horizontal black lines indicate the median values; the top and bottom of the bars corresponds to the 75th and 25th percentiles, respectively. The maximum to minimum range is depicted by the dashed whiskers. The averages of the relative difference between coarse-resolution experiments and OM5 (resp. AM5 for winds) are listed as percentages above the boxes. 96

3.16 Same as Figures 3.15 b and 3.15c for years 2009-2010, including sensitivity experiments OM20w5 and OM5x20. 97
3.17 Same as Figures 3.15 b and 3.15c for years 2010-2011, including sensitivity experiment OM20Cd1.3 99
3.18 (a) Meridional section of the yearly salt fluxes due to brine rejection or sea ice melting, averaged between 2010-2015. The vertical dashed line indicates the transition between positive (left) and negative (right) salt fluxes used to compute the total salt fluxes (numbers on top, in kg/month). (b) Mean water mass transformation rates by surface buoyancy fluxes per potential density class (referenced to the surface). The dashed line indicates potential density anomaly $\sigma_0 = 27.80$ kg/m^3, i.e. the lowest density for Shelf Waters (which includes Dense Shelf Water) set following Kusahara et al. (2011b) . Total shelf water transformation rates are listed on top of the diagram (in Sv). The diagnostics are computed from OM20, OM10, and OM5 outputs on the whole sector for panel (a) and in the box "east" (see Figure 3.1) for panel (b). 100
3.19 Total ice shelf basal melt in the Adélie Land sector simulated in OM20, OM10 and OM5. 101

4.1 Time series of sea ice area integrated over the Adélie Land sector simulated in REF and derived from the observations OSI-450 (OSI SAF Global Sea Ice Concentration Climate Data Record). 114
4.2 Eddy kinetic energy obtained from geostrophic currents simulated in REF (a) and estimated from AVISO (b), averaged over 2011 and 2012. . . 114
4.3 Snapshots of sea ice concentration (black and white shading) and SST (red-green-blue shading) seen by MAR in REF (left) and SMOOTH (right) on 27th Aug. 2013. 115
4.4 Radially averaged power spectrums of the ocean kinetic energy (left) and SST simulated in REF and SMOOTH over the period 2012-2013. The SST is the one seen by MAR and has a resolution of 5 km, while the ocean kinetic energy was recomputed offline and has a resolution of 2 km. The dashed black line indicates the k^{-2} slope, and the vertical black line a wavelength of 150 km. 116

4.5 Schematic view of the response of a surface wind field (black arrows) to a surface temperature front (thick black line), adapted from Chelton and Xie (2010a). Surface winds are weaker over the cool side of the SST front and stronger over its warm side. Winds blowing along the surface temperature front start to curl (orange shaded area) while winds blowing across the surface temperature front diverges (green shaded area). 118

4.6 Binned scatterplots of the small-scale anomalies of: a) the crosswind surface temperature (ST) gradient and the wind curl, b) the downwind ST gradient and the wind divergence, c) the geostrophic current vorticity and the wind curl, d) the geostrophic currents vorticity and the ocean stress curl. Bin widths are 1×10^{-6} °C/m for temperature gradients and 1×10^{-6} s^{-1} for the geostrophic vorticity. Each marker corresponds to the average of all simulated points within the bin range. The binned scatter plots are built from daily outputs over the period 2012-2013. For the "ice free" relationships, only the pixels with a sea ice concentration (SIC) equal to zero are considered. Linear regressions on the bin averages are indicated when such a relationship exists. The slopes (S) and regression coefficients (R) are indicated on each panel. . . 119

4.7 Location of eddies detected in REF between 1st of January 2012 and 31st of December 2013. The green lines indicate the maximum sea ice extent for years 2012 and 2013. The coastline is indicated as a thick black line and the 1200 m isobath as a dashed black line. The insert represent the meridional distribution of eddies. 121

4.8 Composites of the eddies imprint on the sea ice concentration (a-b), sea ice growth rate (c-d), sea ice concentration thermodynamical (e-f), and dynamical (g-h) tendencies simulated in REF. Only the eddies with a sea ice concentration averaged within 3 eddy radius larger than 0.4 are accounted for. Anticyclonic eddy (warm core) and cyclonic eddy (cold core) are shown on the left and right columns of each sub-figure, respectively. Each eddy has been scaled with respect to its radius but the orientation of eddies is not modified. Composites are built from 01/01/12 to 31/12/13. A circle of one eddy radius is drawn on each panel. 122

4.9 Downwind transects of the imprint of eddies on the surface conditions, heat fluxes and atmosphere. a) Surface temperature (weighted average of ocean and sea ice temperatures, light blue and pink) and 2 m air temperature (red and blue), b) 2 m air specific humidity, c) 10 m wind speed, d) planetary boundary layer height, e) latent heat flux, and f) sensible heat flux. A positive heat flux means an energy loss by the surface. The mesoscale part of each field was first extracted following the method described in Section 4.4.4. Eddies were resized with respect to their radius and rotated to be aligned with the local wind. Separated downwind transects are computed for anticyclonic eddies (red or pink) and cyclonic eddies (blue or light blue). The distinction is also done between ice-free (dashed line) and ice-covered ($SIC > 0.4$, solid line) eddies. The composite are computed using daily outputs from REF between 2012 and 2013. 123
4.10 Mean zonal sections of the mesoscale anomalies of the sea surface temperature (top row), sea surface salinity (middle row), and Ekman pumping (bottom row) simulated in REF and SMOOTH. The sections are computed for ice-free (left) and ice-covered (SIC > 0.4, right) eddies. 126
4.11 Mean zonal section of ocean temperature across mesoscale eddies. a) Ocean temperature across ice-free anticyclonic eddies in REF, b) difference of ocean temperature between REF and SMOOTH, e) ocean temperature across ice-covered anticyclonic eddies in REF, and f) difference in ocean temperature between REF and SMOOTH. c), d), g), h): same as a), b), e), f) but for cyclonic eddies. For panels b), d), f) and h), the difference between REF and SMOOTH is statistically significant (2σ) in the undotted areas. To remove the difference in the mean state between REF and SMOOTH, the mean temperature was subtracted at each level for the computation of the differences between REF and SMOOTH. 127
4.12 Same as Figure 4.11 but for ocean salinity. 128
4.13 a) Upper 200 m ocean kinetic energy north of 65°S in REF and SMOOTH. b) Eddy stress work north of 65°S for the whole area (black), the ice-free (SIC=0) area (red), and the ice-covered ($SIC > 0.05$) area (blue). REF and SMOOTH are denoted with solid and dashed lines, respectively. A common sea ice mask is used for the computation of the eddy stress work for ice-free and ice-covered oceans in REF and SMOOTH. A 60 days moving average was applied to the time series. . . 129

4.14 Time series of the total thermodynamical sea ice volume trend (black), sea ice freezing (teal) and melting (orange) simulated in REF and SMOOTH. 130
4.15 Meridional profiles of: a) mean sea ice growth rate, b) total meridional sea ice advection (positive northward), and c), ocean potential density (referenced to the surface) contoured every 0.05 kg/m^3 as simulated in REF and SMOOTH over the year 2013. 131
4.16 Mean sea ice velocities (black arrows) overlayed over the mean sea ice concentration (color shading) averaged over 2013 in REF (left) and SMOOTH (middle). Zonal average of the mean sea ice velocity in REF and SMOOTH (right). 132
4.17 Water mass transformation rate per density class in REF (solid lines) and SMOOTH (dashed lines). The total contribution (black line) is the sum of: the buoyancy flux due to sea ice freezing or melting (blue), the buoyancy flux associated with heat fluxes (latent, sensible, longwave and shortwave) for the ice-free (red) and ice-covered (orange) cases, and the precipitation over the ocean (teal). 133

6.1 LANDSAT natural color images (USGS/NASA Landsat Program) of A) Dibble Ice Shelf region taken on 23 March 2015 and B) Mertz Ice Shelf region taken on 23 November 2014. The black dashed line illustrates the coastline and the red dashed line illustrate the ice shelves front or grounding line. Green dots indicate the location of potentially grounded icebergs. WB: Watt Bay and Ice Shelf, BB: Buchanan Bay, F: Fisher Ice Shelf. 147
6.2 Tidal ellipses for constituents O1 and M2 in simulation BARO overlaying bathymetric contours. Red lines indicates the ice shelf or iceberg edges. Zoom over Dibble Ice Shelf (left), Adélie Depression (middle), Mertz and Ninnis Ice Shelves (right). Note the scale difference between O1 and M2. 148
6.3 Ocean temperatures in the Adélie Depression from the CTD casts performed after 2010 used in the WOA18 climatology. 148
6.4 Ocean transport (counted positive eastward) across the Mertz Trough (Figure 3.1) simulated in REF for: surface waters ($\gamma_n < 28.0$ kg/m^3), mCDW/CDW ($28.0 < \gamma_n < 28.27$ kg/m^3 , T > -1.75°C), and MSW ($\gamma_n > 28.27$ kg/m^3, T >-1.75°C). 149
6.5 2010-2015 averaged basal melt of ice shelves in Adélie Land. a) Dibble ice shelf; b) Mertz and Ninnis ice shelves. Black contours: bathymetry (every 100 m for thin lines, 500 m for thick lines). 149

6.6 Average ocean temperature and velocity in the boundary layer at the ice-ocean interface beneath B9B (left), Mertz (middle) and Ninnis (right) Ice Shelves, simulated in REF (top). Difference between REF and noT (bottom row). 150
6.7 Differences in sea ice production (cumulated during freezing period: April to October), between noI and noA (a) and noT and noA (b). Effect of the interactions between tides and ice shelf (c). 2010-2015 averaged. Black crosses on color shading indicate statistical significance (2σ) 150
6.8 Temperature difference averaged between 200 m and 400 m (2010-2015 average) between noT and noA (a) and noI and noA (b). Temperature changes due to tide–ice shelf interactions (c). (d), (e) ,(f): as for (a), (b), (c) but for ocean salinity. Black crosses on color shading indicate statistical significance (2σ). Bathymetry is indicated as black contours every 200 m. 151
6.9 Same as figure 6.8 but for ocean velocities. 151
6.10 a) Ocean temperature averaged inside the Mertz, Ninnis and B9B cavities in the REF experiment. b) Water mass transformations from ocean–ice shelf interactions (computed following Jeong et al. (2020)) simulated in REF and noT for the years with low basal melt (2008, 2009 and 2012, dashed line) and for the years with high basal melt (2010, 2014 and 2015, solid line). Vertical dashed line indicates the 28.27 neutral density threshold. c) Water mass transformations from ocean–ice shelf interactions simulated in REF and estimated if the ocean temperature was -1.8°C: using the density of REF (FRZ R, solid line), or using the salinity of REF (FRZ S, dashed line). 152
6.11 Mean sea ice concentration simulated in OM5 and observed in the ASI-AMSR 2 dataset in summer (a and b) and winter (c and d) of years 2011 to 2015. 153
6.12 Mean sea ice production averaged over winters of 2010-2015 simulated in OERA5 (a). Differences of the mean sea ice production between OERA5 and OM20 (b) or OERA5 and OM5 (c). Dotted regions indicate statistical significance. Black contours represent the model bathymetry (every 200 m). 154
6.13 Same as Figure 3.18 but for simulations OERA5, OM20, and OM5. 155
6.14 Same as Figure 3.9, but for OERA5 (a and b), OERA5 - OM20 (c and d), and OERA5 - OM5 (e and f). 156

6.15 Average 2 m air temperature (1st column), 10 m zonal wind speed (2nd column), 10 m meridional wind speed (3rd column) and downward longwave radiation (4th column) simulated by MAR in REF, for summer (January to March, 1st row) and winter (May to October, 2nd row). The differences between REF and ERA5 are presented in the two bottom rows, for summer and winter. Black crosses indicate significant differences (2σ). ERA5 data were formerly interpolated on the MAR grid. Average over the 2011-2013 period. 158

6.16 Ocean conservative temperature and absolute salinity simulated by REF (2012-2013) and from the WOA18 climatology (2010-2020). Top: vertical profiles of temperature (left) and salinity (right) averaged between 65°S and 60°S for summer (January-April) and winter (May-October). Bottom: meridional section (averaged over the whole sector) of the mean temperature (left) and salinity (right) as simulated in REF (middle row) and difference with WOA18 (REF-WOA18, bottom row). 159

List of Tables

2.1 Names and descriptions of the simulations performed in the present study. 46
2.2 Yearly sea ice production (km^3) in the polynyas off Adélie Land (see Figure 2.5 for polynya locations) and over the entire continental shelf, as simulated in REF and as estimated by Tamura et al. (2016). Averaged between 2011 and 2013. 51
2.3 Basal melt rate (in m/yr) and its interannual standard deviation for major ice shelves as simulated in REF and as estimated from observations by Rignot et al. (2013), Depoorter et al. (2013) and Adusumilli et al. (2020) (R13, D13 and A20, respectively). 54

Bibliography

Abernathey, R.P., Cerovecki, I., Holland, P.R., Newsom, E., Mazloff, M., Talley, L.D., 2016. Water-mass transformation by sea ice in the upper branch of the Southern Ocean overturning. Nature Geoscience 9, 596–601.

Adkins, J.F., McIntyre, K., Schrag, D.P., 2002. The Salinity, Temperature, and 18O of the Glacial Deep Ocean. Science 298, 1769–1773. URL: https://science.sciencemag.org/content/298/5599/1769, doi:10.1126/science.1076252. publisher: American Association for the Advancement of Science Section: Report.

Adolphs, U., Wendler, G., 1995. A pilot study on the interactions between katabatic winds and polynyas at the Adélie Coast, eastern Antarctica. Antarctic Science 7, 307–314.

Adusumilli, S., Fricker, H.A., Medley, B., Padman, L., Siegfried, M.R., 2020. Interannual variations in meltwater input to the Southern Ocean from Antarctic ice shelves. Nature Geoscience 13, 616–620.

Agosta, C., Amory, C., Kittel, C., Orsi, A., Favier, V., Gallée, H., van den Broeke, M.R., Lenaerts, J.T.M., van Wessem, J.M., van de Berg, W.J., Fettweis, X., 2019. Estimation of the Antarctic surface mass balance using the regional climate model MAR (1979–2015) and identification of dominant processes. The Cryosphere 13, 281–296. URL: https://tc.copernicus.org/articles/13/281/2019/, doi:10.5194/tc-13-281-2019. publisher: Copernicus GmbH.

Alley, R.B., Clark, P.U., Huybrechts, P., Joughin, I., 2005. Ice-sheet and sea-level changes. science 310, 456–460.

Allison, L.C., Johnson, H.L., Marshall, D.P., Munday, D.R., 2010. Where do winds drive the Antarctic Circumpolar Current? Geophysical Research Letters 37. URL: https://agupubs.onlinelibrary.wiley.com/doi/abs/10.1029/2010GL043355, doi:https://doi.org/10.1029/2010GL043355. _eprint: https://agupubs.onlinelibrary.wiley.com/doi/pdf/10.1029/2010GL043355.

Amante, C., Eakins, B.W., 2009. ETOPO1 arc-minute global relief model: procedures, data sources and analysis .

Amores, A., Jordà, G., Arsouze, T., Sommer, J.L., 2018. Up to What Extent Can We Characterize Ocean Eddies Using Present-Day Gridded Altimetric Products? Journal of Geophysical Research: Oceans 123, 7220–7236. URL: https://agupubs.onlinelibrary.wiley.com/doi/abs/10.1029/2018JC014140, doi:10.1029/2018JC014140. _eprint: https://agupubs.onlinelibrary.wiley.com/doi/pdf/10.1029/2018JC014140.

Amory, C., Trouvilliez, A., Gallée, H., Favier, V., Naaim-Bouvet, F., Genthon, C., Agosta, C., Piard, L., Bellot, H., 2015. Comparison between observed and simulated aeolian snow mass fluxes in Adélie Land, East Antarctica .

Andreas, E.L., Decosmo, J., 2002. The Signature of Sea Spray in the Hexos Turbulent Heat Flux Data. Boundary-Layer Meteorology 103, 303–333. URL: http://link.springer.com/10.1023/A:1014564513650, doi:10.1023/A:1014564513650.

Aoki, S., Kobayashi, R., Rintoul, S., Tamura, T., Kusahara, K., 2017. Changes in water properties and flow regime on the continental shelf off the A délie/G eorge VL and coast, E ast A ntarctica, after glacier tongue calving. Journal of Geophysical Research: Oceans 122, 6277–6294.

Aoki, S., Rintoul, S.R., Ushio, S., Watanabe, S., Bindoff, N.L., 2005. Freshening of the Adélie Land Bottom water near 140 E. Geophysical Research Letters 32.

Aoki, S., Yamazaki, K., Hirano, D., Katsumata, K., Shimada, K., Kitade, Y., Sasaki, H., Murase, H., 2020. Reversal of freshening trend of Antarctic Bottom Water in the Australian-Antarctic Basin during 2010s. Scientific reports 10, 1–7.

Armour, K.C., Marshall, J., Scott, J.R., Donohoe, A., Newsom, E.R., 2016. Southern Ocean warming delayed by circumpolar upwelling and equatorward transport. Nature Geoscience 9, 549–554. URL: https://www.nature.com/articles/ngeo2731, doi:10.1038/ngeo2731. number: 7 Publisher: Nature Publishing Group.

Arndt, J.E., Schenke, H.W., Jakobsson, M., Nitsche, F.O., Buys, G., Goleby, B., Rebesco, M., Bohoyo, F., Hong, J., Black, J., others, 2013. The International Bathymetric Chart of the Southern Ocean (IBCSO) Version 1.0—A new bathymetric compilation covering circum-Antarctic waters. Geophysical Research Letters 40, 3111–3117.

Arndt, S., Hoppmann, M., Schmithüsen, H., Fraser, A.D., Nicolaus, M., 2020. Seasonal and interannual variability of landfast sea ice in Atka Bay, Weddell Sea, Antarctica. The Cryosphere 14, 2775–2793. URL: https://tc.copernicus.org/articles/14/2775/2020/, doi:10.5194/tc-14-2775-2020. publisher: Copernicus GmbH.

Arrigo, K.R., Dijken, G.v., Long, M., 2008. Coastal Southern Ocean: A strong anthropogenic CO2 sink. Geophysical Research Letters 35. URL: https://agupubs.onlinelibrary.wiley.com/doi/abs/10.1029/2008GL035624, doi:10.1029/2008GL035624.

Arrigo, K.R., Worthen, D., Schnell, A., Lizotte, M.P., 1998. Primary production in Southern Ocean waters. Journal of Geophysical Research: Oceans 103, 15587–15600. URL: https://agupubs.onlinelibrary.wiley.com/doi/abs/10.1029/98JC00930, doi:10.1029/98JC00930. _eprint: https://agupubs.onlinelibrary.wiley.com/doi/pdf/10.1029/98JC00930.

Arzeno, I.B., Beardsley, R.C., Limeburner, R., Owens, B., Padman, L., Springer, S.R., Stewart, C.L., Williams, M.J., 2014. Ocean variability contributing to basal melt rate near the ice front of Ross Ice Shelf, Antarctica. Journal of Geophysical Research: Oceans 119, 4214–4233.

Bailey, D.A., Lynch, A.H., 2000. Development of an Antarctic Regional Climate System Model. Part I: Sea Ice and Large-Scale Circulation. Journal of Climate 13, 1337–1350. doi:10.1175/1520-0442(2000)013<1337:DOAARC>2.0.CO;2. publisher: American Meteorological Society Section: Journal of Climate.

Ballarotta, M., Ubelmann, C., Pujol, M.I., Taburet, G., Fournier, F., Legeais, J.F., Faugere, Y., Delepoulle, A., Chelton, D., Dibarboure, G., Picot, N., 2019. On the resolutions of ocean altimetry maps. preprint. Operational Oceanography/Sea Level/Surface/All Geographic Regions. URL: https://os.copernicus.org/preprints/os-2018-156/os-2018-156.pdf, doi:10.5194/os-2018-156.

Ballinger, T.J., Overland, J.E., Wang, M., Bhatt, U.S., Hanna, E., Hanssen-Bauer, I., Kim, S.J., Thoman, R.L., Walsh, J.E., 2020. Arctic Report Card 2020: Surface Air Temperature .

Barthélemy, A., Goosse, H., Fichefet, T., Lecomte, O., 2017. On the sensitivity of Antarctic sea ice model biases to atmospheric forcing uncertainties. Climate Dynamics , 1–19.

Barthélemy, A., Goosse, H., Mathiot, P., Fichefet, T., 2012. Inclusion of a katabatic wind correction in a coarse-resolution global coupled climate model. Ocean Modelling 48, 45–54.

Batrak, Y., Müller, M., 2018. Atmospheric Response to Kilometer-Scale Changes in Sea Ice Concentration Within the Marginal Ice Zone. Geophysical Research Letters 45, 6702–6709. URL: https://agupubs.onlinelibrary.wiley.com/doi/abs/10.1029/2018GL078295, doi:https://doi.org/10.1029/2018GL078295. _eprint: https://agupubs.onlinelibrary.wiley.com/doi/pdf/10.1029/2018GL078295.

Beadling, R.L., Russell, J.L., Stouffer, R.J., Mazloff, M., Talley, L.D., Goodman, P.J., Sallée, J.B., Hewitt, H.T., Hyder, P., Pandde, A., 2020. Representation of Southern Ocean Properties across Coupled Model Intercomparison Project Generations: CMIP3 to CMIP6. Journal of Climate 33, 6555–6581. doi:10.1175/JCLI-D-19-0970.1. publisher: American Meteorological Society Section: Journal of Climate.

Beaman, R.J., O'Brien, P.E., Post, A.L., De Santis, L., 2011. A new high-resolution bathymetry model for the Terre Adélie and George V continental margin, East Antarctica. Antarctic Science 23, 95–103.

Beckmann, A., Pereira, A.F., 2003. Lateral tidal mixing in the Antarctic marginal seas. Ocean Dynamics 53, 21–26. URL: http://link.springer.com/10.1007/s10236-002-0020-9, doi:10.1007/s10236-002-0020-9.

van de Berg, W.J., Medley, B., 2016. Brief Communication: Upper-air relaxation in RACMO2 significantly improves modelled interannual surface mass balance variability in Antarctica. The Cryosphere 10, 459–463. Publisher: Copernicus GmbH.

Berthier, E., Raup, B., Scambos, T., 2003. New velocity map and mass-balance estimate of Mertz Glacier, East Antarctica, derived from Landsat sequential imagery. Journal of Glaciology 49, 503–511.

Bintanja, R., Van Oldenborgh, G., Katsman, C., 2015. The effect of increased fresh water from Antarctic ice shelves on future trends in Antarctic sea ice. Annals of Glaciology 56, 120–126.

Boucher, O., Servonnat, J., Albright, A.L., Aumont, O., Balkanski, Y., Bastrikov, V., Bekki, S., Bonnet, R., Bony, S., Bopp, L., others, 2020. Presentation and evaluation of the IPSL-CM6A-LR climate model. Journal of Advances in Modeling Earth Systems 12, 1–52.

Bougeault, P., Lacarrere, P., 1989. Parameterization of orography-induced turbulence in a mesobeta–scale model. Monthly Weather Review 117, 1872–1890.

Boutin, G., Ardhuin, F., Dumont, D., Sévigny, C., Girard-Ardhuin, F., Accensi, M., 2018. Floe size effect on wave-ice interactions: Possible effects, implementation in wave model, and evaluation. Journal of Geophysical Research: Oceans 123, 4779–4805. Publisher: Wiley Online Library.

Bracegirdle, T.J., Holmes, C.R., Hosking, J.S., Marshall, G.J., Osman, M., Patterson, M., Rackow, T., 2020. Improvements in Circumpolar Southern Hemisphere Extratropical Atmospheric Circulation in CMIP6 Compared to CMIP5. Earth and Space Science 7, e2019EA001065. URL: https://agupubs.onlinelibrary.wiley.com/doi/abs/10.1029/2019EA001065, doi:10.1029/2019EA001065. _eprint: https://agupubs.onlinelibrary.wiley.com/doi/pdf/10.1029/2019EA001065.

Brekhovskikh, A.L.M., Fedorov, K.N., Fomin, L.M., Koshlyakov, M.N., Yampolsky, A.D., 1971. Large-scale multi-buoy experiment in the Tropical Atlantic. Deep Sea Research and Oceanographic Abstracts 18, 1189–1206. URL: https://www.sciencedirect.com/science/article/pii/001174717190026X, doi:10.1016/0011-7471(71)90026-X.

Van den Broeke, M.R., Wal, R.S.W.v.d., Wild, M., 1997. Representation of Antarctic Katabatic Winds in a High-Resolution GCM and a Note on Their Climate Sensitivity. Journal of Climate 10, 3111–3130. URL: https://journals.ametsoc.org/view/journals/clim/10/12/1520-0442_1997_010_3111_roakwi_2.0.co_2.xml, doi:10.1175/1520-0442(1997)010<3111:ROAKWI>2.0.CO;2. publisher: American Meteorological Society Section: Journal of Climate.

Bromwich, D.H., Cassano, J.J., Klein, T., Heinemann, G., Hines, K.M., Steffen, K., Box, J.E., 2001. Mesoscale modeling of katabatic winds over Greenland with the Polar MM5. Monthly Weather Review 129, 2290–2309.

Bromwich, D.H., Otieno, F.O., Hines, K.M., Manning, K.W., Shilo, E., 2013. Comprehensive evaluation of polar weather research and forecasting model performance in the Antarctic. Journal of Geophysical Research: Atmospheres 118, 274–292.

Bronselaer, B., Winton, M., Griffies, S.M., Hurlin, W.J., Rodgers, K.B., Sergienko, O.V., Stouffer, R.J., Russell, J.L., 2018. Change in future climate due to Antarctic meltwater. Nature 564, 53–58.

Brun, E., David, P., Sudul, M., Brunot, G., 1992. A numerical model to simulate snow-cover stratigraphy for operational avalanche forecasting. Journal of Glaciology 38, 13–22. Publisher: Cambridge University Press.

Cabanes, C., Grouazel, A., Schuckmann, K.v., Hamon, M., Turpin, V., Coatanoan, C., Paris, F., Guinehut, S., Boone, C., Ferry, N., others, 2013. The CORA dataset: validation and diagnostics of in-situ ocean temperature and salinity measurements. Ocean Science 9, 1–18.

Callaghan, T.V., Johansson, M., Brown, R.D., Groisman, P.Y., Labba, N., Radionov, V., Barry, R.G., Bulygina, O.N., Essery, R.L.H., Frolov, D.M., Golubev, V.N., Grenfell, T.C., Petrushina, M.N., Razuvaev, V.N., Robinson, D.A., Romanov, P., Shindell, D., Shmakin, A.B., Sokratov, S.A., Warren, S., Yang, D., 2011. The Changing Face of Arctic Snow Cover: A Synthesis of Observed and Projected Changes. AMBIO 40, 17–31. URL: https://doi.org/10.1007/s13280-011-0212-y, doi:10.1007/s13280-011-0212-y.

Campagne, P., Crosta, X., Houssais, M.N., Swingedouw, D., Schmidt, S., Martin, A., Devred, E., Capo, S., Marieu, V., Closset, I., others, 2015. Glacial ice and atmospheric forcing on the Mertz Glacier Polynya over the past 250 years. Nature communications 6, 6642.

Carrère, L., Lyard, F., Cancet, M., Guillot, A., Roblou, L., 2012. A new global tidal model taking taking advantage of nearly 20 years of altimetry, in: Proceedings of meeting" 20 Years of Altimetry.

Cassano, J.J., Box, J.E., Bromwich, D.H., Li, L., Steffen, K., 2001. Evaluation of Polar MM5 simulations of Greenland's atmospheric circulation. Journal of Geophysical Research: Atmospheres 106, 33867–33889. doi:10.1029/2001JD900044.

Cassano, J.J., Seefeldt, M.W., Palo, S., Knuth, S.L., Bradley, A.C., Herrman, P.D., Kernebone, P.A., Logan, N.J., 2016. Observations of the atmosphere and surface state over Terra Nova Bay, Antarctica, using unmanned aerial systems. Earth System Science Data 8, 115–126. URL: https://essd.copernicus.org/articles/8/115/2016/, doi:10.5194/essd-8-115-2016. publisher: Copernicus GmbH.

Cassianides, A., Lique, C., Korosov, A., 2021. Ocean Eddy Signature on SAR-Derived Sea Ice Drift and Vorticity. Geophysical Research Letters 48, e2020GL092066. URL: https://agupubs.onlinelibrary.wiley.com/doi/abs/10.1029/2020GL092066, doi:https://doi.org/10.1029/2020GL092066. _eprint: https://agupubs.onlinelibrary.wiley.com/doi/pdf/10.1029/2020GL092066.

Catto, J.L., Shaffrey, L.C., Hodges, K.I., 2010. Can Climate Models Capture the Structure of Extratropical Cyclones? Journal of Climate 23, 1621–1635. doi:10.1175/2009JCLI3318.1. publisher: American Meteorological Society Section: Journal of Climate.

Chanut, J., Barnier, B., Large, W., Debreu, L., Penduff, T., Molines, J.M., Mathiot, P., 2008. Mesoscale Eddies in the Labrador Sea and Their Contribution to Convection and Restratification. Journal of Physical Oceanography 38, 1617–1643. doi:10.1175/2008JPO3485.1. publisher: American Meteorological Society Section: Journal of Physical Oceanography.

Chelton, D., 2013. Mesoscale eddy effects. Nature Geoscience 6, 594–595. URL: https://www.nature.com/articles/ngeo1906, doi:10.1038/ngeo1906. number: 8 Publisher: Nature Publishing Group.

Chelton, D.B., deSzoeke, R.A., Schlax, M.G., Naggar, K.E., Siwertz, N., 1998. Geographical Variability of the First Baroclinic Rossby Radius of Deformation. Journal of Physical Oceanography 28, 433–460. doi:10.1175/1520-0485(1998)028<0433:GVOTFB>2.0.CO;2. publisher: American Meteorological Society Section: Journal of Physical Oceanography.

Chelton, D.B., Esbensen, S.K., Schlax, M.G., Thum, N., Freilich, M.H., Wentz, F.J., Gentemann, C.L., McPhaden, M.J., Schopf, P.S., 2001. Observations of Coupling between Surface Wind Stress and Sea Surface Temperature in the Eastern Tropical Pacific. Journal of Climate 14, 1479–1498. doi:10.1175/1520-0442(2001)014<1479:OOCBSW>2.0.CO;2. publisher: American Meteorological Society Section: Journal of Climate.

Chelton, D.B., Schlax, M.G., Samelson, R.M., 2007. Summertime coupling between sea surface temperature and wind stress in the California Current System. Journal of Physical Oceanography 37, 495–517.

Chelton, D.B., Xie, S.P., 2010a. Coupled ocean-atmosphere interaction at oceanic mesoscales. Oceanography 23, 52–69. URL: https://www.jstor.org/stable/24860862.

Chelton, D.B., Xie, S.P., 2010b. Coupled ocean-atmosphere interaction at oceanic mesoscales. Oceanography 23, 52–69. URL: https://www.jstor.org/stable/24860862. publisher: Oceanography Society.

Comiso, J.C., 2012. Large Decadal Decline of the Arctic Multiyear Ice Cover. Journal of Climate 25, 1176–1193. doi:10.1175/JCLI-D-11-00113.1. publisher: American Meteorological Society Section: Journal of Climate.

Condie, S., 1998. Observations and modeling of Antarctic downslope flows: A review. Antarctic Research Series 75, 29–49.

Cougnon, E., Galton-Fenzi, B., Meijers, A., Legrésy, B., 2013. Modeling interannual dense shelf water export in the region of the Mertz Glacier Tongue (1992–2007). Journal of Geophysical Research: Oceans 118, 5858–5872.

Cougnon, E., Galton-Fenzi, B., Rintoul, S., Legrésy, B., Williams, G., Fraser, A., Hunter, J., 2017. Regional changes in icescape impact shelf circulation and basal melting. Geophysical Research Letters 44.

Craig, A., Valcke, S., Coquart, L., 2017. Development and performance of a new version of the OASIS coupler, OASIS3-MCT_3.0. Geoscientific Model Development 10, 3297–3308. URL: https://gmd.copernicus.org/articles/10/3297/2017/, doi:10.5194/gmd-10-3297-2017. publisher: Copernicus GmbH.

Curry, J.A., Schramm, J.L., Ebert, E.E., 1995. Sea ice-albedo climate feedback mechanism. Journal of Climate 8, 240–247.

De Lavergne, C., Madec, G., Le Sommer, J., Nurser, A.G., Naveira Garabato, A.C., 2016. The impact of a variable mixing efficiency on the abyssal overturning. Journal of Physical Oceanography 46, 663–681.

De Lavergne, C., Palter, J.B., Galbraith, E.D., Bernardello, R., Marinov, I., 2014. Cessation of deep convection in the open Southern Ocean under anthropogenic climate change. Nature Climate Change 4, 278.

De Ridder, K., Gallée, H., 1998. Land surface–induced regional climate change in southern Israel. Journal of applied meteorology 37, 1470–1485.

Delille, B., Vancoppenolle, M., Geilfus, N.X., Tilbrook, B., Lannuzel, D., Schoemann, V., Becquevort, S., Carnat, G., Delille, D., Lancelot, C., others, 2014. Southern Ocean CO2 sink: The contribution of the sea ice. Journal of Geophysical Research: Oceans 119, 6340–6355.

Depoorter, M.A., Bamber, J., Griggs, J., Lenaerts, J.T., Ligtenberg, S.R., van den Broeke, M.R., Moholdt, G., 2013. Calving fluxes and basal melt rates of Antarctic ice shelves. Nature 502, 89.

Dinniman, M.S., Klinck, J.M., Bai, L.S., Bromwich, D.H., Hines, K.M., Holland, D.M., 2015. The effect of atmospheric forcing resolution on delivery of ocean heat to the Antarctic floating ice shelves. Journal of Climate 28, 6067–6085.

Dinniman, M.S., Klinck, J.M., Hofmann, E.E., 2012. Sensitivity of Circumpolar Deep Water Transport and Ice Shelf Basal Melt along the West Antarctic Peninsula to Changes in the Winds. Journal of Climate 25, 4799–4816. doi:10.1175/JCLI-D-11-00307.1. publisher: American Meteorological Society Section: Journal of Climate.

Docquier, D., Grist, J.P., Roberts, M.J., Roberts, C.D., Semmler, T., Ponsoni, L., Massonnet, F., Sidorenko, D., Sein, D.V., Iovino, D., Bellucci, A., Fichefet, T., 2019. Impact of model resolution on Arctic sea ice and North Atlantic Ocean heat transport. Climate Dynamics 53, 4989–5017. URL: https://doi.org/10.1007/s00382-019-04840-y, doi:10.1007/s00382-019-04840-y.

Donat-Magnin, M., Jourdain, N.C., Gallée, H., Amory, C., Kittel, C., Fettweis, X., Wille, J.D., Favier, V., Drira, A., Agosta, C., 2020. Interannual variability of summer surface mass balance and surface melting in the Amundsen sector, West Antarctica. Cryosphere .

Donat-Magnin, M., Jourdain, N.C., Spence, P., Le Sommer, J., Gallée, H., Durand, G., 2017. Ice-Shelf Melt Response to Changing Winds and Glacier Dynamics in the Amundsen Sea Sector, Antarctica. Journal of Geophysical Research: Oceans 122, 10206–10224.

Donlon, C.J., Martin, M., Stark, J., Roberts-Jones, J., Fiedler, E., Wimmer, W., 2012. The operational sea surface temperature and sea ice analysis (OSTIA) system. Remote Sensing of Environment 116, 140–158.

Donohue, K.A., Tracey, K.L., Watts, D.R., Chidichimo, M.P., Chereskin, T.K., 2016. Mean Antarctic Circumpolar Current transport measured in Drake Passage. Geophysical Research Letters 43, 11,760–11,767. URL: https://agupubs.onlinelibrary.wiley.com/doi/abs/10.1002/2016GL070319, doi:https://doi.org/10.1002/2016GL070319. _eprint: https://agupubs.onlinelibrary.wiley.com/doi/pdf/10.1002/2016GL070319.

Drake, H.F., Morrison, A.K., Griffies, S.M., Sarmiento, J.L., Weijer, W., Gray, A.R., 2018. Lagrangian Timescales of Southern Ocean Upwelling in a Hierarchy of Model Resolutions. Geophysical Research Letters 45, 891–898. URL: https://onlinelibrary.wiley.com/doi/abs/10.1002/2017GL076045, doi:10.1002/2017GL076045. _eprint: https://agupubs.onlinelibrary.wiley.com/doi/pdf/10.1002/2017GL076045.

Du Plessis, M., Swart, S., Ansorge, I.J., Mahadevan, A., Thompson, A.F., 2019. Southern Ocean Seasonal Restratification Delayed by Submesoscale Wind–Front Interactions. Journal of Physical Oceanography 49, 1035–1053.

Dufour, C.O., Griffies, S.M., Souza, G.F.d., Frenger, I., Morrison, A.K., Palter, J.B., Sarmiento, J.L., Galbraith, E.D., Dunne, J.P., Anderson, W.G., Slater, R.D., 2015. Role of Mesoscale Eddies in Cross-Frontal Transport of Heat and Biogeochemical Tracers in the Southern Ocean. Journal of Physical Oceanography 45, 3057–3081. URL: https://journals.ametsoc.org/view/journals/phoc/45/12/jpo-d-14-0240.1.xml, doi:10.1175/JPO-D-14-0240.1. publisher: American Meteorological Society Section: Journal of Physical Oceanography.

Dumont, D., Gratton, Y., Arbetter, T.E., 2009. Modeling the dynamics of the North Water polynya ice bridge. Journal of Physical Oceanography 39, 1448–1461.

Duynkerke, P.G., 1988. Application of the E–\epsilon turbulence closure model to the neutral and stable atmospheric boundary layer. Journal of Atmospheric Sciences 45, 865–880.

Ebner, L., Heinemann, G., Haid, V., Timmermann, R., 2014. Katabatic winds and polynya dynamics at Coats Land, Antarctica. Antarctic Science 26, 309–326.

Engedahl, H., 1995. Use of the flow relaxation scheme in a three-dimensional baroclinic ocean model with realistic topography. Tellus A 47, 365–382.

EUMETSAT, 2015. Global sea ice concentration reprocessing data- set 1978-2015 (v1.2).

Eymard, L., 1998. Introduction: The SEMAPHORE experiment. Journal of Geophysical Research: Oceans 103, 25005–25008. URL: https://agupubs.onlinelibrary.wiley.com/doi/abs/10.1029/98JC00980, doi:10.1029/98JC00980. _eprint: https://agupubs.onlinelibrary.wiley.com/doi/pdf/10.1029/98JC00980.

Faghmous, J.H., Frenger, I., Yao, Y., Warmka, R., Lindell, A., Kumar, V., 2015. A daily global mesoscale ocean eddy dataset from satellite altimetry. Scientific Data 2, 150028. URL: https://www.nature.com/articles/sdata201528, doi:10.1038/sdata.2015.28. number: 1 Publisher: Nature Publishing Group.

Farneti, R., Delworth, T.L., Rosati, A.J., Griffies, S.M., Zeng, F., 2010. The Role of Mesoscale Eddies in the Rectification of the Southern Ocean Response to Climate Change. Journal of Physical Oceanography 40, 1539–1557. doi:10.1175/2010JPO4353.1. publisher: American Meteorological Society Section: Journal of Physical Oceanography.

Farneti, R., Downes, S.M., Griffies, S.M., Marsland, S.J., Behrens, E., Bentsen, M., Bi, D., Biastoch, A., Böning, C., Bozec, A., Canuto, V.M., Chassignet, E., Danabasoglu, G., Danilov, S., Diansky, N., Drange, H., Fogli, P.G., Gusev, A., Hallberg, R.W., Howard, A., Ilicak, M., Jung, T., Kelley, M., Large, W.G., Leboissetier, A., Long, M., Lu, J., Masina, S., Mishra, A., Navarra, A., George Nurser, A.J., Patara, L., Samuels, B.L., Sidorenko, D., Tsujino, H., Uotila, P., Wang, Q., Yeager, S.G., 2015. An assessment of Antarctic Circumpolar Current and Southern Ocean meridional overturning circulation during 1958–2007 in a suite of interannual CORE-II simulations. Ocean Modelling 93, 84–120. URL: https://www.sciencedirect.com/science/article/pii/S1463500315001183, doi:10.1016/j.ocemod.2015.07.009.

Favier, L., Durand, G., Cornford, S.L., Gudmundsson, G.H., Gagliardini, O., Gillet-Chaulet, F., Zwinger, T., Payne, A.J., Le Brocq, A.M., 2014. Retreat of Pine Island Glacier controlled by marine ice-sheet instability. Nature Climate Change 4, 117–121. URL: https://www.nature.com/articles/nclimate2094, doi:10.1038/nclimate2094. bandiera_abtest: a Cg_type: Nature Research Journals Number: 2 Primary_atype: Research Publisher: Nature Publishing Group Subject_term: Climate change;Cryospheric science;Environmental sciences Subject_term_id: climate-change;cryospheric-science;environmental-sciences.

Ferrari, R., Wunsch, C., 2009. Ocean Circulation Kinetic Energy: Reservoirs, Sources, and Sinks. Annual Review of Fluid Mechanics 41, 253–282. URL: https://doi.org/10.1146/annurev.fluid.40.111406.102139, doi:10.1146/annurev.fluid.40.111406.102139. _eprint: https://doi.org/10.1146/annurev.fluid.40.111406.102139.

Ferrari, R., Wunsch, C., 2010. The distribution of eddy kinetic and potential energies in the global ocean. Tellus A: Dynamic Meteorology and Oceanography 62, 92–108.

Flather, R.A., 1994. A storm surge prediction model for the northern Bay of Bengal with application to the cyclone disaster in April 1991. Journal of Physical Oceanography 24, 172–190.

Fogwill, C., Phipps, S., Turney, C., Golledge, N., 2015. Sensitivity of the Southern Ocean to enhanced regional Antarctic ice sheet meltwater input. Earth's Future 3, 317–329.

Foster, G., Rahmstorf, S., 2011. Global temperature evolution 1979–2010. Environmental Research Letters 6, 044022. URL: https://doi.org/10.1088/1748-9326/6/4/044022, doi:10.1088/1748-9326/6/4/044022. publisher: IOP Publishing.

Foster, T.D., Foldvik, A., Middleton, J.H., 1987. Mixing and bottom water formation in the shelf break region of the southern Weddell Sea. Deep Sea Research Part A. Oceanographic Research Papers 34, 1771–1794. URL: https://www.sciencedirect.com/science/article/pii/0198014987900537, doi:10.1016/0198-0149(87)90053-7.

Foussard, A., Lapeyre, G., Plougonven, R., 2019. Storm track response to oceanic eddies in idealized atmospheric simulations. Journal of Climate 32, 445–463. Publisher: American Meteorological Society.

Fraser, A.D., Massom, R.A., Michael, K.J., Galton-Fenzi, B.K., Lieser, J.L., 2012. East Antarctic landfast sea ice distribution and variability, 2000–08. Journal of Climate 25, 1137–1156.

Fraser, A.D., Ohshima, K.I., Nihashi, S., Massom, R.A., Tamura, T., Nakata, K., Williams, G.D., Carpentier, S., Willmes, S., 2019. Landfast ice controls on sea-ice production in the Cape Darnley Polynya: A case study. Remote Sensing of Environment 233, 111315.

Frenger, I., Gruber, N., Knutti, R., Münnich, M., 2013. Imprint of Southern Ocean eddies on winds, clouds and rainfall. Nature geoscience 6, 608–612.

Frenger, I., Münnich, M., Gruber, N., Knutti, R., 2015. Southern O cean eddy phenomenology. Journal of Geophysical Research: Oceans 120, 7413–7449. URL: https://onlinelibrary.wiley.com/doi/abs/10.1002/2015JC011047, doi:10.1002/2015JC011047.

Fretwell, P., Pritchard, H.D., Vaughan, D.G., Bamber, J., Barrand, N., Bell, R., Bianchi, C., Bingham, R., Blankenship, D.D., Casassa, G., others, 2013. Bedmap2: improved ice bed, surface and thickness datasets for Antarctica .

Frölicher, T.L., Sarmiento, J.L., Paynter, D.J., Dunne, J.P., Krasting, J.P., Winton, M., 2015. Dominance of the Southern Ocean in anthropogenic carbon and heat uptake in CMIP5 models. Journal of Climate 28, 862–886.

Fyke, J., Sergienko, O., Löfverström, M., Price, S., Lenaerts, J.T., 2018. An overview of interactions and feedbacks between ice sheets and the Earth system. Reviews of Geophysics 56, 361–408. Publisher: Wiley Online Library.

Galeotti, S., DeConto, R., Naish, T., Stocchi, P., Florindo, F., Pagani, M., Barrett, P., Bohaty, S.M., Lanci, L., Pollard, D., Sandroni, S., Talarico, F.M., Zachos, J.C., 2016. Antarctic Ice Sheet variability across the Eocene-Oligocene boundary climate transition. Science 352, 76–80. URL: https://science.sciencemag.org/content/352/6281/76, doi:10.1126/science.aab0669. publisher: American Association for the Advancement of Science Section: Report.

Gallée, H., 1995. Simulation of the Mesocyclonic Activity in the Ross Sea, Antarctica. Monthly Weather Review 123, 2051–2069. doi:10.1175/1520-0493(1995)123<2051:SOTMAI>2.0.CO;2. publisher: American Meteorological Society Section: Monthly Weather Review.

Gallée, H., 1997. Air-sea interactions over Terra Nova Bay during winter: Simulation with a coupled atmosphere-polynya model. Journal of Geophysical Research: Atmospheres 102, 13835–13849.

Gallée, H., Duynkerke, P.G., 1997. Air-snow interactions and the surface energy and mass balance over the melting zone of west Greenland during the Greenland Ice Margin Experiment. Journal of Geophysical Research: Atmospheres 102, 13813–13824. Publisher: Wiley Online Library.

Gallée, H., Guyomarc'h, G., Brun, E., 2001. Impact of snow drift on the Antarctic ice sheet surface mass balance: possible sensitivity to snow-surface properties. Boundary-Layer Meteorology 99, 1–19. Publisher: Springer.

Gallée, H., Preunkert, S., Argentini, S., Frey, M.M., Genthon, C., Jourdain, B., Pietroni, I., Casasanta, G., Barral, H., Vignon, E., 2015. Characterization of the boundary layer at Dome C (East Antarctica) during the OPALE summer campaign. Atmospheric Chemistry and Physics 15, 6225–6236. Publisher: Copernicus GmbH.

Gallée, H., Schayes, G., 1994. Development of a three-dimensional meso-\gamma primitive equation model: katabatic winds simulation in the area of Terra Nova Bay, Antarctica. Monthly Weather Review 122, 671–685.

Garcia, D., 2010. Robust smoothing of gridded data in one and higher dimensions with missing values. Computational Statistics & Data Analysis 54, 1167–1178. URL: https://linkinghub.elsevier.com/retrieve/pii/S0167947309003491, doi:10.1016/j.csda.2009.09.020.

Gaspar, P., Grégoris, Y., Lefevre, J.M., 1990. A simple eddy kinetic energy model for simulations of the oceanic vertical mixing: Tests at station Papa and Long-Term Upper Ocean Study site. Journal of Geophysical Research: Oceans 95, 16179–16193.

Gaube, P., Chelton, D.B., Samelson, R.M., Schlax, M.G., O'Neill, L.W., 2015. Satellite observations of mesoscale eddy-induced Ekman pumping. Journal of Physical Oceanography 45, 104–132.

Gent, P.R., Mcwilliams, J.C., 1990. Isopycnal mixing in ocean circulation models. Journal of Physical Oceanography 20, 150–155.

Giddy, I., Swart, S., Plessis, M.d., Thompson, A.F., Nicholson, S.A., 2021. Stirring of Sea-Ice Meltwater Enhances Submesoscale Fronts in the Southern Ocean. Journal of Geophysical Research: Oceans 126, e2020JC016814. URL: https://agupubs.onlinelibrary.wiley.com/doi/abs/10.1029/2020JC016814, doi:10.1029/2020JC016814. _eprint: https://agupubs.onlinelibrary.wiley.com/doi/pdf/10.1029/2020JC016814.

Golledge, N.R., Keller, E.D., Gomez, N., Naughten, K.A., Bernales, J., Trusel, L.D., Edwards, T.L., 2019. Global environmental consequences of twenty-first-century ice-sheet melt. Nature 566, 65–72.

Goosse, H., Kay, J.E., Armour, K.C., Bodas-Salcedo, A., Chepfer, H., Docquier, D., Jonko, A., Kushner, P.J., Lecomte, O., Massonnet, F., Park, H.S., Pithan, F., Svensson, G., Vancoppenolle, M., 2018. Quantifying climate feedbacks in polar regions. Nature Communications 9, 1919. URL: https://www.nature.com/articles/s41467-018-04173-0, doi:10.1038/s41467-018-04173-0.

Gossart, A., Helsen, S., Lenaerts, J.T.M., Broucke, S.V., Lipzig, N.P.M.v., Souverijns, N., 2019. An Evaluation of Surface Climatology in State-of-the-Art Reanalyses over the Antarctic Ice Sheet. Journal of Climate 32, 6899–6915. URL: https://journals.ametsoc.org/view/journals/clim/32/20/jcli-d-19-0030.1.xml, doi:10.1175/JCLI-D-19-0030.1. publisher: American Meteorological Society Section: Journal of Climate.

Gould, W.J., Schmitz, W.J., Wunsch, C., 1974. Preliminary field results for a Mid-Ocean Dynamics Experiment (MODE-0). Deep Sea Research and Oceanographic Abstracts 21, 911–931. URL: https://www.sciencedirect.com/science/article/pii/0011747174900254, doi:10.1016/0011-7471(74)90025-4.

Gryschka, M., Drüe, C., Etling, D., Raasch, S., 2008. On the influence of sea-ice inhomogeneities onto roll convection in cold-air outbreaks. Geophysical Research Letters 35. URL: https://agupubs.onlinelibrary.wiley.com/doi/abs/10.1029/2008GL035845, doi:10.1029/2008GL035845. _eprint: https://agupubs.onlinelibrary.wiley.com/doi/pdf/10.1029/2008GL035845.

Guerreiro, K., Fleury, S., Zakharova, E., Kouraev, A., Rémy, F., Maisongrande, P., 2017. Comparison of CryoSat-2 and ENVISAT radar freeboard over Arctic sea ice: toward an improved Envisat freeboard retrieval. The Cryosphere 11, 2059.

Gupta, M., Marshall, J., Song, H., Campin, J., Meneghello, G., 2020. Sea-Ice Melt Driven by Ice-Ocean Stresses on the Mesoscale. Journal of Geophysical Research: Oceans 125. URL: https://onlinelibrary.wiley.com/doi/10.1029/2020JC016404, doi:10.1029/2020JC016404.

Haarsma, R.J., Roberts, M.J., Vidale, P.L., Senior, C.A., Bellucci, A., Bao, Q., Chang, P., Corti, S., Fučkar, N.S., Guemas, V., von Hardenberg, J., Hazeleger, W., Kodama, C., Koenigk, T., Leung, L.R., Lu, J., Luo, J.J., Mao, J., Mizielinski, M.S., Mizuta, R., Nobre, P., Satoh, M., Scoccimarro, E., Semmler, T., Small, J., von Storch, J.S., 2016. High Resolution Model Intercomparison Project (HighResMIP v1.0) for CMIP6. Geoscientific Model Development 9, 4185–4208. URL: https://gmd.copernicus.org/articles/9/4185/2016/, doi:10.5194/gmd-9-4185-2016. publisher: Copernicus GmbH.

Hall, A., 2004. The Role of Surface Albedo Feedback in Climate. Journal of Climate 17, 1550–1568. doi:10.1175/1520-0442(2004)017<1550:TROSAF>2.0.CO;2. publisher: American Meteorological Society Section: Journal of Climate.

Hallberg, R., 2013. Using a resolution function to regulate parameterizations of oceanic mesoscale eddy effects. Ocean Modelling 72, 92–103.

Hausmann, U., McGillicuddy Jr, D.J., Marshall, J., 2017. Observed mesoscale eddy signatures in Southern Ocean surface mixed-layer depth. Journal of Geophysical Research: Oceans 122, 617–635. Publisher: Wiley Online Library.

Hausmann, U., Sallée, J.B., Jourdain, N.C., Mathiot, P., Rousset, C., Madec, G., Deshayes, J., Hattermann, T., 2020. The Role of Tides in Ocean-Ice Shelf Interactions in the Southwestern Weddell Sea. Journal of Geophysical Research: Oceans 125, e2019JC015847. URL: https://agupubs.pericles-prod.literatumonline.com/doi/abs/10.1029/2019JC015847, doi:10.1029/2019JC015847. _eprint: https://agupubs.onlinelibrary.wiley.com/doi/pdf/10.1029/2019JC015847.

Hazel, J.E., Stewart, A.L., 2019. Are the near-Antarctic easterly winds weakening in response to enhancement of the Southern Annular Mode? Journal of Climate 32, 1895–1918.

Held, I., Guo, H., Adcroft, A., Dunne, J., Horowitz, L., Krasting, J., Shevliakova, E., Winton, M., Zhao, M., Bushuk, M., others, 2019. Structure and performance of GFDL's CM4. 0 climate model. Journal of Advances in Modeling Earth Systems 11, 3691–3727.

Hellmer, H.H., 2004. Impact of Antarctic ice shelf basal melting on sea ice and deep ocean properties. Geophysical Research Letters 31.

Hermans, T.H.J., Gregory, J.M., Palmer, M.D., Ringer, M.A., Katsman, C.A., Slangen, A.B.A., 2021. Projecting Global Mean Sea-Level Change Using CMIP6 Models. Geophysical Research Letters 48, e2020GL092064. URL: https://agupubs.onlinelibrary.wiley.com/doi/abs/10.1029/2020GL092064, doi:10.1029/2020GL092064. _eprint: https://agupubs.onlinelibrary.wiley.com/doi/pdf/10.1029/2020GL092064.

Hersbach, H., Bell, B., Berrisford, P., Hirahara, S., Horányi, A., Muñoz-Sabater, J., Nicolas, J., Peubey, C., Radu, R., Schepers, D., others, 2020. The ERA5 global reanalysis. Quarterly Journal of the Royal Meteorological Society 146, 1999–2049.

Heuzé, C., 2021. Antarctic Bottom Water and North Atlantic Deep Water in CMIP6 models. Ocean Science 17, 59–90. URL: https://os.copernicus.org/articles/17/59/2021/, doi:10.5194/os-17-59-2021. publisher: Copernicus GmbH.

Heuzé, C., Heywood, K.J., Stevens, D.P., Ridley, J.K., 2013. Southern Ocean bottom water characteristics in CMIP5 models. Geophysical Research Letters 40, 1409–1414.

Heuzé, C., Vivier, F., Sommer, J.L., Molines, J.M., Penduff, T., 2015. Can we map the interannual variability of the whole upper Southern Ocean with the current database of hydrographic observations? Journal of Geophysical Research: Oceans 120, 7960–7978. URL: https://doi.org/10.1002/2015jc011115, doi:10.1002/2015jc011115.

Hewitt, H.T., Roberts, M., Mathiot, P., Biastoch, A., Blockley, E., Chassignet, E.P., Fox-Kemper, B., Hyder, P., Marshall, D.P., Popova, E., others, 2020. Resolving and Parameterising the Ocean Mesoscale in Earth System Models. Current Climate Change Reports , 1–16.

Hogg, A.M., 2010. An Antarctic Circumpolar Current driven by surface buoyancy forcing. Geophysical Research Letters 37. URL: https://agupubs.onlinelibrary.wiley.com/doi/abs/10.1029/2010GL044777, doi:https://doi.org/10.1029/2010GL044777. _eprint: https://agupubs.onlinelibrary.wiley.com/doi/pdf/10.1029/2010GL044777.

Horvat, C., Tziperman, E., Campin, J.M., 2016. Interaction of sea ice floe size, ocean eddies, and sea ice melting. Geophysical Research Letters 43, 8083–8090.

Hu, S., Sprintall, J., Guan, C., McPhaden, M.J., Wang, F., Hu, D., Cai, W., 2020. Deep-reaching acceleration of global mean ocean circulation over the past two decades. Science Advances 6. URL: https://www.science.org/doi/10.1126/sciadv.aax7727, doi:10.1126/sciadv.aax7727. publisher: American Association for the Advancement of Science.

Hughes, C.W., 2005. Nonlinear vorticity balance of the Antarctic Circumpolar Current. Journal of Geophysical Research: Oceans 110. Publisher: Wiley Online Library.

Hughes, C.W., Ash, E.R., 2001. Eddy forcing of the mean flow in the Southern Ocean. Journal of Geophysical Research: Oceans 106, 2713–2722.

Huot, P.V., Fichefet, T., Jourdain, N.C., Mathiot, P., Rousset, C., Kittel, C., Fettweis, X., 2021a. Influence of ocean tides and ice shelves on ocean-ice interactions and dense shelf water formation in the D'Urville Sea, Antarctica. Ocean Modelling (Submitted).

Huot, P.V., Kittel, C., Fichefet, T., Jourdain, N.C., Sterlin, J., Fettweis, X., 2021b. Effects of the atmospheric forcing resolution on simulated sea ice and polynyas off Adelie Land, East Antarctica. Ocean Modelling .

Jacobs, S., Helmer, H., Doake, C.S.M., Jenkins, A., Frolich, R.M., 1992. Melting of ice shelves and the mass balance of Antarctica. Journal of Glaciology 38, 375–387. URL: https://www.cambridge.org/core/product/identifier/S0022143000002252/type/journal_article, doi:10.1017/S0022143000002252.

Jacobs, S.S., 2004. Bottom water production and its links with the thermohaline circulation. Antarctic Science 16, 427–437.

Jacobs, S.S., Amos, A.F., Bruchhausen, P.M., 1970. Ross Sea oceanography and Antarctic bottom water formation, in: Deep Sea Research and Oceanographic Abstracts, Elsevier. pp. 935–962.

Jenkins, A., 1991. A one-dimensional model of ice shelf-ocean interaction. Journal of Geophysical Research: Oceans 96, 20671–20677.

Jenkins, A., Holland, D.M., 2002. A model study of ocean circulation beneath Filchner-Ronne Ice Shelf, Antarctica: Implications for bottom water formation. Geophysical Research Letters 29, 34–1–34–4. URL: https://agupubs.onlinelibrary.wiley.com/doi/abs/10.1029/2001GL014589, doi:10.1029/2001GL014589. _eprint: https://agupubs.onlinelibrary.wiley.com/doi/pdf/10.1029/2001GL014589.

Jenkins, A., Shoosmith, D., Dutrieux, P., Jacobs, S., Kim, T.W., Lee, S.H., Ha, H.K., Stammerjohn, S., 2018. West Antarctic Ice Sheet retreat in the Amundsen Sea driven by decadal oceanic variability. Nature Geoscience 11, 733–738. URL: https://www.nature.com/articles/s41561-018-0207-4, doi:10.1038/s41561-018-0207-4. bandiera_abtest: a Cg_type: Nature Research Journals Number: 10 Primary_atype: Research Publisher: Nature Publishing Group Subject_term: Climate change;Cryospheric science;Physical oceanography Subject_term_id: climate-change;cryospheric-science;physical-oceanography.

Jeong, H., Asay-Davis, X.S., Turner, A.K., Comeau, D.S., Price, S.F., Abernathey, R.P., Veneziani, M., Petersen, M.R., Hoffman, M.J., Mazloff, M.R., others, 2020. Impacts of Ice-Shelf Melting on Water-Mass Transformation in the Southern Ocean from E3SM Simulations. Journal of Climate 33, 5787–5807.

Johnson, G.C., 2008. Quantifying Antarctic bottom water and North Atlantic deep water volumes. Journal of Geophysical Research: Oceans 113.

Jonassen, M.O., Välisuo, I., Vihma, T., Uotila, P., Makshtas, A.P., Launiainen, J., 2019. Assessment of atmospheric reanalyses with independent observations in the weddell sea, the antarctic. Journal of Geophysical Research: Atmospheres 124, 12468–12484. Publisher: Wiley Online Library.

Jones, R.W., Renfrew, I.A., Orr, A., Webber, B.G.M., Holland, D.M., Lazzara, M.A., 2016. Evaluation of four global reanalysis products using in situ observations in the Amundsen Sea Embayment, Antarctica. Journal of Geophysical Research: Atmospheres 121, 6240–6257. Publisher: Wiley Online Library.

Jourdain, N.C., Gallée, H., 2011. Influence of the orographic roughness of glacier valleys across the Transantarctic Mountains in an atmospheric regional model. Climate dynamics 36, 1067–1081.

Jourdain, N.C., Mathiot, P., Gallée, H., Barnier, B., 2011. Influence of coupling on atmosphere, sea ice and ocean regional models in the Ross Sea sector, Antarctica. Climate dynamics 36, 1523–1543. Publisher: Springer.

Jourdain, N.C., Mathiot, P., Merino, N., Durand, G., Le Sommer, J., Spence, P., Dutrieux, P., Madec, G., 2017. Ocean circulation and sea-ice thinning induced by melting ice shelves in the Amundsen Sea. Journal of Geophysical Research: Oceans 122, 2550–2573.

Jourdain, N.C., Molines, J.M., Le Sommer, J., Mathiot, P., Chanut, J., de Lavergne, C., Madec, G., 2019. Simulating or prescribing the influence of tides on the Amundsen Sea ice shelves. Ocean Modelling 133, 44–55.

Jung, T., Serrar, S., Wang, Q., 2014. The oceanic response to mesoscale atmospheric forcing. Geophysical Research Letters 41, 1255–1260.

Jungclaus, J., Fischer, N., Haak, H., Lohmann, K., Marotzke, J., Matei, D., Mikolajewicz, U., Notz, D., Von Storch, J., 2013. Characteristics of the ocean simulations in the Max Planck Institute Ocean Model

(MPIOM) the ocean component of the MPI-Earth system model. Journal of Advances in Modeling Earth Systems 5, 422–446.

Kaleschke, L., Lüpkes, C., Vihma, T., Haarpaintner, J., Bochert, A., Hartmann, J., Heygster, G., 2001. SSM/I sea ice remote sensing for mesoscale ocean-atmosphere interaction analysis. Canadian Journal of Remote Sensing 27, 526–537.

Kessler, E., 1969. On the distribution and continuity of water substance in atmospheric circulations, in: On the distribution and continuity of water substance in atmospheric circulations. Springer, pp. 1–84.

Killworth, P.D., 1983. Deep convection in the world ocean. Reviews of Geophysics 21, 1–26.

Kittel, C., Amory, C., Agosta, C., Delhasse, A., Doutreloup, S., Huot, P.V., Wyard, C., Fichefet, T., Fettweis, X., 2018. Sensitivity of the current Antarctic surface mass balance to sea surface conditions using MAR. Cryosphere 12, 3827–3839.

Kittel, C., Amory, C., Agosta, C., Jourdain, N.C., Hofer, S., Delhasse, A., Doutreloup, S., Huot, P.V., Lang, C., Fichefet, T., 2021. Diverging future surface mass balance between the Antarctic ice shelves and grounded ice sheet. The Cryosphere 15, 1215–1236. Publisher: Copernicus GmbH.

Klein, P., Lapeyre, G., Siegelman, L., Qiu, B., Fu, L.L., Torres, H., Su, Z., Menemenlis, D., Gentil, S.L., 2019. Ocean-Scale Interactions From Space. Earth and Space Science 6, 795–817. URL: https://agupubs.onlinelibrary.wiley.com/doi/abs/10.1029/2018EA000492, doi:10.1029/2018EA000492. _eprint: https://agupubs.onlinelibrary.wiley.com/doi/pdf/10.1029/2018EA000492.

Koentopp, M., Eisen, O., Kottmeier, C., Padman, L., Lemke, P., 2005. Influence of tides on sea ice in the Weddell Sea: Investigations with a high-resolution dynamic-thermodynamic sea ice model. Journal of Geophysical Research: Oceans 110.

Kozlov, I.E., Artamonova, A.V., Manucharyan, G.E., Kubryakov, A.A., 2019. Eddies in the Western Arctic Ocean From Spaceborne SAR Observations Over Open Ocean and Marginal Ice Zones. Journal of Geophysical Research: Oceans 124, 6601–6616. URL: https://agupubs.onlinelibrary.wiley.com/doi/abs/10.1029/2019JC015113, doi:https://doi.org/10.1029/2019JC015113. _eprint: https://agupubs.onlinelibrary.wiley.com/doi/pdf/10.1029/2019JC015113.

Kozlov, I.E., Plotnikov, E.V., Manucharyan, G.E., 2020. Brief Communication: Mesoscale and submesoscale dynamics in the marginal ice zone from sequential synthetic aperture radar observations. The Cryosphere 14, 2941–2947. URL: https://tc.copernicus.org/articles/14/2941/2020/, doi:10.5194/tc-14-2941-2020. publisher: Copernicus GmbH.

Kuhlbrodt, T., Griesel, A., Montoya, M., Levermann, A., Hofmann, M., Rahmstorf, S., 2007. On the driving processes of the Atlantic meridional overturning circulation. Reviews of Geophysics 45. URL: https://onlinelibrary.wiley.com/doi/abs/10.1029/2004RG000166, doi:10.1029/2004RG000166. _eprint: https://onlinelibrary.wiley.com/doi/pdf/10.1029/2004RG000166.

Kusahara, K., Hasumi, H., Fraser, A.D., Aoki, S., Shimada, K., Williams, G.D., Massom, R., Tamura, T., 2017. Modeling Ocean–Cryosphere Interactions off Adélie and George V Land, East Antarctica. Journal of Climate 30, 163–188. URL: https://doi.org/10.1175/jcli-d-15-0808.1, doi:10.1175/jcli-d-15-0808.1.

Kusahara, K., Hasumi, H., Tamura, T., 2010. Modeling sea ice production and dense shelf water formation in coastal polynyas around East Antarctica. Journal of Geophysical Research 115. URL: https://doi.org/10.1029/2010jc006133, doi:10.1029/2010jc006133.

Kusahara, K., Hasumi, H., Williams, G.D., 2011a. Dense shelf water formation and brine-driven circulation in the Adélie and George V Land region. Ocean Modelling 37, 122–138.

Kusahara, K., Hasumi, H., Williams, G.D., 2011b. Impact of the Mertz Glacier Tongue calving on dense water formation and export. Nature communications 2, 159.

König Beatty, C., Holland, D.M., 2010. Modeling landfast sea ice by adding tensile strength. Journal of physical oceanography 40, 185–198.

Labrousse, S., Williams, G., Tamura, T., Bestley, S., Sallée, J.B., Fraser, A.D., Sumner, M., Roquet, F., Heerah, K., Picard, B., others, 2018. Coastal polynyas: Winter oases for subadult southern elephant seals in East Antarctica. Scientific reports 8, 1–15.

Lacarra, M., Houssais, M.N., Herbaut, C., Sultan, E., Beauverger, M., 2014. Dense shelf water production in the Adélie Depression, East Antarctica, 2004-2012: Impact of the Mertz Glacier calving. Journal of Geophysical Research: Oceans 119, 5203–5220. URL: https://doi.org/10.1002/2013jc009124, doi:10.1002/2013jc009124.

Large, W.G., Yeager, S.G., 2004. Diurnal to decadal global forcing for ocean and sea-ice models: the data sets and flux climatologies .

Lavergne, C.d., Madec, G., Sommer, J.L., Nurser, A.J.G., Garabato, A.C.N., 2016. On the Consumption of Antarctic Bottom Water in the Abyssal Ocean. Journal of Physical Oceanography 46, 635–661. doi:10.1175/JPO-D-14-0201.1. publisher: American Meteorological Society Section: Journal of Physical Oceanography.

Lavergne, T., Sørensen, A.M., Kern, S., Tonboe, R., Notz, D., Aaboe, S., Bell, L., Dybkj\textbackslasha er, G., Eastwood, S., Gabarro, C., others, 2019. Version 2 of the EUMETSAT OSI SAF and ESA CCI sea-ice concentration climate data records. The Cryosphere 13, 49–78.

Le Bars, D., Viebahn, J.P., Dijkstra, H.A., 2016. A Southern Ocean mode of multidecadal variability. Geophysical Research Letters 43, 2102–2110. URL: https://agupubs.onlinelibrary.wiley.com/doi/abs/10.1002/2016GL068177, doi:https://doi.org/10.1002/2016GL068177.

Le Toumelin, L., Amory, C., Favier, V., Kittel, C., Hofer, S., Fettweis, X., Gallée, H., Kayetha, V., 2020. Sensitivity of the surface energy budget to drifting snow as simulated by MAR in coastal Adelie Land, Antarctica. The Cryosphere Discussions , 1–27.

Lear, C.H., Lunt, D.J., 2016. How Antarctica got its ice. Science 352, 34–35. URL: https://science.sciencemag.org/content/352/6281/34, doi:10.1126/science.aad6284. publisher: American Association for the Advancement of Science Section: Perspective.

Lecomte, O., Goosse, H., Fichefet, T., De Lavergne, C., Barthélemy, A., Zunz, V., 2017. Vertical ocean heat redistribution sustaining sea-ice concentration trends in the Ross Sea. Nature communications 8, 1–8.

Lecomte, O., Goosse, H., Fichefet, T., Holland, P.R., Uotila, P., Zunz, V., Kimura, N., 2016. Impact of surface wind biases on the Antarctic sea ice concentration budget in climate models. Ocean Modelling 105, 60–70. URL: https://doi.org/10.1016/j.ocemod.2016.08.001, doi:10.1016/j.ocemod.2016.08.001.

Lefebre, F., Gallée, H., Ypersele, J.P.v., Greuell, W., 2003. Modeling of snow and ice melt at ETH Camp (West Greenland): A study of surface albedo. Journal of Geophysical Research: Atmospheres 108. URL: https://agupubs.onlinelibrary.wiley.com/doi/abs/10.1029/2001JD001160, doi:10.1029/2001JD001160. _eprint: https://agupubs.onlinelibrary.wiley.com/doi/pdf/10.1029/2001JD001160.

Lei, R., Li, Z., Cheng, B., Zhang, Z., Heil, P., 2010. Annual cycle of landfast sea ice in Prydz Bay, east Antarctica. Journal of Geophysical Research: Oceans 115. URL: https://agupubs.onlinelibrary.wiley.com/doi/abs/10.1029/2008JC005223, doi:10.1029/2008JC005223. _eprint: https://agupubs.onlinelibrary.wiley.com/doi/pdf/10.1029/2008JC005223.

Lemieux, J.F., Dupont, F., Blain, P., Roy, F., Smith, G.C., Flato, G.M., 2016. Improving the simulation of landfast ice by combining tensile strength and a parameterization for grounded ridges. Journal of Geophysical Research: Oceans 121, 7354–7368.

Lenaerts, J.T.M., Van Tricht, K., Lhermitte, S., L'Ecuyer, T.S., 2017. Polar clouds and radiation in satellite observations, reanalyses, and climate models. Geophysical Research Letters 44, 3355–3364. URL: https://onlinelibrary.wiley.com/doi/abs/10.1002/2016GL072242, doi:10.1002/2016GL072242. _eprint: https://agupubs.onlinelibrary.wiley.com/doi/pdf/10.1002/2016GL072242.

Lin, Y.L., Farley, R.D., Orville, H.D., 1983. Bulk parameterization of the snow field in a cloud model. Journal of Applied Meteorology and climatology 22, 1065–1092.

Liniger, G., Strutton, P.G., Lannuzel, D., Moreau, S., 2020. Calving event led to changes in phytoplankton bloom phenology in the Mertz polynya, Antarctica. Journal of Geophysical Research: Oceans , e2020JC016387.

van Lipzig, N.P., van Meijgaard, E., Oerlemans, J., 2002. Temperature sensitivity of the Antarctic surface mass balance in a regional atmospheric climate model. Journal of climate 15, 2758–2774.

Liu, W., Lu, J., Xie, S.P., Fedorov, A., 2018. Southern Ocean Heat Uptake, Redistribution, and Storage in a Warming Climate: The Role of Meridional Overturning Circulation. Journal of Climate 31, 4727–4743. doi:10.1175/JCLI-D-17-0761.1. publisher: American Meteorological Society Section: Journal of Climate.

Locarnini, R., Mishonov, A., Antonov, J., Boyer, T., Garcia, H., Baranova, O., Zweng, M., Paver, C., Reagan, J., Johnson, D., Hamilton, M., Seidov, D., 2013. World Ocean Atlas2013, Volume 1: Temperature. NOAA Atlas NESDIS 73 Edition: S.Levitus; A.Mishonov.

Locarnini, R., Mishonov, A., Baranova, O., Boyer, T., Zweng, M., Garcia, H., Reagan, J., Seidov, D., Weathers, K., Paver, C., Smolyar, I., 2018. World Ocean Atlas 2018, Volume 1: Temperature. NOAA Atlas NESDIS 81 Edition: A. Mishonov.

Losch, M., 2008. Modeling ice shelf cavities in azcoordinate ocean general circulation model. Journal of Geophysical Research 113. URL: https://doi.org/10.1029/2007jc004368, doi:10.1029/2007jc004368.

Luneva, M.V., Aksenov, Y., Harle, J.D., Holt, J.T., 2015. The effects of tides on the water mass mixing and sea ice in the Arctic Ocean. Journal of Geophysical Research: Oceans 120, 6669–6699. URL: https://doi.org/10.1002/2014jc010310, doi:10.1002/2014jc010310.

Lurton, T., Balkanski, Y., Bastrikov, V., Bekki, S., Bopp, L., Braconnot, P., Brockmann, P., Cadule, P., Contoux, C., Cozic, A., others, 2020. Implementation of the CMIP6 Forcing Data in the IPSL-CM6A-LR Model. Journal of Advances in Modeling Earth Systems 12, e2019MS001940.

Lüpkes, C., Gryanik, V.M., Hartmann, J., Andreas, E.L., 2012. A parametrization, based on sea ice morphology, of the neutral atmospheric drag coefficients for weather prediction and climate models. Journal of Geophysical Research: Atmospheres 117, n/a–n/a. URL: https://doi.org/10.1029/2012jd017630, doi:10.1029/2012jd017630.

Ma, J., Xu, H., Dong, C., Lin, P., Liu, Y., 2015. Atmospheric responses to oceanic eddies in the Kuroshio Extension region. Journal of Geophysical Research: Atmospheres 120, 6313–6330.

Madec, G., 2016. NEMO ocean engine. Note du Pôle de modélisation, Institut Pierre-Simon Laplace (IPSL), France, No 27, ISSN No 1288-1619.

Makinson, K., Holland, P.R., Jenkins, A., Nicholls, K.W., Holland, D.M., 2011. Influence of tides on melting and freezing beneath Filchner-Ronne Ice Shelf, Antarctica. Geophysical Research Letters 38, n/a–n/a. URL: https://doi.org/10.1029/2010gl046462, doi:10.1029/2010gl046462.

Maksym, T., Stammerjohn, S.E., Ackley, S., Massom, R., 2012. Antarctic Sea Ice— A Polar Opposite? Oceanography 25, 140–151. Publisher: JSTOR.

Manganello, J.V., Hodges, K.I., Kinter, J.L., Cash, B.A., Marx, L., Jung, T., Achuthavarier, D., Adams, J.M., Altshuler, E.L., Huang, B., Jin, E.K., Stan, C., Towers, P., Wedi, N., 2012. Tropical Cyclone Climatology in a 10-km Global Atmospheric GCM: Toward Weather-Resolving Climate Modeling. Journal of Climate 25, 3867–3893. doi:10.1175/JCLI-D-11-00346.1. publisher: American Meteorological Society Section: Journal of Climate.

Mantyla, A.W., Reid, J.L., 1983. Abyssal characteristics of the World Ocean waters. Deep Sea Research Part A. Oceanographic Research Papers 30, 805–833.

Manucharyan, G.E., Thompson, A.F., 2017. Submesoscale Sea Ice-Ocean Interactions in Marginal Ice Zones. Journal of Geophysical Research: Oceans 122, 9455–9475. URL: https://doi.org/10.1002/2017jc012895, doi:10.1002/2017jc012895.

Maraldi, C., Chanut, J., Levier, B., Ayoub, N., De Mey, P., Reffray, G., Lyard, F., Cailleau, S., Drévillon, M., Fanjul, E., others, 2013. NEMO on the shelf: assessment of the Iberia-Biscay-Ireland configuration. .

Marchi, S., Fichefet, T., Goosse, H., Zunz, V., Tietsche, S., Day, J.J., Hawkins, E., 2019. Reemergence of Antarctic sea ice predictability and its link to deep ocean mixing in global climate models. Climate Dynamics 52, 2775–2797.

Marshall, D.P., Ambaum, M.H.P., Maddison, J.R., Munday, D.R., Novak, L., 2017. Eddy saturation and frictional control of the Antarctic Circumpolar Current. Geophysical Research Letters 44, 286–292. URL: https://agupubs.onlinelibrary.wiley.com/doi/abs/10.1002/2016GL071702, doi:https://doi.org/10.1002/2016GL071702. _eprint: https://agupubs.onlinelibrary.wiley.com/doi/pdf/10.1002/2016GL071702.

Marshall, J., Speer, K., 2012. Closure of the meridional overturning circulation through Southern Ocean upwelling. Nature Geoscience 5, 171–180. URL: https://www.nature.com/articles/ngeo1391, doi:10.1038/ngeo1391. number: 3 Publisher: Nature Publishing Group.

Marsland, S.J., Bindoff, N., Williams, G., Budd, W., 2004. Modeling water mass formation in the Mertz Glacier Polynya and Adélie Depression, east Antarctica. Journal of Geophysical Research: Oceans 109.

Marsland, S.J., Church, J.A., Bindoff, N.L., Williams, G.D., 2007. Antarctic coastal polynya response to climate change. Journal of Geophysical Research: Oceans 112. URL: https://agupubs.onlinelibrary.wiley.com/doi/abs/10.1029/2005JC003291, doi:10.1029/2005JC003291. _eprint: https://agupubs.onlinelibrary.wiley.com/doi/pdf/10.1029/2005JC003291.

Martin, A., Houssais, M.N., Goff, H.L., Marec, C., Dausse, D., 2017. Circulation and water mass transports on the East Antarctic shelf in the Mertz Glacier region. Deep Sea Research Part I: Oceanographic Research Papers 126, 1–20. URL: https://doi.org/10.1016/j.dsr.2017.05.007, doi:10.1016/j.dsr.2017.05.007.

Martinson, D.G., 2012. Antarctic circumpolar current's role in the Antarctic ice system: An overview. Palaeogeography, Palaeoclimatology, Palaeoecology 335-336, 71–74. URL: https://www.sciencedirect.com/science/article/pii/S0031018211001799, doi:10.1016/j.palaeo.2011.04.007.

Martínez-Moreno, J., Hogg, A.M., England, M.H., Constantinou, N.C., Kiss, A.E., Morrison, A.K., 2021. Global changes in oceanic mesoscale currents over the satellite altimetry record. Nature Climate Change 11, 397–403. URL: https://www.nature.com/articles/s41558-021-01006-9, doi:10.1038/s41558-021-01006-9. bandiera_abtest: a Cg_type: Nature Research Journals Number: 5 Primary_atype: Research Publisher: Nature Publishing Group Subject_term: Environmental health;Physical oceanography;Projection and prediction Subject_term_id: environmental-health;physical-oceanography;projection-and-prediction.

Massom, R., Harris, P., Michael, K.J., Potter, M., 1998. The distribution and formative processes of latent-heat polynyas in East Antarctica. Annals of Glaciology 27, 420–426.

Massom, R.A., Eicken, H., Hass, C., Jeffries, M.O., Drinkwater, M.R., Sturm, M., Worby, A.P., Wu, X., Lytle, V.I., Ushio, S., Morris, K., Reid, P.A., Warren, S.G., Allison, I., 2001. Snow on Antarctic sea ice. Reviews of Geophysics 39, 413–445. URL: https://onlinelibrary.wiley.com/doi/abs/10.1029/2000RG000085, doi:10.1029/2000RG000085. _eprint: https://agupubs.onlinelibrary.wiley.com/doi/pdf/10.1029/2000RG000085.

Mathiot, P., Barnier, B., Gallée, H., Molines, J.M., Sommer, J.L., Juza, M., Penduff, T., 2010. Introducing katabatic winds in global ERA40 fields to simulate their impacts on the Southern Ocean and sea-ice. Ocean Modelling 35, 146–160. URL: https://doi.org/10.1016/j.ocemod.2010.07.001, doi:10.1016/j.ocemod.2010.07.001.

Mathiot, P., Jenkins, A., Harris, C., Madec, G., 2017. Explicit representation and parametrised impacts of under ice shelf seas in the z* coordinate ocean model NEMO 3.6. Geoscientific Model Development 10, 2849–2874. URL: https://doi.org/10.5194/gmd-10-2849-2017, doi:10.5194/gmd-10-2849-2017.

Mathiot, P., Jourdain, N.C., Barnier, B., Gallée, H., Molines, J.M., Sommer, J.L., Penduff, T., 2012. Sensitivity of coastal polynyas and high-salinity shelf water production in the Ross Sea, Antarctica, to the atmospheric forcing. Ocean Dynamics 62, 701–723. URL: https://doi.org/10.1007/s10236-012-0531-y, doi:10.1007/s10236-012-0531-y.

Mauritsen, T., Bader, J., Becker, T., Behrens, J., Bittner, M., Brokopf, R., Brovkin, V., Claussen, M., Crueger, T., Esch, M., others, 2019. Developments in the MPI-M Earth System Model version 1.2 (MPI-ESM1. 2) and its response to increasing CO2. Journal of Advances in Modeling Earth Systems 11, 998–1038.

Mayet, C., Testut, L., Legresy, B., Lescarmontier, L., Lyard, F., 2013. High-resolution barotropic modeling and the calving of the Mertz Glacier, East Antarctica. Journal of Geophysical Research: Oceans 118, 5267–5279. URL: https://doi.org/10.1002/jgrc.20339, doi:10.1002/jgrc.20339.

McWilliams, J.C., 2008. The nature and consequences of oceanic eddies. Ocean modeling in an eddying regime 177, 5–15. Publisher: AGU Monograph.

Menviel, L., Timmermann, A., Timm, O.E., Mouchet, A., 2010. Climate and biogeochemical response to a rapid melting of the West Antarctic Ice Sheet during interglacials and implications for future climate. Paleoceanography 25.

Merino, N., Jourdain, N.C., Le Sommer, J., Goosse, H., Mathiot, P., Durand, G., 2018. Impact of increasing antarctic glacial freshwater release on regional sea-ice cover in the Southern Ocean. Ocean Modelling 121, 76–89.

Merino, N., Sommer, J.L., Durand, G., Jourdain, N.C., Madec, G., Mathiot, P., Tournadre, J., 2016. Antarctic icebergs melt over the Southern Ocean: Climatology and impact on sea ice. Ocean Modelling 104, 99–110. URL: https://doi.org/10.1016/j.ocemod.2016.05.001, doi:10.1016/j.ocemod.2016.05.001.

Mohrmann, M., Heuzé, C., Swart, S., 2021. Southern Ocean polynyas in CMIP6 models. The Cryosphere Discussions , 1–43URL: https://tc.copernicus.org/preprints/tc-2021-23/, doi:10.5194/tc-2021-23. publisher: Copernicus GmbH.

Morales Maqueda, M., Willmott, A., Biggs, N., 2004. Polynya dynamics: A review of observations and modeling. Reviews of Geophysics 42.

Morcrette, J.J., 2002. The Surface Downward Longwave Radiation in the ECMWF Forecast System. Journal of Climate 15, 1875–1892. doi:10.1175/1520-0442(2002)015<1875:TSDLRI>2.0.CO;2. publisher: American Meteorological Society Section: Journal of Climate.

Moreau, S., Penna, A.D., Llort, J., Patel, R., Langlais, C., Boyd, P.W., Matear, R.J., Phillips, H.E., Trull, T.W., Tilbrook, B., Lenton, A., Strutton, P.G., 2017. Eddy-induced carbon transport across the Antarctic Circumpolar Current. Global Biogeochemical Cycles 31, 1368–1386. URL: https://agupubs.onlinelibrary.wiley.com/doi/abs/10.1002/2017GB005669, doi:https://doi.org/10.1002/2017GB005669. _eprint: https://agupubs.onlinelibrary.wiley.com/doi/pdf/10.1002/2017GB005669.

Morozov, E.G., 2020. Polygon-70: Data Interpretation in the Light of New Concepts about Internal Waves. Izvestiya, Atmospheric and Oceanic Physics 56, 428–434. URL: https://doi.org/10.1134/S0001433820040076, doi:10.1134/S0001433820040076.

Mottram, R., Hansen, N., Kittel, C., van Wessem, M., Agosta, C., Amory, C., Boberg, F., van de Berg, W.J., Fettweis, X., Gossart, A., others, 2020. What is the surface mass balance of Antarctica? An intercomparison of regional climate model estimates. The Cryosphere Discussions , 1–42.

Mueller, R., Padman, L., Dinniman, M.S., Erofeeva, S., Fricker, H.A., King, M., 2012. Impact of tide-topography interactions on basal melting of Larsen C Ice Shelf, Antarctica. Journal of Geophysical Research: Oceans 117.

Murakami, K., Nomura, D., Hashida, G., Nakaoka, S.i., Kitade, Y., Hirano, D., Hirawake, T., Ohshima, K.I., 2020. Strong biological carbon uptake and carbonate chemistry associated with dense shelf water outflows in the Cape Darnley polynya, East Antarctica. Marine Chemistry 225, 103842. URL: https://www.sciencedirect.com/science/article/pii/S0304420320300967, doi:10.1016/j.marchem.2020.103842.

Nastrom, G.D., Gage, K.S., Jasperson, W.H., 1984. Kinetic energy spectrum of large-and mesoscale atmospheric processes. Nature 310, 36–38. URL: https://www.nature.com/articles/310036a0, doi:10.1038/310036a0. bandiera_abtest: a Cg_type: Nature Research Journals Number: 5972 Primary_atype: Research Publisher: Nature Publishing Group.

Nicholls, K.W., Makinson, K., Robinson, A.V., 1991. Ocean circulation beneath the Ronne ice shelf. Nature 354, 221–223. URL: https://www.nature.com/articles/354221a0, doi:10.1038/354221a0. bandiera_abtest: a Cg_type: Nature Research Journals Number: 6350 Primary_atype: Research Publisher: Nature Publishing Group.

Nihashi, S., Ohshima, K.I., 2015. Circumpolar mapping of Antarctic coastal polynyas and landfast sea ice: Relationship and variability. Journal of climate 28, 3650–3670.

Norris, J., Hall, A., Neelin, J.D., Thackeray, C.W., Chen, D., 2021. Evaluation of the Tail of the Probability Distribution of Daily and Subdaily Precipitation in CMIP6 Models. Journal of Climate 34, 2701–2721. doi:10.1175/JCLI-D-20-0182.1. publisher: American Meteorological Society Section: Journal of Climate.

Ohshima, K.I., Fukamachi, Y., Williams, G.D., Nihashi, S., Roquet, F., Kitade, Y., Tamura, T., Hirano, D., Herraiz-Borreguero, L., Field, I., others, 2013. Antarctic Bottom Water production by intense sea-ice formation in the Cape Darnley polynya. Nature Geoscience 6, 235.

Olason, E., 2016. A dynamical model of Kara Sea land-fast ice. Journal of Geophysical Research: Oceans 121, 3141–3158. URL: https://doi.org/10.1002/2016jc011638, doi:10.1002/2016jc011638.

Orsi, A., Johnson, G., Bullister, J., 1999. Circulation, mixing, and production of Antarctic Bottom Water. Progress in Oceanography 43, 55–109.

Orsi, A.H., Whitworth, T., 2005. Hydrographic Atlas of the World Ocean Circulation Experiment (WOCE): Volume 1: Southern Ocean. WOCE International Project Office Southampton, UK.

O'Neill, L.W., Chelton, D.B., Esbensen, S.K., Wentz, F.J., 2005. High-Resolution Satellite Measurements of the Atmospheric Boundary Layer Response to SST Variations along the Agulhas Return Current. Journal of Climate 18, 2706–2723. doi:10.1175/JCLI3415.1. publisher: American Meteorological Society Section: Journal of Climate.

Padman, L., Howard, S.L., Orsi, A.H., Muench, R.D., 2009. Tides of the northwestern Ross Sea and their impact on dense outflows of Antarctic Bottom Water. Deep Sea Research Part II: Topical Studies in Oceanography 56, 818–834. URL: https://doi.org/10.1016/j.dsr2.2008.10.026, doi:10.1016/j.dsr2.2008.10.026.

Padman, L., Siegfried, M.R., Fricker, H.A., 2018. Ocean Tide Influences on the Antarctic and Greenland Ice Sheets. Reviews of Geophysics 56, 142–184. URL: https://doi.org/10.1002/2016rg000546, doi:10.1002/2016rg000546.

Pardo, P.C., Pérez, F.F., Khatiwala, S., Ríos, A.F., 2014. Anthropogenic CO2 estimates in the Southern Ocean: Storage partitioning in the different water masses. Progress in oceanography 120, 230–242.

Parish, T.R., 1988. Surface winds over the Antarctic continent: A review. Reviews of Geophysics 26, 169–180. URL: https://agupubs.onlinelibrary.wiley.com/doi/abs/10.1029/RG026i001p00169, doi:10.1029/RG026i001p00169. _eprint: https://agupubs.onlinelibrary.wiley.com/doi/pdf/10.1029/RG026i001p00169.

Parish, T.R., Bromwich, D.H., 1987. The surface windfield over the Antarctic ice sheets. Nature 328, 51–54. Publisher: Nature Publishing Group.

Parish, T.R., Bromwich, D.H., 2007. Reexamination of the Near-Surface Airflow over the Antarctic Continent and Implications on Atmospheric Circulations at High Southern Latitudes. Monthly Weather Review 135, 1961–1973. doi:10.1175/MWR3374.1. publisher: American Meteorological Society Section: Monthly Weather Review.

Parish, T.R., Cassano, J.J., 2003. The Role of Katabatic Winds on the Antarctic Surface Wind Regime. Monthly Weather Review 131, 317–333. doi:10.1175/1520-0493(2003)131<0317:TROKWO>2.0.CO;2. publisher: American Meteorological Society Section: Monthly Weather Review.

Parish, T.R., Waight, K.T., 1987. The Forcing of Antarctic Katabatic Winds. Monthly Weather Review 115, 2214–2226. doi:10.1175/1520-0493(1987)115<2214:TFOAKW>2.0.CO;2. publisher: American Meteorological Society Section: Monthly Weather Review.

Pauling, A.G., Bitz, C.M., Smith, I.J., Langhorne, P.J., 2016. The response of the Southern Ocean and Antarctic sea ice to freshwater from ice shelves in an Earth system model. Journal of Climate 29, 1655–1672.

Pellichero, V., Sallée, J.B., Chapman, C.C., Downes, S.M., 2018. The southern ocean meridional overturning in the sea-ice sector is driven by freshwater fluxes. Nature Communications 9, 1789. URL: https://www.nature.com/articles/s41467-018-04101-2, doi:10.1038/s41467-018-04101-2. number: 1 Publisher: Nature Publishing Group.

Petrelli, P., Bindoff, N., Bergamasco, A., 2008. The sea ice dynamics of Terra Nova Bay and Ross Ice Shelf Polynyas during a spring and winter simulation. Journal of Geophysical Research: Oceans 113.

Pithan, F., Svensson, G., Caballero, R., Chechin, D., Cronin, T.W., Ekman, A.M.L., Neggers, R., Shupe, M.D., Solomon, A., Tjernström, M., Wendisch, M., 2018. Role of air-mass transformations in exchange between the Arctic and mid-latitudes. Nature Geoscience 11, 805–812. URL: https://www.nature.com/articles/s41561-018-0234-1, doi:10.1038/s41561-018-0234-1. bandiera_abtest: a Cg_type: Nature Research Journals Number: 11 Primary_atype: Reviews Publisher: Nature Publishing Group Subject_term: Atmospheric dynamics;Atmospheric science Subject_term_id: atmospheric-dynamics;atmospheric-science.

Poulsen, M.B., Jochum, M., Nuterman, R., 2018. Parameterized and resolved Southern Ocean eddy compensation. Ocean Modelling 124, 1–15. URL: https://www.sciencedirect.com/science/article/pii/S1463500318300258, doi:10.1016/j.ocemod.2018.01.008.

Pritchard, H.D., Ligtenberg, S.R.M., Fricker, H.A., Vaughan, D.G., van den Broeke, M.R., Padman, L., 2012. Antarctic ice-sheet loss driven by basal melting of ice shelves. Nature 484, 502–505. URL: https://www.nature.com/articles/nature10968, doi:10.1038/nature10968. bandiera_abtest: a Cg_type: Nature Research Journals Number: 7395 Primary_atype: Research Publisher: Nature Publishing Group Subject_term: Climate change Subject_term_id: climate-change.

Prodhomme, C., Batté, L., Massonnet, F., Davini, P., Bellprat, O., Guemas, V., Doblas-Reyes, F.J., 2016. Benefits of Increasing the Model Resolution for the Seasonal Forecast Quality in EC-Earth. Journal of Climate 29, 9141–9162. doi:10.1175/JCLI-D-16-0117.1. publisher: American Meteorological Society Section: Journal of Climate.

Purkey, S.G., Johnson, G.C., 2013. Antarctic Bottom Water Warming and Freshening: Contributions to Sea Level Rise, Ocean Freshwater Budgets, and Global Heat Gain. Journal of Climate 26, 6105–6122. URL: https://doi.org/10.1175/jcli-d-12-00834.1, doi:10.1175/jcli-d-12-00834.1.

Purkey, S.G., Smethie, W.M., Gebbie, G., Gordon, A.L., Sonnerup, R.E., Warner, M.J., Bullister, J.L., 2018. A Synoptic View of the Ventilation and Circulation of Antarctic Bottom Water from Chlorofluorocarbons and Natural Tracers. Annual Review of Marine Science 10, 503–527. URL: https://doi.org/10.1146/annurev-marine-121916-063414, doi:10.1146/annurev-marine-121916-063414. _eprint: https://doi.org/10.1146/annurev-marine-121916-063414.

Rahmstorf, S., 2006. Thermohaline ocean circulation. Issue: 10 Publication Title: Encyclopedia of quaternary sciences Volume: 1.

Raphael, M.N., Hobbs, W., Wainer, I., 2011. The effect of Antarctic sea ice on the Southern Hemisphere atmosphere during the southern summer. Climate Dynamics 36, 1403–1417. URL: https://doi.org/10.1007/s00382-010-0892-1, doi:10.1007/s00382-010-0892-1.

Reiser, F., Willmes, S., Hausmann, U., Heinemann, G., 2019. Predominant Sea Ice Fracture Zones Around Antarctica and Their Relation to Bathymetric Features. Geophysical Research Letters 46, 12117–12124. URL: https://onlinelibrary.wiley.com/doi/abs/10.1029/2019GL084624, doi:10.1029/2019GL084624. _eprint: https://onlinelibrary.wiley.com/doi/pdf/10.1029/2019GL084624.

Reiser, F., Willmes, S., Heinemann, G., 2020. A New Algorithm for Daily Sea Ice Lead Identification in the Arctic and Antarctic Winter from Thermal-Infrared Satellite Imagery. Remote Sensing 12, 1957. URL: https://www.mdpi.com/2072-4292/12/12/1957, doi:10.3390/rs12121957. number: 12 Publisher: Multidisciplinary Digital Publishing Institute.

Renault, L., Marchesiello, P., Masson, S., McWilliams, J.C., 2019a. Remarkable Control of Western Boundary Currents by Eddy Killing, a Mechanical Air-Sea Coupling Process. Geophysical Research Letters 46, 2743–2751. URL: https://agupubs.onlinelibrary.wiley.com/doi/abs/10.1029/2018GL081211, doi:10.1029/2018GL081211. _eprint: https://agupubs.onlinelibrary.wiley.com/doi/pdf/10.1029/2018GL081211.

Renault, L., Masson, S., Oerder, V., Jullien, S., Colas, F., 2019b. Disentangling the Mesoscale Ocean-Atmosphere Interactions. Journal of Geophysical Research: Oceans 124,

2164–2178. URL: https://onlinelibrary.wiley.com/doi/abs/10.1029/2018JC014628, doi:10.1029/2018JC014628.

Renault, L., McWilliams, J.C., Masson, S., 2017a. Satellite Observations of Imprint of Oceanic Current on Wind Stress by Air-Sea Coupling. Scientific Reports 7, 17747. URL: https://www.nature.com/articles/s41598-017-17939-1, doi:10.1038/s41598-017-17939-1. number: 1 Publisher: Nature Publishing Group.

Renault, L., McWilliams, J.C., Penven, P., 2017b. Modulation of the Agulhas Current Retroflection and Leakage by Oceanic Current Interaction with the Atmosphere in Coupled Simulations. Journal of Physical Oceanography 47, 2077–2100. doi:10.1175/JPO-D-16-0168.1. publisher: American Meteorological Society Section: Journal of Physical Oceanography.

Renault, L., Molemaker, M.J., McWilliams, J.C., Shchepetkin, A.F., Lemarié, F., Chelton, D., Illig, S., Hall, A., 2016. Modulation of Wind Work by Oceanic Current Interaction with the Atmosphere. Journal of Physical Oceanography 46, 1685–1704. URL: https://doi.org/10.1175/jpo-d-15-0232.1, doi:10.1175/jpo-d-15-0232.1.

Rignot, E., 2002. Mass balance of East Antarctic glaciers and ice shelves from satellite data. Annals of Glaciology 34, 217–227.

Rignot, E., Jacobs, S., Mouginot, J., Scheuchl, B., 2013. Ice-Shelf Melting Around Antarctica. Science 341, 266–270. URL: https://doi.org/10.1126/science.1235798, doi:10.1126/science.1235798.

Rignot, E., Mouginot, J., Scheuchl, B., 2011. Ice Flow of the Antarctic Ice Sheet. Science 333, 1427–1430. URL: https://science.sciencemag.org/content/333/6048/1427, doi:10.1126/science.1208336. publisher: American Association for the Advancement of Science Section: Report.

Rignot, E., Mouginot, J., Scheuchl, B., van den Broeke, M., van Wessem, M.J., Morlighem, M., 2019. Four decades of Antarctic Ice Sheet mass balance from 1979–2017. Proceedings of the National Academy of Sciences 116, 1095–1103. URL: http://www.pnas.org/lookup/doi/10.1073/pnas.1812883116, doi:10.1073/pnas.1812883116.

Rintoul, S.R., 1998. On the origin and influence of Adélie Land Bottom Water. Ocean, ice, and atmosphere: Interactions at the Antarctic continental margin 75, 151–171.

Rintoul, S.R., 2007. Rapid freshening of Antarctic Bottom Water formed in the Indian and Pacific oceans. Geophysical Research Letters 34.

Rintoul, S.R., 2018. The global influence of localized dynamics in the Southern Ocean. Nature 558, 209–218. URL: https://www.nature.com/articles/s41586-018-0182-3, doi:10.1038/s41586-018-0182-3. number: 7709 Publisher: Nature Publishing Group.

Roach, L.A., Dean, S.M., Renwick, J.A., 2018. Consistent biases in Antarctic sea ice concentration simulated by climate models. The Cryosphere 12, 365–383. URL: https://tc.copernicus.org/articles/12/365/2018/, doi:10.5194/tc-12-365-2018.

Roach, L.A., Dörr, J., Holmes, C.R., Massonnet, F., Blockley, E.W., Notz, D., Rackow, T., Raphael, M.N., O'Farrell, S.P., Bailey, D.A., Bitz, C.M., 2020. Antarctic Sea Ice Area in CMIP6. Geophysical Research Letters 47, e2019GL086729. URL: https://agupubs.onlinelibrary.wiley.com/doi/abs/10.1029/2019GL086729, doi:10.1029/2019GL086729. _eprint: https://agupubs.onlinelibrary.wiley.com/doi/pdf/10.1029/2019GL086729.

Roberts, M.J., Hewitt, H.T., Hyder, P., Ferreira, D., Josey, S.A., Mizielinski, M., Shelly, A., 2016. Impact of ocean resolution on coupled air-sea fluxes and large-scale climate. Geophysical Research Letters 43, 10,430–10,438. URL: https://agupubs.onlinelibrary.wiley.com/doi/abs/10.1002/2016GL070559, doi:10.1002/2016GL070559. _eprint: https://agupubs.onlinelibrary.wiley.com/doi/pdf/10.1002/2016GL070559.

Roberts, M.J., Vidale, P.L., Senior, C., Hewitt, H.T., Bates, C., Berthou, S., Chang, P., Christensen, H.M., Danilov, S., Demory, M.E., Griffies, S.M., Haarsma, R., Jung, T., Martin, G., Minobe, S., Ringler, T., Satoh, M., Schiemann, R., Scoccimarro, E., Stephens, G., Wehner, M.F., 2018. The Benefits of Global High Resolution for Climate Simulation: Process Understanding and the Enabling of Stakeholder Decisions at the Regional Scale. Bulletin of the American Meteorological Society 99, 2341–2359. doi:10.1175/BAMS-D-15-00320.1. publisher: American Meteorological Society Section: Bulletin of the American Meteorological Society.

Roquet, F., Madec, G., Brodeau, L., Nycander, J., 2015. Defining a simplified yet "realistic" equation of state for seawater. Journal of Physical Oceanography 45, 2564–2579.

Roquet, F., Williams, G., Hindell, M.A., Harcourt, R., McMahon, C., Guinet, C., Charrassin, J.B., Reverdin, G., Boehme, L., Lovell, P., Fedak, M., 2014. A Southern Indian Ocean database of hydrographic profiles obtained with instrumented elephant seals. Scientific Data 1, 140028. URL: https://doi.org/10.1038/sdata.2014.28, doi:10.1038/sdata.2014.28.

Rousset, C., Vancoppenolle, M., Madec, G., Fichefet, T., Flavoni, S., Barthélemy, A., Benshila, R., Chanut, J., Levy, C., Masson, S., Vivier, F., 2015. The Louvain-La-Neuve sea ice model LIM3.6: global and regional capabilities. Geoscientific Model Development 8, 2991–3005. URL: https://doi.org/10.5194/gmd-8-2991-2015, doi:10.5194/gmd-8-2991-2015.

Sallée, J.B., Matear, R.J., Rintoul, S.R., Lenton, A., 2012. Localized subduction of anthropogenic carbon dioxide in the Southern Hemisphere oceans. Nature Geoscience 5, 579–584. URL: https://www.nature.com/articles/ngeo1523, doi:10.1038/ngeo1523. bandiera_abtest: a Cg_type: Nature Research Journals Number: 8 Primary_atype: Research Publisher: Nature Publishing Group Subject_term: Atmospheric chemistry;Marine chemistry Subject_term_id: atmospheric-chemistry;marine-chemistry.

Sallée, J.B., Shuckburgh, E., Bruneau, N., Meijers, A.J., Bracegirdle, T.J., Wang, Z., 2013a. Assessment of Southern Ocean mixed-layer depths in CMIP5 models: Historical bias and forcing response. Journal of Geophysical Research: Oceans 118, 1845–1862. Publisher: Wiley Online Library.

Sallée, J.B., Shuckburgh, E., Bruneau, N., Meijers, A.J., Bracegirdle, T.J., Wang, Z., Roy, T., 2013b. Assessment of Southern Ocean water mass circulation and characteristics in CMIP5 models: Historical bias and forcing response. Journal of Geophysical Research: Oceans 118, 1830–1844.

Savijärvi, H., 2011. Antarctic local wind dynamics and polynya effects on the Adélie Land coast. Quarterly Journal of the Royal Meteorological Society 137, 1804–1811.

Scher, H.D., Whittaker, J.M., Williams, S.E., Latimer, J.C., Kordesch, W.E.C., Delaney, M.L., 2015. Onset of Antarctic Circumpolar Current 30 million years ago as Tasmanian Gateway aligned with westerlies. Nature 523, 580–583. URL: https://www.nature.com/articles/nature14598, doi:10.1038/nature14598. bandiera_abtest: a Cg_type: Nature Research Journals Number: 7562 Primary_atype: Research Publisher: Nature Publishing Group

Subject_term: Geochemistry;Palaeoceanography;Physical oceanography;Tectonics Subject_term_id: geochemistry;palaeoceanography;physical-oceanography;tectonics.

Schloesser, F., Friedrich, T., Timmermann, A., DeConto, R.M., Pollard, D., 2019. Antarctic iceberg impacts on future Southern Hemisphere climate. Nature Climate Change 9, 672–677.

Scott, R.B., Wang, F., 2005. Direct Evidence of an Oceanic Inverse Kinetic Energy Cascade from Satellite Altimetry. Journal of Physical Oceanography 35, 1650–1666. doi:10.1175/JPO2771.1. publisher: American Meteorological Society Section: Journal of Physical Oceanography.

Semmler, T., Danilov, S., Gierz, P., Goessling, H.F., Hegewald, J., Hinrichs, C., Koldunov, N., Khosravi, N., Mu, L., Rackow, T., others, 2019. Simulations for CMIP6 with the AWI climate model AWI-CM-1-1. Journal of Advances in Modeling Earth Systems , e2019MS002009.

Shepherd, A., Ivins, E., Rignot, E., Smith, B., van den Broeke, M., Velicogna, I., Whitehouse, P., Briggs, K., Joughin, I., Krinner, G., Nowicki, S., Payne, T., Scambos, T., Schlegel, N., Geruo, A., Agosta, C., Ahlstrom, A., Bobonis, G., Barletta, v., Blazquez, A., Bonin, J., Csatho, B., Cullather, R., Felikson, D., Fettweis, X., Forsberg, R., Gallee, H., Gardner, A., Gilbert, L., Groh, A., Gunter, B., Hanna, E., Harig, C., Helm, V., Horvath, A., Horwath, M., Khan, S., Kjeldsen, K.K., Konrad, H., Langen, P., Lecavalier, B., Loomis, B., Luthcke, S., McMillan, M., Melini, D., Mernild, S., Mohajerani, Y., Moore, P., Mouginot, J., Moyano, G., Muir, A., Nagler, T., Nield, G., Nilsson, J., Noel, B., Otosaka, I., Pattle, M.E., Peltier, W.R., Pie, N., Bietbroek, R., Rott, H., Sandberg-Sorensen, L., Sasgen, I., Save, H., Scheuchl, B., Schrama, E., Schroder, L., Seo, K.W., Simonsen, S., Slater, T., Spada, G., Sutterley, T., Talpe, M., Tarasov, L., van de Berg, W., van der Wal, W., van Wessem, M., Vishwakarma, B., Wiese, D., Wouters, B., 2018. Mass balance of the Antarctic Ice Sheet from 1992 to 2017. Nature 558, 219–222. URL: https://doi.org/10.1038/s41586-018-0179-y, doi:10.1038/s41586-018-0179-y. publisher: Nature.

Shepherd, A., Wingham, D., Rignot, E., 2004. Warm ocean is eroding West Antarctic Ice Sheet. Geophysical Research Letters 31. URL: https://agupubs.onlinelibrary.wiley.com/doi/abs/10.1029/2004GL021106, doi:10.1029/2004GL021106. _eprint: https://agupubs.onlinelibrary.wiley.com/doi/pdf/10.1029/2004GL021106.

Shine, K.P., Henderson-Sellers, A., 1985. The sensitivity of a thermodynamic sea ice model to changes in surface albedo parameterization. Journal of Geophysical Research: Atmospheres 90, 2243–2250. URL: https://agupubs.onlinelibrary.wiley.com/doi/abs/10.1029/JD090iD01p02243, doi:10.1029/JD090iD01p02243. _eprint: https://agupubs.onlinelibrary.wiley.com/doi/pdf/10.1029/JD090iD01p02243.

Silvano, A., Rintoul, S.R., Peña-Molino, B., Hobbs, W.R., van Wijk, E., Aoki, S., Tamura, T., Williams, G.D., 2018. Freshening by glacial meltwater enhances melting of ice shelves and reduces formation of Antarctic Bottom Water. Science advances 4, eaap9467.

Simmons, H.L., Jayne, S.R., Laurent, L.C.S., Weaver, A.J., 2004. Tidally driven mixing in a numerical model of the ocean general circulation. Ocean Modelling 6, 245–263. URL: https://www.sciencedirect.com/science/article/pii/S1463500303000118, doi:10.1016/S1463-5003(03)00011-8.

Small, R.J., deSzoeke, S.P., Xie, S.P., O'Neill, L., Seo, H., Song, Q., Cornillon, P., Spall, M., Minobe, S., 2008. Air–sea interaction over ocean fronts and eddies. Dynamics of Atmospheres and Oceans

45, 274–319. URL: https://www.sciencedirect.com/science/article/pii/S0377026508000341, doi:10.1016/j.dynatmoce.2008.01.001.

Small, R.J., Msadek, R., Kwon, Y.O., Booth, J.F., Zarzycki, C., 2019. Atmosphere surface storm track response to resolved ocean mesoscale in two sets of global climate model experiments. Climate Dynamics 52, 2067–2089. Publisher: Springer.

Smith, D.M., Dunstone, N.J., Scaife, A.A., Fiedler, E.K., Copsey, D., Hardiman, S.C., 2017. Atmospheric Response to Arctic and Antarctic Sea Ice: The Importance of Ocean–Atmosphere Coupling and the Background State. Journal of Climate 30, 4547–4565. doi:10.1175/JCLI-D-16-0564.1. publisher: American Meteorological Society Section: Journal of Climate.

Snow, K., Rintoul, S.R., Sloyan, B.M., Hogg, A.M., 2018. Change in Dense Shelf Water and Adélie Land Bottom Water Precipitated by Iceberg Calving. Geophysical Research Letters 45, 2380–2387. URL: https://doi.org/10.1002/2017gl076195, doi:10.1002/2017gl076195.

Snow, K., Sloyan, B., Rintoul, S., Hogg, A.M., Downes, S., 2016. Controls on circulation, cross-shelf exchange, and dense water formation in an Antarctic polynya. Geophysical Research Letters 43, 7089–7096.

Sokolov, S., Rintoul, S.R., 2009. Circumpolar structure and distribution of the Antarctic Circumpolar Current fronts: 1. Mean circumpolar paths. Journal of Geophysical Research: Oceans 114. Publisher: Wiley Online Library.

Solomon, S., Manning, M., Marquis, M., Qin, D., 2007. Climate change 2007-the physical science basis: Working group I contribution to the fourth assessment report of the IPCC. volume 4. Cambridge university press.

Song, H., Marshall, J., McGillicuddy, D.J., Seo, H., 2020. Impact of Current-Wind Interaction on Vertical Processes in the Southern Ocean. Journal of Geophysical Research: Oceans 125, e2020JC016046. URL: https://agupubs.onlinelibrary.wiley.com/doi/abs/10.1029/2020JC016046, doi:https://doi.org/10.1029/2020JC016046. _eprint: https://agupubs.onlinelibrary.wiley.com/doi/pdf/10.1029/2020JC016046.

Song, Q., Chelton, D.B., Esbensen, S.K., Thum, N., O'Neill, L.W., 2009. Coupling between Sea Surface Temperature and Low-Level Winds in Mesoscale Numerical Models. Journal of Climate 22, 146–164. doi:10.1175/2008JCLI2488.1. publisher: American Meteorological Society Section: Journal of Climate.

Soufflet, Y., Marchesiello, P., Lemarié, F., Jouanno, J., Capet, X., Debreu, L., Benshila, R., 2016. On effective resolution in ocean models. Ocean Modelling 98, 36–50. URL: https://www.sciencedirect.com/science/article/pii/S1463500315002401, doi:10.1016/j.ocemod.2015.12.004.

Speer, K., Rintoul, S.R., Sloyan, B., 2000. The Diabatic Deacon Cell. Journal of Physical Oceanography 30, 3212–3222. doi:10.1175/1520-0485(2000)030<3212:TDDC>2.0.CO;2. publisher: American Meteorological Society Section: Journal of Physical Oceanography.

Spence, P., Griffies, S.M., England, M.H., Hogg, A.M., Saenko, O.A., Jourdain, N.C., 2014. Rapid subsurface warming and circulation changes of Antarctic coastal waters by poleward shifting winds. Geophysical Research Letters 41, 4601–4610. URL: https://doi.org/10.1002/2014gl060613, doi:10.1002/2014gl060613.

Spence, P., Saenko, O.A., Dufour, C.O., Sommer, J.L., England, M.H., 2012. Mechanisms Maintaining Southern Ocean Meridional Heat Transport under Projected Wind Forcing. Journal of Physical Oceanography 42, 1923–1931. doi:10.1175/JPO-D-12-03.1. publisher: American Meteorological Society Section: Journal of Physical Oceanography.

Spreen, G., Kaleschke, L., Heygster, G., 2008. Sea ice remote sensing using AMSR-E 89-GHz channels. Journal of Geophysical Research: Oceans 113.

St-Laurent, P., Klinck, J.M., Dinniman, M.S., 2013. On the Role of Coastal Troughs in the Circulation of Warm Circumpolar Deep Water on Antarctic Shelves. Journal of Physical Oceanography 43, 51–64. doi:10.1175/JPO-D-11-0237.1. publisher: American Meteorological Society Section: Journal of Physical Oceanography.

Steele, J.H., 1995. Can ecological concepts span the land and ocean domains?, in: Ecological time series. Springer, pp. 5–19.

Stewart, A.L., Klocker, A., Menemenlis, D., 2018. Circum-Antarctic shoreward heat transport derived from an eddy-and tide-resolving simulation. Geophysical Research Letters 45, 834–845.

Stewart, A.L., Thompson, A.F., 2015. Eddy-mediated transport of warm Circumpolar Deep Water across the Antarctic Shelf Break. Geophysical Research Letters 42, 432–440. URL: https://doi.org/10.1002/2014gl062281, doi:10.1002/2014gl062281.

Stewart, A.L., Thompson, A.F., 2016. Eddy generation and jet formation via dense water outflows across the Antarctic continental slope. Journal of Physical Oceanography 46, 3729–3750.

Stocker, T.F., Wright, D.G., Broecker, W.S., 1992. The influence of high-latitude surface forcing on the global thermohaline circulation. Paleoceanography 7, 529–541.

Storkey, D., Blaker, A.T., Mathiot, P., Megann, A., Aksenov, Y., Blockley, E.W., Calvert, D., Graham, T., Hewitt, H.T., Hyder, P., others, 2018. UK Global Ocean GO6 and GO7: A traceable hierarchy of model resolutions. Geoscientific Model Development 11, 3187–3213.

Swart, N.C., Gille, S.T., Fyfe, J.C., Gillett, N.P., 2018. Recent Southern Ocean warming and freshening driven by greenhouse gas emissions and ozone depletion. Nature Geoscience 11, 836–841. URL: https://doi.org/10.1038/s41561-018-0226-1, doi:10.1038/s41561-018-0226-1.

Swift, J.H., 1984. The circulation of the Denmark Strait and Iceland-Scotland overflow waters in the North Atlantic. Deep Sea Research Part A. Oceanographic Research Papers 31, 1339–1355. URL: https://www.sciencedirect.com/science/article/pii/0198014984900050, doi:10.1016/0198-0149(84)90005-0.

Tamsitt, V., Abernathey, R.P., Mazloff, M.R., Wang, J., Talley, L.D., 2018. Transformation of Deep Water Masses Along Lagrangian Upwelling Pathways in the Southern Ocean. Journal of Geophysical Research: Oceans 123, 1994–2017. URL: https://onlinelibrary.wiley.com/doi/abs/10.1002/2017JC013409, doi:10.1002/2017JC013409. _eprint: https://agupubs.onlinelibrary.wiley.com/doi/pdf/10.1002/2017JC013409.

Tamura, T., Ohshima, K.I., Fraser, A.D., Williams, G.D., 2016. Sea ice production variability in Antarctic coastal polynyas. Journal of Geophysical Research: Oceans 121, 2967–2979.

Tamura, T., Ohshima, K.I., Nihashi, S., 2008. Mapping of sea ice production for Antarctic coastal polynyas. Geophysical Research Letters 35, n/a–n/a. URL: https://doi.org/10.1029/2007gl032903, doi:10.1029/2007gl032903.

Tamura, T., Williams, G.D., Fraser, A.D., Ohshima, K.I., 2012. Potential regime shift in decreased sea ice production after the Mertz Glacier calving. Nature Communications 3. URL: https://doi.org/10.1038/ncomms1820, doi:10.1038/ncomms1820.

Taylor, P.C., Boeke, R.C., Li, Y., Thompson, D.W.J., 2019. Arctic cloud annual cycle biases in climate models. Atmospheric Chemistry and Physics 19, 8759–8782. URL: https://acp.copernicus.org/articles/19/8759/2019/, doi:10.5194/acp-19-8759-2019. publisher: Copernicus GmbH.

Tetzner, D., Thomas, E., Allen, C., 2019. A Validation of ERA5 Reanalysis Data in the Southern Antarctic Peninsula—Ellsworth Land Region, and Its Implications for Ice Core Studies. Geosciences 9, 289.

Thompson, A.F., Garabato, A.C.N., 2014. Equilibration of the Antarctic Circumpolar Current by Standing Meanders. Journal of Physical Oceanography 44, 1811–1828. doi:10.1175/JPO-D-13-0163.1. publisher: American Meteorological Society Section: Journal of Physical Oceanography.

Thompson, A.F., Stewart, A.L., Spence, P., Heywood, K.J., 2018. The Antarctic Slope Current in a Changing Climate. Reviews of Geophysics .

Tournadre, J., Girard-Ardhuin, F., Legrésy, B., 2012. Antarctic icebergs distributions, 2002–2010. Journal of Geophysical Research: Oceans 117. URL: https://agupubs.onlinelibrary.wiley.com/doi/abs/10.1029/2011JC007441, doi:10.1029/2011JC007441. _eprint: https://agupubs.onlinelibrary.wiley.com/doi/pdf/10.1029/2011JC007441.

Uppala, S.M., KÅllberg, P.W., Simmons, A.J., Andrae, U., Bechtold, V.D.C., Fiorino, M., Gibson, J.K., Haseler, J., Hernandez, A., Kelly, G.A., Li, X., Onogi, K., Saarinen, S., Sokka, N., Allan, R.P., Andersson, E., Arpe, K., Balmaseda, M.A., Beljaars, A.C.M., Berg, L.V.D., Bidlot, J., Bormann, N., Caires, S., Chevallier, F., Dethof, A., Dragosavac, M., Fisher, M., Fuentes, M., Hagemann, S., Hólm, E., Hoskins, B.J., Isaksen, L., Janssen, P.a.E.M., Jenne, R., Mcnally, A.P., Mahfouf, J.F., Morcrette, J.J., Rayner, N.A., Saunders, R.W., Simon, P., Sterl, A., Trenberth, K.E., Untch, A., Vasiljevic, D., Viterbo, P., Woollen, J., 2005. The ERA-40 re-analysis. Quarterly Journal of the Royal Meteorological Society 131, 2961–3012. doi:10.1256/qj.04.176. _eprint: https://rmets.onlinelibrary.wiley.com/doi/pdf/10.1256/qj.04.176.

Van Achter, G., Fichefet, T., Goosse, H., Pelletier, C., Huot, P.V., Sterlin, J., Fraser, A.D., Parter-Smith, R., Lemieux, J.F., Haubner, K., 2021. Modelling landfast sea ice and its influence on ocean-ice interactions in the area of the Totten Glacier, East Antarctica. Ocean Modelling (Submitted).

Vancoppenolle, M., Fichefet, T., Goosse, H., Bouillon, S., Madec, G., Maqueda, M.A.M., 2009. Simulating the mass balance and salinity of Arctic and Antarctic sea ice. 1. Model description and validation. Ocean Modelling 27, 33–53. URL: https://doi.org/10.1016/j.ocemod.2008.10.005, doi:10.1016/j.ocemod.2008.10.005.

Villas Bôas, A.B., Sato, O.T., Chaigneau, A., Castelão, G.P., 2015. The signature of mesoscale eddies on the air-sea turbulent heat fluxes in the South Atlantic Ocean. Geophysical Research Letters 42, 1856–1862. Publisher: Wiley Online Library.

Volkov, D.L., Fu, L.L., Lee, T., 2010. Mechanisms of the meridional heat transport in the Southern Ocean. Ocean Dynamics 60, 791–801. Publisher: Springer.

Volkov, D.L., Lee, T., Fu, L.L., 2008. Eddy-induced meridional heat transport in the ocean. Geophysical Research Letters 35. Publisher: Wiley Online Library.

Walin, G., 1982. On the relation between sea-surface heat flow and thermal circulation in the ocean. Tellus 34, 187–195. Publisher: Wiley Online Library.

Walsh, K., Lavender, S., Scoccimarro, E., Murakami, H., 2013. Resolution dependence of tropical cyclone formation in CMIP3 and finer resolution models. Climate Dynamics 40, 585–599. URL: https://doi.org/10.1007/s00382-012-1298-z, doi:10.1007/s00382-012-1298-z.

Wang, G., Garcia, D., Liu, Y., de Jeu, R., Johannes Dolman, A., 2012. A three-dimensional gap filling method for large geophysical datasets: Application to global satellite soil moisture observations. Environmental Modelling & Software 30, 139–142. URL: https://www.sciencedirect.com/science/article/pii/S1364815211002453, doi:10.1016/j.envsoft.2011.10.015.

Wang, Q., Danilov, S., Hellmer, H., Sidorenko, D., Schröter, J., Jung, T., 2013. Enhanced cross-shelf exchange by tides in the western Ross Sea. Geophysical Research Letters 40, 5735–5739. URL: https://doi.org/10.1002/2013gl058207, doi:10.1002/2013gl058207.

Wang, Q., Danilov, S., Sidorenko, D., Timmermann, R., Wekerle, C., Wang, X., Jung, T., Schröter, J., 2014. The Finite Element Sea Ice-Ocean Model (FESOM) v. 1.4: formulation of an ocean general circulation model. Geoscientific Model Development 7, 663–693.

Wang, Y., 2001. An Explicit Simulation of Tropical Cyclones with a Triply Nested Movable Mesh Primitive Equation Model: TCM3. Part I: Model Description and Control Experiment. Monthly Weather Review 129, 1370–1394. doi:10.1175/1520-0493(2001)129<1370:AESOTC>2.0.CO;2. publisher: American Meteorological Society Section: Monthly Weather Review.

Waterman, S., Jayne, S.R., 2011. Eddy-Mean Flow Interactions in the Along-Stream Development of a Western Boundary Current Jet: An Idealized Model Study. Journal of Physical Oceanography 41, 682–707. doi:10.1175/2010JPO4477.1. publisher: American Meteorological Society Section: Journal of Physical Oceanography.

Weatherall, P., Marks, K.M., Jakobsson, M., Schmitt, T., Tani, S., Arndt, J.E., Rovere, M., Chayes, D., Ferrini, V., Wigley, R., 2015. A new digital bathymetric model of the world\textbackslashtextquotesingles oceans. Earth and Space Science 2, 331–345. URL: https://doi.org/10.1002/2015ea000107, doi:10.1002/2015ea000107.

Weijer, W., Veneziani, M., Stössel, A., Hecht, M.W., Jeffery, N., Jonko, A., Hodos, T., Wang, H., 2017. Local atmospheric response to an open-ocean polynya in a high-resolution climate model. Journal of Climate 30, 1629–1641.

Weiss, J., Dansereau, V., 2017. Linking scales in sea ice mechanics. Philosophical Transactions of the Royal Society A: Mathematical, Physical and Engineering Sciences 375, 20150352. URL: https://royalsocietypublishing.org/doi/full/10.1098/rsta.2015.0352, doi:10.1098/rsta.2015.0352. publisher: Royal Society.

Wendler, G., Stearns, C., Weidner, G., Dargaud, G., Parish, T., 1997. On the extraordinary katabatic winds of Adélie Land. Journal of Geophysical Research: Atmospheres 102, 4463–4474.

van Wessem, J.M., Reijmer, C.H., van de Berg, W.J., van Den Broeke, M.R., Cook, A.J., van Ulft, L.H., van Meijgaard, E., 2015. Temperature and wind climate of the Antarctic Peninsula as simulated by a high-resolution regional atmospheric climate model. Journal of Climate 28, 7306–7326.

Whitworth III, T., Orsi, A., Kim, S.J., Nowlin Jr, W., Locarnini, R., 1998. Water masses and mixing near the Antarctic Slope Front. Ocean, ice, and atmosphere: interactions at the Antarctic continental margin 75, 1–27.

Williams, G., Maksym, T., Wilkinson, J., Kunz, C., Murphy, C., Kimball, P., Singh, H., 2015. Thick and deformed Antarctic sea ice mapped with autonomous underwater vehicles. Nature Geoscience 8, 61–67. URL: https://www.nature.com/articles/ngeo2299, doi:10.1038/ngeo2299. bandiera_abtest: a Cg_type: Nature Research Journals Number: 1 Primary_atype: Research Publisher: Nature Publishing Group Subject_term: Cryospheric science;Geomorphology;Physical oceanography Subject_term_id: cryospheric-science;geomorphology;physical-oceanography.

Williams, G.D., Bindoff, N.L., Marsland, S.J., Rintoul, S.R., 2008. Formation and export of dense shelf water from the Adélie Depression, East Antarctica. Journal of Geophysical Research 113. URL: https://doi.org/10.1029/2007jc004346, doi:10.1029/2007jc004346.

Williams, P.D., Alexander, M.J., Barnes, E.A., Butler, A.H., Davies, H.C., Garfinkel, C.I., Kushnir, Y., Lane, T.P., Lundquist, J.K., Martius, O., Maue, R.N., Peltier, W.R., Sato, K., Scaife, A.A., Zhang, C., 2017. A Census of Atmospheric Variability From Seconds to Decades. Geophysical Research Letters 44, 11,201–11,211. URL: https://agupubs.onlinelibrary.wiley.com/doi/abs/10.1002/2017GL075483, doi:10.1002/2017GL075483. _eprint: https://agupubs.onlinelibrary.wiley.com/doi/pdf/10.1002/2017GL075483.

Yan, X., Kang, D., Curchitser, E.N., Pang, C., 2019. Energetics of Eddy–Mean Flow Interactions along the Western Boundary Currents in the North Pacific. Journal of Physical Oceanography 49, 789–810. doi:10.1175/JPO-D-18-0201.1. publisher: American Meteorological Society Section: Journal of Physical Oceanography.

Zappa, G., Shaffrey, L.C., Hodges, K.I., 2013. The Ability of CMIP5 Models to Simulate North Atlantic Extratropical Cyclones. Journal of Climate 26, 5379–5396. doi:10.1175/JCLI-D-12-00501.1. publisher: American Meteorological Society Section: Journal of Climate.

Zhang, Z., Vihma, T., Stössel, A., Uotila, P., 2015. The role of wind forcing from operational analyses for the model representation of Antarctic coastal sea ice. Ocean Modelling 94, 95–111.

Zweng, M., Reagan, J., Antonov, J., Mishonov, A., Boyer, T., Garcia, H., Baranova, O., Johnson, D., Seidov, D., Biddle, M., 2013. World Ocean Atlas2013, Volume 2: Salinity. NOAA Atlas NESDIS 74 Edition: S.Levitus; A.Mishonov.

Zweng, M., Reagan, J., Seidov, D., Boyer, T., Locarnini, R., Garcia, H., Mishonov, A., Baranova, O., Weathers, K., Paver, C., Smolyar, I., 2018. World Ocean Atlas 2018, Volume 2: Salinity. NOAA Atlas NESDIS 82 Edition: A. Mishonov.